INAUGURAL-DISSERTATION

zur

Erlangung der Doktorwürde

der

Gesamtfakultät für Mathematik,

Ingenieur- und Naturwissenschaften

der

Ruprecht–Karls–Universität

Heidelberg

vorgelegt von

M.Sc. Nils Schorndorf

Tag der mündlichen Prüfung: 04-12-2024

Soil-Sensitive Proxies in Northeast Yucatán Speleothems Since the Classic Maya Period

Gutachter: Prof. Dr. Wolfgang Stinnesbeck
Prof. Dr. Norbert Frank

Abstract

In this thesis, hydroclimatic and environmental changes in the northeastern Yucatán Peninsula (YP), Mexico, over the past 1,400 years were reconstructed using multi-proxy analyses of stalagmites from Áaktun Kóopo Cave. This region is crucial for understanding interactions between climate and Maya civilization, though detailed records linking changes in hydroclimate and vegetation to major societal transitions have thus far been lacking. The high uranium contents in these stalagmites enabled precise ^{230}Th/U dating, and some stalagmite chronologies could be further improved by analyzing seasonal variations in certain trace element ratios through LA-ICP-MS analyses.

The main findings are that multiple elements and isotopes together can trace major transitions in soil and vegetation conditions. Following a growth hiatus, stalagmite E0-C reveals a persistent shift in soil-sensitive proxies (δ^{13}C, dead carbon fraction (DCF), U/Ca) around the onset of the Medieval Warm Period (MWP). This shift can be understood as reflecting major changes in soil CO_2 levels, openness of the system, and vegetation (C3/C4 plants). Although there is no direct evidence of past agriculture above the cave, the proxies suggest that human activities such as deforestation and cultivation may have impacted the soil environment before and after the Terminal Classic Period (TCP). At the same time, the YP experiences a shift toward wetter conditions at the beginning of the MWP, suggesting atmospheric reorganization that was likely linked to tropical Atlantic sea surface temperature (SST) and trade wind patterns.

Finally, a composite δ^{18}O record from Áaktun Kóopo Cave provides a qualitative high-resolution rainfall history for the northeastern YP over the last 1,400 years, capturing prominent centennial-scale hydroclimate fluctuations. These variations align with other stalagmite records from the YP and beyond, indicating common forcings such as tropical SSTs in the Atlantic (and Pacific) and displacements in the mean path of the Intertropical Convergence Zone (ITCZ). Preliminary spectral analyses show periodicities consistent with ENSO variability and solar cycles, indicating that solar forcing may influence regional hydroclimate, though this relationship varies over time. These findings underscore the importance of further research in speleothem archives to better understand Mesoamerican climate dynamics on both local and regional scales.

Zusammenfassung

In dieser Arbeit wurden hydroklimatische und umweltbezogene Veränderungen im Nordosten der mexikanischen Halbinsel Yucatán (YP) in den letzten 1.400 Jahren anhand von Multi-Proxy-Analysen von Stalagmiten aus der Áaktun Kóopo-Höhle rekonstruiert. Diese Region ist für das Verständnis der Wechselwirkungen zwischen dem Klima und der Maya-Zivilisation von entscheidender Bedeutung, obwohl detaillierte Aufzeichnungen, die Veränderungen des Hydroklimas und der Vegetation mit größeren gesellschaftlichen Übergängen in Verbindung bringen, bisher fehlten. Die hohen Urangehalte in diesen Stalagmiten ermöglichten eine präzise ^{230}Th/U-Datierung, und einige Stalagmiten-Chronologien konnten durch die Analyse saisonaler Schwankungen bestimmter Spurenelementverhältnisse mittels LA-ICP-MS-Analysen weiter verbessert werden.

ie wichtigsten Ergebnisse zeigen, dass mehrere Elemente und Isotope zusammen große Übergänge in den Boden- und Vegetationsbedingungen nachzeichnen können. Nach einer Wachstumspause zeigt der Stalagmit E0-C eine anhaltende Verschiebung bei bodensensitiven Proxies (δ^{13}C, toter Kohlenstoffanteil (DCF), U/Ca) um den Beginn der mittelalterlichen Warmzeit (MWP). Diese Verschiebung kann als Ausdruck größerer Veränderungen im CO_2-Gehalt des Bodens, der Offenheit des Systems und der Vegetation (C3/C4-Pflanzen) verstanden werden. Obwohl es keine direkten Beweise für eine frühere Landwirtschaft oberhalb der Höhle gibt, deuten die Proxies darauf hin, dass menschliche Aktivitäten wie Abholzung und Kultivierung das Bodenmilieu vor und nach der Terminal Classic Period (TCP) beeinträchtigt haben könnten. Gleichzeitig erfährt die YP zu Beginn der MWP eine Verschiebung hin zu feuchteren Bedingungen, was auf eine atmosphärische Umstrukturierung hindeutet, die wahrscheinlich mit der Meeresoberflächentemperatur (SST) des tropischen Atlantiks und den Passatwindmustern zusammenhing.

Zu guter Letzt liefert ein zusammengesetzter δ^{18}O-Datensatz aus der Áaktun Kóopo-Höhle eine qualitativ hochauflösende Niederschlagsgeschichte für die nordöstliche YP über die letzten 1.400 Jahre, die ausgeprägte Schwankungen des Hydroklimas auf Jahrhundertskalen erfasst. Diese Schwankungen stimmen mit anderen Stalagmitenaufzeichnungen der YP und darüber hinaus überein und deuten auf gemeinsame Einflüsse wie tropische SST im Atlantik (und Pazifik) und Verschiebungen im mittleren Verlauf der intertropischen Konvergenzzone (ITCZ) hin.

Erste Spektralanalysen zeigen Periodizitäten, die mit ENSO-Variabilität und Sonnenzyklen übereinstimmen, was darauf hindeutet, dass der solare Einfluss das regionale Hydroklima beeinflussen kann, auch wenn diese Beziehung im Laufe der Zeit variiert. Diese Ergebnisse unterstreichen die Bedeutung weiterer Forschungen in Speläothemarchiven für ein besseres Verständnis der mesoamerikanischen Klimadynamik sowohl auf lokaler als auch auf regionaler Ebene.

Contents

List of Abbreviations

AD Anno Domini

AMOC Atlantic Meridional Overturning Circulation

AMS Accelerator Mass Spectrometer

CE Common Era

CLLJ Caribbean Low Level Jet

DCF Dead Carbon Fraction

DFT Distance From Top

DIC Dissolved Inorganic Carbon

DWL Drip Water Line

EDW Estrella Drip Water

GMWL Global Meteoric Water Line

GP Growth Period

ICD Incongruent Carbonate Dissolution

ITCZ Inter-Tropical Convergence Zone

KDE Kernel Density Estimate

LA-ICP-MS Laser Ablation Inductively Coupled Plasma Mass Spectrometry

LIA Little Ice Age

LMWL Local Meteoric Water Line

LOD Limit Of Detection

MAT Mean Annual Temperature

MCA/MWP Medieval Climate Anomaly/Medieval Warm Period

MSD Midsummer Drought

MSWD Mean Squared Weighted Deviation

NASH North Atlantic Subtropical High

P-E Precipitation minus Evaporation

PCP Prior Calcite Precipitation

pMC Percent Modern Carbon

RH Relative Humidity

SLP Sea Level Pressure

SOM Soil Organic Matter

SST Sea Surface Temperature

SW Sea Water

TCP Terminal Classic Period

THL Temperature/Humidity Logger

TOC Total Organic Carbon

VPDB Vienna Pee Dee Belemnite

VSMOW Vienna Standard Mean Ocean Water

XRD X-ray Diffraction

YP Yucatán Peninsula

yr BP Years Before Present

ZAC Zero-Age Carbonate/Calcite

Preface

The northern part of the Yucatán Peninsula (YP) in southeastern Mexico (Fig. 1) is a region of significant climatic and cultural interest due to its challenging environmental conditions, including limited fertile soil, scarce freshwater resources, and frequent extreme weather events, such as hurricane (Ward, 1985). Despite these challenges, the Maya civilization thrived for centuries, developing complex societal structures and adapting to a dynamic climate, until around 800–1000 AD, when the Classic Maya experienced a period of profound social and political upheaval, leading to widespread population decline and abandonment of many urban centers (e.g., Douglas et al., 2015).

The Maya established one of the most prominent complex societies in Mesoamerica characterized by the cultivation of staple crops and the establishment of advanced cities. The first Maya cities developed around 750 BC (Olmedo Vera et al., 1997), and from approximately 250 AD, the Classic period is largely defined by the Maya raising sculpted monuments with Long Count dates. The disintegration of the Classic Maya civilization between 800 and 1000 AD, an interval known as the Terminal Classic Period (TCP; Fig. 2) (Lowe, 1985), likely involved both cultural and climatic factors (e.g., Haug et al., 2003; Kennett et al., 2012). Over the past few decades, studies have indicated that a series of unprecedented droughts contributed to this societal disintegration (Curtis et al., 1996; Haug et al., 2001; Medina-Elizalde and Rohling, 2012; Douglas et al., 2016; Hoggarth et al., 2017; Evans et al., 2018). However, the idea that drought alone was the primary cause of this societal collapse is now largely dismissed. Furthermore, there is increasing evidence for earlier periods of temporary urban abandonment, population declines, and construction hiatuses, observed from approximately 150 to 200 AD (e.g., Dunning et al., 2012), which have also been linked to unusually dry conditions (Hodell et al., 2001, 2005, 2007; Rosenmeier et al., 2002; Wahl et al., 2007; Webster et al., 2007). Consequently, climate change was most likely accompanied by land use changes. The first evidence of substantial and recurring droughts during the TCP (800–1000 AD) was provided by sediment records from

Lake Chichancanab (Figs. 1 and 2), which revealed a 200-year shift in the net water balance of evaporation minus precipitation (E-P) (Hodell et al., 1995), marking the TCP as one of the driest periods in the northern YP during the Holocene. Hodell et al. (1995) suggested that these droughts may have been regional in extent, with spatially varying ecological and anthropological consequences. Further evidence of spatial and temporal precipitation variability is presented through numerous marine and lacustrine records (Douglas et al., 2015; Haug et al., 2003; Curtis et al., 1996; Hodell et al., 2001, 2005, 2007; Rosenmeier et al., 2002; Wahl et al., 2007; Hodell et al., 1995; Aragón-Moreno et al., 2012; Vela-Pelaez et al., 2018; Stansell et al., 2020), speleothems (Kennett et al., 2012; Webster et al., 2007; Medina-Elizalde et al., 2010; Lachniet et al., 2012; Akers et al., 2016), and, to a lesser extent, fossil corals (Wu et al., 2017) and tree rings (Stahle et al., 2011). A review of climate proxy data by Douglas et al. (2016) summarized the spatial variability in drought timing and intensity during the Classic Period, with evidence for earlier and stronger droughts in Belize and the central Petén relative to the northern YP.

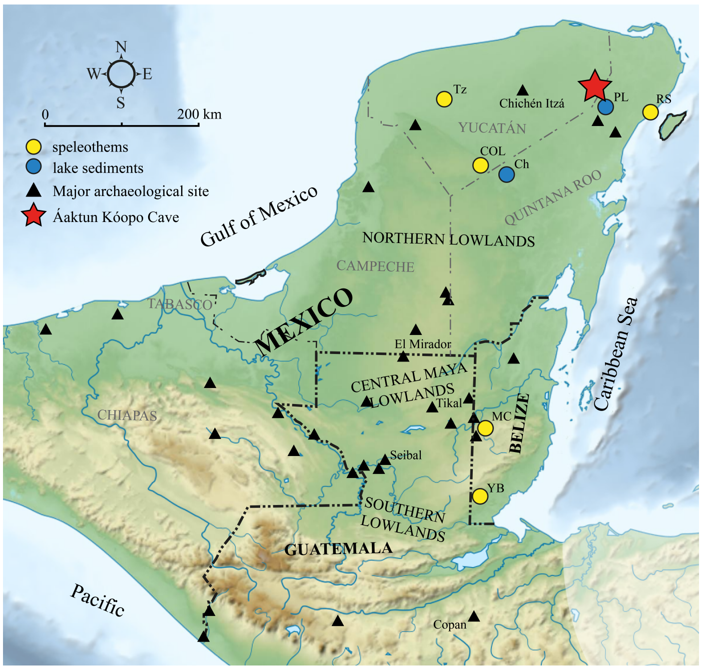

Figure 1. Location of proxy records in the Maya Lowlands. (Yellow dots) speleothem records, (blue dots) sediments from lakes. (Red star) Location of Áaktun Kóopo Cave. Major archaeological sites are shown as black triangles. In Detail: Northern Maya Lowlands (Tz: Tzabnah Cave (Medina-Elizalde et al., 2010; James, 2023); PL: Punta Laguna (Curtis et al., 1996); RS: Rio Secreto Cave (Medina-Elizalde et al., 2016a); Ch: Chichancanab (Hodell et al., 2005); COL: Columnas Cave (James, 2023)). Central Lowlands and Belize (MC: Macal Chasm Cave (Akers et al., 2016); YB: Yok Balum Cave (Kennett et al., 2012; Ridley et al., 2015; Asmerom et al., 2020)). Figure redrawn after Turner and Sabloff (2012), with modifications.

Speleothems have been frequently used to reconstruct paleo-precipitation in Central America and the Caribbean across the late Holocene, most commonly through stable isotope variability (e.g., Medina-Elizalde et al., 2010; Lachniet et al., 2012; Medina-Elizalde et al., 2016a; Ridley et al., 2015; Asmerom et al., 2020; Pollock et al., 2016; Lechleitner et al., 2017) (Fig. 2). In some cases, decadal-resolution stable isotope records have revealed up to eight pronounced drought intervals between 800 and 950 AD (Medina-Elizalde et al., 2010) (Fig. 2). Assuming less than 20% variation in annual mean precipitation (Medina-Elizalde and Rohling, 2012), their careful assessment indicated a 20–65% decrease during the TCP, which was subsequently confirmed by other studies (Douglas et al., 2016; Evans et al., 2018). In contrast to the recurring droughts of the 9th century, the period between ∼520 BC and 166 AD reveals a prolonged interval of wet conditions, termed the "Late Preclassic Humid Period" (Medina-Elizalde et al., 2016a), with only a few substantial drought intervals. Medina-Elizalde et al. (2016a) suggested that the Preclassic abandonment of major centers in the Maya Lowlands was synchronous with two multi-decadal events of major precipitation reductions, with magnitudes of $-55 \pm 13\%$ and $-49 \pm 12\%$, centered at 186 and 234 AD, respectively.

Clear evidence has thus been presented of climate-driven changes in regional precipitation and/or the P-E water balance, resulting in substantially below-average moisture conditions, as well as the impact of these droughts on Maya cultural evolution. However, no single forcing mechanism has yet been identified to fully explain these drought events (Douglas et al., 2016). The northern YP is primarily influenced by the North Atlantic, while Belize and central Petén are more affected by the Pacific, emphasizing the need for improved characterization of spatial variability in drought impacts (Douglas et al., 2015, 2016; Oster et al., 2019; Nooren et al., 2018). While precipitation and water availability were likely critical factors influencing Maya society, their role remains debated due to the varied rainfall patterns across the YP, the accessibility of cenotes as water sources, and the Maya's advanced ability to adapt to challenging environmental conditions (Scarborough and Gallopin, 1991; Bhattacharya et al., 2022). Numerous studies have shown that multi-proxy approaches can significantly improve the interpretation of climate change (Warken et al., 2018; Serrato-Marks et al., 2021; Vieten et al., 2024a). For the YP, recent studies from the Holocene have used δ^{18}O and δ^{13}C values in combination with trace element ratios to reconstruct regional moisture and precipitation (Asmerom et al., 2020; Serrato-Marks et al., 2021; Jamieson et al., 2016; Lechleitner et al., 2016; Warken et al., 2021). These initial records of stalagmite Mg/Ca, Sr/Ca and U/Ca ratios from the YP highlight their potential use as proxies for wet/dry conditions in this area. The use of in-situ laser ablation inductively coupled plasma mass spectrometry (LA-ICP-MS) permits element/Ca ratio quantification on tens of micrometers spatial scales, corresponding to ultra-high temporal resolution, revealing largely underexplored potential for drought reconstruction (Warken et al., 2018; Treble et al., 2003; Borsato et al., 2007). In addition to reconstructing precipitation, trace and minor elements in speleothems provide insights into soil and host rock weathering, element transport, carbonate formation, and may even reveal human impacts on soil carbon storage (Warken et al., 2018, 2021; Treble et al., 2003; Borsato et al., 2007; Fairchild and Treble, 2009). Such ultra-high-resolution analyses require a highly precise chronology of speleothem growth, which can now be achieved with advances in ultra-precise age determination using ^{230}Th/U dating, providing sub-decadal age precision and enabling the examination of growth rate variability (Asmerom et al., 2020; Arps, 2017; Kerber et al., 2023).

Further investigation into the spatial variability of drought timing, intensity and its consequences for soil carbon cycling and land-use are needed, particularly given the sharp precipitation gradient across the YP, both latitudinally and meridionally (De la Barreda et al., 2020) (Fig. I.1).

This dissertation aims, therefore, to improve our understanding of climate proxies and to pinpoint the timing and strength of key climate events by using trace elements and stable isotopes from stalagmites in Áaktun Kóopo Cave in the northeastern YP. This site was selected for its unique potential to provide a continuous climate record covering different periods of Maya cultural history—from the thriving Classic Period to the population and cultural decline during the TCP, and through the Postclassic and Historic periods. Additionally, the many regional studies available make it an ideal site for comparison (Figs. 1 and 2).

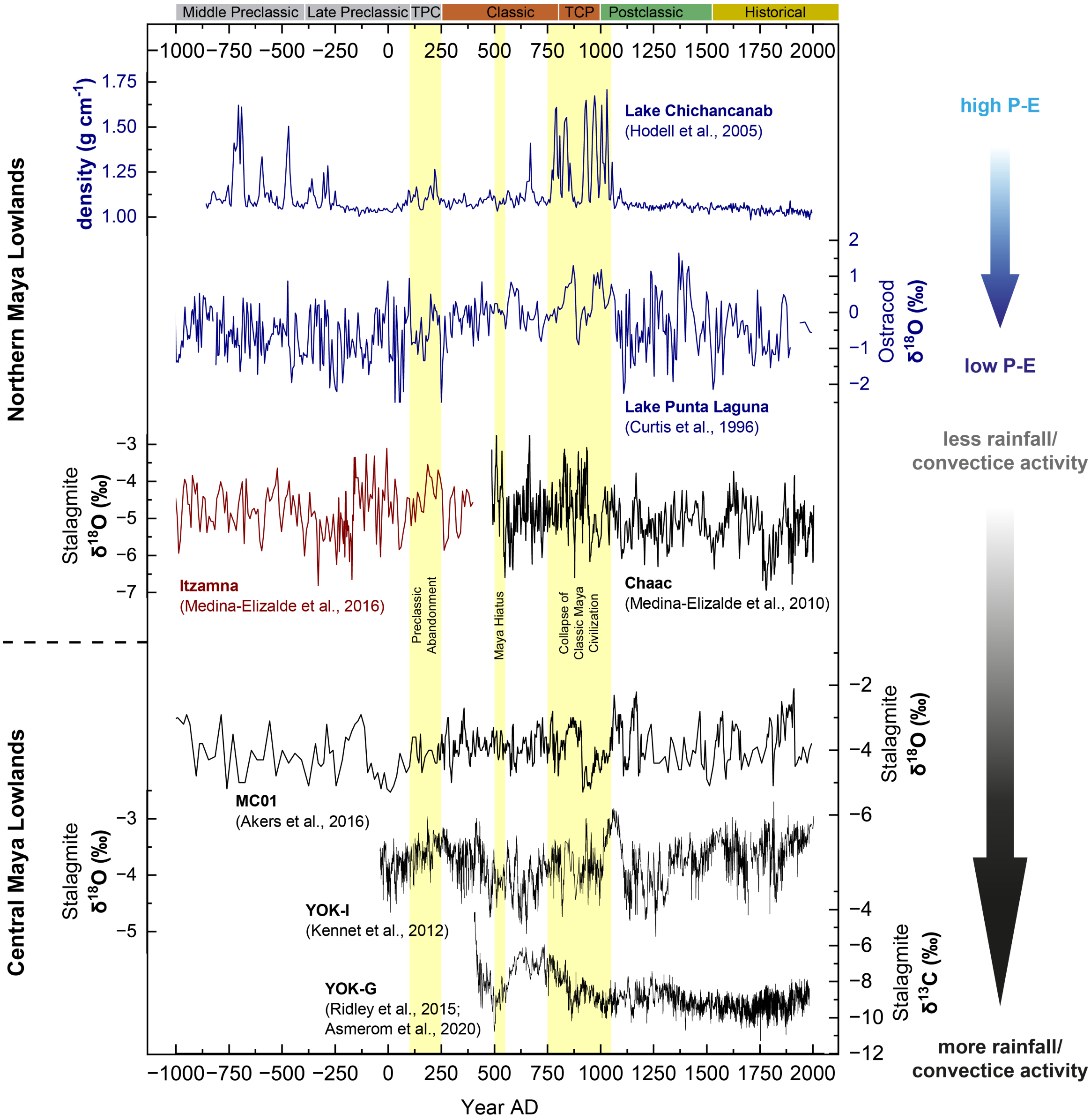

Figure 2. Compilation of proxy records from the Northern and Central Maya Lowlands, illustrating changes in precipitation and the precipitation minus evaporation (P–E) water balance over the past 3,000 years. Top panel shows the records from the northern Maya Lowlands: Lake Chichancanab (Hodell et al., 2005); Lake Punta Laguna (Curtis et al., 1996); Stalagmite records from Río Secreto (Medina-Elizalde et al., 2016a) and Tzabnah Cave (Medina-Elizalde et al., 2010). Bottom panels show the stalagmite records from the Central Lowlands and Belize: Macal Chasm Cave (Akers et al., 2016) and Yok Balum Cave (Kennett et al., 2012; Ridley et al., 2015; Asmerom et al., 2020). Vertical yellow bars indicate the timing of major societal disintegration events and/or urban abandonments, as discussed in the main text.

Chapter Overview

Following the foundational concepts presented in Chapter I and the description of methodologies in Chapter II, this dissertation is organized into four main chapters:

Chapter III presents the ^{230}Th/U dating results for speleothems from Áaktun Kóopo Cave on the northeastern YP, demonstrating continuous carbonate deposition over the past 2.7 kyr, covering the entire period of Maya civilization. High growth rates and uranium concentrations allowed precise dating, while seasonal changes in Sr/Ca ratios further refined individual stalagmite chronologies. This chapter also addresses the handling of elevated and variable ^{230}Th contamination, a common issue in ^{230}Th/U-dating of tropical speleothems. Despite these challenges, the constructed chronologies provide a solid basis for reconstructing hydroclimate and vegetation changes across key periods, such as the TCP.

Chapter IV explores how seasonal and interannual changes in trace elements (Mg, Sr, Ba, U, etc.) and stable isotopes (δ^{13}C, δ^{18}O) in the stalagmites reflect external climate conditions and internal cave processes. Detecting seasonal changes in YP stalagmite trace elements is still poorly understood, as very few studies have examined these dynamics. This chapter demonstrates that changes in elements like Sr, Ba, Na, and U closely follow growth rates, while Mg/Ca behaves differently, suggesting that processes such as prior calcite precipitation (PCP) may play a significant role.

Chapter V examines how both climate changes and possible human activities affected the environment around the cave before and after the TCP. The record from stalagmite E0-C, the first from the northeastern YP spanning the past ∼1400 years, shows significant shifts in soil-sensitive proxies (δ^{13}C, U/Ca, and dead carbon fraction (DCF)) at the onset of the Medieval Warm Period (MWP) around 1000 AD. These shifts indicate significant changes in vegetation and soil conditions above the cave, likely reflecting forest recovery driven either by the cessation of agricultural activities and/or by a broader climate shift associated with tropical Atlantic SSTs, which brought wetter conditions at the onset of the MWP.

Chapter VI combines the δ^{18}O records from stalagmites E0-C, E1, and E23-3 to create a high-resolution composite rainfall record for the northeastern YP over the past 1,400 years. This record captures prominent centennial-scale changes in rainfall and aligns with other regional records, confirming that hydroclimate variability in the region is closely linked to tropical Atlantic SSTs, ITCZ shifts, and solar cycles. Periodic patterns related to ENSO and solar cycles suggest that solar activity may influence regional climate.

I Introduction

The following sections provide a brief summary of the fundamental aspects of the study region and its climate, followed by an overview of the principles behind using speleothems as paleoclimate archives.

I.1 Environment and Climate of the Yucatán Peninsula

The Yucatán Peninsula (YP) is situated in southeastern Mexico, bounded by the Gulf of Mexico to the west and the Caribbean Sea to the east (Fig. 1). It is shared by the Mexican states of Yucatán, Campeche, and Quintana Roo in the north, and by Guatemala and Belize in the southeast. The peninsula comprises an extensive limestone platform formed by carbonate rocks dating from the Cretaceous to Pleistocene periods (Weidie, 1985; Ward et al., 1995; Perry et al., 2009). This terrain features predominantly shallow, calcium carbonate-rich leptosols (Torrescano-Valle and Folan, 2015). The limestone landscape has given rise to the Yucatán Karst Aquifer, the world's largest network of underwater caves, formed through gradual dissolution processes (Weidie, 1985; Smart et al., 2006). Water infiltration is rapid due to the high permeability of the limestone, resulting in minimal surface runoff (Bauer-Gottwein et al., 2011).

This geological setting has profoundly influenced the region's cultural history, which spans at least 13,000 years (González González et al., 2008; González et al., 2013; Chatters et al., 2014; Stinnesbeck et al., 2017a), with access to water primarily reliant on wells and cenotes (Luzzadder-Beach, 2000). Cenotes, derived from the Yucatec Mayan term ”ts'ono'ot,” refer to locations with accessible groundwater and geologically represent water-filled sinkholes. The YP hosts thousands of cenotes (Bauer-Gottwein et al., 2011), which have historically and contemporarily served as crucial water sources and ceremonial sites for Maya communities (Smith and Sioui, 2022). As a result, artifacts and human remains from the Maya civilization are often found within these underwater cave systems. Additionally, cenotes and submerged caves are of significant interest to paleontologists, as they contain rich fossil deposits of late Pleistocene American megafauna (e.g., McDonald et al., 2017; Stinnesbeck et al., 2017b, 2018a; Schubert et al., 2019). In the past decade, ten well-preserved human skeletons have been discovered in the submerged caves of the Tulum area, dating from 13,000 to 9,000 years BP, and have been pivotal in discussions about the early peopling of the Americas (González González et al., 2008; González et al., 2013; Chatters et al., 2014; Stinnesbeck et al., 2017a, 2020, 2018b; Wrobel et al., 2021).

There is a sharp precipitation gradient across the YP, both latitudinally and meridionally. For the Mexican part of the peninsula, for example, the northwest receives the least rainfall (<500 mm per year), while the northeast receives >1200 mm per year, and precipitation further increases towards the southeast (~2000 mm per year) (De la Barreda et al., 2020) (Fig. I.1a). With the Caribbean Sea serving as the primary moisture source, precipitation variability in the YP is linked to that of the broader Caribbean region (Medina-Elizalde et al., 2017). The annual precipitation cycle can be divided into three distinctive seasons: Dry, Rainy, and Nortes (De la Barreda et al., 2020). The dry season occurs from March to May when the peninsula experiences the lowest rainfall amounts. At the same time, a stronger influence of the North Atlantic subtropical high (NASH) causes higher evaporation in the region. The Rainy season (June–October), also known as the "hurricane" season provides 50–90% of the total annual rainfall (Medina-Elizalde et al., 2017, 2016b; Lases-Hernandez et al., 2019). Although model outputs indicate a clear midsummer drought (MSD) feature, locally known as the *canicula*, in the eastern part of the YP, where July and August experience approximately a 25–30% decrease in precipitation compared to June and September (Karmalkar et al., 2011), this feature is generally relatively weak in the Yucatán compared to regions further south, including Guatemala, Honduras, El Salvador, and Nicaragua (De la Barreda et al., 2020; Magaña et al., 1999; Anderson et al., 2019; Lases-Hernández et al., 2020). In the area around Áaktun Kóopo Cave in the northern YP, local weather stations only show a minor reduction in precipitation for July (Fig. I.1c). During the Nortes season (November–February), northwestern cold fronts can bring cold weather and significant rainfall to the region (DiMego et al., 1976; Henry, 1979).

The main driver of spatial and temporal precipitation variability on seasonal to millennial scales is the meridional position of the Intertropical Convergence Zone (ITCZ), which is associated with convection, low-level moisture transport, cyclone activity, and mid-latitude air intrusions (Amador et al., 2016) (Fig. I.1). During the past millennia, the dynamic response of the seasonal ITCZ, along with associated trajectories and trade wind strength—as well as extra-tropical forcing—varied regionally (Lechleitner et al., 2017; Singarayer et al., 2017). Evidence has been reported for both latitudinal shifts (Haug et al., 2003; Lechleitner et al., 2017) as well as the contraction and expansion of the ITCZ (Asmerom et al., 2020; Singarayer et al., 2017). Besides a potential influence of solar activity (Hodell et al., 2001; Warken et al., 2021), volcanic and anthropogenic aerosols have been suggested to influence the regional water balance of evaporation minus precipitation (E–P), potentially exacerbating or prolonging predominant drought intervals during the past centuries (Ridley et al., 2015; Waite et al., 2020). Consequently, regional precipitation varies widely over time and across space in Central America and the Caribbean, including the YP (Douglas et al., 2016; Stansell et al., 2020; Oster et al., 2019; Steinman et al., 2022; Wojewódka-Przybył et al., 2022; Obrist-Farner et al., 2023).

With 176 tropical cyclone landfalls (including 79 hurricanes) recorded between 1851 and 2023 (National Oceanic and Atmospheric Administration, 2023), tropical storms and hurricanes represent significant elements of the climate in the YP. Particularly in the northeastern YP, which receives approximately 10–15% of its annual rainfall from tropical cyclones (Prat and Nelson, 2013), changes in tropical cyclone activity may exert a more pronounced influence on water resources within this region.

The highest precipitation amounts and tropical cyclone frequencies occur during boreal summer when the ITCZ reaches its northernmost position. Although the core region of convective activity does not extend as far north as the YP (Donohoe et al., 2013; Schneider et al., 2014), the annual movement of the ITCZ indirectly impacts seasonal precipitation variability through its influence on the strength and position of the NASH, Caribbean Low Level Jet (CLLJ), and sea surface temperatures (SST) in the tropical Atlantic (Oster et al., 2019). However, the spatio-temporal variability of the ITCZ extends beyond latitudinal migrations, encompassing contractions/expansions and changes in seasonal residence times along its boundaries (Asmerom et al., 2020; Byrne et al., 2018). These fluctuations correlate with the broader patterns of SST variability across the tropical North Atlantic (Bhattacharya et al., 2017; Schmitt et al., 2020). Over the instrumental period, the difference between wet and dry years on the YP is linked to a tripole SST pattern, highlighting the role of North Atlantic SST variability in determining regional precipitation (Travis-Taylor et al., 2023). The strong easterly zonal winds produced by the NASH facilitate the transport of moisture from the Atlantic Ocean into the Caribbean Sea, where the flow intensifies, forming the CLLJ (Amador Astúa, 1998; Mestas-Nunez and Enfield, 2007; Muñoz et al., 2008). Throughout the boreal summer months in the western Caribbean, the CLLJ bifurcates into two distinct branches (Wang, 2007). One of these branches turns northward, traversing over the western Gulf of Mexico, thereby conveying moisture towards the YP. The climate in Central America and the YP is further influenced by SSTs in the eastern Pacific, leading to a zonal fluctuation in sea level pressure (SLP) between the eastern equatorial Pacific and the Atlantic (Giannini et al., 2000). While there is no consistent hydroclimate pattern across Central America during most of the Common Era (Steinman et al., 2022; Wojewódka-Przybył et al., 2022; Obrist-Farner et al., 2023), a synthesis of proxy records reveals severe drying between 800 and 1050 AD (Bhattacharya et al., 2017). In a comparative study of YP paleoclimate records and tropical Atlantic SSTs, Gibson et al. (2023) suggest that multidecadal- to centennial-scale drought events in the Maya Lowlands over the past 2000 years, including the extreme drying of the TCP, may have been driven by a westward expansion of the NASH. This expansion of the NASH increases the meridional SLP gradient, strengthening trade winds, which, in turn, reduces SSTs and leads to drier conditions on the YP (Bhattacharya et al., 2017; Wang, 2007).

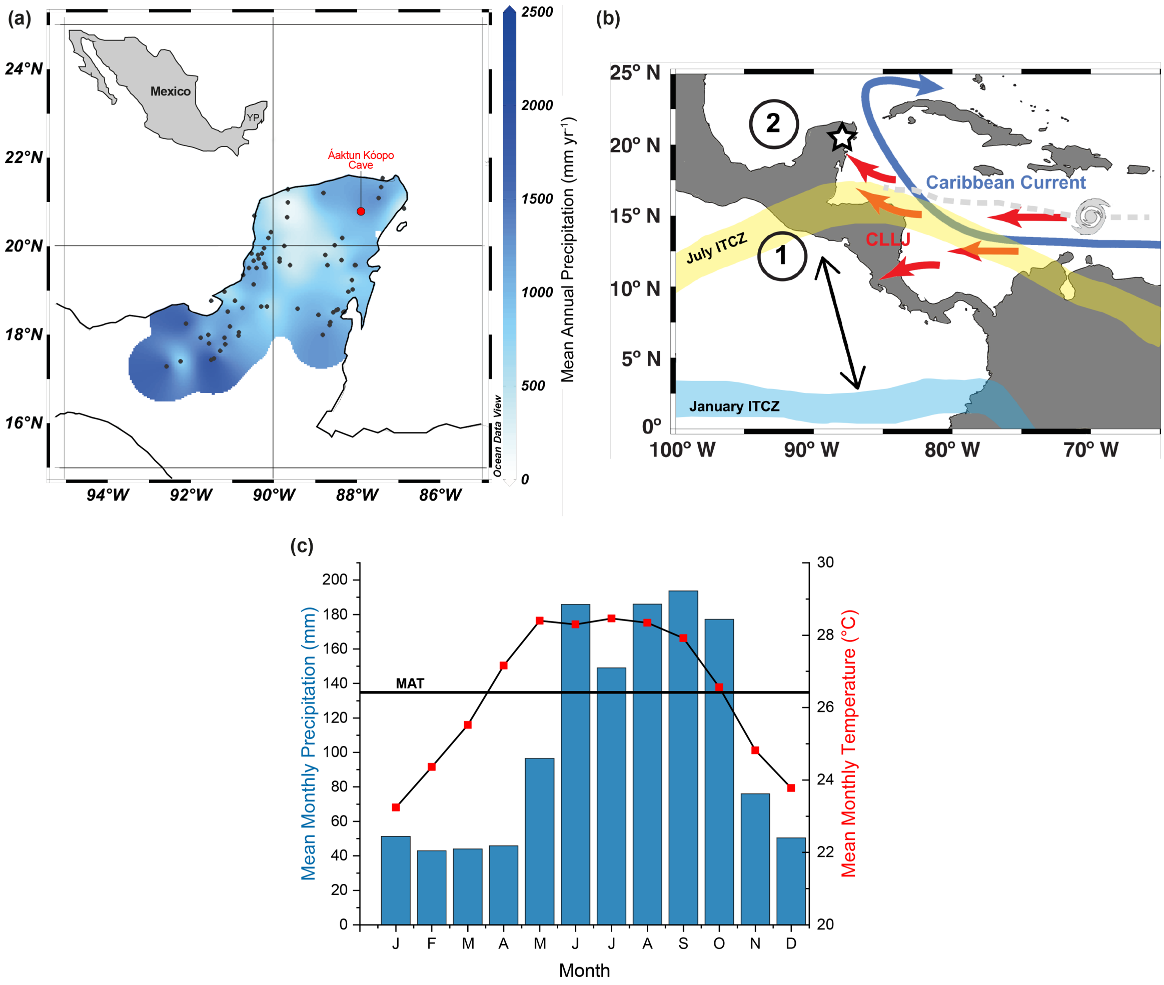

Figure I.1. **(a)** Mean annual precipitation across the northern Yucatán Peninsula (YP), based on daily meteorological data from 70 weather stations within the Global Historical Climatology Network (GHCN) spanning various intervals from 1921 to 2021 (Menne et al., 2012). The location of Áaktun Kóopo Cave, situated in the northeastern YP, is indicated by a red dot. **(b)** Sources of high precipitation (1) and drought regions (2), illustrating the complex interactions of atmospheric moisture transport in the Caribbean, influenced by the seasonal migration of the Intertropical Convergence Zone (ITCZ) and the strength of the Caribbean Low-Level Jet (CLLJ). The figure is modified from Wu et al. (2017) and Asmerom et al. (2020). Again, the location of Áaktun Kóopo Cave is marked by a star. **(c)** Mean monthly precipitation and temperature data (1991–2020) from five CONAGUA weather stations (CONAGUA, 2021) within a 25 km radius of Áaktun Kóopo Cave. The annual mean precipitation in this area is 1300 mm, while the annual mean temperature is 26.42°C (black horizontal line).

I.2 Speleothems as Paleoclimate Archives

I.2.1 Formation of Speleothems

Speleothems (derived from the ancient Greek words *spēlaion*, meaning ”cave”, and *thema*, meaning ”deposit”) are secondary cave deposits that primarily form in the epikarst above the water table. To date, over 300 different cave minerals have been identified (Hill and Forti, 1997). The most common $CaCO_3$ polymorphs found in speleothems are calcite and aragonite, which precipitate from percolating water passing through the soil and karst zone until reaching the cave. During this process, three distinct steps occur: first, CO_2 uptake in the soil zone; followed by dissolution of $CaCO_3$ minerals in the epikarst between the soil zone and the cave; and finally, re-precipitation of the dissolved $CaCO_3$ inside the cave. High concentrations of CO_2 in the soil zone, up to 100,000 ppm pCO_2 (McDermott, 2004), result from plant root exhalation and microorganisms decomposing organic material (Raich and Potter, 1995; Amundson et al., 1998; Bond-Lamberty et al., 2004; Kuzyakov, 2006).

$$C_6H_{12}O_6 + 6O_2 \rightarrow 6H_2O + 6CO_2 \tag{I.1}$$

The respired CO_2 in the soil then dissolves in water, reacting to form carbonic acid (H_2CO_3), which further dissociates to bicarbonate (${HCO_3}^-$) and carbonate (${CO_3}^{2-}$) ions:

$$CO_{2(g)} + H_2O \rightleftharpoons H_2CO_3 + CO_{2(aq)} \tag{I.2}$$

$$H_2CO_3 \rightleftharpoons HCO_3^- + H^+ \rightleftharpoons CO_3^{2-} + 2H^+ \tag{I.3}$$

While ${HCO_3}^-$ predominates in the total dissolved inorganic carbon pool (DIC) at near-neutral pH values, the relatively smaller presence of ${CO_3}^{2-}$ is crucial for determining the stability of carbonate minerals (Fairchild and Baker, 2012). When this acidic water reaches the karst zone, the surrounding limestone ($CaCO_3$) dissolves, and the carbon from the host rock ($CaCO_3$) mixes with the carbon from the soil ${HCO_3}^-$:

$$CO_2 + H_2O + CaCO_3 \rightleftharpoons Ca^{2+} + 2HCO_3^- \tag{I.4}$$

Here, two conditions of $CaCO_3$ dissolution can be distinguished (Hendy, 1971): an ”open” and a ”closed” dissolution system. In an open system, the karst water is in permanent contact with soil CO_2, resulting in a constant replacement of dissolved carbon with soil CO_2. Consequently, the dissolved carbon in the water entering the cave will not show any imprint of host rock carbon while fully conserving the carbon fingerprint of the soil and atmosphere. Under closed dissolution conditions, on the other hand, there is no exchange between the soil air and the percolating water during $CaCO_3$ dissolution. Consequently, the dissolved carbon in the water entering the cave will then consist of 50% soil carbon and 50% host rock carbon. These two dissolution systems can be considered as idealized endpoints, whereas natural systems typically exhibiting intermediate conditions due to the often limited availability of gaseous CO_2 (e.g., Genty et al., 1998; Rudzka et al., 2011). The degree of mixture between carbon originating from the soil and limestone is also evident in the stable carbon isotopes of the DIC, consequently influencing speleothem composition. Hence, a thorough comprehension of the diverse processes along the water pathway through vegetation, soil, and epikarst is crucial for utilizing speleothems as climate archives.

After passing through the karst zone, percolating water eventually enters a cave environment with significantly lower pCO_2 levels compared to the preceding epikarst. Consequently, this leads to CO_2 outgassing until equilibrium with the ambient pCO_2 level is achieved (Dreybrodt and Fohlmeister, 2022). The decrease in CO_2 results in the supersaturation of dripwater with respect to calcite, initiating the precipitation of $CaCO_3$ and subsequent formation of speleothems.

$$Ca^{2+} + 2HCO_3^- \rightleftharpoons CO_2 \uparrow + CaCO_3 \downarrow + H_2O \tag{I.5}$$

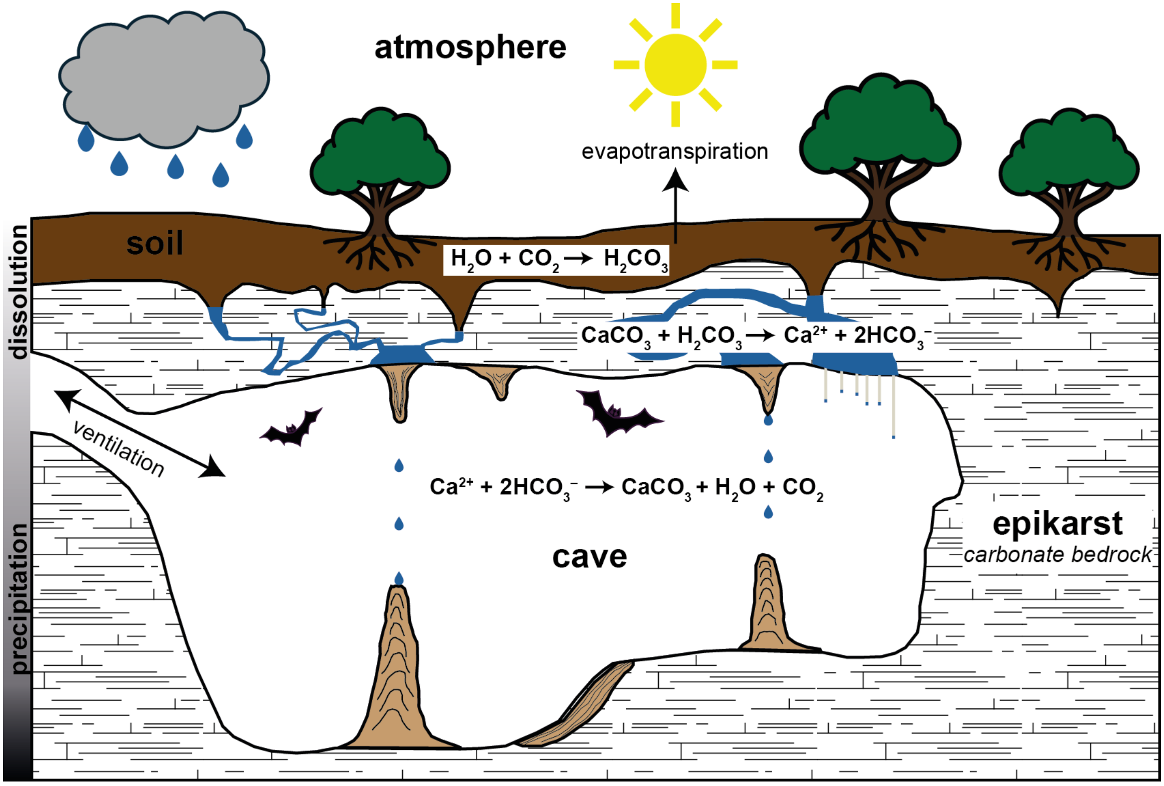

Figure I.2. Schematic illustration of dissolution and precipitation processes within the atmosphere-soil-karst system, depicting the three phases of speleothem formation and associated chemical reactions: CO_2 uptake by water in the soil layer, dissolution of $CaCO_3$ in the epikarst, and subsequent re-precipitation of $CaCO_3$ within the cave environment. Figure adapted from Johnson (2021), with certain elements redrawn, and additional annotations incorporated to highlight key features.

I.2.2 Dating of Speleothems

^{230}Th/U-dating

The chronology of stalagmites and other carbonate-based archives of the past can be accurately determined by various dating methods. One of the most robust techniques is via ^{230}Th/U dating. This radiometric method can be applied to carbonate samples as old as 600,000 years, and in some cases, even up to 800,000 years (Cheng et al., 2013). The reliability of U-series dating depends on two key assumptions: first, that highly soluble uranium was carried from the karst above the cave to the stalagmite by drip water, and second, that the system stayed closed after the carbonate formed, meaning no isotopes were lost or added after the carbonate was deposited (Scholz and Hoffmann, 2008). The relevant isotopes of the decay chain of ^{238}U leading to its stable end product ^{208}Pb are depicted in Fig. I.3. For this dating method, the age is determined by quantifying the return to the secular equilibrium state, in which all activity ratios of the isotopes along the decay chain are 1. Since the isotopes of

^{234}Th and ^{234}Pa are very short-lived, they are not at play for the decay chain and can be neglected for the age determination. Therefore, only ^{234}U and ^{230}Th are used in the age calculation which involves the following equations derived by Ivanovich and Harmon (1992):

$$\left(\frac{^{234}U}{^{238}U}\right)(t) = \left(\left(\frac{^{234}U}{^{238}U}\right)_{\text{init}} - 1\right) e^{-\lambda_{234}\cdot t} + 1 \tag{I.6}$$

$$\left(\frac{^{230}Th}{^{238}U}\right)(t) = 1 - e^{-\lambda_{230}\cdot t} + \left(\frac{\delta^{234}U}{1000}\right)\cdot\left(\frac{\lambda_{230}}{\lambda_{230}-\lambda_{234}}\right)\cdot\left(1 - e^{-(\lambda_{230}-\lambda_{234})\cdot t}\right) \tag{I.7}$$

with:

$$\delta^{234}U = \left(\left(\frac{^{234}U}{^{238}U}\right)_{meas} - 1\right)\cdot 1000\ (‰) \tag{I.8}$$

Here, t symbolizes the age of the sample, λ signifies the decay constants of the respective isotopes, and the activity ratios of the two isotopes are indicated within parentheses. The ^{230}Th/U dating method further relies on the perturbation of a secular equilibrium, wherein the activities of parent and daughter isotopes within the decay chain are equilibrated (Richards and Dorale, 2003). This perturbation occurs during the formation of $CaCO_3$, wherein uranium (U) becomes separated from thorium (Th) due to the strong difference in solubility between both elements in the hydrosphere. Uranium primarily exists as U^{6+} and is therefore highly soluble in water, forming uranyl ions (UO^{2+}) (Bourdon et al., 2003). On the other hand, thorium, in its most common state as Th^{4+}, exhibits very low solubility (Langmuir and Herman, 1980) but is highly particle-reactive. Consequently, natural waters contain dissolved uranium but lack thorium, thus preventing the incorporation of ^{230}Th not produced by in situ decay (Ivanovich, 1994). This process effectively 'resets' the radiometric clock and is a fundamental condition for the ^{230}Th/U dating method.

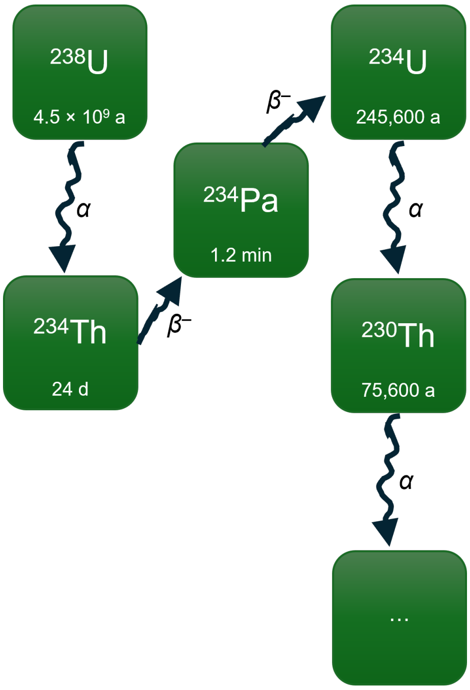

Figure I.3. First isotopes of the ^{238}U decay chain, also known as the *uranium series*, which are relevant for the ^{230}Th/U dating method along with their corresponding half-lives. Half-lives are taken from Jaffey et al. (1971) for ^{238}U, Bourdon et al. (2003) for ^{234}Th, Duchemin et al. (1994) for ^{234}Pa and Cheng et al. (2013) for ^{234}U and ^{230}Th. Because of their short half-lives, resulting in minimal accumulation, ^{234}Pa and ^{234}Th can be neglected in ^{230}Th/U dating.

Detritus correction

In practice, however, a certain amount of ^{230}Th, not produced by in situ decay, may be incorporated at the time of deposition. Gascoyne (1992) estimated that speleothems may contain a wide range of Th concentrations, up to 10 µg g^{-1}. Previous studies have demonstrated that the incorporation of thorium is typically associated with a detrital component that becomes cemented or occluded within the speleothem during its growth. Additionally, thorium may enter voids and/or spaces within the deposited carbonate in colloidal phases or become attached to organic molecules (Richards and Dorale, 2003). There are two sources of Th contamination: (1) hydrogenous Th transported by drip waters and incorporated into the calcite matrix during carbonate precipitation, and (2) detrital particles, such as clays (Kaufman et al., 1998), which can be cemented or occluded within a speleothem as it grows. Furthermore, it has been suggested that in a two-component system, such as those found in clays, the high ^{230}Th component exhibits a low (^{230}Th/^{232}Th) activity ratio, while the low ^{232}Th component, found in hydrogenous forms for instance, displays a high (^{230}Th/^{232}Th) activity ratio (Dorale et al., 2004).

Although Th has a low solubility in natural waters it commonly adsorbs onto clay minerals and humic acids (Morton et al., 2001; Reiller et al., 2002; Nascimento et al., 2019), allowing it to be mobile and transported. The analysis of soil leachates and zero-age calcite in central Texas caves suggests that soil material is a source of detrital Th in the stalagmites and accounts for the observed elevated (^{230}Th/^{232}Th) activity ratios (Wortham et al., 2022). Here it was suggested that Th adsorbs on clay minerals in soils, is transported as particulates through the karst system and subsequently precipitates out of solution with iron and/or manganese-oxides.

To accurately date a sample, it is therefore essential to estimate the content of ^{230}Th not derived from the decay of ^{234}U but initially incorporated during carbonate formation (hereafter referred to as "detrital Th"). However, distinguishing between detrital ^{230}Th initially incorporated and ^{230}Th produced by the radioactive decay of ^{234}U is practically impossible. Nevertheless, ^{232}Th, being highly abundant, chemically equivalent to ^{230}Th (Langmuir and Herman, 1980), and essentially stable due to its extremely long half-life ($t_{1/2}$=1.401$\times$ 10^{10} years) (Bourdon et al., 2003), can be utilized to estimate detrital ^{230}Th contamination.

In the early stages of ^{230}Th/U-dating using alpha spectrometers, it was assumed that samples with a (^{230}Th/^{232}Th) activity ratio of >20 did not require corrections (Schwarcz, 1989; Bischoff and Fitzpatrick, 1991). With advancements in dating techniques, particularly thermal ionization mass spectrometry (TIMS), it was proposed that the influence of this detrital fraction on age determination is significant for samples with (^{230}Th/^{232}Th) activity ratios of <300 (Richards and Dorale, 2003). However, a later study demonstrated that even a threshold of 300 is arguably too low, and that for consistency, speleothem ^{230}Th/U-ages should be routinely corrected for initial ^{230}Th incorporation, regardless of whether the measured (^{230}Th/^{232}Th) activity ratio is high enough to render the age adjustment insignificant (Hellstrom, 2006). The main challenge with detrital correction comes from the difficulty in accurately measuring the (^{230}Th/^{232}Th) activity ratio of detrital material, which can vary depending on the characteristics of the host rock and soil.

At present, for a geological material in ^{238}U–^{234}U–^{230}Th secular equilibrium, assuming a crustal Th/U ratio of 3.8 (Taylor and McLennan, 1985), which approximates the ratio of ^{232}Th to ^{238}U due to their abundance as the most prevalent isotopes of their respective elements, and with an assumed error of 50%, the ^{230}Th/^{232}Th atomic ratio of $4.4 \pm 2.2 \times 10^{-6}$ is commonly utilized (Ludwig and Paces, 2002). This ratio is used for deducing the initial ^{230}Th and for correcting calculated ^{230}Th/U ages. It should be noted that many studies wrongly cite the work of Wedepohl (1995) when using a ^{232}Th/^{238}U value of 3.8 for the upper continental crust. A detailed explanation of the origin of this misquotation is provided in Appendix VII. In fact, calculating the Th/U ratio based on the mean elemental concentrations reported by Wedepohl (1995) for the upper crust results in a ^{232}Th/^{238}U value of 4.1 ± 2.05. The correct reference for the 3.8 ratio is the study by Taylor and McLennan (1985). However, caution is necessary, as some environments may exhibit inherited anomalous (^{230}Th/^{232}Th) ratios (Richards and Dorale, 2003).

Recent studies, particularly from tropical regions such as the Caribbean, further highlight this issue by reporting significantly higher activity ratios, up to 80 times greater than the commonly used ratio for the upper crust (e.g., Ridley et al., 2015; Vieten et al., 2024a; Warken et al., 2021; Stinnesbeck et al., 2020; Richards and Dorale, 2003; Beck et al., 2001; Partin et al., 2007; Hoffmann et al., 2010; Carolin et al., 2013; Arienzo et al., 2015; Moseley et al., 2015; Steidle et al., 2021; Vieten et al., 2024b) (Table I.1). For example, speleothem studies from the Bahamas show a wide range of (^{230}Th/^{232}Th) activity ratios from 2.2 to 18.7 (Richards and Dorale, 2003; Beck et al., 2001; Hoffmann et al., 2010; Arienzo et al., 2015). This variability is supported by other studies that have observed significant fluctuations in U and Th concentrations in carbonates and waters of the Bahamas, along with several potential sources of detrital Th, including aeolian inputs (Robinson et al., 2004). Bornean speleothems contaminated with detrital limestone have been shown to have initial (^{230}Th/^{232}Th) activity ratios as high as 10 to 21 (Partin et al., 2007; Carolin et al., 2013). In a recent monitoring study conducted in Qianlong Cave in China, it has been shown that the initial (^{230}Th/^{232}Th) activity ratio in drip water not only differs among individual caves but can also vary at different drip sites within a single cave (Li et al., 2022). The authors of this study further pointed out that the initial (^{230}Th/^{232}Th) activity ratio may reasonably be expected to change over time with changes in climate, vegetation, and aerosol inputs, as well as the evolution of flow paths and karst conditions (Li et al., 2022).

Study site	**^{232}Th/^{238}U$_{ppm}$**	**^{230}Th/^{232}Th$_{ppm}$**	**(^{230}Th/^{232}Th)**	**Approach**	**Reference**
Bahamas			18.7±2.9	isochrons	Beck et al. 2001
Bahamas			7.8±4.0	isochrons	Hoffmann et al. 2010
Bahamas			3.7±0.6	Stratigraphic constrain	Hoffmann et al. 2010
Belize		42–223	8–41	Drip water; zero-age carbonate	Ridley et al. 2015
Borneo		56±11 111±41	10–21	isochrons	Partin et al. 2007 Carolin et al. 2013
Cuba			8±4	Stratigraphic constrain	Fensterer et al. 2010, 2012
Cuba			8±4	Stratigraphic constrain	Warken et al. 2019
Puerto Rico	0.35±0.175		9±4.5	Stratigraphic constrain	Rivera-Collazo et al. 2015
Puerto Rico			23.7±7.5	isochrons	Warken et al. 2020
Puerto Rico			35±17.5	Stratigraphic constrain	Vieten et al. 2024b
Puerto Rico			61.1±61.1	Stratigraphic constrain	Vieten et al. 2024a
YP, Mexico			14±4	isochrons	Moseley et al. 2015
YP, Mexico			3.5±1.75	isochrons	Stinnesbeck et al. 2020
YP, Mexico		117±10 170±10	22–32	Testing for consistency with layer count	Kennett et al. 2022

Table I.1. Reported elevated (^{230}Th/^{232}Th) activity ratios from Caribbean speleothems. Typically, a bulk Earth detrital (^{230}Th/^{232}Th) activity ratio of 0.75–0.89 is assumed for the upper continental crust (Taylor and McLennan, 1985; Heier and Carter, 1963; Heier and Rogers, 1963).

In general, there are two main approaches to assess the initial ^{230}Th in speleothems: (1) directly measuring the (^{230}Th/^{232}Th) ratio of the contaminating phase, which may involve analyzing in-situ cave drip water, soil, or recently deposited calcite (Wortham et al., 2022; Li et al., 2022; Hu et al., 2008); and (2) estimating the isotopic composition of the detrital phase a priori. However, in cases where active carbonate deposition or accessible drip water is not available at the sampling site, the isochron method can serve as an alternative (Ludwig and Titterington, 1994). This method requires at least three to four sub-samples from the same lamina or a group of laminae, which must exhibit a substantial variation in ^{232}Th/^{238}U ratios to construct a reliable regression line (Dorale et al., 2004; Hellstrom, 2006). Although effective in certain contexts, the isochron approach is often labor-intensive, requires a significant amount of material, and can sometimes fail due to the presence of multiple thorium sources (Richards and Dorale, 2003; Lin et al., 1996; Denniston et al., 2013a).
Alternatively, the stratigraphic constraint can be applied to assess initial ^{230}Th values (Hellstrom, 2006). In this method, an initial (^{230}Th/^{232}Th) activity ratio is selected in such a way that the corrected ages consistently increase with increasing distance from the top of the speleothem, thereby ensuring stratigraphic consistency.

Once the initial ^{230}Th/^{232}Th activity ratio is determined, corrected ages can be calculated by incorporating the (^{230}Th/^{238}U)$_{corr}$ ratio into Equation I.7 as follows:

$$\left(\frac{^{230}Th}{^{238}U}\right)_{corr} = \left(\frac{^{230}Th}{^{238}U}\right)_{meas} - \left(\frac{^{232}Th}{^{238}U}\right)_{meas} \cdot \left(\frac{^{230}Th}{^{232}Th}\right)_{detr,init} \cdot e^{-\lambda_{230} \cdot t} \tag{I.9}$$

Besides terrestrial carbonates, the detrital Th correction is also of great importance for marine archives, such as corals, including both tropical (warm-water) and deep-sea (cold-water) corals. Correction factors for (^{230}Th/^{232}Th) ranging between 0.4 to 80 have been reported in these contexts (e.g., Lomitschka and Mangini, 1999; Cheng et al., 2000; Schröder-Ritzrau et al., 2003; Frank et al., 2004; Shen et al., 2008).

Radiocarbon dating

The basis of radiocarbon dating is the decay of the radioactive isotope ^{14}C to ^{14}N, with a physical half-life of 5730±40 years (Godwin, 1962).

$$^{14}_{6}\mathrm{C} \rightarrow ^{14}_{7}\mathrm{N} + e^{-} + \bar{\nu}_e \tag{I.10}$$

^{14}C is the naturally occurring radioactive isotope of carbon and is continuously produced in the upper atmosphere and stratosphere through nuclear reactions with ^{14}N atoms and thermal neutrons (Anderson et al., 1947).

$$^{1}_{0}\mathrm{n} + ^{14}_{7}\mathrm{N} \rightarrow ^{14}_{6}\mathrm{C} + ^{1}_{1}\mathrm{p} \tag{I.11}$$

This results in a quasi-steady state in Earth's atmosphere. However, over longer time scales, variations in the cosmic ray flux, changes in the geomagnetic field, and shifts in the carbon cycle modulate its concentration in the atmosphere (Bronk Ramsey, 2008; Burke and Robinson, 2012). Along with the stable carbon isotopes ^{12}C and ^{13}C, which make up almost all carbon atoms with abundances of 98.9% and 1.1%, respectively (Mook, 2000), the radioactive ^{14}C is far less abundant, making up only about 10^{-12}% of the total carbon. The highly reactive ^{14}C atoms rapidly undergo oxidation by atmospheric oxygen to form ^{14}CO, which subsequently converts to $^{14}CO_2$. As an integral component of the carbon cycle, $^{14}CO_2$ is readily dispersed throughout the hydrosphere and biosphere. Through metabolic processes such as photosynthesis and ingestion, ^{14}C is continually incorporated into plants and other living organisms. This continuous exchange can cease upon the demise of an organism. From this point onward, no further carbon is incorporated, and the radiocarbon activity diminishes over time according to the principles of radioactive decay. If the initial number of

^{14}C atoms (N_0) is known, the starting time of the radioactive decay clock t can be calculated by using the following equation:

$$t = \frac{1}{\lambda} \cdot ln\left(\frac{N_0}{N(t)}\right) \tag{I.12}$$

Here, λ represents the decay constant ($\lambda_{\mathrm{Lib}}^{-1} = 8033$ years) (Arnold and Libby, 1951), N_0 is the initial number of ^{14}C atoms in a sample, and $N(t)$ refers to the remaining number of atoms at the time of measurement.

The assumption of a constant atmospheric ^{14}C concentration during the last ~50,000 years (Libby, 1946) was later proven to be incorrect. Combined inter-calibration records such as IntCal20 (Reimer et al., 2020; Bronk Ramsey et al., 2023) demonstrate that natural variations of atmospheric ^{14}C concentrations exceeded 50% throughout the last 50,000 years. Therefore, conventional radiocarbon ages need to be converted into calendar ages, which requires sufficient knowledge of the past evolution of atmospheric ^{14}C concentration. For the younger period up to approximately 14,000 years BP, overlapping tree-ring records are the preferred archives for reconstructing past changes in atmospheric ^{14}C, as their layering permits accurate age determination (e.g., Schaub et al., 2008; Hua et al., 2009; Reimer et al., 2013). For the older period up to 50,000 years BP, other archives such as stalagmites (e.g., Beck et al., 2001; Hoffmann et al., 2010; Southon et al., 2012), sediment cores (Bronk Ramsey et al., 2012), and corals (e.g., Hughen et al., 2006; Bard et al., 2013; Durand et al., 2013; Heaton et al., 2013) provide additional sources of data. The long-term trends observed in atmospheric Δ^{14}C are indicative of fluctuations in the equilibrium between radiocarbon input and output within the atmosphere. These shifts are influenced by natural factors such as cosmic radiation, solar activity, geomagnetic field variation, changes in carbon cycling (e.g., Burke and Robinson, 2012; Burchuladze et al., 1980; Muscheler et al., 2004, 2005; Köhler et al., 2006; Scifo et al., 2019), and anthropogenic factors including fossil fuel combustion and nuclear testing (Tans et al., 1979; Levin et al., 2010). The current standard for Δ^{14}C calibration is the inter-calibration dataset ”IntCal”, with its most recent instance *IntCal20* (Reimer et al., 2020). This curve shows the variations in Δ^{14}C in the atmosphere over the last 50,000 years with respect to the radiocarbon reference year of 1950 (Fig.I.4). To ensure consistency across samples measured at varying times, all radiocarbon dates are reported relative to the defined activity and isotopic signature of the oxalic acid standard materials (OxI and OxII) (Stuiver, 1983) and expressed relative to the year 1950 AD in the unit ”yr BP” (years before present), with ”present” denoting the year 1950 AD.

An alternative method for expressing ^{14}C dating results, apart from the conventional radiocarbon age t (Equation I.12), is through its activity a^{14}C, expressed in the unit "pmC" (*percent modern carbon*) (Stenström et al., 2011).

$$a^{14}C = \frac{A_{SN}}{A_{ON}} \cdot 100\% \,(pmC) = e^{-\lambda_{Lib} \cdot t_{14C}} \cdot 100\% \,(pmC) \tag{I.13}$$

In this context, the activity of the analyzed sample ($\mathrm{A_{SN}}$) is evaluated relative to the atmospheric activity in 1950 AD ($\mathrm{A_{ON}}$), as determined by the oxalic acid standard materials (OxI & OxII). Furthermore, when interpreting ^{14}C dating outcomes within the framework of atmospheric radiocarbon levels, the delta-notation is commonly utilized.

$$\Delta^{14}C = \left(\frac{A_{SN}}{A_{ON}} - 1\right) \cdot 1000\,‰ = (a^{14}C - 1) \cdot 1000\,‰ \tag{I.14}$$

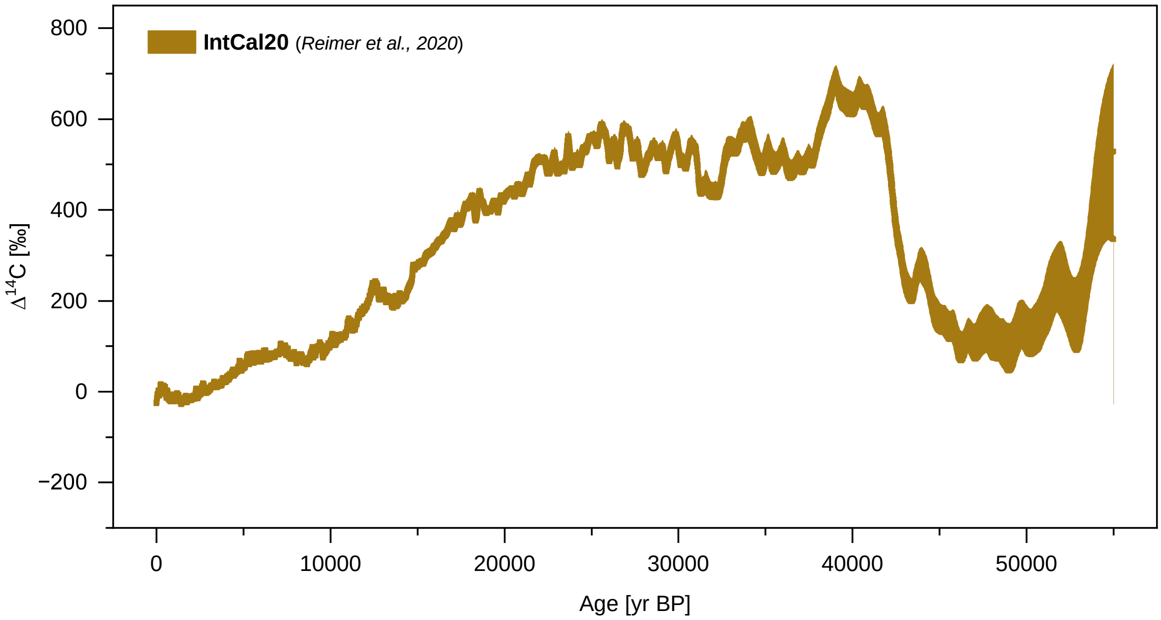

Figure I.4. Variations in atmospheric ^{14}C concentrations over the last 55,000 years, based on the most recent Δ^{14}C calibration record (IntCal20) (Reimer et al., 2020).

I.2.3 Hydroclimate Proxies in Stalagmites

Stable oxygen isotopes (δ^{18}O)

The stable oxygen isotopic composition, i.e. the ratio of (δ^{18}O) is widely reported as a climate proxy in speleothems, particularly stalagmites (Comas-Bru et al., 2020), and is generally interpreted with respect to the infiltrating rainwater and groundwater that reach the cave (Lachniet, 2009). Stable oxygen isotopes are usually expressed in the δ-notation, which reports the deviation of the isotopic ratio of the sample relative to that of a standard:

$$\delta^{18}O = \left(\frac{{}^{18}O/{}^{16}O_{sample} - {}^{18}O/{}^{16}O_{standard}}{{}^{18}O/{}^{16}O_{standard}}\right) \cdot 1000 \tag{I.15}$$

For carbonate samples, such as stalagmites, the Vienna Pee Dee Belemnite (VPDB) (Coplen, 1996) is used as a standard, while the preferred standard for water samples is the Vienna Standard Mean Ocean Water (VSMOW) (Gonfiantini, 1978). Interpreting speleothem δ^{18}O values, however, is not straightforward, as a variety of processes can modulate the isotopic composition of the water along its journey from the source region until it ends up as $CaCO_3$ inside a cave. Two main stages of oxygen isotope fractionation occur during phase shifts as water transfers from the ocean (source) to the speleothem (target). The hydrologic cycle begins with ocean surface evaporation, atmospheric vapor transport, and cloud formation, resulting in meteoric precipitation. Further fractionation may occur as water travels through the soil zone and epikarst above the cave, leading to $CaCO_3$ precipitation within the cave.

The initial control on the δ^{18}O value of the water is the δ^{18}O value of the ocean ($\delta^{18}O_{SW}$), where the majority of the Earth's evaporation takes place (Dansgaard, 1964). On a local scale, $\delta^{18}O_{SW}$ values are related to salinity, influenced by sea ice melt, evaporation, precipitation over the ocean, freshwater runoff, and oceanic and atmospheric transport (Lachniet, 2009). The latter causes, for example, an enrichment of the Caribbean Sea due to evaporation and removal of freshwater as rainfall to the Pacific Ocean (Zaucker and Broecker, 1992; Schmidt et al., 2007). Water vapor forming from the evaporation of ocean water ($\delta^{18}O_{SW} \approx 0$ ‰) will have a δ^{18}O value of –9.34 ‰, assuming a temperature of 25°C and a relative humidity (RH) of 100 ‰ (Clark and Fritz, 1997). If evaporation occurs under RH of less than 100 ‰, kinetic fractionation will result in even lower δ^{18}O values of the vapor formed from ocean water (Clark and Fritz, 1997). On longer timescales (glacial-/interglacial cycles), the $\delta^{18}O_{SW}$ value varies by up to 1.2 ‰, due to the build up and break down of large ice sheets on the continents, known as the *ice volume effect* (e.g., Schrag et al., 2002; Lea et al., 2002; Sharp, 2007). During glacial periods, for instance, the $\delta^{18}O_{SW}$ value significantly increased due to the preferential removal of light stable ^{16}O isotopes during evaporation, followed by subsequent storage in continental ice sheets. For middle to high latitudes, a positive correlation between mean annual temperature (MAT) and mean δ^{18}O values of precipitation can be observed (Lachniet, 2009;

Dansgaard, 1964). This *temperature effect* on precipitation stable oxygen isotopes is also manifested on a seasonal scale, although variations in moisture source and rayleigh distillation along moisture trajectories contribute to this. The *continental effect*, present in both high-latitude and low-latitude regions, describes the decrease in water δ^{18}O values with distance from the ocean, manifesting as progressive cooling and rainout of an air mass as it traverses a continent (Dansgaard, 1964; Clark and Fritz, 1997; Rozanski et al., 1993). The *altitude effect* describes a similar phenomenon, where water vapor that crosses an orographic obstacle becomes isotopically depleted as a result of increased rainout. Stalagmite δ^{18}O records in tropical and subtropical regions are generally interpreted as reflecting local precipitation amounts due to the so-called '*amount effect*', which describes the inverse relationship between precipitation amount and rainfall δ^{18}O values (Dansgaard, 1964) and has been shown to exist on seasonal to interannual timescales (e.g., Medina-Elizalde et al., 2016a, 2017; Lases-Hernandez et al., 2019; Lases-Hernández et al., 2020; Vuille et al., 2003; Lachniet and Patterson, 2009). It was further shown that the low δ^{18}O values associated with tropical cyclones can have an impact on the oxygen isotopic composition of the drip water and thus the growing stalagmite (Lases-Hernández et al., 2020; Frappier, 2013; Vieten et al., 2018). This effect should be most notable when the water volume of the reservoir is low, such as during a persistent meteorological drought. Considering that the northern YP receives ~20%, sometimes up to 50%, of its annual rainfall from tropical cyclones (Prat and Nelson, 2013; Escolero et al., 2007), this effect might be of great importance. On the other hand, the isotopic signature of tropical cyclone rainfall might be masked when the size of the reservoir is large enough (Lases-Hernández et al., 2020; Vieten et al., 2018).

The δ^{18}O value of soil water is largely determined by the amount-weighted mean of infiltrating waters, which can be subsequently altered by evaporation, leading to elevated δ^{18}O values within the soil moisture (Clark and Fritz, 1997; Tang and Feng, 2001). Heavy precipitation events, such as tropical storms, commonly associated with low δ^{18}O values, are expected to be the main driver of recharge into the soil zone, consequently counteracting the isotopic enrichment attributed to evaporation (Clark and Fritz, 1997; Rozanski et al., 1993). After passing through the soil zone, water percolates through the epikarst either as diffuse seepage through porous bedrock, fissures, and joints, or as conduit flow, such as cave streams (Gillieson, 1996; Klimchouk, 2000). The observation of cave seepage waters exhibiting higher δ^{18}O values compared to the mean annual precipitation may be attributed to evaporation occurring within air-filled voids within the soil and epikarst (Bar-Matthews et al., 1996, 2003; Carrasco et al., 2006). The water finally reaching the tip of a stalagmite represents a composite downstream mixture of recharge from various sources with varying δ^{18}O values (Long and Putnam, 2004), resulting in differences in δ^{18}O values of coeval speleothems (Treble et al., 2022). A global meta-analysis of drip monitoring sites and speleothem records has demonstrated that within-cave differences in mean δ^{18}O values of coeval speleothems are common worldwide, with a global average speleothem $\Delta\delta^{18}O_{mean}$ of 0.37 ‰$_{VPDB}$ (Treble et al., 2022). The study further reveals that such within-cave isotopic variability is independent of hydroclimate, host rock geology, or cave microclimate but may be inherited from the dripwater δ^{18}O and thus attributed differences in karst architecture (recharge thresholds, physical flowpaths) (Treble et al., 2022).

Stable carbon isotopes (δ^{13}C)

Stable carbon isotopes (^{12}C, ^{13}C) within speleothems are regularly examined in conjunction with stable oxygen isotopes and expressed in the δ-notation, analogous to δ^{18}O (see Equation I.15). Although stable carbon isotopes offer valuable insights into past climate and vegetation changes (e.g., Ridley et al., 2015; McDermott, 2004; Fohlmeister et al., 2020), numerous processes can influence speleothem δ^{13}C values. These processes include vegetation type/density, rainfall amount/moisture availability, and in-cave processes such as prior carbonate precipitation (PCP), carbon exchange of bicarbonate with water, and fractionation during CO_2 degassing and $CaCO_3$ precipitation (Skiba and Fohlmeister, 2023). Although disentangling these processes to interpret speleothem δ^{13}C values accurately is often challenging, in certain cases, they prove to be more interpretable than corresponding δ^{18}O records (e.g., Mischel et al., 2017; Scholz et al., 2012).

The carbon within speleothems originates primarily from three sources: atmospheric CO_2, biogenic CO_2 from soil respiration, and carbon from carbonate bedrock (Lechleitner et al., 2021) (Fig. I.5). Additionally, it has been proposed that deep underground carbon reservoirs or deeply rooted vegetation may contribute to the karst carbon cycle as well (Breecker et al., 2012; Noronha et al., 2015; Mattey et al., 2016; Bergel et al., 2017). The main carbon sources contributing to stalagmite formation are outlined in Table I.2. Atmospheric CO_2 exhibits relatively stable δ^{13}C values of around −6 to −8.5 ‰ over the last 155 kyr (Elsig et al., 2009; Schmitt et al., 2012; Eggleston et al., 2016; Graven et al., 2017). This carbon dioxide can permeate the soil through diffusion processes. Conversely, atmospheric CO_2 is assimilated by plants during photosynthesis to produce glucose, which is then respired in the soil as CO_2. Climate-driven changes in vegetation types (e.g., C_3 vs C_4 plants) are the primary drivers of fluctuations in δ^{13}C values of soil CO_2, as the CO_2 produced by those plants differs markedly in δ^{13}C. Soils that are dominated by C_3 plants (trees and shrubs) generally exhibit δ^{13}C values between –27 ‰ and –20 ‰, whereas C_4 vegetation (grasses) produces soil CO_2 with slightly higher δ^{13}C values, typically in the range of –16 ‰ to –10 ‰ (McDermott, 2004; Cerling, 1984). The δ^{13}C values of organic carbon derived from vegetation above a cave are subject to the influence of changes in temperature and atmospheric pCO_2, which govern the extent of photosynthetic discrimination. For instance, under drier and hotter climatic conditions, there is a heightened vapor pressure deficit and reduced soil water content, resulting in less negative δ^{13}C values of organic carbon (Wong and Breecker, 2015). Simultaneously, low respiration rates can contribute to a significant presence of atmospheric CO_2 in belowground pore spaces, consequently elevating the δ^{13}C values of CO_2 in the soil and epikarst (Genty et al., 2001). Revegetation of the area above a cave following deglaciation or human-induced forest/vegetation clearing results in increasing soil respiration rates and, consequently, decreasing δ^{13}C values of speleothems (Baldini et al., 2005; Cruz et al., 2006; Moreno et al., 2010; Denniston et al., 2013b). During the dissolution of host rock limestone, carbon with significantly higher δ^{13}C values, around 0–1 ‰ (Craig, 1953), is introduced into the carbon pool of the percolating water, causing a shift in its stable carbon isotopic signature towards higher values, diverging from the low soil gas signature. Consequently, the quantities of carbon present in both pools (atmospheric/soil CO_2 vs. host rock carbon) play a crucial role in determining the δ^{13}C value of the drip water entering a cave and subsequently forming a speleothem. As explained in section I.2.1, the influence of the host rock is more pronounced under a 'closed system', leading to elevated δ^{13}C values, while it is negligible in an 'open system', resulting in more negative δ^{13}C values (Hendy, 1971). The extent to which each carbon pool contributes to the final carbon isotopic composition in the speleothem is primarily modulated by temperature and hydroclimate. Changes in climate may coincide with alterations in vegetation composition (Braun et al., 2019), soil respiration (Genty et al., 2003), and soil turnover rates (Rudzka et al., 2011). Conversely, the dissolution regime of carbonate bedrock (open vs. closed) may also undergo changes over time, thus impacting the isotopic composition of speleothems (Hendy, 1971). In order to gain a better understanding of the dominant processes that modulate the speleothem δ^{13}C variability within a given cave system, it is advisable to consider a multi-proxy approach, including stable oxygen isotopes (δ^{18}O), radiocarbon (^{14}C), trace elements (Mg, Sr, Ba, U,etc.), or crystal fabrics (e.g., Rudzka et al., 2011; Oster et al., 2010; Griffiths et al., 2012; Fohlmeister et al., 2017; Therre et al., 2020). Additionally, analyzing multiple speleothems from within a single cave system allows for the elimination of site-specific, localized variability (Skiba and Fohlmeister, 2023) and provides a better understanding of the general relationship between δ^{13}C values and climate above the cave.

Stalagmite Stable Isotopes on the Yucatán Peninsula

Monitoring work and speleothem studies from the northern YP inicate that precipitation amount is the main control on rainfall δ^{18}O values in this region (Medina-Elizalde et al., 2016a; Lases-Hernandez et al., 2019; Lases-Hernández et al., 2020). Furthermore, it has been shown that rainfall δ^{18}O on the YP can also be influenced by varying contributions from moisture sources in the Caribbean and Pacific (Lachniet and Patterson, 2009). Additionally, during November to February, northwestern cold fronts can bring significant rainfall with a distinctive isotopic composition to the YP, which may contribute to the isotopic composition of the water reservoir (DiMego et al., 1976; Henry, 1979). Consequently, stalagmite δ^{18}O records from Áaktun Kóopo Cave in the northeastern YP are interpreted as reflecting a composite signal of local rainfall amount, convective activity, tropical cyclone influence, and moisture source variability, consistent with findings from nearby studies (e.g., Asmerom et al., 2020; Warken et al., 2021; Braun et al., 2023).

Several studies also consider speleothem δ^{13}C values as reliable indicators of effective rainfall, local recharge, and drought variability (e.g., Webster et al., 2007; Ridley et al., 2015; Asmerom et al., 2020; Serrato-Marks et al., 2021; Jamieson et al., 2016; Warken et al., 2021; Travis-Taylor et al., 2023; Braun et al., 2023; Frappier et al., 2002; Baldini et al., 2016). This interpretation is based on the influence of rainfall on factors such as soil pCO_2, water residence time, host rock dissolution, PCP, and CO_2 degassing. Drier conditions reduce soil moisture, increase PCP and host rock carbon contributions, resulting in higher δ^{13}C values, whereas wetter conditions lead to more negative δ^{13}C values (Fohlmeister et al., 2020).

In addition, the vegetation above the cave can impact speleothem δ^{13}C values through the relative proportions of C_4 to C_3 plants (Fleitmann et al., 2009). Elevated soil δ^{13}C values in the Maya region have been associated with the cultivation of up to 15 different food plant species, including maize, the most well-known, that use the C_4 photosynthetic pathway (Webb et al., 2004; Fedick and Santiago, 2022). Thus, elevated δ^{13}C values in stalagmites from this area could indicate forest disturbance and an increase in C_4 plants due to the cultivation of crops, legumes, and other food plants, as has been suggested for a stalagmite on the southern YP (Akers et al., 2016). A recent study from the YP showed that there is a strong relationship between increased maize cultivation, tropical forest decline, and dry periods (Islebe et al., 2022). Since both natural factors (e.g., drier climate, C_4 plant prevalence) and anthropogenic activities (e.g., maize cultivation) result in higher δ^{13}C values in respired soil CO$_2$, and consequently in the stalagmite, distinguishing between these influences is challenging.

Radiocarbon in stalagmites

The carbon that ultimately incorporates into the crystal lattice of secondary carbonates, such as stalagmites, is a mixture derived from both the atmosphere/soil zone and the limestone bedrock, as discussed in section I.2.3. The mixture of carbon from these reservoirs, including carbon with (near)-atmospheric ^{14}C concentration and carbon devoid of ^{14}C, determines the final radiocarbon (^{14}C) content of the percolating drip water and, consequently, of the stalagmite (Fig. I.5). As atmospheric/soil CO$_2$ is transported downwards through the karst zone, its initially high ^{14}C activity diminishes, a process known as 'aging.' To convert the measured ^{14}C activity ($a^{14}\mathrm{C}_{\mathrm{meas}}$) to the initial radiocarbon activity at the time of speleothem formation ($a^{14}\mathrm{C}_{\mathrm{init}}$), the 'true' age of the speleothem sample ($t_{\mathrm{U/Th}}$) must be determined, typically through ^{230}Th/U dating.

$$a^{14}C_{init} \;=\; a^{14}C_{meas} \cdot e^{-\lambda_{Lib} \cdot t_{U/Th}} \tag{I.16}$$

Subsequently, the ^{14}C activity of the speleothem sample is compared to the corresponding radiocarbon activity of the atmosphere at the time of speleothem formation, providing a measure of the *dead carbon fraction* (DCF) (Genty and Massault, 1997), also termed the 'dead carbon proportion' or 'reservoir effect'.

$$DCF\,[\%] = \left(1 - \frac{a^{14}C_{init}}{a^{14}C_{atm}}\right) \cdot 100\% \tag{I.17}$$

As explained in sections I.2.1 and I.2.3, in a theoretical case of a closed dissolution system, carbon sourced from the limestone bedrock constitutes 50% of the dissolved carbon incorporated into the speleothem, resulting in a DCF of 50% (Hendy, 1971; Genty et al., 2001). Conversely, the opposite theoretical extreme, a fully open dissolution system, would yield a DCF of 0%. However, in reality, intermediate systems between closed and open dissolution systems occur, tending toward either theoretical paradigm. Nonetheless, DCF values surpassing 50% have been observed in near-closed dissolution systems. In these instances, excess limestone dissolution facilitated by sulfuric acid as a consequence of pyrite oxidation (Spötl et al., 2016; Bajo et al., 2017; Chervyatsova et al., 2020; Wolf et al., 2024) or the incorporation of aged soil organic matter (SOM) (Therre et al., 2020), introduces additional carbon with markedly reduced radiocarbon activities. Furthermore, variations in soil gas

pCO_2 and fractionation processes during the exchange of carbon between cave air CO_2 and DIC in drip water can significantly impact the magnitude of DCF (Fohlmeister et al., 2011). These primary drivers of DCF are, in turn, subject to the influence of a multitude of parameters, including hydrological and environmental conditions above the cave. Numerous studies have observed a positive correlation between infiltration and stalagmite DCF (e.g., Lechleitner et al., 2016; Griffiths et al., 2012; Bajo et al., 2017; Noronha et al., 2014). These studies argue that a closed system is typically associated with humid climates, wherein pore spaces in soils and karst formations become waterlogged. This reduces the exchange opportunities between DIC species and soil gas CO_2, consequently leading to higher DCF values. Conversely, under drier conditions with lower infiltration rates, pore spaces are less waterlogged, resulting in a more open dissolution system and, consequently, lower DCF values. The main carbon sources contributing to stalagmite formation are outlined in Table I.2.

Consequently, the analysis of radiocarbon in speleothems offers a broad spectrum of applications, such as serving as a dating method (e.g., Hua et al., 2017) or infering changes in soil carbon cycling (e.g., Trumbore, 2009). However, constraining the influence of each carbon reservoir— atmosphere, biosphere, soil, and bedrock— on the final carbon signature in stalagmites is crucial for making reliable statements. This entails possessing proper knowledge of the DCF in a stalagmite and its variability over time, which becomes particularly relevant for speleothem studies seeking to reconstruct past atmospheric ^{14}C levels, such as for the purposes of ^{14}C calibration.

carbon source	$\delta^{13}C$	$a^{14}C$
atmospheric CO_2	–6‰ to –8.5‰	$\approx a^{14}C_{atm}$
soil CO_2 (C3 vegetation)	–27‰ to –20‰	$\approx a^{14}C_{atm}$
soil CO_2 (C4 vegetation)	–16‰ to –10‰	$\approx a^{14}C_{atm}$
aged SOM (1 yr to 10^3 yr)	$\approx$ soil CO_2	$\approx a^{14}C_{atm}$ to 0.6 $a^{14}C_{atm}$
bedrock (limestone)	–2 to 2‰	0

Table I.2. $\delta^{13}C$ values and ^{14}C activity of major carbon sources in speleothems. The table is adapted from Therre (2020) with slightly modified values. Data were collected from McDermott (2004); Hendy (1971); Eggleston et al. (2016); Graven et al. (2017); Cerling (1984); Genty et al. (2001); Bajo et al. (2017); Fohlmeister et al. (2011).

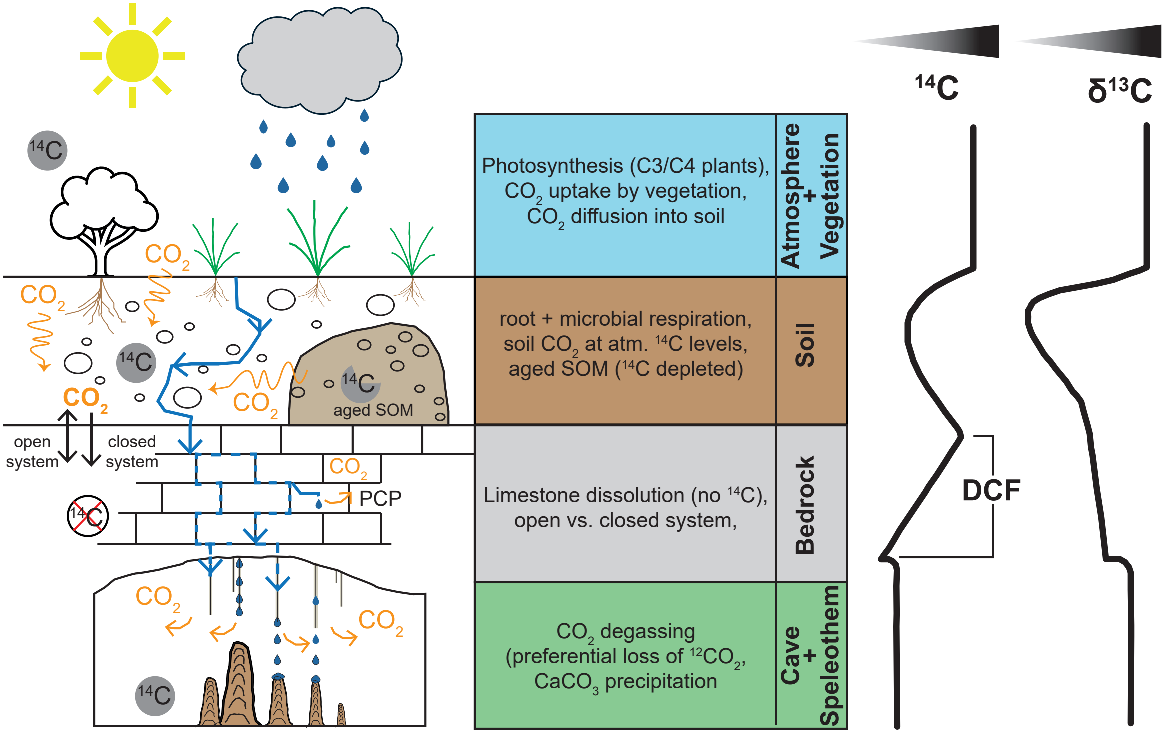

Figure I.5. Sources of carbon (δ^{13}C) and radiocarbon (^{14}C) in speleothems. Atmospheric CO_2 is absorbed by vegetation during photosynthesis and subsequently respired into the soil. Soil air CO_2 can diffuse outward, while atmospheric CO_2 may infiltrate. The low δ^{13}C values of soil gas primarily depend on the type of vegetation (C_3 vs. C_4), while aged SOM can decrease the ^{14}C concentration. 'Dead carbon,' with higher δ^{13}C, is introduced during limestone dissolution, varying by system type (open vs. closed). Prior calcite precipitation (PCP) can elevate δ^{13}C in percolation water.CO_2 degasses due to pCO_2 differences between water and cave air, leading to $CaCO_3$ precipitation and speleothem formation. The two paths on the right illustrate the potential evolution of ^{14}C and δ^{13}C for CO_2 and percolation water. Figure adapted from Lechleitner et al. (2016) and slightly modified based on Rudzka et al. (2011) and Therre (2020).

Trace elements in speleothems

An increasing number of studies are utilizing the additional information from minor and trace elements (e.g., Mg, Sr, Ba, P, U, ...) to assess interpretations based on the more conventional proxies of δ^{18}O and δ^{13}C (e.g., Treble et al., 2003; Borsato et al., 2007; Fairchild and Treble, 2009; Fairchild et al., 2000; Griffiths et al., 2010; Sliwinski et al., 2023; Faraji et al., 2023). Efforts have been made to synthesize existing paleoclimate records that make use of these hydroclimate-sensitive proxies (Kaushal et al., 2024). Along with the precipitation of speleothem carbonate (typically either as calcite or aragonite), minor and trace elements present in the dripwater may additionally be incorporated into the crystal lattice. Most 'salt-like' elements (e.g., Mg, Sr, Ba, etc.) have partition coefficients $D_X < 1$, indicating that only a fraction of the dissolved element will be incorporated into the speleothem's crystal lattice (e.g., Day and Henderson, 2013; Tremaine and Froelich, 2013; Borsato et al., 2015; Drysdale et al., 2019; Kost et al., 2023).

$$D_X = \frac{(X/Ca)_{CaCO_3}}{(X/Ca)_{Aq}} \tag{I.18}$$

The majority of studies focus on elements that produce divalent cations upon dissolution, thus acting as substitutes for Ca^{2+} within the carbonate crystal lattice, notably Mg^{2+}, Sr^{2+}, and Ba^{2+}. These elements are often interpreted as proxies for PCP, which refers to the precipitation of carbonate minerals (calcite or aragonite) from supersaturated water in the epikarst or at the cave ceiling before the drip water reaches the stalagmite surface (Fairchild et al., 2000). This process becomes more dominant under conditions of reduced infiltration, particularly when the host rock above the cave contains more air-filled cavities and the drip rate diminishes. Considering that D_{Mg} and D_{Sr} are <1, both Mg and Sr preferentially remain in solution during calcite precipitation, while Ca readily precipitates into the solid phase (Fairchild and Treble, 2009). Consequently, PCP leads to elevated concentrations of Mg, Sr, and Ba in the drip water, subsequently reflected in the stalagmite relative to Ca, thereby increasing the ratios of Mg/Ca and Sr/Ca, respectively (Fairchild et al., 2006; Johnson et al., 2006; Sinclair et al., 2012). Nevertheless, other factors, such as temperature, pH, variations in partitioning coefficients, incongruent carbonate dissolution (ICD) or growth rate, can also influence these trace elements, potentially causing a decoupling between Sr and Ba from Mg in the stalagmite (Warken et al., 2018; Borsato et al., 2007; Fairchild et al., 2000; Day and Henderson, 2013; Sinclair et al., 2012; Rodriguez-Cruz et al., 1999; Stoll et al., 2012; Huang and Fairchild, 2001; Sinclair, 2011; Tremaine et al., 2016; Wassenburg et al., 2020). Consequently, Mg/Ca, Sr/Ca, and Ba/Ca often do not covary in coeval stalagmites in ways expected from PCP (Sinclair et al., 2012; Stoll et al., 2012). While there is no consensus about the control of growth rate on Sr incorporation (e.g., Borsato et al., 2007; Sliwinski et al., 2023; Day and Henderson, 2013; Wassenburg et al., 2020; Belli et al., 2017), it has been shown that Sr incorporation is affected by the presence of other ions (e.g., Mg, Na, etc.) in the solution (Drysdale et al., 2019; Wassenburg et al., 2020).

Unlike hydroclimate-sensitive elements such as Mg, Ba, and Sr, U concentrations in speleothems are not commonly utilized as proxies, likely due to the complexity of its origin, transmission through the karst aquifer, and subsequent incorporation into the speleothem. It is suggested that uranium in cave drip waters, and consequently in speleothems, is primarily sourced from overlying soils and the dissolution of limestone (Bourdin et al., 2011; Smedley and Kinniburgh, 2023). Under certain conditions, uranium can also be derived from external sources, such as Saharan dust (Frumkin and Stein, 2004). Several hypotheses have been proposed to explain the mechanisms influencing uranium transport into caves. One potential factor is PCP, where increased PCP during drier periods generally raises uranium concentrations in cave drip waters due to the low distribution coefficient of uranium ($D_U < 1$) (Fairchild and Treble, 2009; Day and Henderson, 2013; Kost et al., 2023). This process would result in a positive correlation between U/Ca ratios and proxies like $\delta^{13}C$, Mg/Ca, Sr/Ca, and Ba/Ca. However, some studies suggest that increased PCP may instead reduce uranium concentrations through uranium and phosphorus scavenging onto mineral surfaces (Johnson et al., 2006), potentially leading to a negative correlation with these proxies.

Soil redox conditions also play a role, as less oxidizing conditions in soil can reduce uranium transport into the cave. During warmer, more humid periods, increased vegetation and soil moisture create a less oxidizing environment, which inhibits the oxidation of [U(IV)] to its more soluble form [U(VI)], thus decreasing uranium availability in percolating waters (Hellstrom and McCulloch, 2000). Conversely, during colder and drier periods, the opposite effect occurs, increasing uranium availability (Warken et al., 2019; Chen et al., 2016, 2020).

Another mechanism involves interactions between phosphorus and uranium, as observed in a study from southwestern Australia, where a correlation between these elements in speleothems was linked to vegetation dynamics (Treble et al., 2003). It was suggested that wetter climate conditions promote vegetation growth and decay, which could result in higher phosphorus concentrations. This, in turn, may support the formation of uranyl phosphate complexes, thereby increasing both phosphorus and uranium concentrations in the stalagmite.

Finally, soil pCO_2 has been shown to significantly enhance uranium solubility. Increased soil pCO_2, resulting from heightened plant respiration during warm and wet periods, can raise uranium concentrations in speleothems (Langmuir, 1978). Elevated soil pCO_2 is also associated with a decrease in the $\delta^{13}C$ signature due to the incorporation of strongly fractionated carbon isotopes (Lechleitner et al., 2021). Furthermore, increased soil pCO_2 favors more open-system dissolution of host rock carbonate, which further decreases both $\delta^{13}C$ values and the DCF in cave drip water (Hendy, 1971; Stoll et al., 2023). Thus, if soil pCO_2 is the predominant driver of uranium concentrations and carbon isotopes in speleothems, U/Ca ratios should exhibit an anticorrelation with $\delta^{13}C$ values and the DCF.

Another suite of trace elements comprises poorly soluble elements, such as Y^{3+}, Zn^{2+},

Cu^{2+}, Co^{2+}, Pb^{2+}, and P^{3+}, which can be transported through the karst using various ligating/chelating agents, typically colloidal organic matter (Borsato et al., 2007). The association with natural organic matter is reflected in annual UV-fluorescent layers in the stalagmite (Sliwinski and Stoll, 2021). Borsato et al. (2007) speculated that peaks of these elements record the mobilization and delivery during heavy autumnal infiltration in the cave. However, other studies have shown that the connection of this effect to seasonal peaks in stalagmites is more complex, and Sliwinski et al. (2023) propose that the incorporation of Y is predominantly governed by crystallization processes rather than by flux.

Furthermore, the crystal fabric itself has an influence on the incorporation of specific elements (Vanghi et al., 2019), where for example detrital and colloidal transported particles (e.g., Si, P, Mn, Fe, Al, Y, etc.) are ’trapped’ and enriched in stromatolite-like and micrite layers compared to elongated columnar fabrics.

In a study that combined the mapping of trace element distribution in speleothem calcite via LA-ICP-MS with mapping of entrapped water via Fourier Transform Infrared Focal-Plane Array (FTIR-FPA) imaging, new evidence is provided concerning the influence of submicroscopic fluid inclusions on the trace element content of stalagmites (Kost et al., 2023). The study suggests that a significant portion of Na may be hosted in entrapped water (fluid inclusions) rather than in the calcite matrix (Kost et al., 2023).

Combining the knowledge gained through the analysis of stable isotopes ($\delta^{18}O$, $\delta^{13}C$) and trace elements (Mg, Ba, Sr, U, etc.) provides a better understanding on how to interpret those individual hydroclimate proxies.

II Material and Methods

The here investigated samples have been retrieved from Áaktun Kóopo Cave, northern YP (Mexico) during three field visits in 2018, 2022, and 2023. Although I participated only in the latter two visits, I will provide a concise description of the 2018 expedition, as most of the material analyzed in this study was collected during that field trip. Along with carbonate samples drilled from speleothems inside the cave, a total of ten stalagmites were extracted from the cave during the three visits. Additionally, a few drip water samples were collected, and two temperature/humidity loggers as well as one drip logger were installed in the cave.

First, a detailled description of the study site (Áaktun Kóopo Cave), including pre-Hispanic activities and archaeological discoveries, is presented. This is followed by a summary of the objectives of each field trip. Finally, a detailed description of the selected stalagmites, including petrographic observations, and the methods and analyses employed in this study are provided. Significant contributions to this PhD project were made by two bachelor theses (Adrian, 2023; Stange, 2024) and one master thesis (Kolb, 2024), all of which were conducted at the Institute of Environmental Physics at Heidelberg University.

The sampling and analysis of drip water samples, along with the data from the loggers, will be briefly addressed in the Appendix VII.

II.1 Study Site – Áaktun Kóopo Cave

Location and Description of Áaktun Kóopo Cave

Áaktun Kóopo Cave is located in “La Estrella”, a small Maya community which belongs to the municipality of Chemax and is located at about 30 km northeast of this village and 7 km west of Xcan. This community is situated within the territory of Cocoyol, giving rise to a noticeable tension among the inhabitants of both places (Tec, 2021).

The cave entrance is located southwest of the Estrella village, approximately 50 meters northwest of the intersection with Federal Highway 186 to Cancún, at 20°48’26.7”N, 87°44’15.8W”. Next to the cave entrance stands an Alamo tree (*Ficus cotinifolia;* Kunth et al., 1976) that grows from inside the cave and gives the cave its name ”Kóopo” (Yucatec Maya name for Alamo tree). The entrance to the cave comprises a sinkhole measuring 5.1 meters in length, 2.7 meters in width, and 4.5 meters in depth (Tec, 2021). Since 2017, a wooden staircase built by the villagers has made it easier to access the cave. In 2007, a first survey to the cave was performed by the AJAU group of cave explorers where they also started with the documentation of archaeological remains inside the cave. In 2010, AJAU and a group of French cave explorers returned to Estrella and, during several visits, explored the cave to a length of 1900 meters and a depth of 21 meters (Fig. II.1) (Thomas et al., 2011). According to the most recently updated map, the cave extends horizontally to over 2100 meters, yet additional sections remain to be fully mapped (Tec, 2021). There are at least nine different water bodies inside the cave and their water levels fluctuate seasonally (rainy season vs. dry season), which occasionally leads to flooding of some parts of the cave, making them inaccessible for a period of time (Tec, 2021). The soils in Áaktun Kóopo Cave are dry, wet, or muddy and consist mostly of red clay (*kankab*).

Pre-Hispanic Activities and Archaeological Discoveries

The presence of numerous Maya archaeological remains, such as cave paintings, polychrome pottery and skeletal remains of 23 individuals, both juvenile and adults, suggest that the cave might have been used as a Maya burial ground or for ritual practices (Gómez, 2020). These archaeological remains have been dated to the late Preclassic (–250 to 300 AD) and early Classic (300 to 600 AD) periods (Gómez, 2020), suggesting that the area above or around the cave might have been inhabited during that time. The cave was also modified by the Maya, who built simple walls of limestone blocks and soil to artificially separate cave segments and “chambers”.

In occasions, they used existing stalagmites to place limestone blocks between them, while other wall segments are piled up by unconsolidated limestone blocks cemented with either mortar or soil. At least seven constructions are present in various sections of the cave (Tec, 2021).

The archaeological findings demonstrate that the pre-Hispanic Maya attributed sacred significance to the cave, as evidenced by their perception of it as a site for ritual activities, the preservation of ancestral remains, pilgrimages, or water collection (Tec, 2021). Gómez (2020) notes that the presence of imported artifacts, such as flint and obsidian, suggests privilege among the group that interacted in the cave.

The skeletal remains from Áaktun Kóopo Cave indicate that it was utilized by a human group for domestic and ritual activities, coinciding with the occupation of surface settlements in the Xcan region (Gómez, 2020) (Fig. A4). The social group utilizing the cave likely belonged to the local elite, with mortuary practices reinforcing social memory and identity (Gómez, 2020). The cave's mortuary deposit underwent transformation over time, leading to its eventual abandonment and subsequent disturbance by outsiders (Gómez, 2020).

II.2 Field Trips and Sample Material

II.2.1 Field Trips

Field Trip 1 (June 2018)

In 2018, Wolfgang Stinnesbeck from Heidelberg University established personal contact with the local group of cave explorers (Grupo Espeleológico AJAU, Mérida) from the Mexican state of Yucatán and visited Áaktun Kóopo Cave together with collaborators from the Staatliches Museum für Naturkunde in Karlsruhe in June 2018 to assess its future research potential.

During the cave visit with AJAU, Wolfgang Stinnesbeck and his colleagues were permitted by the excavation team to retrieve eight stalagmites (E0, E1, E2, E3, E4, E6, E7, E8). Care was taken in selecting the stalagmites to ensure that they appeared relatively young—i.e., that they had grown during the last ∼3000 years—and ideally also showed active growth.

In addition to retrieving several stalagmites, a temperature and humidity logger *TGP-4500 TinyTag Plus 2* (± 0.5°C precision) was installed inside the central part of the cave (Fig. A5) on a speleothem column below the cave ceiling to record changes in cave temperature and relative humidity every 30 minutes. A full list of the stalagmites collected during this field trip is provided in Table A3.

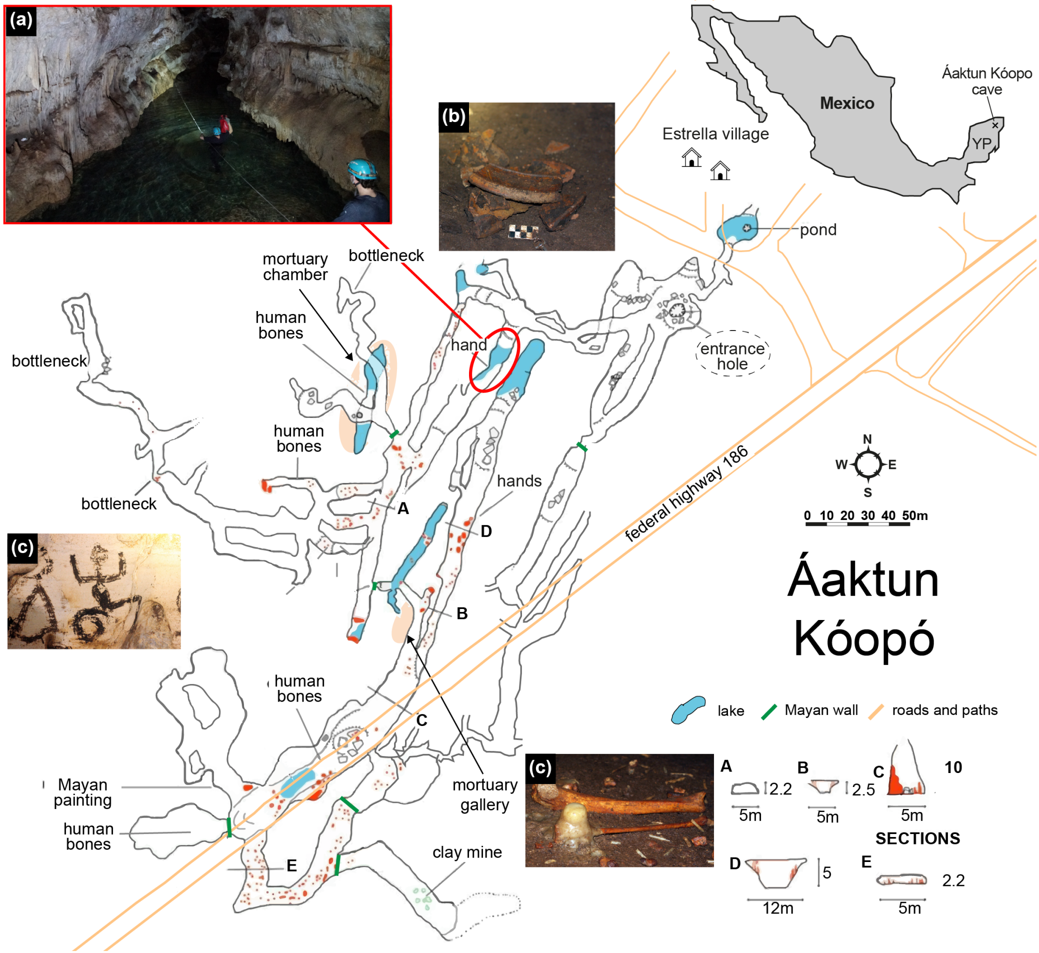

Figure II.1. Map of Áaktun Kóopo Cave, located southwest of Estrella village, Yucatán, Mexico. The southern part of the cave extends beneath Federal Highway 186. **(a)** One of nine water bodies within the cave, which must be waded or swum through to access the deeper sections (Tec, 2021). The cave also contains numerous Maya archaeological remains, including simple stone walls that form small chambers and divide specific sections of the cave, as well as pottery **(b)**, paintings **(c)**, and human bones **(d)**. The map is based on Thomas et al. (2011) and modified after Gómez (2020) and Tec (2021). Photographs were taken by Jeronimo Aviles Olguin.

Field Trip 2 (March 16, 2022)

In March 2022, I had the pleasure of visiting the cave with one of our project partners from Yucatán, Mexico, Dr. Jeronimo Avilés Olguín. During the visit, we placed two temperature and humidity loggers *TinyTag Plus 2* (± 0.5°C precision) in different parts of the cave (Fig. A5). Additionally, we placed a drip logger (STALAGMATE) below one drip site. Stalagmite E-23-3, which was fed by this drip site, appeared to be actively growing. I retrieved the stalagmite from the cave the following year since it turned out that the stalagmites collected in 2018 did not grow continuously during the last 150 years (see later Chapter III.3). Furthermore, we collected three drip water samples (EDW-1, EDW-2 and EDW-3) from different parts of the cave (Fig. A5) for the analysis of stable water and thorium isotopes. EDW-3 is unique as it consists of water collected from different drips (soda straws) within an area of about 1 m^2 in the western part of the cave, specifically within the chamber where most of the analyzed stalagmites were extracted (Fig. A5). Due to very low drip rates on the day of the cave visit, we had to improvise by manually moving the plastic bottle from one soda straw to another to obtain a sufficient amount of drip water. From the floor below the drip site EDW-1, we collected a small sample of what appeared to be modern carbonate precipitates. Furthermore, we took a small piece of carbonate from a flowstone. A full list of the collected carbonate and drip water samples is provided in Table A4. Furthermore, we measured the CO_2 concentration in eleven different parts of the cave (Fig. A5) with a handheld CO_2 probe (*Amprobe*: usable up to 5000 ppm with ± 30 ppm +5% rdg). This device also measures the temperature (±0.6°C).

Field Trip 3 (April 1, 2023)

This time I was again accompanied by Dr. Jeronimo Aviles Olguin, who helped me navigate through the cave and collect carbonate and drip water samples. At first, the two temperature and humidity loggers and one drip logger that had been installed the year before were read out and restarted. Drip water was sampled at the same sites as the year before, with one additional sample from a different part of the cave, making a total of four drip water samples. The tops and bottoms of two stalagmites were drilled with a battery-powered drilling machine, equipped with a core drilling head, to obtain small drill cores for ^{230}Th/U-dating. The promising stalagmite E-23-3, where we had placed the drip logger below its drip the year before, was extracted from the cave. A full list of the carbonate and drip water samples that have been collected during this field trip is provided in Table A5. Again, temperature and CO_2 concentration were measured with a handheld CO_2 probe (*Amprobe*: usable up to 5000 ppm with ± 30 ppm +5% rdg; ±0.6°C) at the same parts of the cave as the year before (n=11).

II.2.2 Stalagmite Samples

During the cave visits in 2018 and 2023, a total of ten stalagmites, ranging from 6.5 to 34 cm in length, were retrieved from Áaktun Kóopo Cave. For six of these stalagmites (E0, E1, E2, E7, E8, E23-3) their drip site was still actively dripping at the time of collection. Stalagmites E0, E1, E7, and E8 were all collected from a 2 m^2 area in the northwestern part of the cave (Fig. A5). Interestingly, both E0 and E7 exhibited an L-shaped, or ”double” formation (Fig. II.2). This morphology occurs when a stalagmite falls over, and continued carbonate precipitation causes growth to proceed at a perpendicular angle to the original axis, resulting in the observed L-shape. Notably, E0 was not calcified to the ground but rather embedded in soft sediment, which may have contributed to its collapse. During the extraction, a third stalagmite (E0-A) was uncovered beneath 10 cm of sediment. Stalagmite E2 was collected from the central part of the cave, while stalagmite E4 was retrieved from the northeastern section, closer to the cave's entrance. Stalagmite E3 was collected from the southern portion, located in front of a large Maya wall. During the sampling process, a small stalagmite (EMW5) detached from this wall and was subsequently collected. As an initial step in the analysis, the stalagmites were cut along their presumed growth axes. Depending on the diameter of each stalagmite, one or two slices were extracted for further analyses, as described in the subsequent sections.

II.3 Methods

II.3.1 Mineralogical Characterization of Stalagmites

The stalagmites from Áaktun Kóopo Cave, utilized in this thesis to develop multi-proxy climate records, were examined for their mineralogical composition and crystal fabric. This analysis involved X-ray diffraction (XRD) measurements and thin section microscopy, both of which will be briefly outlined in the following sections.

XRD Measurements

Slices cut from the extracted stalagmites from Áaktun Kóopo Cave revealed several changes in color throughout their growth (Fig. II.2), which may be attributed to variations in mineralogy (calcite vs. aragonite) or differences in crystal fabric. XRD was employed to distinguish between calcium carbonate polymorphs such as calcite and aragonite. Nine powder samples were drilled from visually distinct sections of stalagmite E0-C for XRD analysis (Fig. A6), and one sample was collected from the bottom portion of stalagmite E1. Based on the fan-like crystal texture and silky gloss observed in this section (Fig. II.2), the sample was expected to be composed of aragonite.

Each sample consisted of approximately 1 g of carbonate powder, obtained by drilling with a Proxxon machine equipped with a diamond-coated stainless steel drill bit. XRD measurements were performed at the Institute of Earth Sciences, Heidelberg University, using a Bruker D8 ADVANCE Eco diffractometer (parameters: Cu K radiation source, 30 kV voltage, 33 mA current, Ni filter, SSD160 detector). The

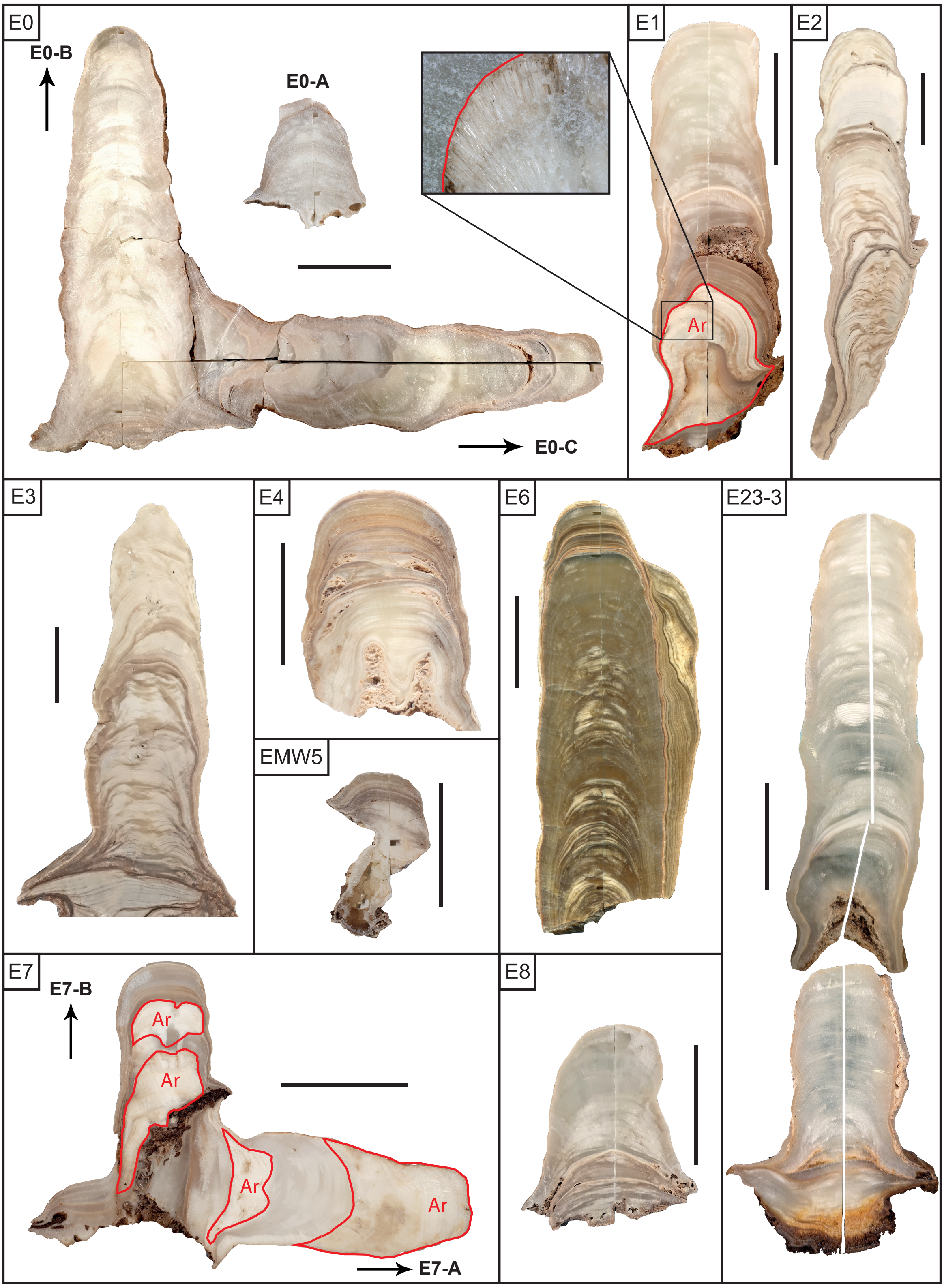

Figure II.2. Scans of slices cut from ten stalagmites recovered from Áaktun Kóopo Cave during two field trips in 2018 and 2023. The scale bar, shown as a black line, represents 5 cm in all images. Areas outlined in red highlight macroscopically identifiable aragonite phases in stalagmites E1 and E7. The inset figure of stalagmite E1 shows millimeter-long aragonite crystals situated directly adjacent to the more compact calcite phase.

samples were analyzed in rotating sample holders over an angular range of 2θ from 5° to 70°, with increments of 0.019° and a counting time of 1 second per step. Peak positions and intensity data were analyzed using Diffrac.Suite EVA software (Bruker). The results of the XRD analysis revealed characteristic diffraction peaks (2θ) corresponding to calcite in all analyzed samples from the E0-C stalagmite (Fig. A6a). In contrast, the assumption of an aragonitic composition for the sample from the bottom portion of the E1 stalagmite was confirmed by the presence of typical 2θ peaks of aragonite (Fig. A6b). These findings demonstrate that the speleothems from Áaktun Kóopo Cave can consist of both $CaCO_3$ derivatives: calcite and aragonite. Since aragonite is less stable than calcite, there is a high probability that aragonite may recrystallize to calcite over time. This recrystallization can lead to isotope exchange, which compromises the closed system necessary for accurate ^{230}Th/U dating. Such isotope alteration can affect the accuracy of age models used for reconstructing past climatic and environmental conditions. Therefore, it is essential to assess potential recrystallization, as it can alter the isotope composition of the stalagmites.

While XRD is an effective method to determine speleothem mineralogy, a comprehensive analysis across multiple stalagmites would require a larger number of samples. Another useful approach is the examination of thin sections under a microscope, which allows for detailed characterization of speleothem mineralogy and crystal fabrics, as well as the identification of potential signs of recrystallization (e.g., Frisia et al., 2002; Perrin et al., 2014). This method will be briefly outlined in the following section.

Thin Section Analyses

To further investigate the mineralogy (calcite vs. aragonite) of the stalagmites and identify potential signs of recrystallization, thin sections from stalagmites E0-B, E0-C, E4, E8, and the upper section of E1 were examined using a polarized transmitted-light microscope (KEYENCE VHX-6000) at the Institute of Earth Sciences, Heidelberg University. The thin section analyses revealed only calcite phases, which consisted of two major fabrics: open elongated calcite and compact elongated calcite, where crystals exhibit a length-to-width ratio greater than 6:1 (Frisia, 2015) (Fig. II.3). The more open fabric appears whitish macroscopically, while the compact elongated calcite phase appears more translucent (Fig. II.2). Despite the macroscopically visible growth interruptions (hiatuses) in the form of major flooding layers, smaller detrital layers were often identified, typically near the tops of the stalagmites but occasionally also throughout their growth.

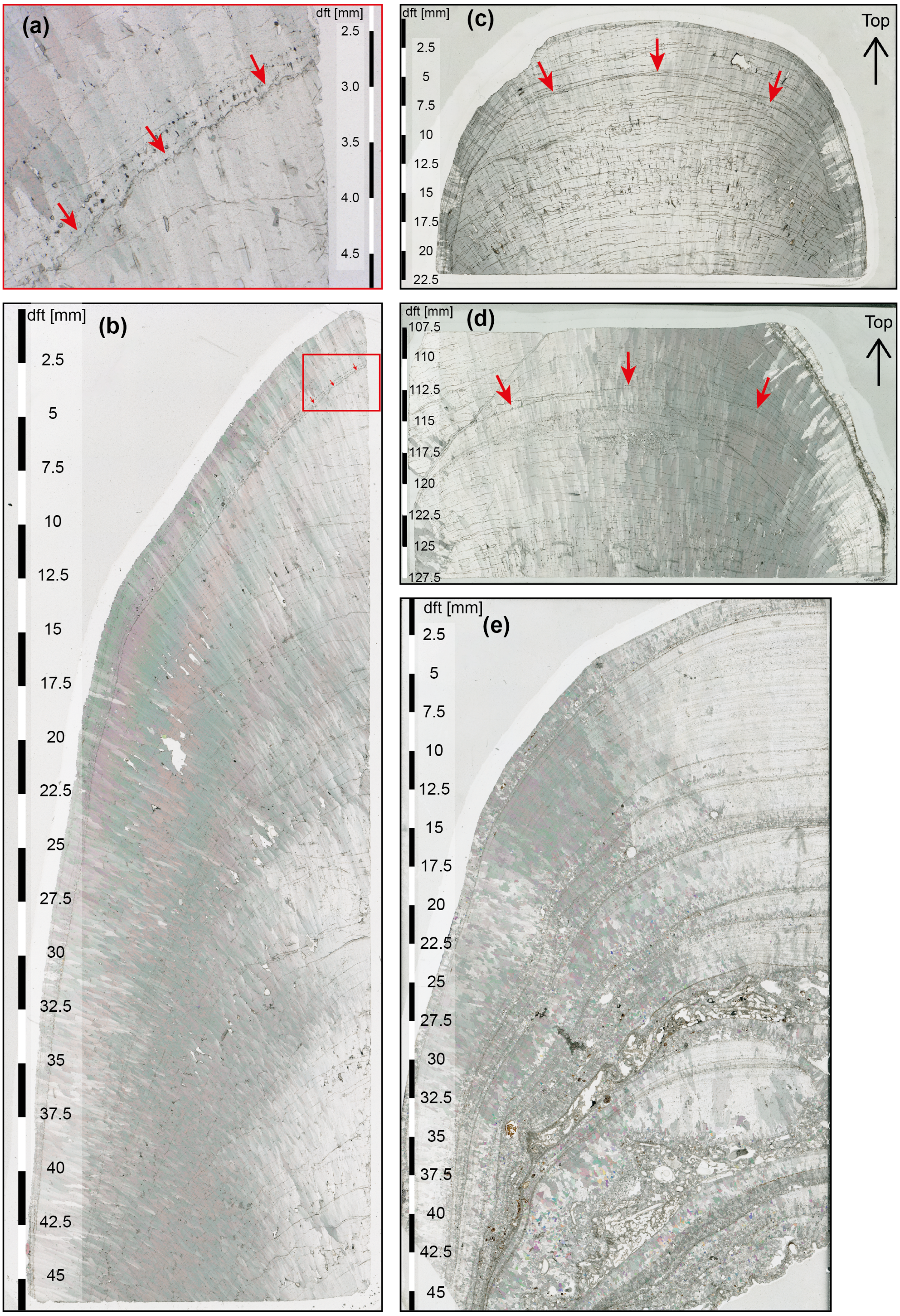

Figure II.3. Thin section photographs of stalagmites E0-C, E1 and E4 from Áaktun Kóopo Cave. **(a)** Zoom-in of the top part of stalagmite E1. Red arrows highlight the hiatus at 2.8 mm distance from top (dft). **(b)** Top part of stalagmite E1, consisting mostly of compact elongated calcite and to some minor extent of open elongated calcite. The red square near the top indicates the zoom-in image shown in (a). **(c)** Top of stalagmite E0-C consisting of both compact and elongated columnar calcite. Red arrows highlight the hiatus at 5 mm dft. **(d)** Another hiatus occurring around 113 mm dft in stalagmite E0-C, indicated by rhombohedral crystal terminations (red arrows). **(e)** Top part of stalagmite E4 showing many growth interruptions as indicated by the layering. Some of these layers consist of detrital material, likely indicating recurrent flooding of the stalagmite.

Under the microscope, these interruptions were characterized by clear rhombohedral crystal terminations and the presence of detrital minerals, such as clay (Fig. II.3). Since no signs of aragonite-to-calcite recrystallization, such as preserved original aragonite textures or 'ghosts' of aragonite (Frisia et al., 2002; Perrin et al., 2014), were observed under the microscope, it can be assumed that stalagmites E0-B, E0-C, E4, E8, and the upper portion of stalagmite E1 consist of primary calcite, predominantly in the form of compact or slightly open elongated fabrics.

II.3.2 Dating Techniques

^{230}Th/U-Dating

156 speleothem samples from Áaktun Kóopo Cave have been investigated by high-precision ^{230}Th-U dating using a multi-collector inductively coupled plasma source mass spectrometer (MC-ICP-MS, Thermo Fisher Neptune$^{\text{plus}}$) at the Institute of Environmental Physics, Heidelberg University. For this analysis, small calcite plates, approximately 1 mm in width, were cut using a diamond wire saw from slices of the stalagmites perpendicular to their growth direction. This method was employed to minimize mixing of multiple layers, resulting in sample sizes of approximately 100 mg. To ensure optimal ionization efficiency and prevent interferences in the mass spectrum, U and Th were purified from their calcium matrices. This chemical preparation involved leaching of the sample plate, followed by dissolution, spiking, and wet column extraction chromatography using Eichrom UTEVA resin, following previously published procedures by Douville et al. (2010), Matos et al. (2015), and Wefing et al. (2017). The mass spectrometry techniques and data treatment are detailed in Kerber et al. (2023). U-series isotope measurements were conducted using a semi-static multi-cup setting according to Arps (2017). Ages were calculated employing the half-lives provided by Cheng et al. (2013). Uncertainties are reported at the 2σ level and do not include half-life errors.

Radiocarbon Dating

Radiocarbon (^{14}C) measurements were conducted along the entire length of stalagmite E0-C and at the tops of stalagmites E1 and E8. The measurements on stalagmite E0-C were performed as part of Celine Kolb's master thesis at the Institute of Environmental Physics at Heidelberg University (Kolb, 2024). The required amount of carbonate material varied depending on the measurement system employed. Here, two different approaches were utilized:

First Approach: Small calcite samples (10–20 mg) were cut from the tops of stalagmites E0-C, E1, and E8, as well as along the growth axis of E0-C, using a diamond wire saw at the Institute of Environmental Physics, Heidelberg University. To avoid contamination by ambient air, the samples were leached in 4% hydrochloric acid prior to hydrolysis and graphitization. A detailed description of the sample preparation routine is provided in Therre et al. (2021). The resulting graphite–iron compounds were measured using a 200 kV tandem mini carbon dating system (MICADAS) accelerator mass spectrometer (AMS) at the Curt-Engelhorn Center for Archaeometry in Mannheim, Germany (Synal et al., 2007; Kromer et al., 2013). Since 2018, a total of 138 blanks have been measured to assess the background signal and detect contamination during sample processing, with a long-term blank value of 0.190 ± 0.064 pMC (50.794 ± 2.813 ka) (Therre et al., 2021; Beisel, 2024). Oxalic acid II standards, graphitized from previously extracted CO_2, were used for calibration. To ensure reproducibility, the IAEA C2 standard is measured with each series of analyses. The mean value of all measurements since 2018 is 41.15 ± 0.16 pMC (7,132 ± 31 years) (Therre et al., 2021; Beisel, 2024), matching the assigned literature value of 41.14 ± 0.03 pMC (Rozanski et al., 1992).

Second Approach: A specific section of stalagmite E0-C was later sampled at a higher resolution (1–2 mm steps) using a Micromill (2010A *Sherline*) equipped with a micro milling cutter (TiSiN) of 500 µm in diameter. Due to the smaller sample quantities (3–4 mg), radiocarbon measurements of these samples (n=20) were performed on a MICADAS AMS equipped with a gas-ion source at ETH Zurich. This setup enables the direct ionization of CO_2, bypassing the need for sample graphitization, resulting in faster analysis and a reduction in sample size. Calibration was performed using the NIST SRM 4990C oxalic acid II standard. The methodology and performance of MICADAS are well-documented in previous studies (e.g., Synal et al., 2007; Ruff et al., 2007; Haghipour et al., 2018).

Annual Layer Count

In principle, two main types of annual laminae in stalagmites can be distinguished: (1) laminae that are visible to the naked eye or through optical microscopy and (2) laminae that are not visible by conventional optical microscopy techniques (e.g., Sliwinski et al., 2023; Baker et al., 2021; Borsato et al., 2021). Seasonal changes in carbonate mineralogy or fabric, reflecting changes in crystal arrangement and particle concentration due to hydrological or colloidal matter input, create physical or textural laminae in stalagmites. On the other hand, laminae associated with dissolved organic compounds in the carbonate are not visible by conventional optical microscopy, but can be observed through fluorescence or confocal microscopy (e.g., Sliwinski et al., 2023; Sliwinski and Stoll, 2021; Orland et al., 2014). Additionally, ”invisible” chemical laminae, characterized by cyclic changes in trace element concentration, can be analyzed through techniques such as secondary ionization mass spectrometry (Roberts et al., 1998) or laser ablation ion coupled plasma mass spectrometry (LA-ICP-MS) (Treble et al., 2003). The recent application of creating two-dimensional trace element maps of a stalagmite slab through synchrotron micro-X-ray fluorescence (S-μXRF) (Borsato et al., 2007, 2021; Wang et al., 2019) allows for accounting for geometric/lateral variability in trace element concentrations. Similarly, measuring two to three parallel tracks via LA-ICP-MS techniques also provides information regarding lateral variability.

Another way to group speleothem lamina types is through its formation process – hydrologically controlled vs. cave-climate controlled. The preservation of physical annual laminae in speleothems is thought to be controlled by seasonal ventilation and cave air pCO_2, as well as water supersaturation and influx from surface compounds, affecting crystal growth (Baker et al., 2021; Frisia et al., 2000). While annual laminae, composed of organic matter, particles, and colloids, typically reflect the transport of soil-derived material during the wet season, cyclic variations in concentrations of bedrock-derived trace elements (e.g., Mg, Sr) can be directly linked to seasonal changes in the extent of rock-water interaction or PCP, with elevated concentrations of these elements characterizing the dry season (Treble et al., 2003; Tremaine and Froelich, 2013; Johnson et al., 2006).

For some stalagmites (E1, E8, E23-3) from Áaktun Kóopo Cave, seasonal changes in element ratios such as Sr/Ca are very pronounced and can be continuously counted, allowing for an improvement of the age-depth models based on ^{230}Th/U dating.

After plotting the Sr/Ca ratio of the stalagmite, derived from LA-ICP-MS measurements (see section II.3.3), against the distance from the top (dft), the annual layers were manually counted across the entire stalagmite or for individual sections in case of growth interruptions or sections with unclear or absent cycles (Fig. II.4). In each case, the distance between two Sr/Ca minima was counted as one year, as the minima are sharper and can be determined more precisely than the wider maxima. For some years, the seasonal variations are less pronounced or even absent, which introduces uncertainty to the layer count. Since this uncertainty is difficult to quantify, an arbitrary uncertainty of ±0.5 layers per 10 counted layers is assumed for all stalagmites. For stalagmites where continuous growth up to the point of extraction can be assumed, the counted layers can be correlated with the age of the topmost layer, corresponding to the year of extraction from the cave. If continuous growth cannot be assumed, the chronology of the layer count is aligned with the age having the smallest error margin, which introduces an additional uncertainty to the age determination.

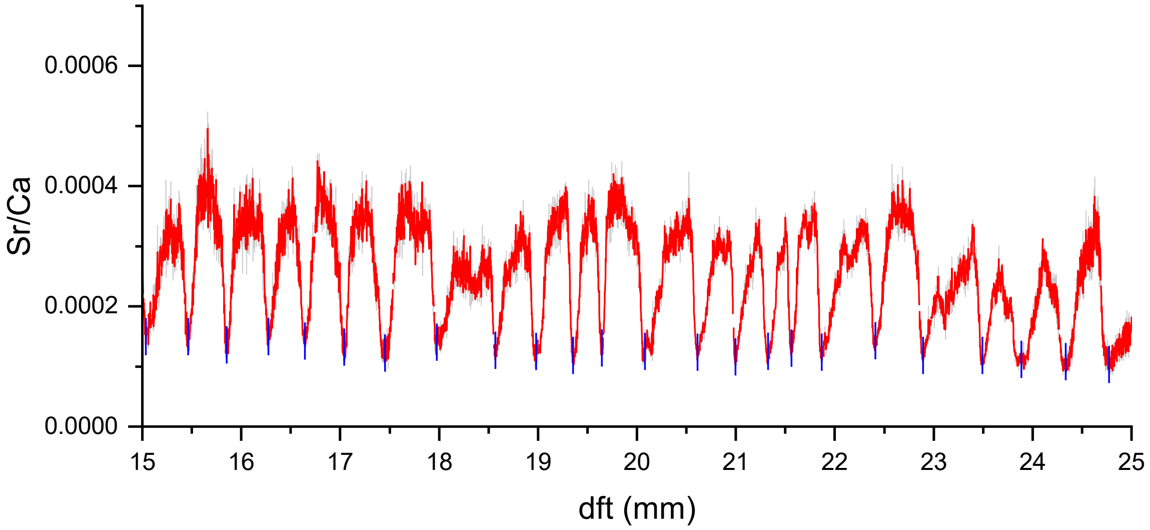

Figure II.4. The counting of seasonal Sr/Ca cycles in stalagmites from Áaktun Kóopo Cave is exemplarily shown for the section between 25 and 15 mm dft of stalagmite E23-3. The Sr/Ca ratios are shown in light grey, with a moving average of 30 in orange. The counted Sr/Ca minima (blue vertical bars) in this section correspond to 25±1 years, assuming a counting error of 0.5 layers per 10 counted layers.

II.3.3 Trace Element Analysis via LA-ICP-MS

Trace element analysis was conducted on the stalagmites E0-C, E1, E4, E8 and E-23-3 from Áaktun Kóopo Cave via LA-ICP-MS using a 193 nm ArF excimer laser (NWR193$^{\mathrm{UC}}$ by New Wave Research) coupled to an inductively coupled plasma quadrupole mass spectrometer (Thermo Fisher iCAP-Q) at the Institute of Environmental Physics, Heidelberg University. The analyses of stalagmites E1, E8, and E23-3 were carried out as part of two Bachelor theses (Adrian, 2023; Stange, 2024), which contributed to this PhD project. Line scans were performed along the growth axes of the stalagmite slabs using a rectangular spot size of 25 × 100 µm for most of the stalagmites (with the longer side being vertical and perpendicular to the track). Since the measurement settings (spot size, scan speed, repetition rate, etc.) varied slightly for each stalagmite, they are listed in Table A6. To avoid potential surface contamination, the scan path was always pre-ablated by using a circular spot of 150 µm in diameter at a scan speed of 100 µm s^{-1} and a repetition rate of 10 Hz. Background counts were measured with the laser in the off mode and subtracted from the raw data. Further data processing involved an outlier correction, in which a floating 1.5 interquartile range (IQR) was applied. To account for matrix effects, the blank-corrected count rates of the analyzed isotopes (^{25}Mg, ^{88}Sr, ^{138}Ba, etc.) were normalized relative to the intensity of the ^{44}Ca signal, which served as the internal standard. Silicate glass NIST SRM 612 was analyzed for external calibration of the trace element analyses using the reference values provided by Jochum et al. (2011). A drift correction was applied through linear interpolation between two standard measurements taken before and after each ablation path. The resulting element/Ca ratios are presented as mass concentration ratios. Due to a premature termination of the laser measurements on the E0-C stalagmite, the top 2.5 mm of the sample were missing. To ensure completeness, the upper part (0–39.5 mm dft) was re-measured. Prior to interpreting the resulting element/Ca ratios, it is crucial to ensure the reliability of the data. This is typically achieved by assessing whether the difference between the measured signal intensity ($\mathrm{I_{sig}}$) and the background noise ($\mathrm{I_{bkg}}$) is sufficiently large, which is quantified using the signal-to-noise ratio (SNR). The SNR is calculated by subtracting the mean background intensity from the mean signal intensity and dividing the result by the standard deviation of the background noise (σ_{bkg}):

$$SNR = \frac{\overline{I_{\mathrm{sig}}} - \overline{I_{\mathrm{bkg}}}}{\sigma_{\mathrm{bkg}}} \tag{II.1}$$

Data with an $SNR \leq 3$ are classified as below the limit of detection (LOD) and are rejected.

II.3.4 Stable Isotopes of Oxygen and Carbon

For stalagmites E0-C, E1, E8, and E23-3, samples for stable isotope analysis were drilled either on top of or directly adjacent to the trace element tracks. Approximately 50–90 µg of powdered samples were obtained using a Micromill (2010A *Sherline*) equipped with a micro milling cutter (TiSiN) of 500 µm in diameter. The spacing between samples varied from 100 to 500 µm (250 µm most of the time). Detailed information regarding the total number of samples, the spacing between them, and the analysis methodology will be provided for each stalagmite in subsequent sections.

All samples were analyzed at the Institute of Earth Sciences, Heidelberg University, using a ThermoFinnigan MAT253Plus gas source mass spectrometer equipped with a Thermo Fisher Scientific Kiel IV carbonate device, unless stated otherwise. The δ^{13}C and δ^{18}O values are reported relative to Vienna Pee Dee Belemnite (VPDB) standard through the analysis of an in-house standard (Solnhofen limestone, $\delta^{13}\mathrm{C_{VPDB}} = +1.38 \pm 0.03‰$ and $\delta^{18}\mathrm{O_{VPDB}} = -4.59 \pm 0.06‰$) calibrated to the reference material IAEA-603 (calcite; $\delta^{13}C_{VPDB} = +2.46 \pm 0.01‰$ and $\delta^{18}O_{VPDB} = -2.37 \pm 0.04‰$). External reproducibility, based on repeated measurements of an in-house standard, was better than 0.02‰ for $\delta^{13}C$ and 0.07‰ for $\delta^{18}O$ at the 1σ confidence level.

E0-C: A total of 528 samples for stable isotope analysis were drilled next to the trace element tracks at a spatial resolution ranging between 100 and 500 µm. One-third of the samples (n=175) were analyzed at the Institute of Earth Sciences, Heidelberg University, as described above. The other two-thirds (n=353) were analyzed at Elemtex Ltd., Cornwall, UK, using an isotope ratio mass spectrometer (IRMS) (Thermo Scientific Delta V coupled with a Gasbench II). Quality control is performed using a Carrara marble standard ($\delta^{13}C = 2.10‰$, $\delta^{18}O = -2.01‰$) and a second in-house calcite standard ($\delta^{13}C = 2.89‰$, $\delta^{18}O = -6.15‰$), calibrated directly against NBS18 and NBS19. The reported long-term precision (1σ level) is 0.022‰ for $\delta^{13}C$ and 0.040‰ for $\delta^{18}O$ values.

E1: A total of 389 samples were drilled next to the trace element tracks at a spatial resolution ranging between 100 and 250 µm. For the top part of the stalagmite (0–7 mm), samples were drilled at a resolution of 100 µm.

E8: A total of 208 samples were drilled next to the trace element tracks at a spatial resolution of 250 µm. For the top part of the stalagmite (0–2 mm), samples were drilled at a resolution of 100 µm.

E23-3: A total of 224 samples were drilled next to the trace element tracks at a spatial resolution of 250 µm for the section between 0 and 30 mm dft, and at 500 µm for the section between 30 and 84 mm dft.

II.3.5 Time Series Analyses

Time series analyses of the proxy records ($\delta^{13}C$, $\delta^{18}O$) were conducted using both spectral and wavelet analyses. Spectral analysis was performed with the 'REDFIT' algorithm (Schulz and Mudelsee, 2002), implemented in the open-source R package 'dplR' (Bunn et al., 2020). The 'REDFIT' algorithm applies a first-order autoregressive (AR1) process to unevenly spaced time series, enabling robust spectral analysis. In addition, wavelet analyses were conducted using the R package 'Biwavelet' (Gouhier et al., 2019), providing insights into the time-frequency domain of the data.

III Speleothem Chronologies

In this chapter, the ^{230}Th/U dating results of speleothem samples from Áaktun Kóopo Cave are discussed. This includes addressing the handling of elevated and variable ^{230}Th contamination and constructing individual stalagmite age-depth models that together encompass the last ~2.7 kyr.

These chronologies provide the basis for the following two chapters of this thesis (Chapters V and VI), which focus on the paleoclimatic and paleoenvironmental information that can be gathered from these stalagmites, as well as a possible linkage to key periods of Maya cultural evolution, such as the Terminal Classic Period (TCP).

Most of the findings of this chapter are part of the manuscript *High-Resolution ^{230}Th/U Dating of Speleothems from Áaktun Kóopo Cave, Yucatán, Mexico: Methodology and Chronology Over the Last 2.7 kyr* (Schorndorf et al., in preparation).

^{230}Th/U dating requires a closed system for U and Th exchange following the formation of secondary carbonate, along with the absence of initial ^{230}Th. A closed system behavior is generally difficult to test, as the U-series boundary conditions, such as the U concentration, δ^{234}U, and ^{232}Th, can vary significantly in karst waters. It is, however, well known from previous studies that caves in the northern Yucatán Peninsula yield elevated initial ^{230}Th, which thus needs to be carefully assessed prior to age modelling and interpretation of speleothem growth during the past 2.7 kyr.

III.1 Detrital ^{230}Th Contamination

A total of 157 speleothem samples from Áaktun Kóopo Cave were analyzed for ^{230}Th/U-dating (Table A7). Most samples have a low ^{232}Th concentration of <0.1 ng g^{-1}, resulting in (^{230}Th/^{232}Th) activity ratios of >300, indicating a minor influence of the detrital fraction on age determination. However, some samples exhibit a significant detrital influence due to relatively low uranium concentrations, elevated detrital ^{232}Th (up to 26.5 ng g^{-1}), young ages, or a combination of these factors.

Consequently, a few uncorrected ^{230}Th/U-ages do not align stratigraphically with the chronology established by the majority of other samples. Most of these age inversions are associated with elevated ^{232}Th and persist when utilizing a bulk Earth detrital (^{230}Th/^{232}Th) activity ratio of 0.75–0.89 for the upper continental crust (Taylor and McLennan, 1985; Heier and Carter, 1963; Heier and Rogers, 1963), suggesting the likely presence of higher initial ^{230}Th values within these samples. Furthermore, since samples that contain more detrital ^{232}Th generally also contain more detrital ^{230}Th, a relationship between the activity ratios of (^{230}Th/^{238}U) and (^{232}Th/^{238}U) can be expected in cases of significant detrital contamination (Ludwig, 2003). Indeed, such a relationship can be observed for stalagmite samples from Áaktun Kóopo Cave (Fig. III.1).

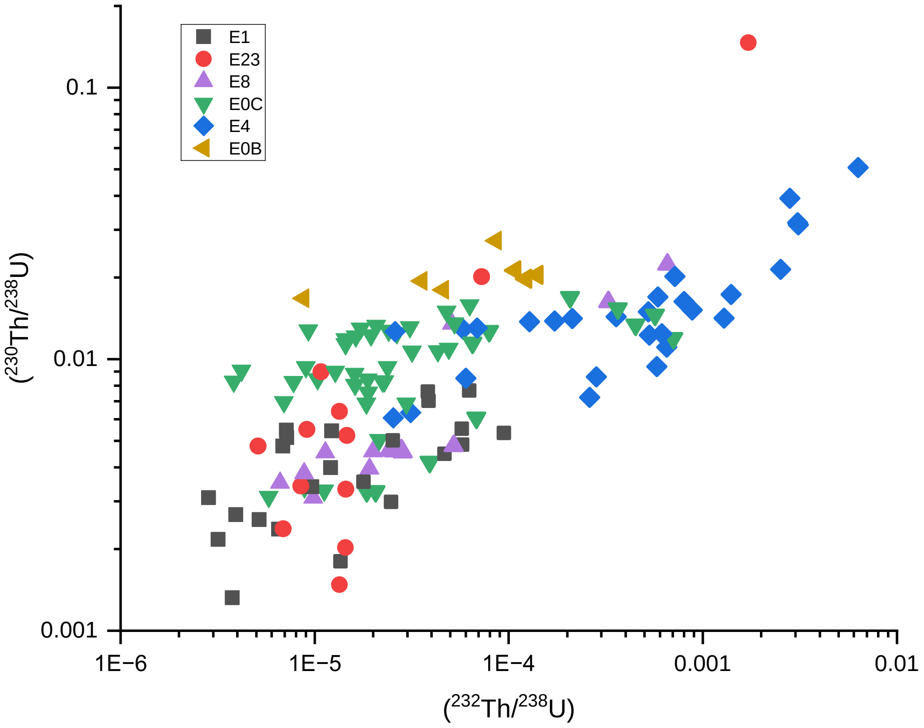

Figure III.1. (^{230}Th/^{238}U) vs. (^{230}Th/^{232}Th) of samples from different stalagmites in Áaktun Kóopo Cave. The linear relationship between these activity ratios suggests significant detrital contamination of the samples. Different symbols and colors represent the various stalagmites. Note the logarithmic scale on both axes.

Measurements of (^{230}Th/^{232}Th) activity ratios in three drip water samples from Áaktun Kóopo Cave range from 1.659 ± 0.046 to 8.9 ± 1.0 (see Chapter VII). Additionally, a supposedly modern carbonate sample (zero-age calcite, "ZAC") yielded a (^{230}Th/^{232}Th) activity ratio of 6.57 ± 0.03, confirming the presence of elevated initial ^{230}Th within the drip water and speleothem samples.

However, when using these elevated values to correct the stalagmite's ^{230}Th/U ages, many age inversions still persist. Therefore, higher (^{230}Th/^{232}Th) activity ratios are needed to correct for detrital Th contamination and to adhere to the stratigraphic constraint of increasing ages from top to bottom of the analyzed stalagmites.

To estimate the range and variability of (^{230}Th/^{232}Th) activity ratios of the contaminating phase, various approaches were employed. One method utilizes the stratigraphic constraint of increasing ages from the top to the bottom of the stalagmites. In this approach, two types of samples were used: (1) Samples with no detectable ^{232}Th, as their ages are not influenced by detrital contamination, and therefore serve as anchor points in the stratigraphy. (2) Samples from the tops of the stalagmites, which contain elevated ^{232}Th. These samples are assumed to be younger than the uncorrected ages of samples below them but older than the year of collection.

In some stalagmites, distinct seasonal variations in Sr/Ca ratios, obtained through LA-ICP-MS measurements, allow for annual layer counting (Fig. II.4). The information obtained from this layer counting can then be used to estimate an appropriate (^{230}Th/^{232}Th) activity ratio for correcting the ^{230}Th/U ages of the stalagmite for detrital ^{230}Th contamination. Further details on this methodology are provided in Chapter II.3.2.

Additionally, due to the dense sampling of some stalagmites for ^{230}Th/U dating, an isochron approach was employed to further estimate the range and variability of the initial (^{230}Th/^{232}Th) activity ratio of the contaminating phase within these secondary carbonates. Specifically, linear two-endmember mixing regressions (Osmond type 1 isochrons) were calculated using ISOPLOT software for different sections of the stalagmites (Ludwig and Titterington, 1994; Ludwig, 2008; Vermeesch, 2018), following the methodologies outlined by Fensterer et al. (2010) and Warken et al. (2020). To maintain the assumption of contemporaneous deposition, only samples in close proximity to each other were collected, assuming they were deposited within a few years to decades—a timeframe consistent with the uncertainty of analytical dating. However, this approach often yielded unsatisfactory results, as indicated by scattering around the isochron, elevated mean squared weighted deviation (MSWD) values, and low probabilities of fit. This is not unexpected, as the sub-samples likely do not possess identical ages, despite selecting those closest to each other for analysis. Furthermore, detrital Th, commonly associated with clay minerals, may consist of multiple components with different (^{230}Th/^{232}Th) activity ratios. Additionally, the (^{230}Th/^{232}Th) ratio of the hydrogenous component could differ from that of the detritus (Bischoff and Fitzpatrick, 1991).

Nevertheless, five isochrons from three different stalagmites (E0-C, E4, E8), with fit probabilities >0.05 and MSWD values <1, were successfully derived (Ludwig and

Titterington, 1994). The resulting (^{230}Th/^{232}Th) activity ratios range from 6.4 ± 2.4 to 19 ± 10 (Fig. A7).

The various approaches used to estimate the range and variability of (^{230}Th/^{232}Th) activity ratios of the contaminating phase demonstrate the difficulty of accurately constraining these values and introduce significant uncertainty. Consequently, all samples with a (^{230}Th/^{232}Th) activity ratio <200 ($n=68$) were excluded from the construction of individual stalagmite age-depth models and from further discussion (Fig. III.2). This exclusion also includes all samples within 7.5 mm of the stalagmite tops, due to the young age of these carbonates and limited ^{230}Th accumulation, which makes it particularly challenging to develop a robust age model for the uppermost sections of the stalagmites.

Using the above discussed findings it must be assumed that variable (^{230}Th/^{232}Th) activity ratios ranging between 3 and 68 are needed to correct the stalagmites from Áaktun Kóopo Cave in order to adhere to the stratigraphic constraint of increasing ages from top to bottom of the stalagmites (Table A7). Notably, an activity ratio of 68 was required for only one sample from stalagmite E1 to correct its age. For most other samples, the upper range of required (^{230}Th/^{232}Th) activity ratios is roughly between 30 and 50. However, to account for the full range of possible values up to 68, a mean of 35.5 ± 32.5 was used for samples where the initial (^{230}Th/^{232}Th) activity ratio couldn't be estimated (Table A7).

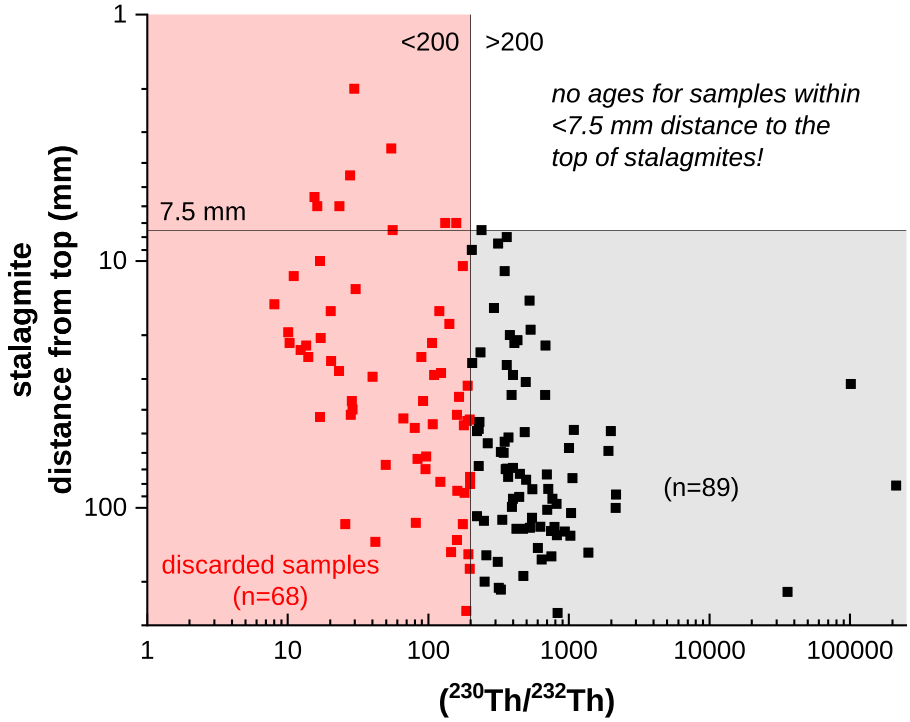

Figure III.2. Samples with (^{230}Th/^{232}Th) activity ratios <200 (n=68, red squares) are excluded due to significant detrital Th impact. Included samples (n=89, black squares) are used in age-depth models and further discussion. No samples with ratios >200 are found within 7.5 mm of the top, due to the young age of these carbonates and limited ^{230}Th accumulation.

Similar high activity ratios, up to 80 times greater than the commonly utilized range of 0.75–0.89 for the upper continental crust (Taylor and McLennan, 1985; Heier and Carter, 1963; Heier and Rogers, 1963), have been reported in other speleothem studies, particularly those from tropical regions such as the Caribbean (e.g., Ridley et al., 2015; Vieten et al., 2024a; Warken et al., 2021; Stinnesbeck et al., 2020; Richards and Dorale, 2003; Beck et al., 2001; Partin et al., 2007; Hoffmann et al., 2010; Carolin et al., 2013; Arienzo et al., 2015; Moseley et al., 2015; Steidle et al., 2021; Vieten et al., 2024b) (Table I.1). For instance, speleothem studies from the Bahamas show a wide range of (^{230}Th/^{232}Th) activity ratios, ranging from 2.2 to 18.7 (Richards and Dorale, 2003; Beck et al., 2001; Hoffmann et al., 2010; Arienzo et al., 2015). This variability is corroborated by other studies that have documented significant fluctuations in U and Th concentrations in the carbonates and waters of the Bahamas, alongside several potential sources of detrital Th, including aeolian inputs (Robinson et al., 2004). Bornean speleothems contaminated with detrital limestone have shown initial (^{230}Th/^{232}Th) activity ratios as high as 10 to 21 (Partin et al., 2007; Carolin et al., 2013). In a study conducted in the southern YP, (^{230}Th/^{232}Th) activity ratios ranging between 8 and 41 were used to correct a stalagmite for detrital Th contamination

(Ridley et al., 2015), while ratios of 35±17.5 and 61.1±61.1 were applied for the correction of two Puerto Rican stalagmites (Vieten et al., 2024a,b). Although many studies use these elevated and variable ratios to correct ^{230}Th/U ages, few discuss the potential sources of these high values or the factors that drive the observed variability over time.

Despite the low solubility of Th in natural waters, it commonly adsorbs onto clay minerals and humic acids (Morton et al., 2001; Reiller et al., 2002; Nascimento et al., 2019), facilitating its mobility and transport. The analysis of soil leachates and ZAC in central Texas caves suggests that soil material is a source of detrital Th in the stalagmites and accounts for the observed elevated (^{230}Th/^{232}Th) activity ratios (Wortham et al., 2022). It was suggested that Th adsorbs onto clay minerals in soils, is transported as particulates through the karst system, and subsequently precipitates out of solution with iron and/or manganese-oxides. The authors of this study further propose that monitoring (^{230}Th/^{232}Th) activity ratios in ZAC can reliably determine the detrital (^{230}Th/^{232}Th) activity ratios to use for the correction of ^{230}Th/U ages, thereby providing an alternative approach to isochron techniques (Wortham et al., 2022). While this approach provides a useful estimation of the potential range of initial (^{230}Th/^{232}Th) activity ratios relevant for an individual cave (drip) site, it has strong limitations. Specifically, it does not offer insights into the factors driving variability over time or how to estimate individual (^{230}Th/^{232}Th) activity ratios for specific points in time. Such information, however, is crucial for accurately constraining a precise stalagmite age model, especially for very young stalagmites of only a few hundred to a thousand years in age, for which the detrital Th correction has a major impact on the final age. Additionally, it is important to note that not all caves exhibit active carbonate deposition. Thus, caution should be exercised when considering visually active or fresh speleothems, or speleothems with drip water, as ZAC. This is because speleothem growth may be absent despite ongoing water dripping (Li et al., 2022; Chen and Li, 2018).

For the fresh-looking carbonate sample from Áaktun Kóopo Cave, however, it is likely that it is of modern age, since the (^{230}Th/^{232}Th) activity ratio of 6.57 ± 0.03, which is required to correct the sample to zero-age, falls within the range of (^{230}Th/^{232}Th) activity ratios measured in the three drip water samples from Áaktun Kóopo Cave (1.659 ± 0.046 to 8.9 ± 1.0). While these samples already exhibit elevated (^{230}Th/^{232}Th) activity ratios compared to average crustal values (0.75–0.89: Heier and Carter, 1963; Heier and Rogers, 1963; Mclennan et al., 1980), they do not account for the significantly higher ratios, reaching up to 68, that are necessary to adjust individual ages to align with the sedimentary sequence of the stalagmites.

An extensive monitoring program conducted over several years, including repetitive measurements of (^{230}Th/^{232}Th) activity ratios in soil, host rock, drip water, and zero-age carbonate, could help constrain the sources and drivers of elevated detrital thorium and its variability over time in groundwater and speleothems from Áaktun Kóopo Cave.

The generation of individual stalagmite age-depth models, along with the (^{230}Th/^{232}Th) activity ratios used, will be discussed in the following section.

III.2 Stalagmite Age-Depth Models

The age-depth models for stalagmites E0-B, E0-C, E1, E4, E8, and E23-3 were constructed using multiple techniques: *linear interpolation*, *linear regression*, *Bchron* (Haslett and Parnell, 2008), *Bacon* (Blaauw and Christen, 2011; Blaauw et al., 2019), *COPRA* (Breitenbach et al., 2012), and *StalAge* (Scholz and Hoffmann, 2011), following a similar approach to that used by the Speleothem Isotopes Synthesis and Analysis (SISAL) working group. The code used for constructing the age models is derived from SISAL.AM on GitHub. The final age-depth model, representing the weighted mean age $\bar{A}$, was calculated as:

$$\bar{A} = \frac{\sum_{i=1}^{n} \frac{A_i}{\sigma_{i+}^2 + \sigma_{i-}^2}}{\sum_{i=1}^{n} \frac{1}{\sigma_{i+}^2 + \sigma_{i-}^2}} \tag{III.1}$$

where:

- A_i is the age of the i-th age model,
- σ_{i+} is the positive uncertainty of the i-th age model,
- σ_{i-} is the negative uncertainty of the i-th age model,
- n is the total number of age models.

Stalagmite E0-B

Eight samples from stalagmite E0-B were analyzed for ^{230}Th/U dating (Table A7). The uranium content ranged from 476 to 555 ng g^{-1}. Three samples were rejected due to low (^{230}Th/^{232}Th) activity ratios (<200). Of the remaining five, one was corrected with a stratigraphically derived (^{230}Th/^{232}Th) ratio of 43.75 ± 24.25, while the other four used a mean ratio of 35.5 ± 32.5. Based on the weighted mean of the used age models, stalagmite E0-B grew from 633 ± 161 BC until 403 ± 54 AD (Fig. III.3).

The growth rate in the lower part of the stalagmite, between 222 and 110 mm dft, is slightly lower at 170 µm a^{-1} compared to the upper section between 110 and 0 mm dft, where it is 292 µm a^{-1}.

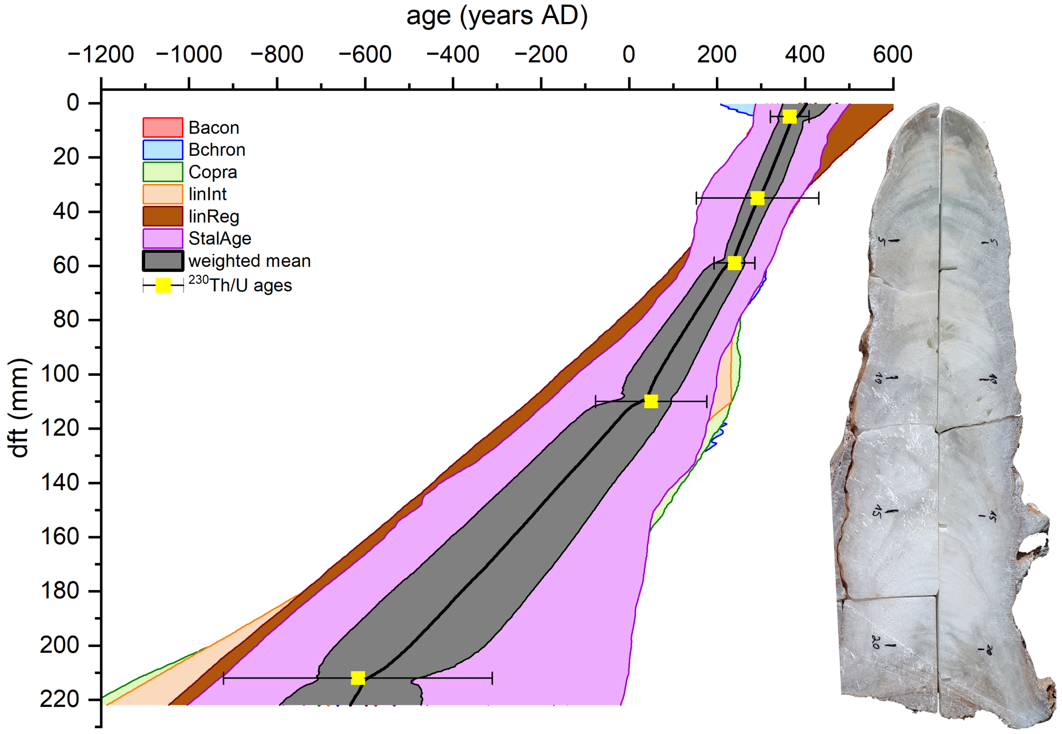

Figure III.3. Various age-depth models of stalagmite E0-B, including *Bacon*, *Bchron*, *Copra*, *linInt*, *linReg*, and *StalAge*. The weighted mean age-depth relationship is shown in black, with its corresponding uncertainty band in grey. The five ^{230}Th/U ages involved are also shown. A scan of the stalagmite is shown on the right.

Stalagmite E0-C

A total of 51 samples were analyzed for ^{230}Th/U dating from stalagmite E0-C (Table A7). The uranium content of the stalagmite ranges between 355 and 1324 ng g^{-1}. 15 samples were rejected due to low (^{230}Th/^{232}Th) activity ratios (<200). The remaining 36 samples were corrected using individual (^{230}Th/^{232}Th) ratios between 7 and 49, derived from isochron techniques and stratigraphic constraints. One sample remained unordered chronologically and was excluded.

The growth of E0-C is divided into three periods separated by hiatuses: (1) 538 ± 56 AD to 811 ± 52 AD; (2) 994 ± 29 AD to 1311 ± 15 AD; and (3) 1451 ± 22 AD to 1835 ± 53 AD (Fig. III.4). The average growth rates were 372 µm a^{-1}, 294 µm a^{-1}, and 94 µm a^{-1}, respectively. No age model is provided for the top section due to a hiatus at 5 mm dft. However, a radiocarbon measurement from the tip of the stalagmite suggests modern growth (post-1950 AD) (see Appendix VII).

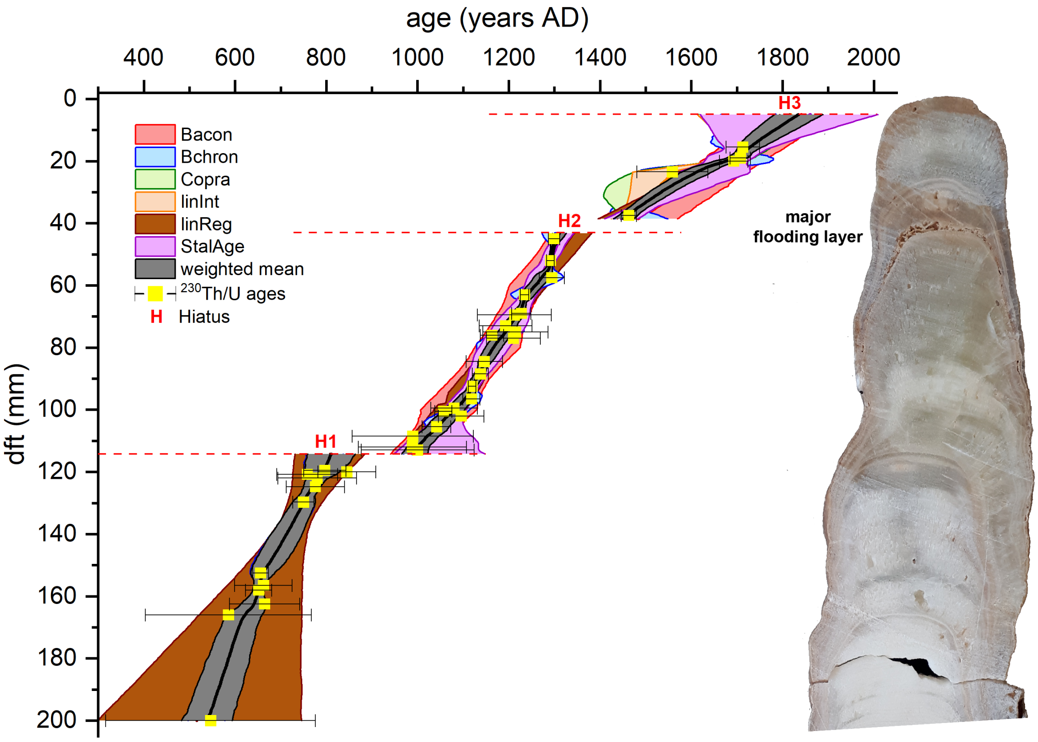

Figure III.4. Various age-depth models, including *Bacon*, *Bchron*, *Copra*, *linInt*, *linReg*, and *StalAge*, are presented for the three growth periods of stalagmite E0-C. The weighted mean age-depth relationship is shown in black, with its corresponding uncertainty band in grey. The three growth hiatuses (H1–H3) are indicated, along with the ^{230}Th/U ages used. The major flooding layer corresponding to H2 is visible on a scan of the stalagmite.

Stalagmite E1

A total of 25 samples were analyzed for ^{230}Th/U dating from stalagmite E1 (Table A7). The uranium content of the stalagmite ranges between 1202–2237 ng g^{-1}. Twelve samples were excluded due to low (^{230}Th/^{232}Th) activity ratios (<200). Of the 13 remaining samples, one was adjusted with a stratigraphically derived ratio of 49 ± 19. The other 12 were adjusted with a mean ratio of 35.5 ± 32.5.

Stalagmite E1 grew from 1440 ± 39 AD to around 1577 ± 42 AD with a growth rate of 281 µm a^{-1} (Fig. III.5). Growth resumed around 1635 ± 24 AD and continued until around 1926 ± 20 AD at ~3 mm dft, with a growth rate of approximately 230 µm a^{-1}.

Additionally, it was possible to count individual growth years based on the seasonal variations in Sr/Ca ratios obtained through LA-ICP-MS measurements (see Methods II.3.3). For the section between 3 and 61 mm dft, 311±16 Sr/Ca cycles were counted, while for the lower portion between 61 and 96 mm dft, a total of 182±9 cycles were counted. To test the reliability of the detritus-corrected ^{230}Th/U ages, the age model based on Sr/Ca cycles between 3 and 61 mm dft was anchored to the ^{230}Th/U age at 39 mm dft, which contains no measurable ^{232}Th and therefore does not require any detrital Th correction (Fig. III.5). For the lower section, the Sr/Ca-based age-depth model was anchored to the bottommost ^{230}Th/U age, which corresponds to the highest measured (^{230}Th/^{232}Th) activity ratio in this section of the stalagmite and is therefore least affected by detrital Th correction. Considering the uncertainties of both the ^{230}Th/U-based and the Sr/Ca-based age-depth models, both align perfectly. No age model is provided for the top section due to a hiatus at 3 mm dft. However, a radiocarbon measurement from the tip of the stalagmite suggests modern growth (post-1950 AD) (see Appendix VII). For the construction of a composite proxy record in Chapter VI, the ^{230}Th/U-based model will be used.

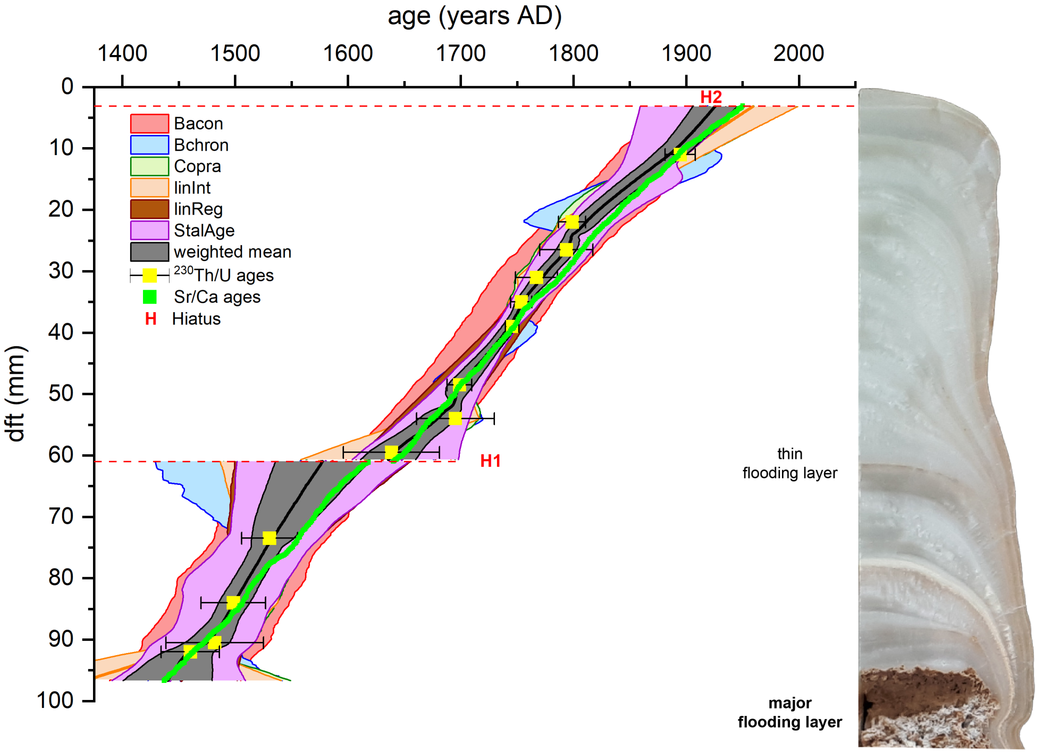

Figure III.5. Various age-depth models, including *Bacon*, *Bchron*, *Copra*, *linInt*, *linReg*, and *StalAge*, are presented for the two growth periods of stalagmite E1. The weighted mean age-depth relationship is shown in black, with its corresponding uncertainty band in grey. The two growth hiatuses (H1 and H2) are indicated, along with the ^{230}Th/U ages used. The two flooding layers are visible on a scan of the stalagmite.

Stalagmite E4

A total of 28 samples were analyzed for ^{230}Th/U dating from stalagmite E4 (Table A7). The uranium content of the stalagmite ranges between 604 and 1740 ng g^{-1}. Almost all of the samples (n=24) were excluded as they exhibit high ^{232}Th concentrations of up to

26.5 ng g^{-1}, resulting in (^{230}Th/^{232}Th) activity ratios of less than 200. One isochron, comprising a subset of three samples, yielded an initial (^{230}Th/^{232}Th) activity ratio of 8.2±1.3, with a probability of fit greater than 0.05 and an MSWD of 0.0001 (Fig. A7d) (Vermeesch, 2018). Two of these samples were therefore corrected with a value of 8.2±1.3. The other two samples from the top part of the stalagmite were corrected with a mean ratio of 35.5±32.5.

The growth of stalagmite E4 started around 228±88 AD and continued until 1611±118 AD with an average growth rate of 53 µm a^{-1}, assuming uninterrupted and constant growth (Fig. III.6).

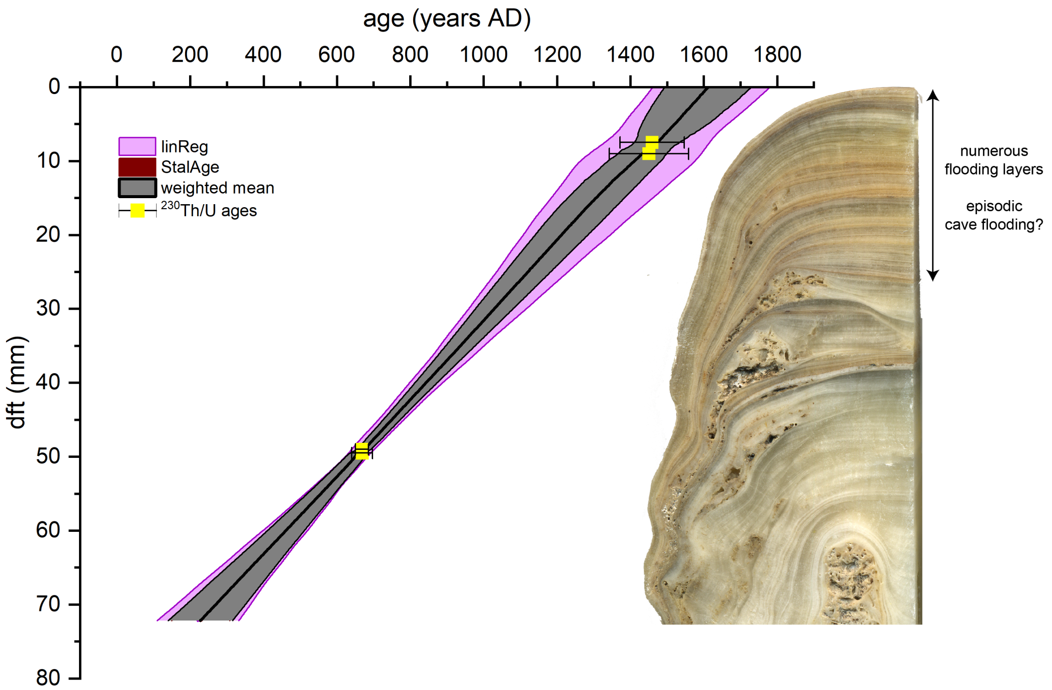

Figure III.6. The age-depth models for stalagmite E4 were constructed using *linReg* and *StalAge*. The weighted mean age-depth relationship is represented by the black line, with the corresponding uncertainty band shown in grey. The four ^{230}Th/U ages involved are also shown. A scan of the stalagmite reveals fine lamination in its upper half, characterized by alternating layers of carbonate and mud/clay, likely resulting from episodic cave flooding events.

Stalagmite E8

A total of 15 samples were analyzed for ^{230}Th/U dating from stalagmite E8 (Table A7). The uranium content of the stalagmite ranges between 524 and 1368 ng g^{-1}. Seven samples were excluded due to low (^{230}Th/^{232}Th) activity ratios (<200). One isochron, comprising a subset of four samples with a probability of fit >0.05 and MSWD of 0.016, was derived (Vermeesch, 2018). The derived isochron yielded an initial (^{230}Th/^{232}Th) activity ratio of 6.4±2.4 (Fig. A7e). Between 3 and 43 mm dft, it was possible to count individual growth years based on the seasonal variations in Sr/Ca ratios obtained through LA-ICP-MS measurements. In general, three different growth periods of stalagmite E8 can be distinguished.

Due to the presence of only two samples with the same age within uncertainty for the lowermost part of stalagmite E8 between 65 and 50 mm dft, an age-depth model was not constructed for this section. Nevertheless, the two ^{230}Th/U ages at 60.5 and 55 mm dft suggest some growth between 565 and 927 AD (Fig. III.7).

Following a hiatus at 50 mm dft, a second growth phase can be observed between 50 and 27.9 mm dft. Using the isochron-derived (^{230}Th/^{232}Th) activity ratio of 6.4 ± 2.4 for detritus correction of the sample at 29 mm dft results in a ^{230}Th/U age of 1541 ± 9 AD. However, the uncorrected age at 42 mm dft is 1533 ± 9 AD, which is already too young compared to the number of Sr/Ca layers counted between 29 and 42 mm dft (40 ± 2 layers). Consequently, a definitive age model for this section of the stalagmite cannot be provided.

Following another minor growth interruption at 27.9 mm dft, a third growth phase continues until 0.8 mm dft. Due to a hiatus at 0.8 mm dft, the layer-counted age-depth model for this section was anchored to the ^{230}Th/U age at 14.5 mm dft. This age corresponds to the highest measured (^{230}Th/^{232}Th) activity ratio within the stalagmite and is therefore least affected by detrital Th correction. For the detritus correction of this sample, a broad (^{230}Th/^{232}Th) activity ratio of 35.5 ± 32.5 was used. The ages of the three other samples between 8.5 and 26 mm dft were then corrected with individual (^{230}Th/^{232}Th) activity ratios, ranging between 7 and 35.5, to match the layer-counted age-depth model. This step considers not only the uncertainty of the anchor age at 14.5 mm dft but also the uncertainty of the Sr/Ca layer counting, which assumes a counting error of 0.5 layers per 10 counted layers (see Methods II.3.2). Applying these corrections, growth resumed at 27.9 mm dft around 1605 ± 24 AD, with an average growth rate of 215 µm a^{-1} until 1733 ± 33 AD at 0.8 mm dft, where growth ceased again (Fig. III.7).

Since no seasonal Sr/Ca layers are visible within the topmost 3 mm, information on the time covered by the topmost 0.8 mm of the stalagmite cannot be provided. However, a radiocarbon measurement from the tip of the stalagmite suggests modern growth (post-1950 AD) (see Appendix VII).

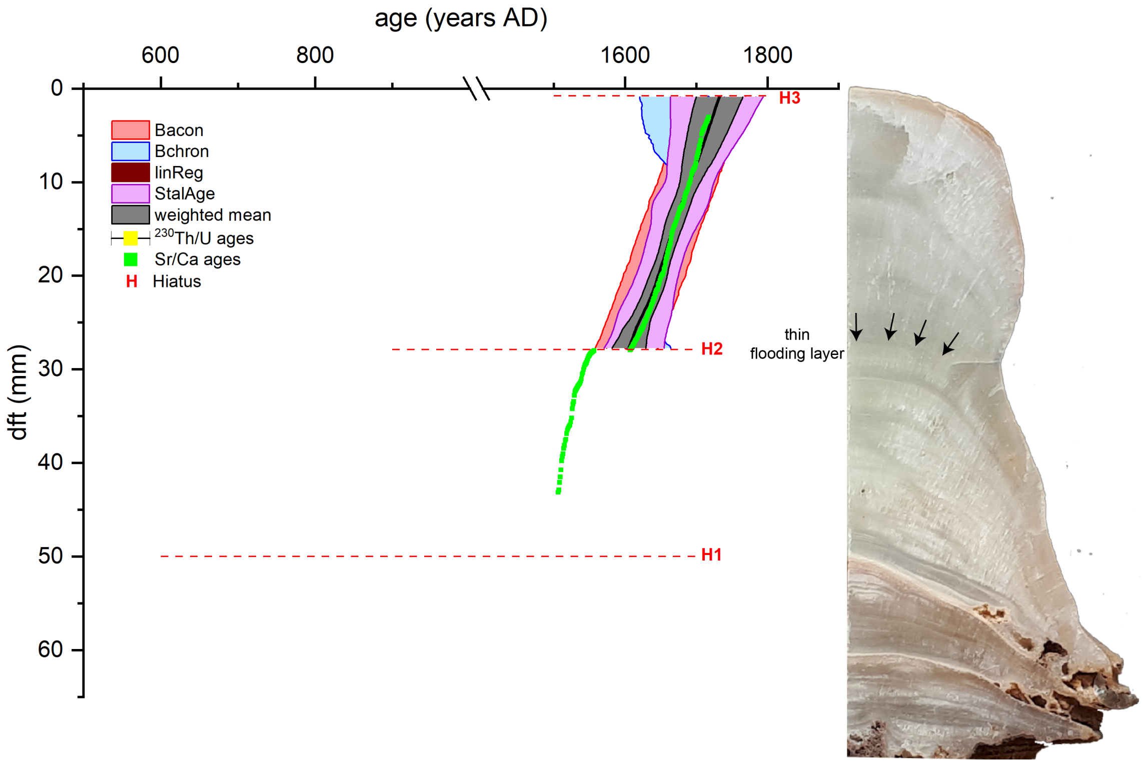

Figure III.7. Age-depth models, including *Bacon*, *Bchron*, *linReg*, and *StalAge*, are presented for the upper part of stalagmite E8. The four ^{230}Th/U ages involved were corrected for detrital Th to match the counted Sr/Ca ages. The counting of seasonal Sr/Ca cycles was anchored to the age at 14.5 mm depth, which is least affected by detrital Th correction. The weighted mean age-depth relationship is shown in black, with its corresponding uncertainty band in grey. For the lower portion of the stalagmite below the second hiatus (H2) at 27.9 mm dft, it was not possible to construct a definitive age-depth model. Note the broken x-axis between 1000 AD and 1400 AD. The thin flooding layer at around 28 mm depth is indicated by black arrows on the scan of the stalagmite due to its poor visibility.

Stalagmite E23-3

A total of eight samples were analyzed for ^{230}Th/U dating from stalagmite E23-3 (Table A7). The uranium content of the stalagmite ranges between 1134 and 1501 ng g^{-1}. All samples exhibit a low ^{232}Th concentration of <0.06 ng g^{-1}, resulting in (^{230}Th/^{232}Th) activity ratios of >200, except for the two topmost samples due to their young age. All uncorrected ages appear in stratigraphic order. As for the E1 and E8 stalagmites, individual growth years were determined based on the seasonal variations in Sr/Ca ratios. From 0 to 84 mm dft, a total of 331±17 layers were counted. Assuming the topmost layer was deposited in 2022, the layer at 84 mm depth corresponds to the year 1691±17 AD. This additional information was used to estimate the contribution of detrital Th to the ^{230}Th/U ages. An (^{230}Th/^{232}Th) activity ratio of 26±7 was selected to align the ^{230}Th/U ages with the layer-counted age model within the uncertainties. For the construction of the final age-depth model, an artificial sample at 0 mm dft with an age corresponding to the year 2022 AD was used. The growth history of stalagmite E23-3 can be divided into two periods, separated by a growth interruption between 188 and 167 mm dft (Fig. III.8). The older part, consisting of two ^{230}Th/U ages, ranges from 1070±7 AD to 1347±9 AD, with an average growth rate of 283 µm yr^{-1}. The upper part of the stalagmite consists of five ^{230}Th/U ages (including one artificial age at the stalagmite top), spanning the period from 1441±5 AD until 2022 AD, assuming that the stalagmite was growing until it was collected. The growth rate in the upper part is quite similar to the older portion, with a mean value of 269 µm yr^{-1}.

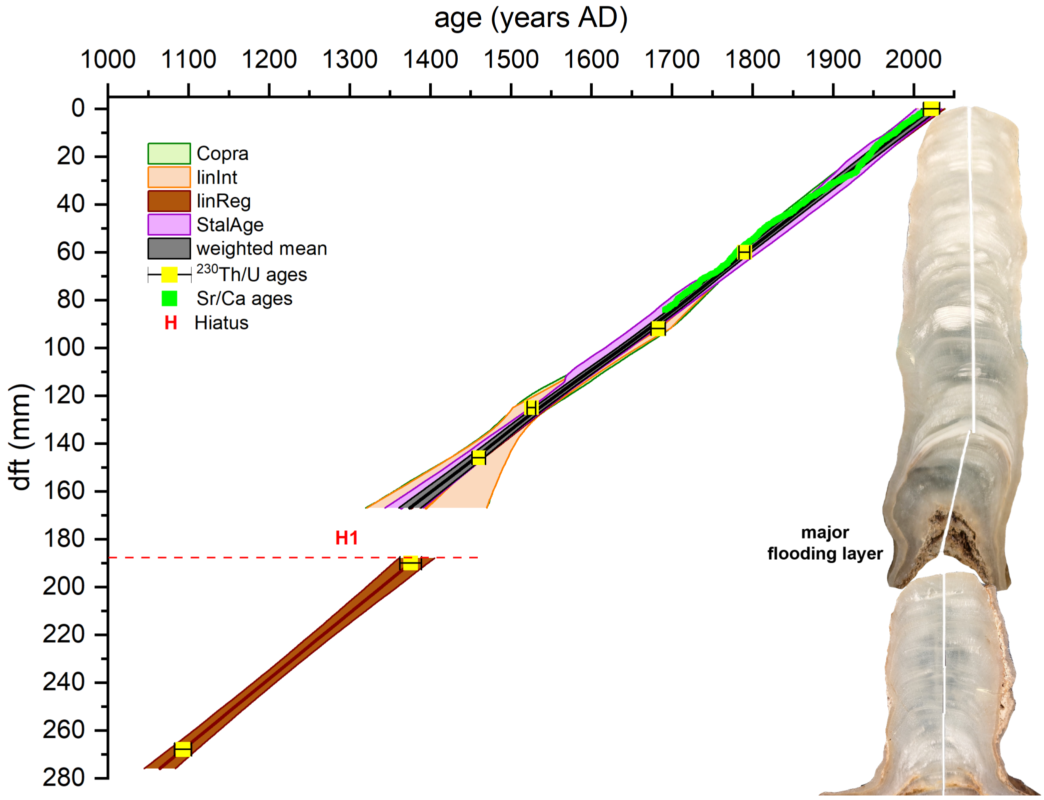

Figure III.8. Various age-depth models, including *Copra*, *linInt*, *linReg* and *StalAge*, are presented for stalagmite E23-3. The ^{230}Th/U age at 60 mm dft was corrected for detrital Th to match the counted Sr/Ca ages, assuming the top of the stalagmite corresponds to the year of extraction (2022 AD). The weighted mean age-depth relationship is shown in black, with the corresponding uncertainty band in grey. The growth hiatus between 188 and 167 mm dft (H1) is indicated, along with the ^{230}Th/U ages used, including an artificial age at the top of the stalagmite, corresponding to 2022 AD. A major flooding layer corresponding to H1 is visible on a scan of the stalagmite.

III.3 Speleothem Age Distribution

The corrected ages span from as old as 353±7 kyr to as young as 0.13±0.015 kyr, with the majority of the samples (84 out of 89) being younger than 3 kyr (Fig. III.9a,b). Nonetheless, the five older samples indicate some speleothem growth during previous glacial/interglacial periods (Fig. III.9b). Since the focus of this thesis is on the last ∼3,000 years, only stalagmites that appear to be of a young age and ideally show active growth have been collected (see Methods II.2.1). Additionally, following initial ^{230}Th/U dating of the tops and bottoms of these stalagmites, further ^{230}Th/U dating was performed only on those stalagmites that span the period of interest, which explains the sampling bias towards younger ages.

Although most of the analyzed stalagmites exhibit decade-long growth interruptions, their age models show overlapping growth during the last approximately 2.7 kyr (Fig. III.10). The absence of samples with ages close to the present (<130 years) can be attributed to the rejection of samples with a low (^{230}Th/^{232}Th) activity ratio <200 (Fig. III.2). This ratio is typically low for carbonate samples that have recently formed due to the combined effects of 'detrital' Th contamination and the limited accumulation of ^{230}Th through radioactive decay since formation. However, the seasonal variations in Sr/Ca ratios, observable in some of the analyzed stalagmites, suggest that carbonate deposition in Áaktun Kóopo Cave has occurred within the last 130 years, extending up to the present (see Chapter III.2). Furthermore, radiocarbon (^{14}C) measurements from the tops of stalagmites E0-C, E1, and E8 also indicate modern speleothem growth (post-1950 AD) (see Appendix VII).

The uranium content of the analyzed speleothems ranges from 106 to 2237 ng g^{-1}. Focusing on samples from the last 2.7 kyr reveals a distinct shift in uranium concentration around 1.1 kyr. Between 2.7 and 1.1 kyr, uranium concentrations are relatively low and less variable (mean = 532 ng g^{-1}, σ = 127 ng g^{-1}), despite one outlier around 2 kyr ago, compared to the period from 1.1 kyr to the present (mean = 1250 ng g^{-1}, σ = 319 ng g^{-1}) (Fig. III.9c). This bimodal distribution is further illustrated by Kernel Density Estimates (KDEs) for the two individual time periods and for both combined (Fig. III.9d). The possible causes and significance of the shift in speleothem uranium concentration will be discussed in detail later in Chapter V.

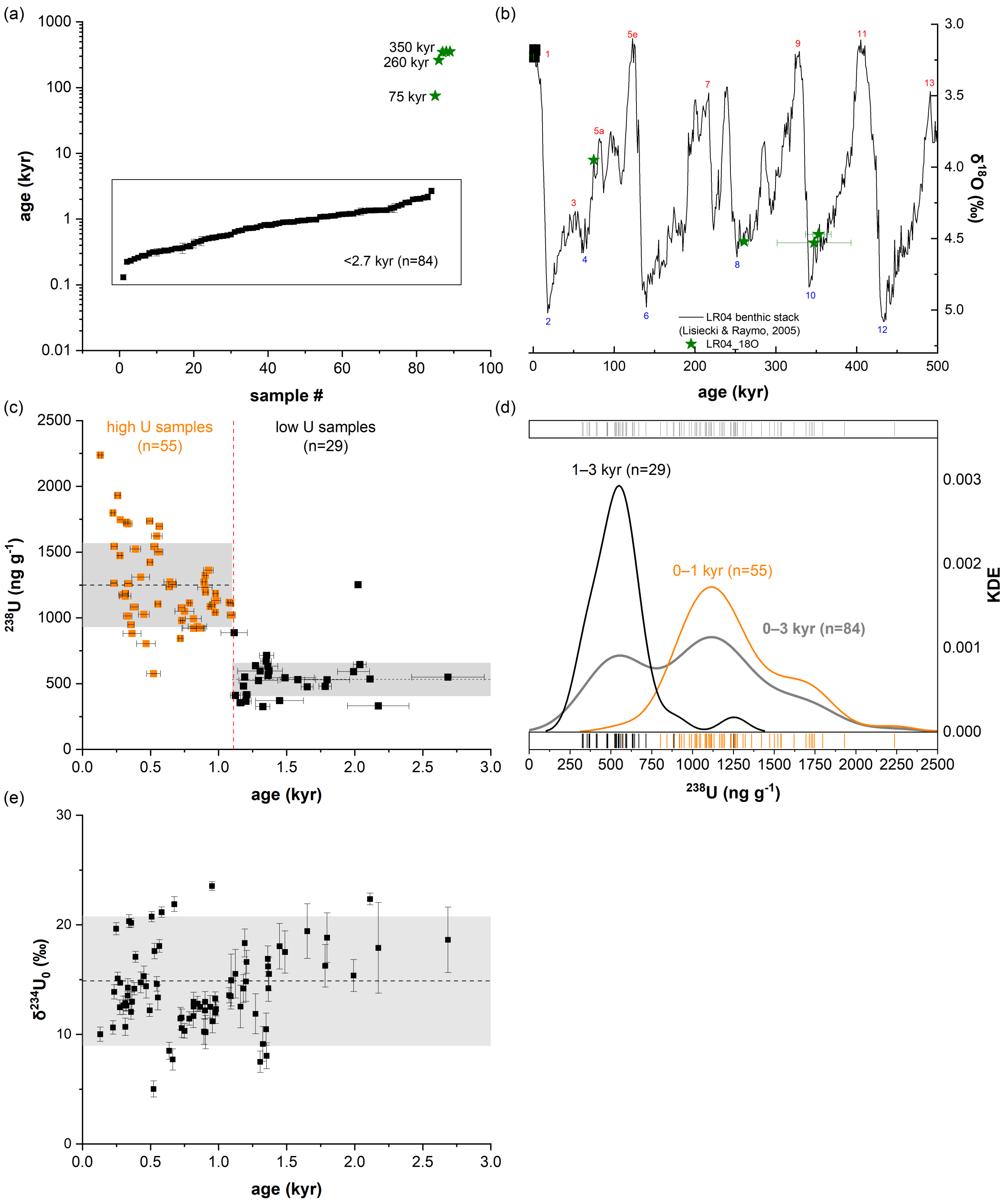

Figure III.9. **(a)** Distribution of speleothem samples according to their corrected ages, shown on a logarithmic scale. Most samples are younger than 2.7 kyr, while a few show carbonate deposition at approximately 75 kyr, 260 kyr, and 350 kyr. **(b)** ^{230}Th/U ages of speleothems plotted against the LR04 benthic δ^{18}O stack from Lisiecki and Raymo (2005), highlighting deposition during earlier glacial and interglacial periods as shown in (a), with marine isotope stages indicated by blue and red numbers. **(c)** Speleothem uranium concentrations display a significant shift around 1.1 kyr. Between 2.7 and 1.1 kyr, the uranium concentrations are relatively low and less variable, with one notable outlier around 2 kyr. In contrast, from 1.1 kyr to the present, uranium concentrations are higher and more variable. **(d)** Kernel Density Estimates (KDEs) illustrate the bimodal distribution of uranium concentrations for the two distinct time periods (pre- and post−1.1 kyr) and the combined dataset. **(e)** Initial uranium isotopic composition ($\delta^{234}U_0$) plotted against sample age. Over the last 2.7 kyr, $\delta^{234}U_0$ values are near equilibrium (mean = 15‰, σ = 6‰).

$\delta^{234}U_0$ values of the speleothem samples reflect the ($^{234}U/^{238}U$) activity ratios of the local ground and drip water from which they were precipitated. Over the last 2.7 kyr, $\delta^{234}U_0$ values are close to equilibrium (mean = 15‰) and exhibit only minor changes over time (σ = 6‰). The few older samples, dating between 75 kyr and 350 kyr, show slightly different values ranging from 4‰ to 45‰. Such variations over long timescales are expected and may result from the interplay of several mechanisms, such as the alpha-recoil process, host rock dissolution, and the redox behavior of uranium (Bonotto and Andrews, 1993; Paces et al., 2002; Maher et al., 2014; Priestley et al., 2018).

The growth rates of the analyzed stalagmites are quite high and similar, with mean values of around 200 to 300 µm a^{-1}, except for stalagmite E4 and the top section of E0-C, which exhibit mean growth rates of only 53 and 94 µm a^{-1}, respectively. Based on the $^{230}Th/U$ ages of stalagmite E0-C, there may be an additional hiatus between 23.5 and 20 mm dft (Fig. III.4). This hiatus was not considered in the construction of the age-depth model but could explain the lower observed mean growth rate for this section of the stalagmite.

For stalagmite E4, there are several potential explanations for the overall lower growth rate. First, while stalagmites E0-B, E0-C, E1, E8, and E23-3 were all located in the same chamber of the cave, stalagmite E4 grew in a different part of the cave, closer to the entrance (Fig. A5), where conditions for carbonate deposition may have been slightly different. Secondly, the age-depth model of E4 consists of only four $^{230}Th/U$ ages, two from the bottom and two from the top of the stalagmite, increasing the likelihood of missing hiatuses in between (Fig. III.6). The stalagmite also exhibits fine lamination with alternating layers of carbonate and mud/clay (Fig. III.6), which explains the high contamination with detrital Th in nearly all of the analyzed samples. These recurrent flooding events, which cover the top of the stalagmite with thin layers of clay, lead to frequent interruptions in growth (micro hiatuses). Although it is difficult to estimate the exact number and duration of these growth interruptions, they suggest that the ”actual” growth rate of carbonate deposition was likely higher.

Based on these observations, the growth rates of the different analyzed stalagmites appear to be similarly high, around 200–300 µm a^{-1}, over the last approximately 2.7 kyr. This finding highlights that the conditions of carbonate growth driven by the saturation state of drip water, cave CO_2, drip rates, etc., remained in narrow ranges, except for the contribution of U from the soil and host rock solution, which shows a systematic change as indicated above.

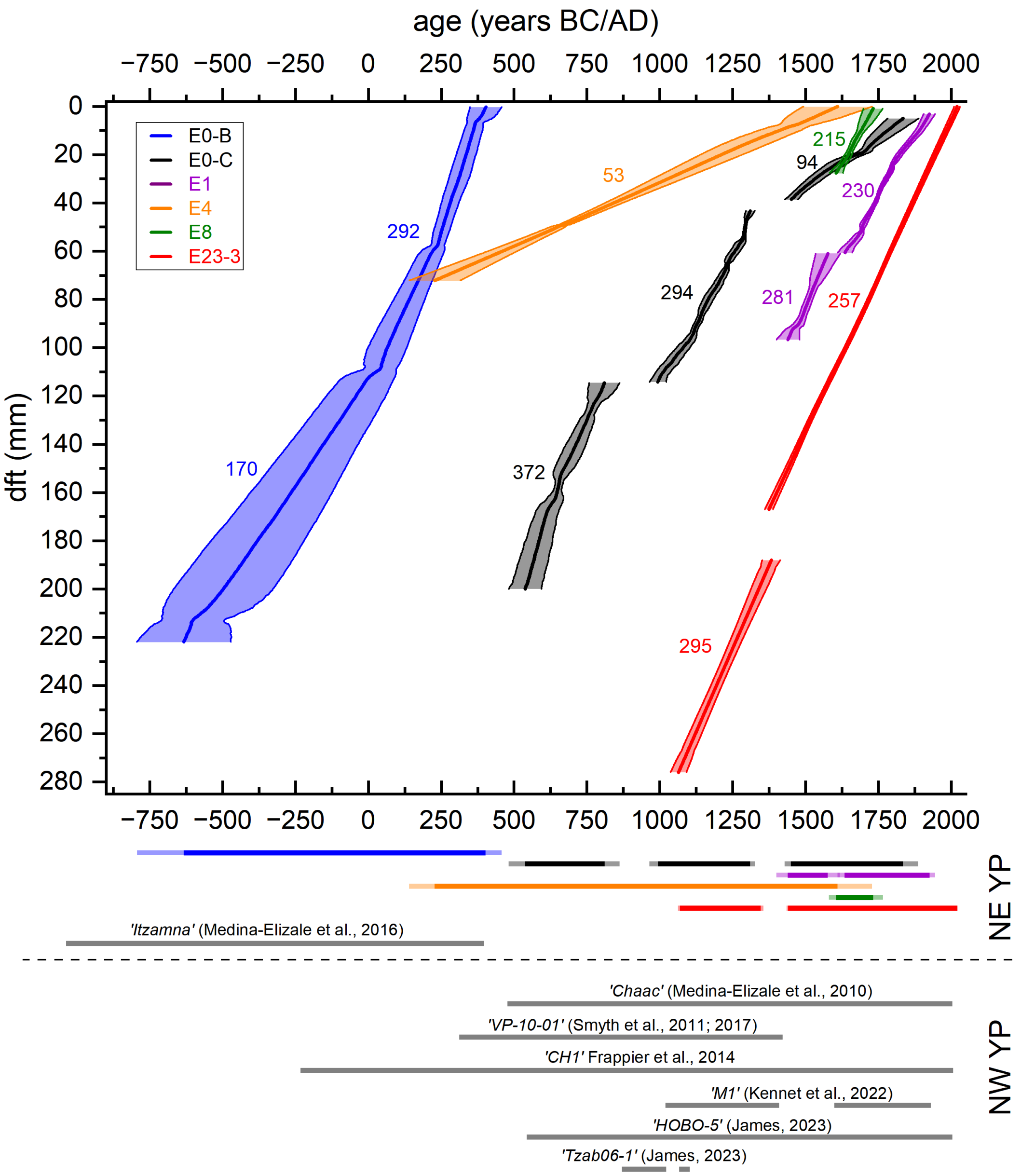

Figure III.10. Mean age-depth models for stalagmites E0-B, E0-C, E1, E4, E8, and E23-3 from Áaktun Kóopo Cave. Numbers indicate the average growth rates (in µm a^{-1}) during different growth periods. The colored horizontal bars at the bottom illustrate the overlapping growth periods of the stalagmites over the last ~2.7 kyr, highlighting intervals of simultaneous growth across multiple stalagmites. Lighter shades within the bars reflect the associated age uncertainties. Grey bars indicate periods covered by other published stalagmite records from the northern Yucatán Peninsula. Notably, while most records are from the northwestern Yucatán Peninsula (NW YP) (Medina-Elizalde et al., 2010; James, 2023; Kennett et al., 2022; Smyth et al., 2011, 2017a; Frappier et al., 2014), there is a marked absence of stalagmite proxy records from the northeastern Yucatán Peninsula (NE YP) for the last 1600 years, with only one record covering an earlier period between 1037 BC and 397 AD (Medina-Elizalde et al., 2016a).

Compared to the few existing stalagmite studies from the northern YP that focus on the last approximately 3,000 years—a period encompassing the entire era of the Maya civilization—(Medina-Elizalde et al., 2010, 2016a; Kennett et al., 2022; Smyth et al., 2011, 2017a; Frappier et al., 2014; Intveld et al.)—the growth rates of around 200–300 µm a^{-1} observed in stalagmites from Áaktun Kóopo Cave are among the highest reported. Notably, only one of these studies is from the northeastern part of the YP and covers only the period between 1037 BCE and 397 AD, corresponding to the Preclassic and early Classic periods of Maya history (Medina-Elizalde et al., 2016a).

While some of the growth interruptions in the stalagmites from Áaktun Kóopo Cave, as suggested by the distribution of ^{230}Th/U ages, are only detectable through thin section analysis or by large and abrupt changes in certain trace elements (e.g., Mg/Ca or U/Ca) identified using LA-ICP-MS, other hiatuses are clearly visible to the naked eye as millimeter- to centimeter-thick layers of mud encrusted in carbonate. These layers suggest a flooding event in the cave that covered the stalagmites with mud/clay.

There are at least nine water bodies inside the cave, each with different dimensions, and with water level fluctuations depending on the season (Fig. II.1) (Tec, 2021). It is known that the rainy season causes a substantial increase in water depth, submerging some areas and making them more difficult to access (Tec, 2021). Therefore, it is plausible that during an intense rainy season or an extraordinary heavy precipitation event (e.g., a major hurricane), which may occur only once every hundred to a few hundred years, the water level of the cave pools rose to a point where the section of the cave containing stalagmites E0-C, E1, and E8 became flooded. Alternatively, a water-mud mixture may have entered the cave through fissures, cracks, or other natural openings.

The most obvious feature of this event is the centimeter-thick layer of carbonate-encrusted mud, which appears in stalagmites E0-C, E1, and E23-3 (Figs. III.4,III.5,III.8). For stalagmite E0-C, this flooding layer separates growth phase 2 (994 ± 29 AD to 1311 ± 15 AD) from growth phase 3 (1451 ± 22 AD to 1835 ± 53 AD) (Fig. III.4). In stalagmite E23-3, the layer separates the lower part (1070 ± 7 to 1347 ± 9 AD) from the upper part (1441 ± 5 AD to 2022 AD) (Fig. III.8), while in stalagmite E1, this layer appears just below the lowermost part of the analyzed section (<1440 ± 39 AD) (Fig. III.5).

Considering the individual uncertainties in timing, it is likely that this growth interruption in the three stalagmites was caused by a single major flooding event around 1400 AD. During this event, at least the part of the cave where these stalagmites are located was flooded with water and mud, leaving the stalagmites covered by a few centimeters of mud once the water had receded. With continued dripping from the drip sites that fed these stalagmites, the covering mud was progressively washed away, soaked, or calcified, leaving behind a spongy calcareous section with only traces of the former mud. It likely took several years to decades for the stalagmite surface to become flat and stable enough to resume conventional growth layer by layer.

Another layer of mud, though substantially smaller in scale (0.5–1 mm thick), is recognized in stalagmites E1 and E8. In stalagmite E1, this layer appears at approximately 61 mm depth, separating the lower (1440±39 AD to 1577±42 AD) from the upper (1635±24 AD to 1926±20 AD) part. In stalagmite E8, this layer appears at about 27.9 mm depth, corresponding to the year 1605±24 AD. Considering the age models of both stalagmites, it is highly likely that this thin flooding layer in both stalagmites originated from the same event. Unlike the centimeter-thick flooding layer, the growth interruption caused by this thin layer probably lasted only a few months to a few years. If this is the case, then this thin flooding layer could serve as a time marker, much like ash layers in marine sediments or ice deposits. This would provide a valuable opportunity to anchor individual proxy records and improve overall chronologies.

Additionally, speleothems located closer in elevation to the cave pools would likely be more prone to flooding events. Understanding these flood layers over time and depth below the surface could provide valuable insights into the paleo groundwater table of the cave.

III.4 Conclusions

The ^{230}Th/U dating of speleothems from Áaktun Kóopo Cave, Yucatán, Mexico, indicates continuous carbonate deposition over the past 2.7 kyr, encompassing the entire era of Maya civilization. Additionally, a few ^{230}Th/U ages suggest some speleothem growth during earlier glacial and interglacial periods. The high growth rates of these stalagmites, averaging 200–300 µm a^{-1}, allow for the development of high-resolution (sub)annual multi-proxy records of past hydroclimate and vegetation changes.

The uranium concentrations in the speleothems are notably high, averaging 1 ppm, which aids in precise ^{230}Th/U dating. However, elevated ^{232}Th concentrations result in (^{230}Th/^{232}Th) activity ratios below 300, reflecting significant initial detrital, colloidal, or dissolved thorium. This complication is common in the dating of stalagmites from the Yucatán Peninsula. To address this, high and variable (^{230}Th/^{232}Th) ratios ranging between 3 and 68 were used for corrections, and samples with ratios below 200 were excluded to ensure stratigraphic consistency.

Clear seasonal cycles in Sr/Ca ratios were observed in some of the analyzed stalagmites, which can be counted and compared to the ^{230}Th/U-based chronology. Although the high uncertainty in detrital correction and frequent growth interruptions complicate the correlation of Sr/Ca cycles with ^{230}Th/U ages, these cycles nonetheless help to refine the chronology and facilitate the study of individual events, such as droughts or hurricanes, on a sub-seasonal scale.

Overall, despite the challenges posed by high and variable ^{230}Th contamination, the speleothems from Áaktun Kóopo Cave have the potential to provide valuable records of local hydroclimate and vegetation changes over the past 2.7 kyr. These records can offer insights into the environmental conditions that may have influenced Maya cultural evolution during key periods, such as the Terminal Classic Period (TCP), and provide a basis for future research into historical natural disasters, such as droughts or hurricanes.

IV Stalagmite Proxies – Results and Interpretation

Seasonal variations in the trace element composition of stalagmites provide valuable insights into past environmental and climatic conditions at high temporal resolution. Stalagmites from karst systems, such as those found in Áaktun Kóopo Cave, record changes in cave drip water chemistry, which are influenced by external climate drivers such as precipitation and temperature, as well as internal cave processes like cave ventilation dynamics and prior calcite precipitation (PCP). In stalagmites from Áaktun Kóopo Cave, these seasonal patterns are particularly well-preserved in trace element ratios such as Sr/Ca, Na/Ca, U/Ca, and P/Ca, each responding differently to changes in cave hydrology and growth rate.

This chapter focuses on the seasonal cyclic variations observed in the trace element ratios of multiple stalagmites from Áaktun Kóopo Cave, with particular emphasis on stalagmite E23-3. By analyzing the synchronicity of these variations across different elements, this study aims to identify the processes driving these geochemical signatures and their relationship to both seasonal climate variability and in-cave dynamics.

Moreover, the relationship between different trace elements on longer timescales, beyond seasonal variations, will be evaluated alongside patterns in stable carbon (δ^{13}C) and stable oxygen isotopes (δ^{18}O), providing further insights into how climatic and environmental processes are recorded in the stalagmites from Áaktun Kóopo Cave.

The knowledge gained from this evaluation provides valuable details on how to interpret the various stalagmite proxies applied for reconstructing changes in the local hydroclimate and paleoenvironment, which will be the focus of the final two chapters of this thesis (Chapter V and Chapter VI).

IV.1 Stalagmite Trace Elements

IV.1.1 Limit of Detection and Range of Trace Elements

Following the outlier correction, in which a floating 1.5 interquartile range (IQR) was applied, the limit of detection (LOD), defined as the signal-to-noise ratio where $SNR \leq 3$, was calculated for each measured element in the analyzed stalagmites to ensure data reliability (see Methods II.3.3). For each element, the LOD was determined from individual measurement tracks—typically three to five tracks per stalagmite—and an average value was calculated to represent the mean LOD for each element in each stalagmite.

The percentage of data above the LOD varied across the different trace elements and stalagmites (Fig. A8). Elements such as Na, Mg, Ca, Co, Ni, Cu, Sr, Ba, and U consistently showed high detection rates, with 95–100% of the data exceeding the LOD across all stalagmites. In contrast, elements like Al and Zn exhibited significantly lower detection rates, ranging from 27% to 97% for Al and from 14% to 69% for Zn. For P, only 53% of the measured data exceeded the LOD in stalagmite E0-C, while for the other analyzed stalagmites (E1, E4, E8, and E23-3), less than 5% of the data were above the LOD. Although P and Al exhibit significantly lower detection rates in comparison to other elements, they are included in the later discussion on the observed seasonal variations of trace elements in the stalagmites from Áaktun Kóopo Cave, as they may still provide valuable insights into geochemical processes despite their lower detectability.

LA-ICP-MS analysis of the studied stalagmites (E0-C, E1, E4, E8, and E23-3) revealed element concentrations that are generally of the same order of magnitude (Fig. IV.1), which suggests a consistent geochemical environment.

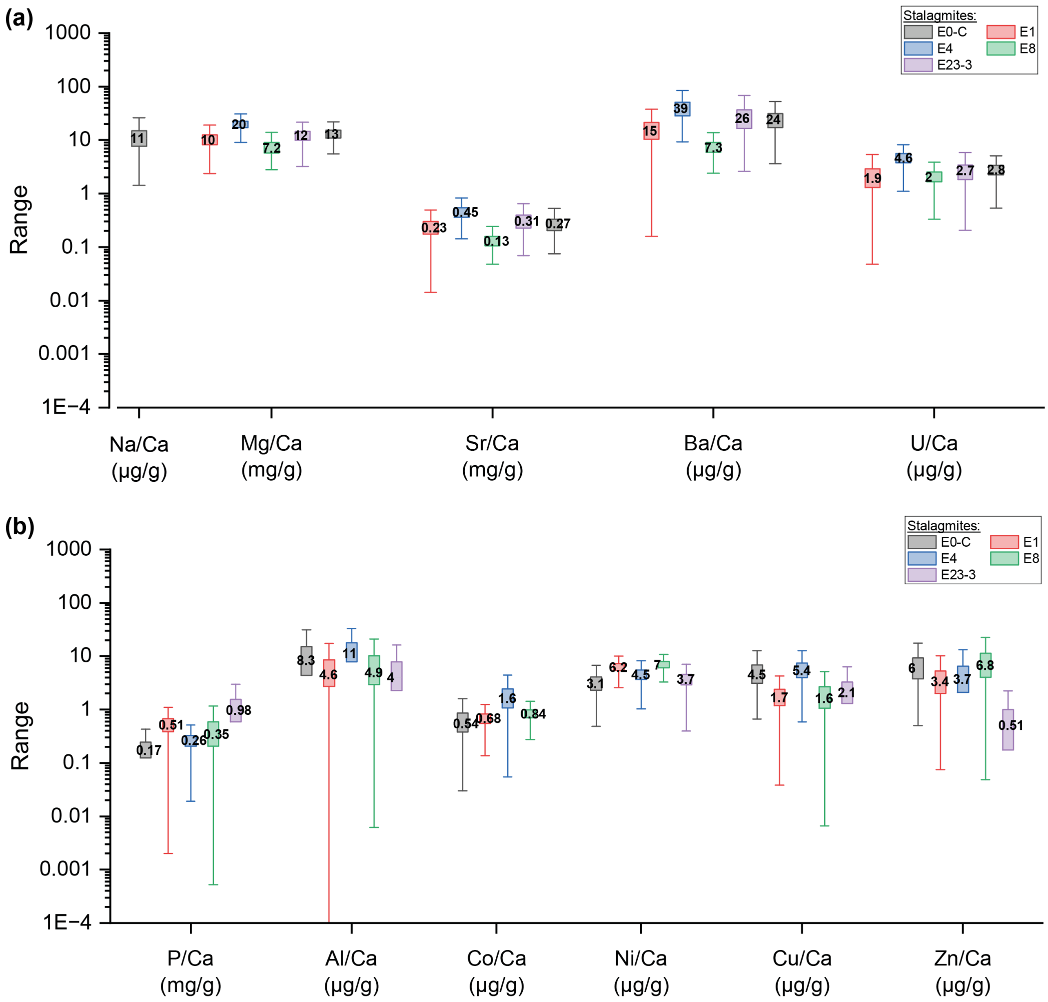

Figure IV.1. Boxplot representation showing the range of elemental ratios in the studied stalagmites E0-C, E1, E4, E8, and E23-3 from Áaktun Kóopo Cave. **(a)** Boxplot depicting the variability of elemental ratios (Na/Ca, Mg/Ca, Sr/Ca, Ba/Ca, U/Ca) within and between the different stalagmites. **(b)** Boxplot showing the variability of additional elemental ratios (P/Ca, Al/Ca, Co/Ca, Ni/Ca, Cu/Ca, Zn/Ca) across the stalagmites. The boxes, with colors indicating the different stalagmites, represent the interquartile range (25%–75%), while the whiskers extend to 1.5 times the interquartile range (IQR). Numbers on the boxes indicate the median values for each element ratio. Note the logarithmic scale of the y-axis.

IV.1.2 Seasonal Variation of Stalagmite Trace Elements

The observed seasonal variations in Sr/Ca ratios, which were used for constructing the age-depth model of stalagmite E23-3 (see Chapter III.2), are also evident in other trace elements, including Mg/Ca, Ba/Ca, Na/Ca, U/Ca, P/Ca, Al/Ca, and Cu/Ca, although not always as distinctly as in the case of Sr/Ca (Fig. IV.2). These elements exhibit synchronized cyclic variations, with minima in Sr/Ca, Ba/Ca, Na/Ca, U/Ca, and to some extent Mg/Ca coinciding with maxima in P/Ca, Al/Ca and Cu/Ca (Fig. IV.2).

These seasonal patterns are not unique to stalagmite E23-3 but are also present throughout stalagmite E1 and much of E8 (Figs. A9 and A10). However, they are only observed in certain sections of stalagmite E0-C and are largely absent in stalagmite E4 (Fig. A10). The absence of these patterns in stalagmite E4 may be due to its location in a distinct part of the cave, closer to the entrance, where the cave's climate and speleothem growth conditions may have been different. In the case of stalagmite E0-C, slight differences in measurement settings (e.g., scan speed, spot size) during LA-ICP-MS analysis may explain why these seasonal patterns are absent throughout most of the stalagmite. These patterns are only visible in the top section (0–40 mm dft), which was remeasured using settings similar to those used for the other analyzed stalagmites (see Tab. A6). Another possible explanation for the absence of pronounced seasonal variations in the trace element ratios of E0-C is its age. The majority of stalagmite E0-C, specifically the section between 42 and 170 mm dft, corresponds to older growth phases between approximately 800 and 1300 AD, which are not covered by any of the other analyzed stalagmites (E1, E8, E23-3) (see Fig. III.10). Therefore, it is possible that during these older growth phases, the environmental conditions differed in a way that did not lead to pronounced seasonal variations in the trace element concentrations of E0-C.

Nonetheless, the observed seasonal patterns of trace element concentrations are consistent for multiple stalagmites from Áaktun Kóopo Cave and represent a persistent feature over at least the past 600 years. The following section explores potential explanations for these observed variations.

IV.1.3 PCP and Growth Rate Effects on Stalagmite Geochemistry

The observed synchronized variations in Sr/Ca, Ba/Ca, Na/Ca, U/Ca, and, to a lesser extent, Mg/Ca ratios in multiple stalagmites from Áaktun Kóopo Cave suggest that changes in the extent of prior calcite precipitation (PCP)—that is, carbonate precipitation occurring before the drip reaches the stalagmite surface—may play a significant role in controlling these element ratios. This is because the partition coefficient for these elements is much less than one (e.g., Fairchild and Treble, 2009; Day and Henderson, 2013; Tremaine and Froelich, 2013; Borsato et al., 2015; Drysdale et al., 2019; Kost et al., 2023), meaning that these elements preferentially remain in solution during calcite precipitation, while calcium is readily incorporated into the solid phase. Consequently, element ratios such as Mg/Ca, Sr/Ca, Ba/Ca, Na/Ca, and U/Ca in drip water, and thus in the stalagmite, increase as the extent of PCP increases, and vice versa.

One approach to assess whether PCP significantly influences Mg and Sr concentrations in stalagmites is to calculate the regression between ln(Mg/Ca) and ln(Sr/Ca) (Sinclair et al., 2012). If the resulting slope falls between 0.71 and 1.45, it indicates that PCP likely exerts a substantial influence on both Sr and Mg (Sinclair et al., 2012; Wassenburg et al., 2020). For the upper sections of stalagmites E1, E8, and E23-3, the calculated slopes are 0.86, 0.91, and 0.88, respectively (Fig. A11b,d,e), which places them near the lower end of the predicted range for PCP slopes. As these stalagmite sections are of similar age, spanning the last 400 years (see Chapter III.1), this suggests that PCP likely had a significant impact on the incorporation of Sr and Mg into these stalagmites during this period (Fig. A11f). For stalagmites E0-C, E4 and the lower sections of stalagmites E1 and E8, the calculated slopes fall below the predicted range (Fig. A11a–d). Although these data fall outside the assumed range of slopes, this does not necessarily imply the absence of PCP influence, as growth rate effects on the distribution coefficients of Sr and Ba (Borsato et al., 2007; Huang and Fairchild, 2001) may also play a role.

PCP is suggested to be enhanced during drier climate conditions (associated with lower drip intervals) or under lower cave air CO_2 concentrations (Fairchild et al., 2006; Sherwin and Baldini, 2011; Wong et al., 2011). On the northern YP, the dry season generally lasts from November to May (De la Barreda et al., 2020) (Fig. I.1c). From November to March, external temperatures generally drop below the cave's internal temperature (Fig. I.1c), which reflect the annual mean surface temperature (see Appendix VII), resulting in seasonally varying temperature contrasts between surface- and cave-air. This contrast drives buoyancy-driven cave-air CO_2 exchange with surface-air CO_2, leading to increased ventilation, reduced cave pCO_2, enhanced PCP and subsequent increases in Sr/Ca, Ba/Ca, Na/Ca, and U/Ca ratios.

CO_2 concentrations measured inside Áaktun Kóopo Cave during the field trips in March 2022 and April 2023 exceeded 5000 ppm in the chamber where stalagmites E0-C, E1, E8, and E23-3 were located (Tab. A1). Although no data are available on potential seasonal variations in cave pCO_2, it is plausible that buoyancy-driven ventilation occurs seasonally in response to external temperature fluctuations, as has been observed in the well-monitored Rio Secreto Cave System, located approximately 68 km east of Áaktun Kóopo Cave (Lases-Hernandez et al., 2019; Lases-Hernández et al., 2020) and in other tropical caves (e.g., Vieten et al., 2016; Sekhon et al., 2021). Seasonal water level fluctuations of the cave's water bodies may also influence ventilation dynamics, particularly the water body connecting the more ventilated entrance section to the deeper parts of the cave (Fig. II.1a). Depending on the water level, the passage allowing air exchange with the deeper sections (the space between the water surface and cave ceiling) may vary in size, becoming larger, smaller, or even completely blocked, thereby significantly impacting cave ventilation (Gabrovšek, 2023). However, at present, the occurrence of seasonal cave ventilation in Áaktun Kóopo Cave is only speculative, and proving and fully understanding the airflow patterns would require a multi-year monitoring effort.

As the cave's pCO_2 is expected to decrease during colder months due to increased ventilation, not only is PCP expected to increase, but stalagmite growth as well. This may explain the broader maxima in Sr/Ca, Ba/Ca, Na/Ca, and U/Ca, compared to the sharper minima (Fig. IV.2). Moreover, Sr/Ca, Ba/Ca, Na/Ca, and U/Ca ratios show a clear connection to growth rate (Fig. IV.3). Although Mg/Ca ratios show a similar long-term trend to Sr/Ca and Ba/Ca, they behave inversely with growth rate. For Sr/Ca, Ba/Ca, Na/Ca, and U/Ca ratios, seasonal variations appear to be of the same magnitude as long-term variations (Fig. IV.2). In contrast, seasonal variations in Mg/Ca ratios are less pronounced compared to long-term changes. Furthermore, Sr/Mg ratios show a stronger alignment with growth rate compared to Sr/Ca ratios and growth rate. This can be explained by the findings of Sliwinski et al. (2023), who showed that the Sr/Mg ratio of speleothem calcite is directly proportional to D_{Sr}, as this ratio accounts for the effects of PCP on D_{Sr}, leaving solely growth rate as the dominant factor influencing Sr/Ca ratios.

During the rainy season, corresponding to the warmer months from May to September on the YP (Fig. I.1c), elevated cave air CO_2 concentrations may reduce stalagmite growth to a minimum. This reduction in growth likely results in lower Sr/Ca, Ba/Ca, Na/Ca, and U/Ca ratios within the stalagmite. The contrasting patterns of P/Ca, Cu/Ca, and Al/Ca ratios, characterized by sharp maxima coinciding with minima in Sr/Ca, Ba/Ca, Na/Ca, and U/Ca (Fig. IV.2), further support the hypothesis of strongly reduced stalagmite growth during the rainy season. During this period, P, Cu, Al, and other soil-derived elements are likely transported through the karst system as organic or inorganic particulates (Borsato et al., 2007; Hartland et al., 2012).

A study conducted on the Southern Cook Islands in the Pacific observed a similar relationship between these elements on a seasonal scale, with maximum values for Mg, Sr, Ba, Na, and U corresponding to minima for P and Y (Faraji et al., 2021). These authors suggest that the negative correlation of Mg, Sr, Ba, Na, and U with infiltration likely reflects increased PCP and rock-water interaction during drier periods, while they attribute the positive correlation of P and Y to enhanced transport of soil-derived elements during wet periods, likely due to increased drip rates or organic complexation (Faraji et al., 2023, 2021).

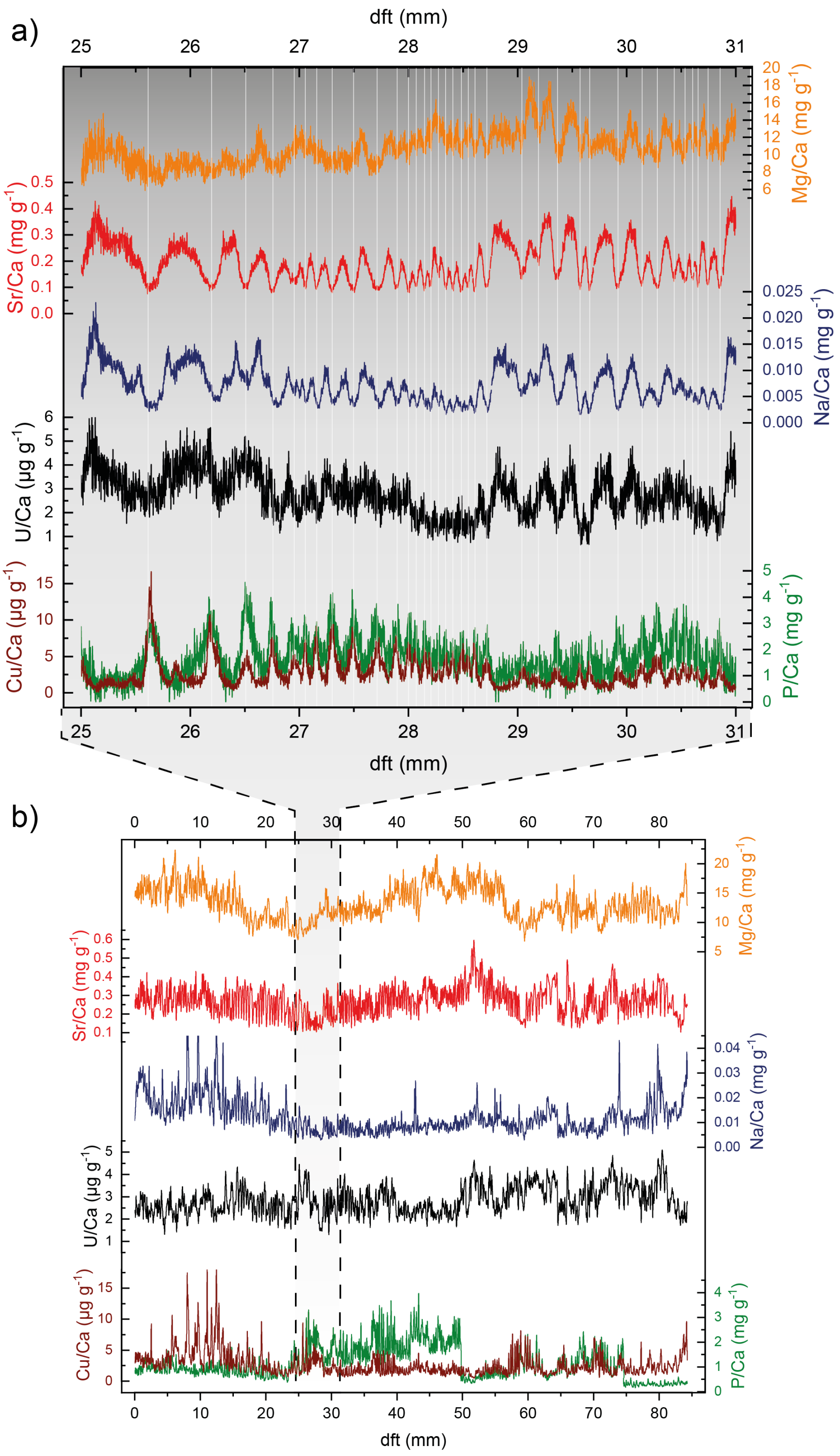

Figure IV.2. **(a)** Seasonal variations in trace elements for the section between 25 and 31 mm distance from the top (dft) of stalagmite E23-3. Minima in Mg/Ca, Sr/Ca, Ba/Ca, Na/Ca, and U/Ca coincide with maxima in P/Ca and Cu/Ca. The section between two vertical lines, which represent Sr/Ca minima, corresponds to one year of stalagmite growth, totaling 37 years for the section from 25 to 31 mm dft. Based on the spacing between the vertical lines, a clear relationship between the magnitude of certain elemental ratios and stalagmite growth rates is observed. **(b)** Seasonal variations in trace elements for the section between 0 and 84 mm dft of stalagmite E23-3.

Taken together, the observations indicate that seasonal variations in trace element ratios in the stalagmites from Áaktun Kóopo Cave are likely driven by a combination of growth rate, PCP, and trasnport processes. Sr/Ca, Ba/Ca, Na/Ca, and U/Ca ratios appear to be primarily controlled by changes in growth rate on both seasonal and longer-term scales, with only minor influence from PCP. In contrast, Mg/Ca ratios seem to be predominantly influenced by varying degrees of PCP, particularly on interannual timescales. Furthermore, the inverse long-term trend of Mg/Ca with growth rate suggests that periods of enhanced speleothem growth, beyond seasonal variations, occur during overall wetter climatic conditions, during which PCP is expected to be reduced.

To further support these interpretations, stable isotopes (δ^{13}C, δ^{18}O) of stalagmites E0-C, E1, E8, and E23-3 were analyzed from samples taken directly adjacent to or on top of the LA-ICP-MS tracks (see Methods II.3.4). Although (sub)seasonal resolution was not achieved for the stable isotope data, they provide valuable context for interpreting trends in trace element ratios, such as Mg/Ca. Conversely, the trace element data offer crucial insights into the processes influencing stable isotope variations, making these data sets complementary.

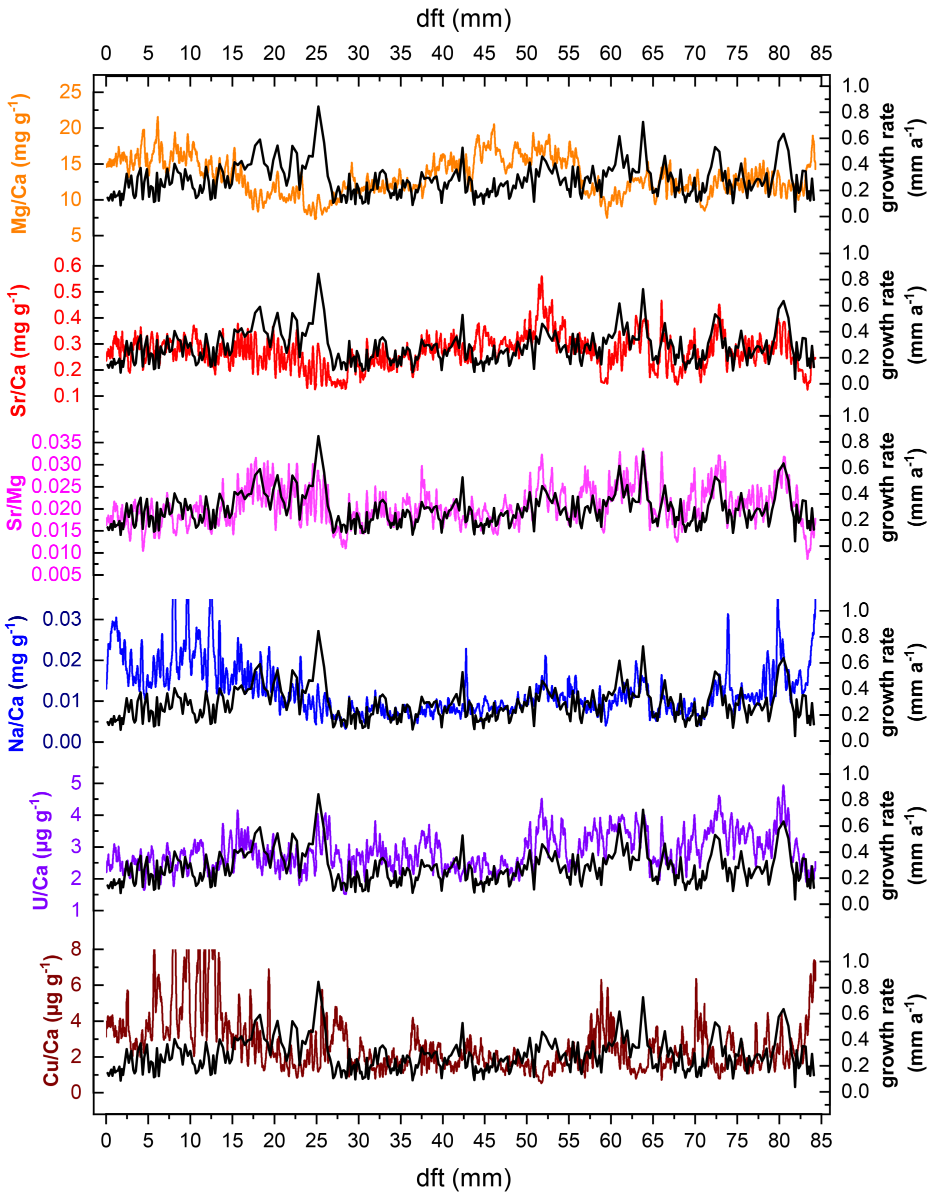

Figure IV.3. Trace elements vs. growth rates of stalagmite E23-3. Variability in Sr/Ca, U/Ca, Na/Ca, and Sr/Mg ratios is closely coupled with the stalagmite's growth rate. As Ba/Ca ratios exhibit an almost identical pattern to Sr/Ca ratios, they are not shown here. However, for Na/Ca, this connection diminishes within the topmost 25 mm, where Na/Ca ratios show a significant increase while the growth rate remains low and even slightly decreases. Similarly, Cu/Ca ratios increase towards the top of the stalagmite, but a clear connection to growth rate is absent. Mg/Ca ratios do not display as clear a pattern as the other element ratios and tend to behave inversely to growth rates over the long term. This inverse relationship between Mg/Ca ratios and growth rate can also be inferred from the close-up view in Figure IV.2a.

IV.2 Stalagmite Stable Isotopes

The stable isotopes of oxygen and carbon analyzed in stalagmites E0-C, E1, E8, and E23-3 from Áaktun Kóopo Cave yielded δ^{13}C values ranging from −5.72‰ to −12.2‰ in E0-C, while they vary between −8.22‰ and −12.4‰ in E1, E8, and E23-3 (IV.4). Notably, the lowest δ^{13}C values in all four stalagmites are quite similar, ranging from −12.1‰ to −12.4‰.

In comparison to δ^{13}C values, the range of δ^{18}O values is smaller, with the largest range again observed in stalagmite E0-C (−3.39‰ to −7.22‰). Stalagmite E1 also shows a relatively large range, from −3.87‰ to −7.14‰, whereas the ranges in E8 and E23-3 are more constrained.

The wider spread of δ^{13}C values in E0-C is largely attributed to its longer growth history (see III.2), and further details on this are discussed in Chapter V.

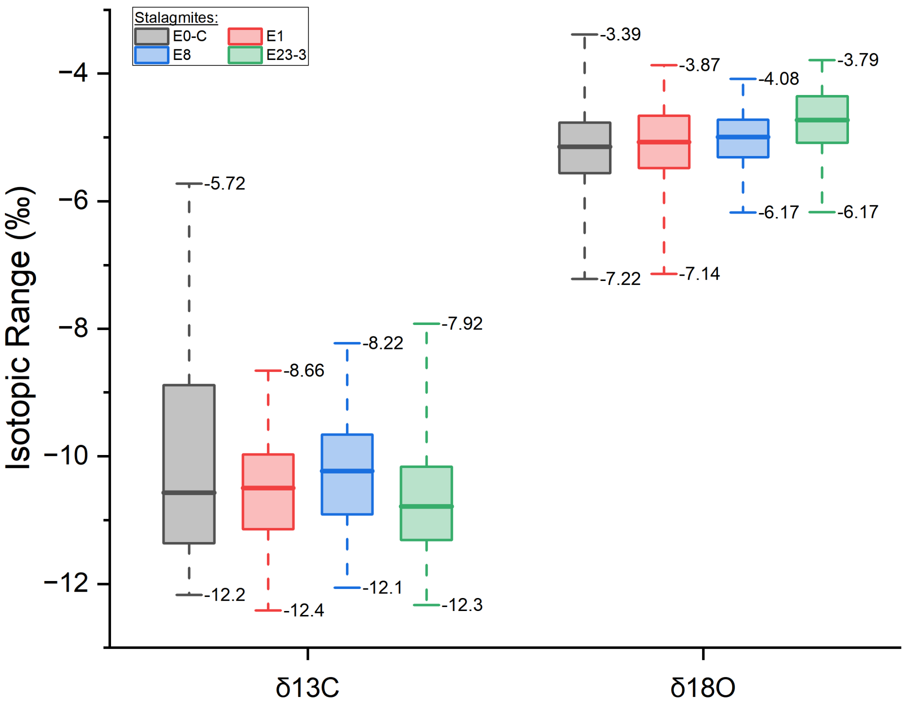

Figure IV.4. Range in δ^{13}C and δ^{18}O values in stalagmites E0-C, E1, E8, and E23-3 from Áaktun Kóopo Cave, northern Yucatán Peninsula. Different colors represent individual stalagmites. The boxes show the interquartile range (25th–75th percentile), with the horizontal line inside each box indicating the median value. All stable isotope data is provided in Appendix Tables A8–A11.

Since stalagmite E23-3 has the most reliable age model and is the most modern, I will briefly discuss some additional details regarding its geochemical characteristics.

While Sr/Ca, Ba/Ca, Na/Ca, and U/Ca ratios exhibit a strong connection with growth rate, the relationship between δ^{13}C values and growth rate in stalagmite E23-3 is more moderate (Fig. IV.5). This weaker association between growth rate and δ^{13}C values is also observed in stalagmites E1 and E8 (Fig. A12). However, this relationship does not appear to hold for δ^{18}O values and growth rate. Both δ^{13}C and δ^{18}O values seem to follow long-term variations in Mg/Ca ratios, which range between approximately 10 and 20 mg g^{-1} (Fig. IV.5). This is consistent with the expectation that Mg/Ca ratios are primarily influenced by changes in the extent of PCP and/or water-rock interaction, as discussed earlier. Enhanced PCP and/or water-rock interaction are typically associated with drier climate conditions, leading to increased Mg/Ca ratios and higher δ^{13}C values in stalagmites. At the same time, δ^{18}O values would be expected to decrease, reflecting reduced precipitation and/or convective activity, as demonstrated by numerous studies from the YP (e.g., Medina-Elizalde et al., 2016a; Asmerom et al., 2020; Warken et al., 2021; Lases-Hernandez et al., 2019; Lases-Hernández et al., 2020; Braun et al., 2023).

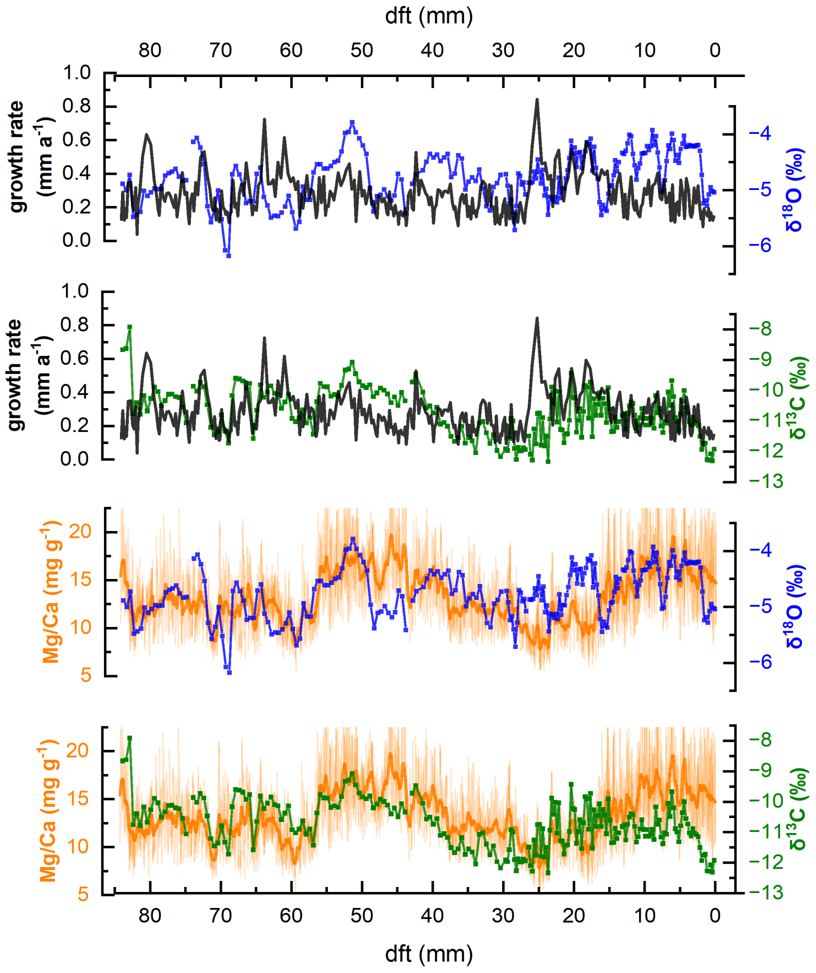

Figure IV.5. Stable isotopes (δ^{18}O, δ^{13}C) vs. growth rates and Mg/Ca of stalagmite E23-3. Growth rates were estimated based on the distance between consecutive Sr/Ca minima, determined through LA-ICP-MS measurements (see Methods II.3.2). The solid orange curve represents the filtered Mg/Ca ratio, using the Lomb-Scargle method (500 points; 2nd-order polynomial).

IV.3 Conclusion

The observed seasonal variations in trace element ratios (e.g., Sr/Ca, Na/Ca, U/Ca, P/Ca, Cu/Ca) across multiple stalagmites from Áaktun Kóopo Cave provide insights into the interplay between climate conditions and cave processes on both seasonal and longer-term timescales. These patterns indicate that growth rate is a key contrtrol on the incorporation of trace elements into Áaktun Kóopo Cave stalagmites. During the dry season, cooler temperatures may enhance growth rates via increased cave ventilation, therby elevating Sr/Ca, Ba/Ca, Na/Ca, and U/Ca ratios. Conversely, during the rainy season, reduced ventilation and higher cave pCO_2 lead to lower growth rates and a decrease in these ratios. The contrasting seasonal peaks in P/Ca, Al/Ca, and Cu/Ca during the rainy season suggest that other processes, such as soil-derived element transport, may be involved. While the relationship between Sr/Ca, Ba/Ca, Na/Ca, and U/Ca ratios and growth rate holds on both seasonal and long-term scales, Mg/Ca shows an inverse relationship with growth rate over extended timescales, suggesting that prior calcite precipitation (PCP) primarily influences Mg/Ca ratios. Although proxies such as Sr/Ca, Ba/Ca, Na/Ca, and U/Ca exhibit seasonal variations that align with their long-term trends, care should be taken when interpreting these proxies on longer timescales, as seasonal effects may introduce variability to long-term patterns.

On the other hand, δ^{13}C values show a moderate connection to growth rate, particularly in stalagmites E23-3, E1, and E8, where higher growth rates tend to correspond with higher δ^{13}C values. However, the connection between δ^{13}C and Mg/Ca ratios appears stronger, particularly on longer timescales, which suggests a strong affect of PCP on both stable carbon isotopes and Mg/Ca ratios. In contrast, δ^{18}O values do not show a connection with growth rate but instead track long-term trends in Mg/Ca ratios. Enhanced PCP and water-rock interaction during drier climate periods likely result in elevated Mg/Ca ratios and higher δ^{13}C values, while δ^{18}O values tend to decrease in response to reduced precipitation and/or convective activity above Áaktun Kóopo Cave.

Overall, the observed patterns in the trace elements and stable isotopes highlight the importance of considering both PCP and growth rate effects across timescales when interpreting these proxies in the stalagmites from Áaktun Kóopo Cave. Stable oxygen isotopes (δ^{18}O) appear primarily related to rainfall amount and convective activity, consistent with observations from other sites across the YP and the broader Caribbean region.

V Paleoenvironmental Shift across the Terminal Classic Period (800–1000 AD)

Although proxy data suggest variable hydroclimate conditions in Central America throughout much of the Common Era (Steinman et al., 2022; Wojewódka-Przybył et al., 2022; Obrist-Farner et al., 2023), most paleorecords from the region indicate severe dry conditions between 800 and 1050 AD (Bhattacharya et al., 2017; Atwood et al., 2021). This time span, known as the Terminal Classic Period (TCP), coincides with the disintegration of the Classic Maya civilization. Over the past few decades, studies have suggested that a series of unprecedented droughts contributed to this demographic decline (Curtis et al., 1996; Haug et al., 2001; Medina-Elizalde and Rohling, 2012; Douglas et al., 2016; Hoggarth et al., 2017; Evans et al., 2018). However, the idea that drought alone caused this political collapse has been largely rejected and it is now recognized that multiple factors—including warfare, epidemics, political instability, resource depletion, and recurrent droughts—likely played interconnected roles in driving the profound changes during the TCP (e.g., Haug et al., 2003; Kennett et al., 2012; Turner and Sabloff, 2012; Webster, 2002; Gill et al., 2007; Ebert et al., 2015).

For the subsequent centuries, including the Medieval Warm Period (MWP) (∼950–1250 AD), the interpretation of proxy records remains ambiguous. While some studies suggest a shift toward wetter conditions occurred around 900/1000 AD (e.g., Douglas et al., 2016; Fensterer et al., 2013), regional variability and differences in proxy resolution have made it challenging to establish a definitive hydroclimate pattern for this period (Wu et al., 2019).

Based on the stalagmite chronologies presented in Chapter III.3, stalagmite E0-C from Áaktun Kóopo Cave, which grew between 538±56 AD and 1835±53 AD (Chapter III.2), is well-suited to address this question.

In this chapter, I present an in-depth examination of the geochemical signals preserved in stalagmite E0-C from Áaktun Kóopo cave, located in the northeastern Yucatán Peninsula (YP). Utilizing a multi-proxy approach—including stable oxygen and carbon isotope analyses (δ^{18}O, δ^{13}C) (Chapter II.3.4), trace element analyses (Mg, Ba, Sr, P, U) (Chapter II.3.3), and radiocarbon (^{14}C) measurements (Chapter II.3.2)—this study aims to enhance our understanding of the climatic and environmental changes in the northern YP surrounding key periods of Maya cultural evolution, such as the TCP, as well as the onset of the MWP.

By comparing the E0-C data with other regional paleoenvironmental records, this study aims to provide a more detailed understanding of environmental changes across the YP during the late Holocene, emphasizing the complex interactions between climate variability and human activities.

The stalagmite's dead carbon fraction (DCF) values, discussed in this chapter, are derived from radiocarbon (^{14}C) measurements conducted as part of Celine Kolb's master thesis at the Institute of Environmental Physics, Heidelberg University (Kolb, 2024).

V.1 Trace Elements and Stable Isotopes as Hydroclimate Indicators

At the onset of the TCP toward the end of the first millennium, E0-C exhibits the highest δ^{18}O values in the record before stalagmite growth ceased in 811±52 AD (Fig. V.1). These δ^{18}O values are interpreted as indicators of rainfall amounts and/or the intensity of convective activity (see Chapter IV), with the observed increase pointing to a shift toward drier climatic conditions above the cave. Concurrently, δ^{13}C values and Mg/Ca ratios also increase, which indicates enhanced prior calcite precipitation (PCP), that is, carbonate precipitation occurring before the drip water reaches the stalagmite surface, due to reduced recharge and drier conditions (Johnson et al., 2006; Cruz et al., 2007). These prolonged arid conditions during the TCP may have ultimately led to the drainage of the epikarst above Áaktun Kóopo Cave, causing the cessation of E0-C stalagmite growth after 811 ± 52 AD until growth resumed in 994 ± 29 AD. The E0-C proxy record represents the first stalagmite record from the northeastern YP to suggest that this region experienced drier climatic conditions at the onset of the TCP (and likely prevailing throughout), as previously indicated by studies of lacustrine paleorecords (Curtis et al., 1996; Hodell et al., 2005, 2007, 1995; Aragón-Moreno et al., 2012; Carrillo-Bastos et al., 2010).

V.2 Geochemical Shifts across the Terminal Classic Period

As the growth of stalagmite E0-C resumed around 994±29 AD, at the end of the TCP, several shifts in proxies are observed (Fig. V.1). Notably, δ^{13}C values decrease by 3‰, U/Ca ratios double, and DCF values decline from approximately 21% (622–808 AD) to around 14% (994–1313 AD). Concurrently, δ^{18}O and $\delta^{234}U_0$ values shift towards lower mean values; however, these changes are less pronounced than those observed in U/Ca and δ^{13}C. While Mg/Ca ratios decrease following the TCP, this change is less persistent compared to the variations in U/Ca and δ^{13}C. Interestingly, the shift in uranium concentration is not unique to stalagmite E0-C but is observed across all speleothems within the cave system (Fig. III.9c). This system-wide trend reveals a marked increase in uranium concentrations around 900 AD, transitioning from relatively low and stable values in earlier periods to significantly higher concentrations in more recent times. However, due to the hiatus in stalagmite growth between 811±52 and 994±29 AD, the precise timing and duration of these transitions remain uncertain. Nevertheless, the timing is particularly intriguing, as it coincides with the TCP—a period marked by the disintegration of major Classic Maya polities throughout the YP (Ebert et al., 2015).

One potential explanation for the contrasting behavior of decreasing δ^{13}C values and increasing U/Ca ratios is a change in the extent of PCP (Treble et al., 2003; Johnson et al., 2006). Generally, increased PCP during drier periods is expected to elevate δ^{13}C values and Mg, Sr, Ba, and U concentrations in cave drip waters, since $D_X < 1$ (Fairchild and Treble, 2009; Day and Henderson, 2013; Kost et al., 2023). This process would typically result in a positive relationship between U/Ca ratios and δ^{13}C values in the stalagmite, which contrasts with the observed trends in E0-C. However, it has also been proposed that increased PCP could reduce uranium concentrations in drip waters due to uranium scavenging, potentially along with phosphorus, onto mineral surfaces (Johnson et al., 2006). In this scenario, U/Ca ratios would exhibit a negative relationship with δ^{13}C, which could potentially explain the observed shifts in these proxies. While P/Ca ratios generally follow the U/Ca trend in the older sections of E0-C (growth period 1) and increase across the TCP, they do not align with the U/Ca pattern during the later periods (growth periods 2 and 3) (Fig. V.1).

Moreover, the ambiguous results from the regression between ln(Mg/Ca) and ln(Sr/Ca)—a test for the effects of PCP on Sr and Mg incorporation (see Chapter IV)—along with the absence of significant shifts in Mg/Ca and δ^{18}O values across the

TCP, suggest that the observed shifts in stable carbon isotopes and uranium concentration are unlikely to result from variations in water availability. Furthermore, the fact that the shift in uranium concentration occurs consistently across all speleothems in the cave system implies that a process specific to individual drip sites, such as PCP, cannot account for this system-wide change (Fohlmeister et al., 2020).

Therefore, alternative mechanisms must be considered to explain the observed long-term shifts in stable carbon isotopes, uranium concentrations, DCF, and uranium isotopes.

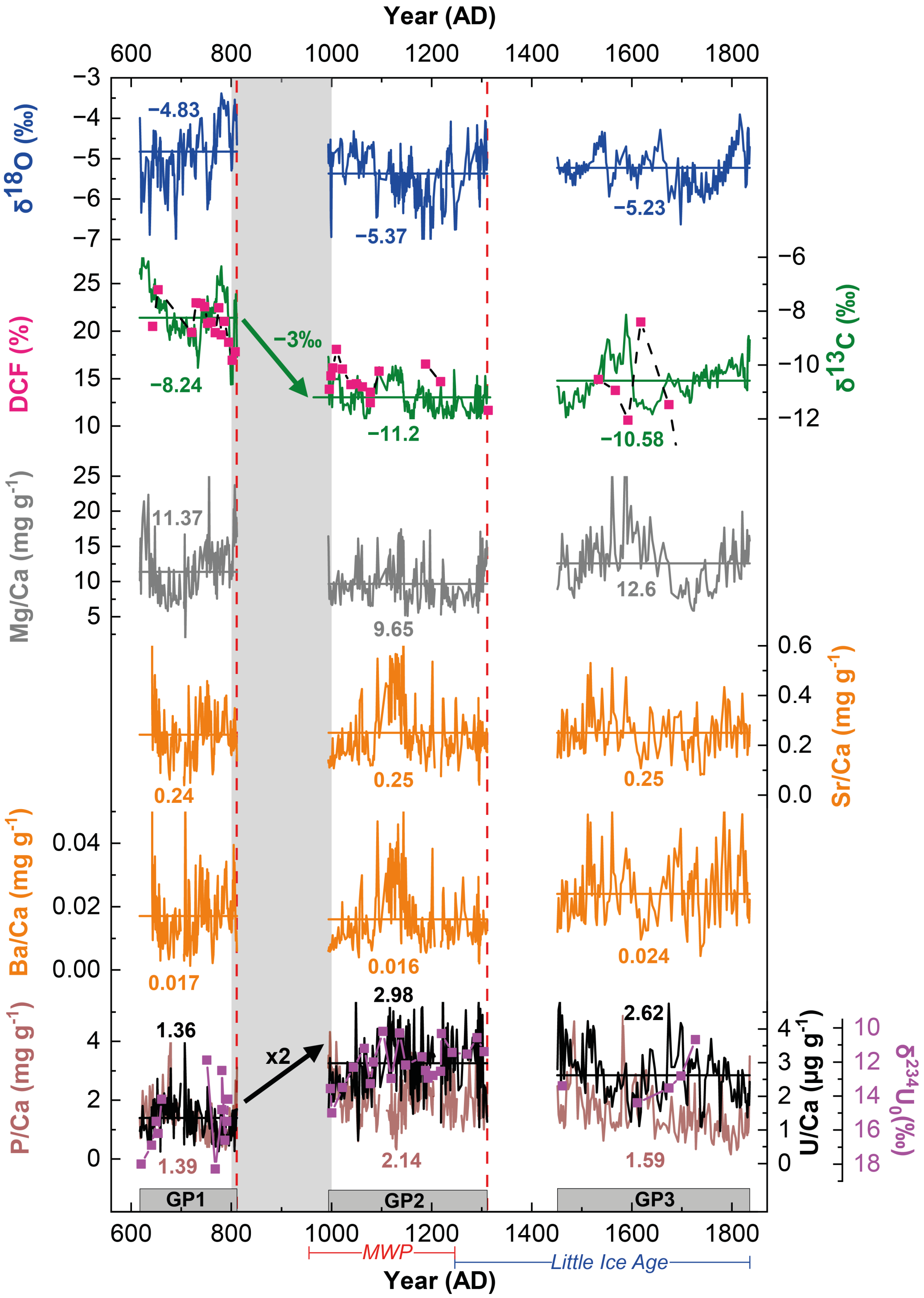

Figure V.1. E0-C proxy record. Shown are stable oxygen and carbon isotopes, element/Ca ratios, dead carbon fraction (DCF), and $\delta^{234}U_0$ values of stalagmite E0-C. The stable mean values of each proxy are provided for the three growth periods (GP1–GP3). Notably, $\delta^{13}C$ values, DCF, U/Ca ratios, and $\delta^{234}U_0$ values show a pronounced shift in mean values across the Terminal Classic Period (TCP). DCF values were derived from radiocarbon measurements conducted as part of Celine Kolb's master thesis (Kolb, 2024), while data on the Uranium isotopic composition ($\delta^{234}U_0$) were obtained from $^{230}Th/U$ dating (Table A7). Note the inverted y-axis for $\delta^{234}U_0$. The grey shading marks the TCP. Colored bars indicate major historical periods: MWP = Medieval Warm Period, Little Ice Age.

V.3 Soil Carbon and Vegetation Dynamics: Insights from δ^{13}C, U/Ca, and DCF

As PCP can be ruled out as the main driver of the changes in the stalagmite's U/Ca ratios and δ^{13}C values, these shifts may instead be explained by changes in soil carbon processes and vegetation dynamics.

The stable carbon isotopic composition of speleothems is strongly influenced by the soil environment, as a significant portion of the carbon in speleothems originates from respired soil CO_2 (Lechleitner et al., 2021). The soil respiration rate, which serves as an indicator of vegetation productivity, depends primarily on factors such as vegetation density and type (e.g., woody vs. herbaceous plants), nutrient availability (e.g., P, N), soil composition, soil thickness, and soil moisture. Soil moisture is, in turn, controlled by temperature and precipitation (Vargas and Allen, 2008). Consequently, changes in vegetation type (e.g., shifts between C3 and C4 plants), nutrient availability, and moisture above the cave can induce shifts in the E0-C stable carbon proxy record. The concurrent, cave-wide shift in speleothem U/Ca ratios further supports the hypothesis of a significant change in soil chemistry, as factors such as oxygenation, carbonate dissolution rate and efficiency, soil pCO_2, and pH collectively influence the mobilization and transport of uranium (Bourdon et al., 2003).

Modeling studies suggest a relationship between the δ^{13}C values of drip water and soil pCO_2, assuming a constant vegetation type, with more positive δ^{13}C values corresponding to lower soil pCO_2 (Fohlmeister et al., 2011). Furthermore, it has been demonstrated that soil pCO_2 influences the mobility of uranium in groundwater (Langmuir, 1978). A decrease in vegetation density, soil microbial activity, and soil carbon turnover during dry periods or sustained deforestation, as may have occurred during the TCP (e.g., Beach et al., 2015), would likely have resulted in synchronous soil CO_2 depletion and reduced carbonate dissolution above Áaktun Kóopo Cave. Consequently, this would have led to lower U/Ca ratios and more positive δ^{13}C values in the E0-C stalagmite (Fig. V.1). Additionally, reduced vegetation density, leading to lower soil CO_2 concentrations, would result in higher pH and more positive δ^{13}C values in the drip water (Fohlmeister et al., 2011). In contrast, elevated soil CO_2 concentrations promote more open-system dissolution of the karst host rock carbonate (Fohlmeister et al., 2011; Stoll et al., 2023), leading to lower δ^{13}C values of the drip water while simultaneously enhancing the mobility of uranium.

Considering these factors, the observed shift across the TCP in the E0-C stalagmite toward more negative δ^{13}C values and higher U/Ca ratios (Fig. V.1) likely reflects a subsequent increase in vegetation productivity and elevated soil pCO_2 concentrations above the cave. This interpretation is further supported by the concurrent change in $\delta^{234}U_0$ values, which show slightly elevated values (15‰ on average) from 622–808 AD and lower values (12‰ on average) after the TCP (994–1313 AD), indicating an inverse relationship with U/Ca ratios. Although individual data points do not show a strong relationship, the overall trend is consistent with the expected pattern.

With the onset of the MWP around 950–1000 AD, an increase in precipitation (indicated by more negative $\delta^{18}O$ values) can be linked to higher soil CO_2 concentrations, more efficient carbonate dissolution, and consequently increased uranium concentrations alongside lower $\delta^{234}U_0$ values, as the effect of the alpha recoil process diminishes (Ivanovich and Harmon, 1992). In addition to carbonate dissolution, the $\delta^{234}U_0$ values of percolating water are influenced by the residence time of water in the karst, which is controlled by precipitation amounts, explaining the similar patterns observed between $\delta^{234}U_0$ and $\delta^{18}O$ values.

Analyzing DCF in stalagmites offers additional valuable insights into soil carbon processes (e.g., Trumbore, 2009). In conjunction with the observed shifts in $\delta^{13}C$ values and U/Ca ratios in the E0-C stalagmite across the TCP, the DCF also shows a notable decrease from approximately 21% between 622 and 808 AD to around 14% between 996 and 1313 AD. Previous studies have reported increasing DCF in stalagmites during periods of heightened rainfall, which has been attributed to a shift in the dissolution system toward a more closed configuration, with reduced open gas volume in the soil environment(Lechleitner et al., 2016; Griffiths et al., 2012; Bajo et al., 2017; Noronha et al., 2014). However, the definition and underlying processes governing the openness of the dissolution system and local hydrology are not yet well constrained (Lechleitner et al., 2021; Owen et al., 2018). Moreover, other processes, such as human-induced changes in soil and vegetation composition (from C4 to C3), may also account for the observed shifts in $\delta^{13}C$ values, DCF, and U/Ca ratios.

To further explore the potential mechanisms behind these shifts, modeling approaches such as CaveCalc can provide valuable insights into the influence of environmental variables on DCF and $\delta^{13}C$ in speleothems.

Numerical Modeling of Speleothem Geochemistry

CaveCalc, a PHREEQC-based model, simulates the equilibration of meteoric water with soil CO_2, host rock dissolution, and CO_2 degassing to form speleothems (Owen et al., 2018). This model was used for sensitivity tests of DCF and $\delta^{13}C$, with respect to the soil CO_2 concentration and the degree of system openness. In this context, openness reflects the amount of free CO_2 gas in the soil water that can dissolve the carbonate rock and is replenished by soil respiration processes. This parameter allows to obtain a high soil CO_2 dominated carbonate dissolution, in contrast to a closed system in which each carbonate ion in the karst water generates a carbonate ion from the host rock, thus leading to high DCF values (∼50%). Several sensitivity and limit tests were performed using CaveCalc as part of Celine Kolb's master thesis (Kolb, 2024). The general dependencies of the key parameters in CaveCalc are shown in Figure V.2. This Figure demonstrates that the carbonate isotopes behave largely non-linear for a given vegetation type (constant here) and become most sensitive when the system is closed (low openness) and when soil CO_2 is minimal. Consequently, even small shifts in soil CO_2 and openness have a strong influence on $\delta^{13}C$ and DCF. It is important to note that the figure presents the mathematical solution of the equations; however, stalagmite growth requires a certain degree of openness and soil CO_2, which are not depicted here. Furthermore, input $\delta^{13}C$ may vary with vegetation type, while host rock $\delta^{13}C$ can generally be assumed constant.

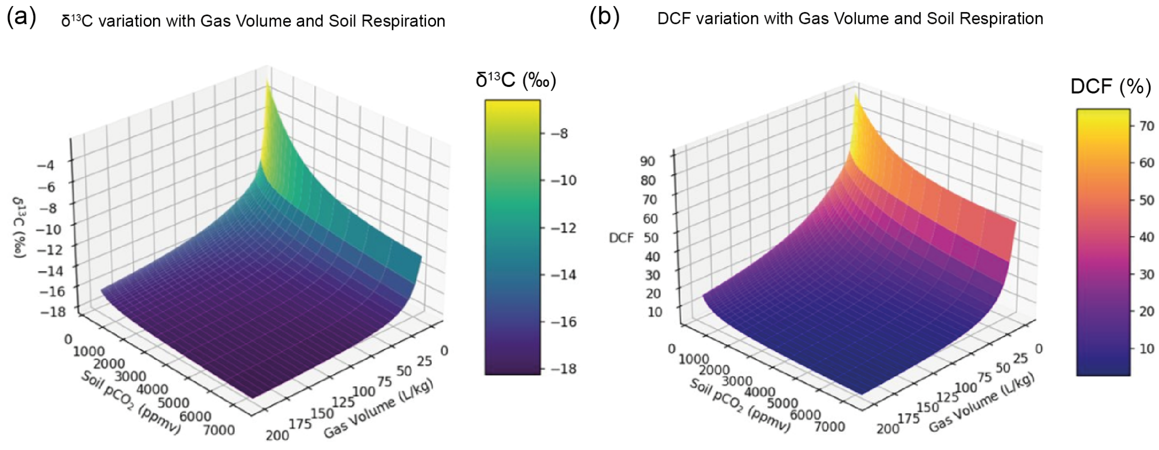

Figure V.2. 3D Plots of CaveCalc Sensitivity Tests. (a) Modeled variations in $\delta^{13}C$ values with different combinations of soil pCO_2 concentrations (in ppmv) and gas volume (L/kg). **(b)** Modeled variations in DCF values with different combinations of soil pCO_2 concentrations (in ppmv) and gas volume (L/kg). These model tests were conducted as part of Celine Kolb's master thesis, from which this figure was taken (Kolb, 2024).

The following sections briefly summarize key findings from the application of a complex evolutionary Rainforest reverse model (e.g., Gehrke et al., 2000; Wolfensberger et al., 2021), which uses a decision tree to estimate initial conditions leading to the observed ^{14}C and $\delta^{13}C$ values in stalagmite E0-C. As this is the work of Celine Kolb, we solely refer to her findings here, while the methodology for constructing the Rainforest Model to run CaveCalc is detailed in her master thesis and pending publication.

The models generate a training and test dataset from which the probability and associated uncertainties of driving parameters are extracted. In the figure below, the final prediction of observed ^{14}C and $\delta^{13}C$ values and real data is displayed, achieving correlation coefficients of r=0.95 and r=0.97, respectively. This model predicts soil CO_2 and openness as key parameters influencing both ^{14}C and $\delta^{13}C$, as anticipated. Notably, without any presumption on data origin, the model predicts a significant increase in soil CO_2 following the TCP, accompanied by an increase in system openness. Additionally, the model coupling further includes the possibility of significant changes in the abundance of C3 and C4 plants, which critically affect the evolution of $\delta^{13}C$.

Openness in CaveCalc, referred to as gas volume (GV), shows substantial variability, ranging from 20 L kg^{-1} to 500 L kg^{-1}. While this parameter contributes less significantly to changes in $\delta^{13}C$ than soil CO_2 levels and the C3/C4 plant ratio, the modeling results strongly support the interpretation that observed shifts in soil-sensitive proxies, such as $\delta^{13}C$ values, DCF, and U/Ca ratios in the E0-C stalagmite, are most likely responses to changes in vegetation composition, soil fertility, carbonate dissolution processes, and soil pCO_2 levels across the TCP.

The subsequent sections will explore the potential roles of human activities, regional climate shifts, and other long-term environmental drivers to provide a more comprehensive understanding of the processes responsible for the observed paleoenvironmental changes across the TCP. It is important to note that the observed changes in DCF, U/Ca, and $\delta^{13}C$ are the most notable shifts, but they are also very diffcult to explain.

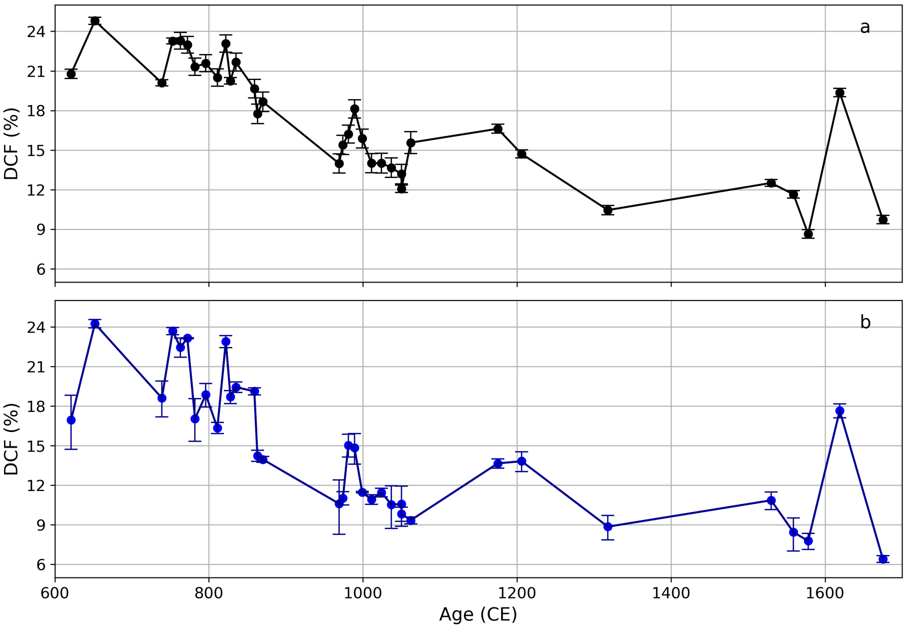

Figure V.3. The top panel displays the measured speleothem DCF values, while the bottom panel shows the results after running the reverse model outputs through CaveCalc. The correlation coefficient for DCF is r = 0.95. These model tests were conducted as part of Celine Kolb's master thesis, from which this figure was taken (Kolb, 2024).

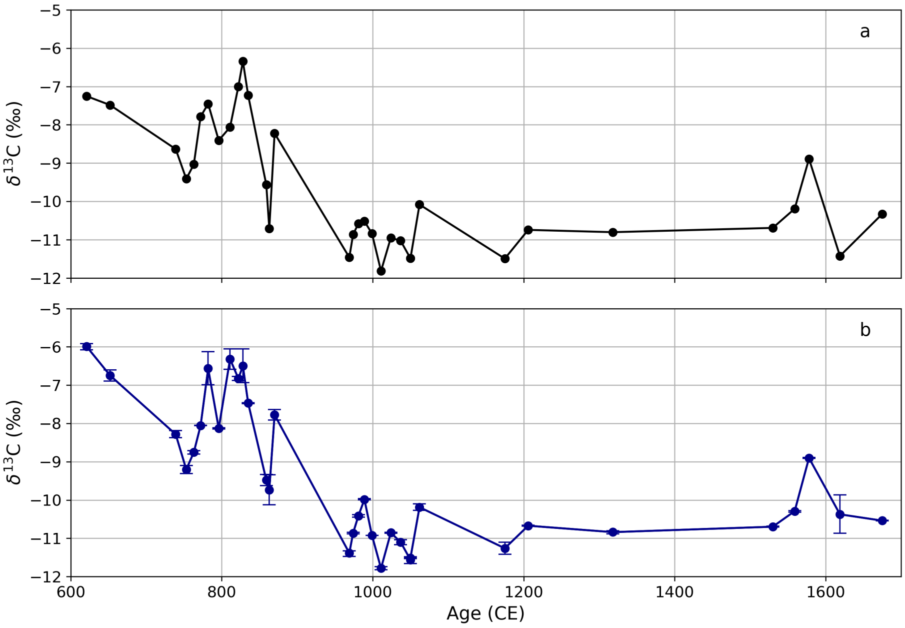

Figure V.4. The top panel displays the measured speleothem δ^{13}C values, while the bottom panel shows the results after running the reverse model outputs through CaveCalc. The correlation coefficient for δ^{13}C is r = 0.97. These model tests were conducted as part of Celine Kolb's master thesis, from which this figure was taken (Kolb, 2024).

V.4 Impact of Human Activities on Vegetation and Soil Environment

Human activities, such as deforestation and plant cultivation, can significantly impact vegetation types, net primary productivity (influenced by sunlight, nutrients, and moisture), as well as soil pCO_2 through bacterial and root respiration, among other factors. It is well known that the land-use practices of the Maya had a substantial impact on their environment (e.g., Beach et al., 2015; Morell-Hart et al., 2023). Some modeling studies even suggest that the decreased rainfall observed during the TCP may have been exacerbated by extensive deforestation (Oglesby et al., 2010; Cook et al., 2012). Palynological records from the Maya Lowlands indicate a persistent presence of disturbance taxa throughout the Classic Period, which weakens after the TCP, followed by evidence of forest regrowth starting around 900/1000 AD (Wahl et al., 2007; Islebe et al., 2022; Carrillo-Bastos et al., 2010; Beach et al., 2015; Islebe et al., 1996; Curtis et al., 1998; Wahl et al., 2006; Anselmetti et al., 2007; Mueller et al., 2010; Battistel et al., 2018). A study conducted in the Macal Chasm cave on the Vaca Plateau in the southern YP interprets the rapid drop in residual stalagmite $\delta^{13}C$ values during the TCP as indicative of regional land abandonment and the subsequent recovery of C_3-dominated forests following the decline in Maya cultural activity (Akers et al., 2016).

This raises the question of whether similar processes, such as agricultural establishment (deforestation and cultivation) followed by abandonment and subsequent natural vegetation regrowth, contributed to the observed changes in the soil environment above Áaktun Kóopo Cave before and after the TCP. Although Áaktun Kóopo Cave is not near any major known Maya settlements, nor is there direct evidence of large-scale land modification for agricultural purposes, the cave's archaeological remains suggest a more complex relationship with the surrounding landscape (Gómez, 2020). The closest major Maya sites—Punta Laguna, Coba, El Naranjal, and Ek Balam—are situated 20–40 km from Áaktun Kóopo Cave (Folan et al., 2009; Kurnick et al., 2023; Benítez and Albuerne, 2004; De la Peña et al., 2020) (Fig. A4). However, the discovery of Maya artifacts, including pottery and human skeletons, in Áaktun Kóopo Cave indicates its use for domestic and ritual activities during the late Preclassic (−250 to 300 AD) and early Classic (300 to 600 AD) periods, coinciding with the occupation of smaller surface settlements in the Xcan region, less than 10 km from the cave (Tec, 2021; Gómez, 2020) (Fig. A4).

The sustained use of the cave for mortuary and ritual practices suggests that the communities involved may have lived in the surrounding area (Gómez, 2020). The integration of the cave into the daily lives of these communities (Gómez, 2020) suggests that they may have engaged in agricultural activities, such as clearing forested areas for the cultivation of maize and other crops, thereby directly affecting the vegetation and soil environment above Áaktun Kóopo Cave.

The observed shift in soil- and carbonate dissolution-sensitive proxies (DCF, δ^{13}C, U/Ca and $\delta^{234}U_0$) in stalagmite E0-C across the TCP may thus reflect a cessation of agricultural activities above the cave during this period, coinciding with the regrowth of natural vegetation. This interpretation aligns with broader regional trends, where a reduction in human activity allowed for forest recovery during the transition from the Classic to Postclassic periods.

V.5 Hydroclimate Shifts in the Yucatán Peninsula During the TCP and MWP

While anthropogenic activities likely contributed to long-term alterations in the soil environment above Áaktun Kóopo Cave, another important factor may have been a shift in the regional hydroclimate. This interpretation is supported by changes in δ^{18}O values and Mg/Ca ratios in stalagmite E0-C (Fig. V.1), both of which serve as indicators of hydroclimatic variability, as discussed in Chapter IV.

Soil respiration is highly sensitive to changes in precipitation, with variations in soil moisture influencing this process to different extents across biomes, depending on soil and vegetation type (Liu et al., 2016; Du et al., 2020). Furthermore, rising surface temperatures, in combination with soil moisture excess, can enhance respiration rates, as increased temperatures accelerate soil carbon turnover (Karhu et al., 2014).

Evidence from Lake Chichancanab and Lake Punta Laguna in the northern YP indicates a wetter climate at the end of the TCP, around 1000 AD, as reflected by increased sediment carbonate content and decreasing δ^{18}O values of ostracods and gastropods (Curtis et al., 1996; Hodell et al., 2007, 1995) (Fig. V.5c,d). Similarly, δ^{18}O values from the stalagmite named 'Chaac' in the northwestern YP suggest a shift towards wetter conditions around 942±15 AD (Fig. V.5 h) (Medina-Elizalde et al., 2010). This hydroclimatic shift is also observed in lake and speleothem records from the southern YP (Fig. V.5e,f) (Ridley et al., 2015; Asmerom et al., 2020; Wahl et al., 2013, 2014), indicating a widespread change across the region around 900–1000 AD (Douglas et al., 2016). It is important to note that while the carbonate content in lake sediments or the δ^{18}O values of ostracods and gastropods reflect changes in the net water balance of precipitation minus evaporation (P–E), stable oxygen (and in cases carbon isotopes) in speleothems more directly capture rainfall amounts and convective activity (e.g., Medina-Elizalde et al., 2010; Asmerom et al., 2020). The apparent rapidity of this shift, as observed in some studies (Medina-Elizalde et al., 2010) (Fig. V.5h), contrasts with the more gradual transition reported in others (Akers et al., 2016; Ridley et al., 2015; Asmerom et al., 2020) (Fig. V.5f,g), which could be due to differences in sample resolution or undetected hiatuses within the records. While numerous proxy records from the YP reflect a hydroclimate shift across the TCP into the MWP, some do not show this pattern. For example, stalagmite YOK-I from the southern YP in Belize, from the same cave as YOK-G, does not show a major change across the TCP, despite an extended drought between 1020 and 1100 AD (Fig. 2). A clear explanation for the discrepancy between YOK-I and YOK-G is still lacking, but it has been suggested that this may be related to distinct hydrological pathways, with YOK-G being more sensitive to long-term rainfall shifts, while YOK-I likely responds more strongly to short-term droughts (Ridley et al., 2015).

Considering these factors, along with variations in the precision of individual age models, it is likely that this climatic shift occurred concurrently—within a few decades to a century—across large parts of the YP toward the end of the TCP and the onset of the MWP. Furthermore, given the spatial extent of the observed shift, these changes likely reflect broader atmospheric and oceanic processes operating on multi-decadal to centennial timescales.

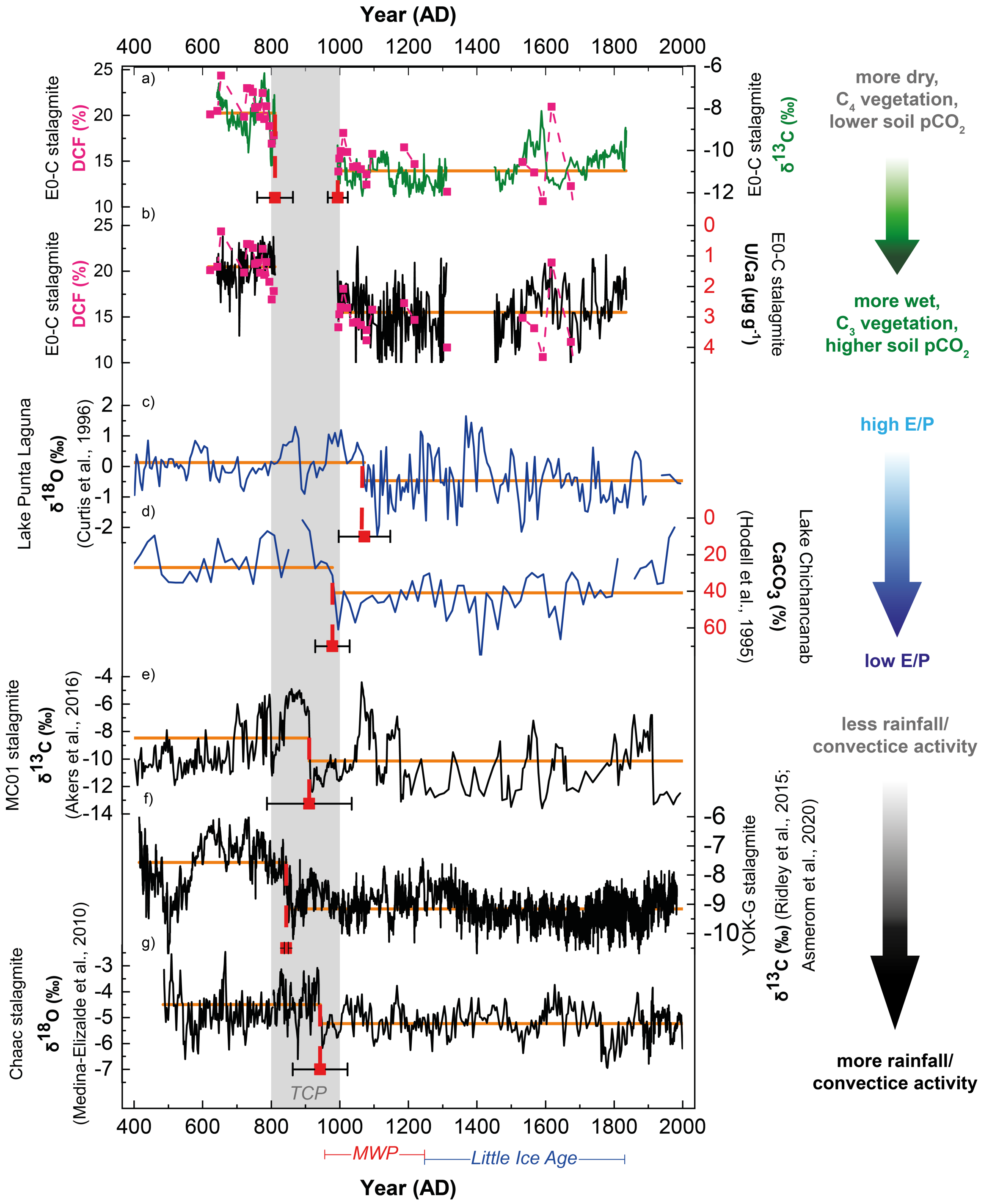

Figure V.5. Comparison of the E0-C stalagmite record ($\delta^{13}C$, U/Ca, DCF) with other paleoenvironmental proxies from the YP. From top to bottom: **(a)** DCF and $\delta^{13}C$ values from E0-C; **(b)** DCF and U/Ca ratios from E0-C; **(c)** $\delta^{18}O$ of ostracods from Lake Punta Laguna, northern YP, Mexico (Curtis et al., 1996; Hodell et al., 2007); **(d)** $CaCO_3$ content in Lake Chichancanab, northern YP, Mexico (Hodell et al., 1995); **(e)** $\delta^{13}C$ values of MC01 stalagmite from Macal Chasm Cave, southern YP, Belize (Akers et al., 2016); **(f)** $\delta^{13}C$ values from YOK-G stalagmite, Yok Balum Cave, southern YP, Belize (Ridley et al., 2015; Asmerom et al., 2020); **(g)** $\delta^{18}O$ values from Chaac stalagmite, Tzabnah Cave, northwestern YP, Mexico (Medina-Elizalde et al., 2010). Grey shading marks the Terminal Classic Period (TCP), during which the proxies' mean values shift. Colored bars indicate major historical periods: Medieval Warm Period (MWP) and Little Ice Age. Red labels on the Y-axes indicate that the axes are inverted.

V.6 SST Variability and Atmospheric Dynamics at the Onset of the MWP

At the onset of the MWP around 900–950 AD, temperatures in the North Atlantic, including the Caribbean, increased rapidly (Sicre et al., 2008; Wurtzel et al., 2013; Zhuravleva et al., 2023) (Fig. V.6c–d). Proxy records from various regions worldwide suggest that the MWP (∼950–1250 AD) was characterized by notable changes in atmospheric circulation patterns across the Northern Hemisphere, potentially driven by an intensified zonal Indo-Pacific SST gradient (Graham et al., 2011). Simultaneously, rising summer SSTs in the tropical Atlantic (Wurtzel et al., 2013) (Fig. V.6c) led to enhanced moisture convergence, resulting in wetter conditions across the circum-Caribbean region during the MWP, as evidenced by multiple proxy records (Haug et al., 2003; Curtis et al., 1996; Haug et al., 2001; Hodell et al., 2007; Medina-Elizalde et al., 2010; Asmerom et al., 2020; Fensterer et al., 2013; Wahl et al., 2014; Peros et al., 2023) (Fig. V.5). Spatio-temporal correlation analysis of precipitation data shows that SSTs in the tropical Atlantic significantly influence seasonal rainfall variability in the Caribbean region on interannual time scales (Medina-Elizalde et al., 2017). Both instrumental records and proxy-based SST reconstructions suggest that winter SST variations drive interannual SST variability across the tropical North Atlantic (Wurtzel et al., 2013; Czaja, 2004) (Fig. V.7). *G. bulloides*, which reflects local upwelling conditions and dominates the foraminifera assemblage in the Cariaco Basin during winter and spring, is commonly used in proxy reconstructions to represent upwelling season (winter/spring) water temperatures at around 30 m depth (Wurtzel et al., 2013). This species reaches its minimum abundance during the summer and fall months, when *G. ruber*, a subtropical to tropical species, dominates (Wurtzel et al., 2013). Given that the YP receives 50–90% of its annual rainfall during the 'Rainy' season (June–October), this explains why the δ^{18}O values of stalagmite E0-C align more closely with reconstructed summer/fall SSTs from the Cariaco Basin on multi-decadal to centennial scales, rather than with winter/spring SSTs, which reflect subsurface temperatures (∼30 m) (Fig. V.5d,e). Interestingly, summer/fall SSTs from the Cariaco Basin increase by over 1.2°C between 900 and 1150, while the reconstructed winter/spring SSTs show a cooling of roughly 1.5°C across the TCP (Wurtzel et al., 2013). Along with rising summer/fall SSTs, tropical storms and hurricanes became more frequent. Indeed, a recent study suggests an increase in both hurricane frequency and convective activity around 900 AD, coinciding with the onset of the MWP (Yang et al., 2024) (Fig. V.6e).

In the context of broader atmospheric dynamics, an increase of approximately 5–6 ppm in atmospheric CO_2 concentrations beginning around 1000 AD can be observed (Fig. V.6f). Although the drivers of atmospheric CO_2 changes during the Common Era remain debated, changes in land carbon storage driven by climate variability are considered to play a key role (e.g., Bauska et al., 2015; Rubino et al., 2016). Rising surface temperatures likely contributed to this CO_2 increase by enhancing soil microbial activity and respiration rates, which resulted in greater carbon release from terrestrial ecosystems (Atkin et al., 2005; Cai et al., 2010). Although photosynthetic carbon uptake also increases with higher temperatures, this effect is generally outweighed by the stronger impact of enhanced respiration, particularly in tropical and temperate regions (Atkin et al., 2005; Cai et al., 2010).

V.7 Drivers of Persistent Environmental Change

As previously discussed, numerous proxy records from the Circum-Caribbean region, including the paleoenvironmental record from stalagmite E0-C, indicate a significant regime shift at the end of the TCP and the onset of the MWP. For stalagmite E0-C from Áaktun Kóopo Cave in the northern YP, changes in uranium concentration, stable carbon isotopes, and DCF suggest a sustained alteration in vegetation type and/or productivity, along with modifications in the soil environment (soil pCO_2) and carbonate dissolution processes. This raises the key question: What are the primary drivers behind these long-term environmental changes?

Aside from potential anthropogenic impacts, such as deforestation and agriculture, which may have influenced the soil environment above the cave over the long term (as discussed previously), vegetation density and type are primarily controlled by soil moisture, which is in turn driven by temperature and precipitation patterns (Fohlmeister et al., 2020; Genty et al., 2006). Although, $\delta^{18}O$ values in E0-C show good agreement with Atlantic SST patterns on multi-decadal to centennial timescales, they do not exhibit the same persistent shift in mean values as observed in the $\delta^{13}C$ values, U/Ca ratios, and DCF (Fig. V.7).

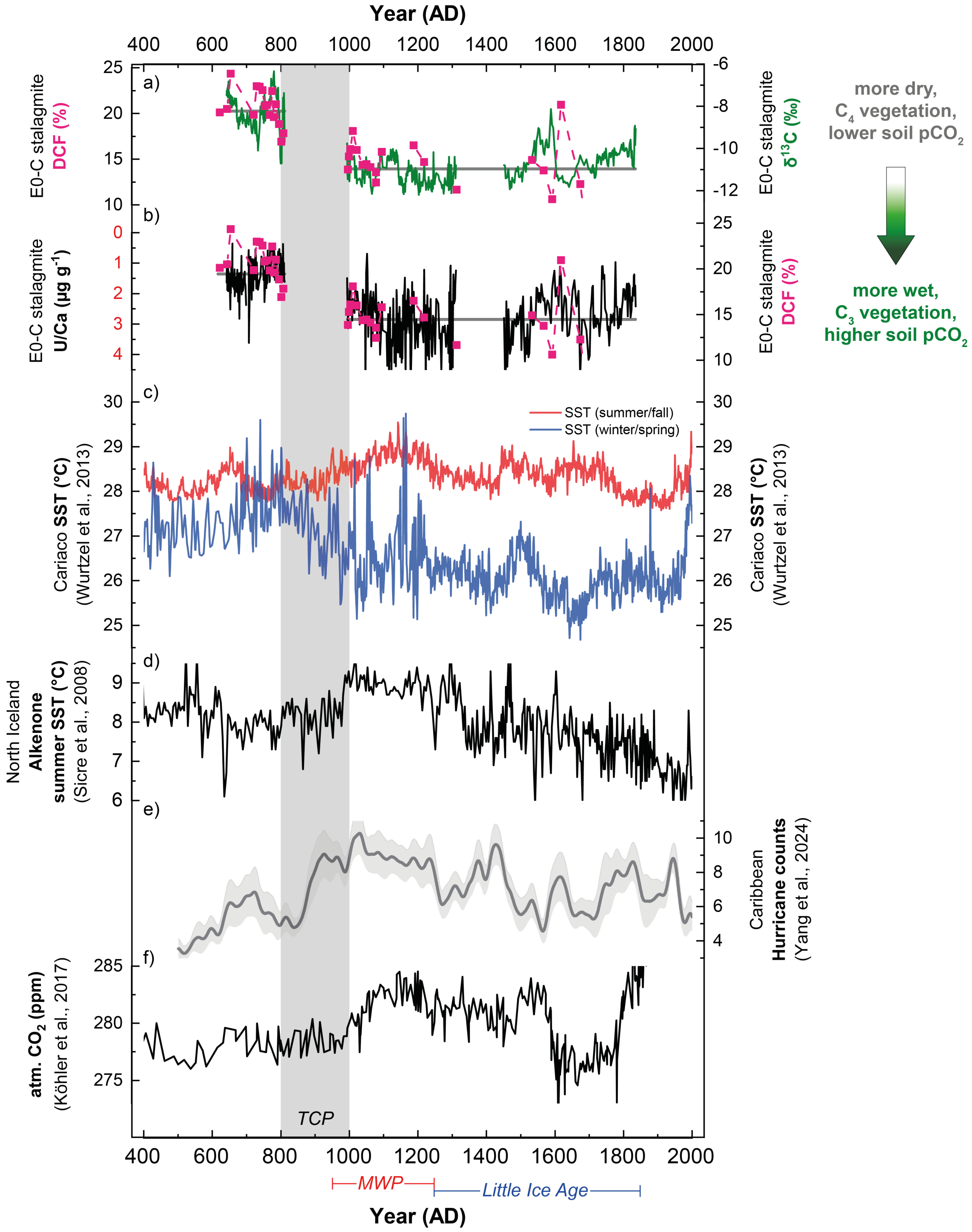

Figure V.6. Comparison of the E0-C record (δ^{13}C, U/Ca, DCF) with other hemispheric climate responses and paleoenvironmental records across the Terminal Classic Period (TCP) and Medieval Warm Period (MWP). From top to bottom: **(a)** DCF and δ^{13}C values of stalagmite E0-C; **(b)** DCF and U/Ca ratios of E0-C; **(c)** Summer/Fall (red curve) and Winter/Spring (blue curve) SST reconstructions from the Cariaco Basin in northern Venezuela (Wurtzel et al., 2013); **(d)** Alkenone-derived summer SSTs from North Iceland (Sicre et al., 2008); **(e)** Reconstructions of tropical Atlantic hurricane activity (Yang et al., 2024); ; **(f)** Concentration of atmospheric CO_2 (Köhler et al., 2017). Grey shading marks the TCP. Colored bars indicate major historical periods: Medieval Warm Period (MWP), Little Ice Age.

An interesting observation by Wurtzel et al. (2013) from the Cariaco Basin suggests an increase in the temperature gradient between *G. ruber* (representing summer/fall SST) and *G. bulloides* (representing winter/spring SST) beginning around 900 AD, which coincides with the shifts in E0-C proxies (Fig. V.7a,c). The authors suggest that this gradient increase may reflect heightened local water column stratification, driven either by an intensified Atlantic Meridional Overturning Circulation (AMOC) or a long-term reduction in trade wind-induced upwelling intensity (Wurtzel et al., 2013). Additionally, certain cold phases in the North Atlantic have been linked to reductions in surface circulation strength, which led to Caribbean salinification and Gulf of Mexico freshening, suggesting that shifts in meridional salt advection may have influenced climate variability during the Common Era (Zhuravleva et al., 2023). Furthermore, a decline in *G. bulloides* abundance, a proxy for trade wind intensity and upwelling variability, starting around 1200 AD and continuing to the present, suggests a significant decrease in Cariaco Basin productivity (Black et al., 2001). Wurtzel et al. (2013) note that although this 50% reduction in *G. bulloides* abundance is not exactly synchronous with the large temperature divergence starting around 900 AD (Fig. V.6c), both trends point to a long-term increase in local water column stratification, likely driven by reduced trade wind-induced upwelling. Since stronger trade winds, associated with a stronger NASH, have been shown to evaporatively cool SSTs through a wind-SST-evaporation feedback mechanism, thereby reducing precipitation in Central America (Giannini et al., 2000), a persistent decrease in trade wind strength would result in rising SSTs and increased precipitation across the region, including the YP. These sustained changes in the coupled ocean-atmosphere system, potentially exacerbated by the cessation of agricultural practices and the subsequent regrowth of natural vegetation (tropical forest), may explain the persistent changes observed in soil-sensitive proxies (DCF, δ^{13}C values, and U/Ca ratios) in stalagmite E0-C. These environmental shifts, which are also evident in other hydroclimate records from the YP, indicate a widespread transformation across the region during the TCP, leading into the MWP.

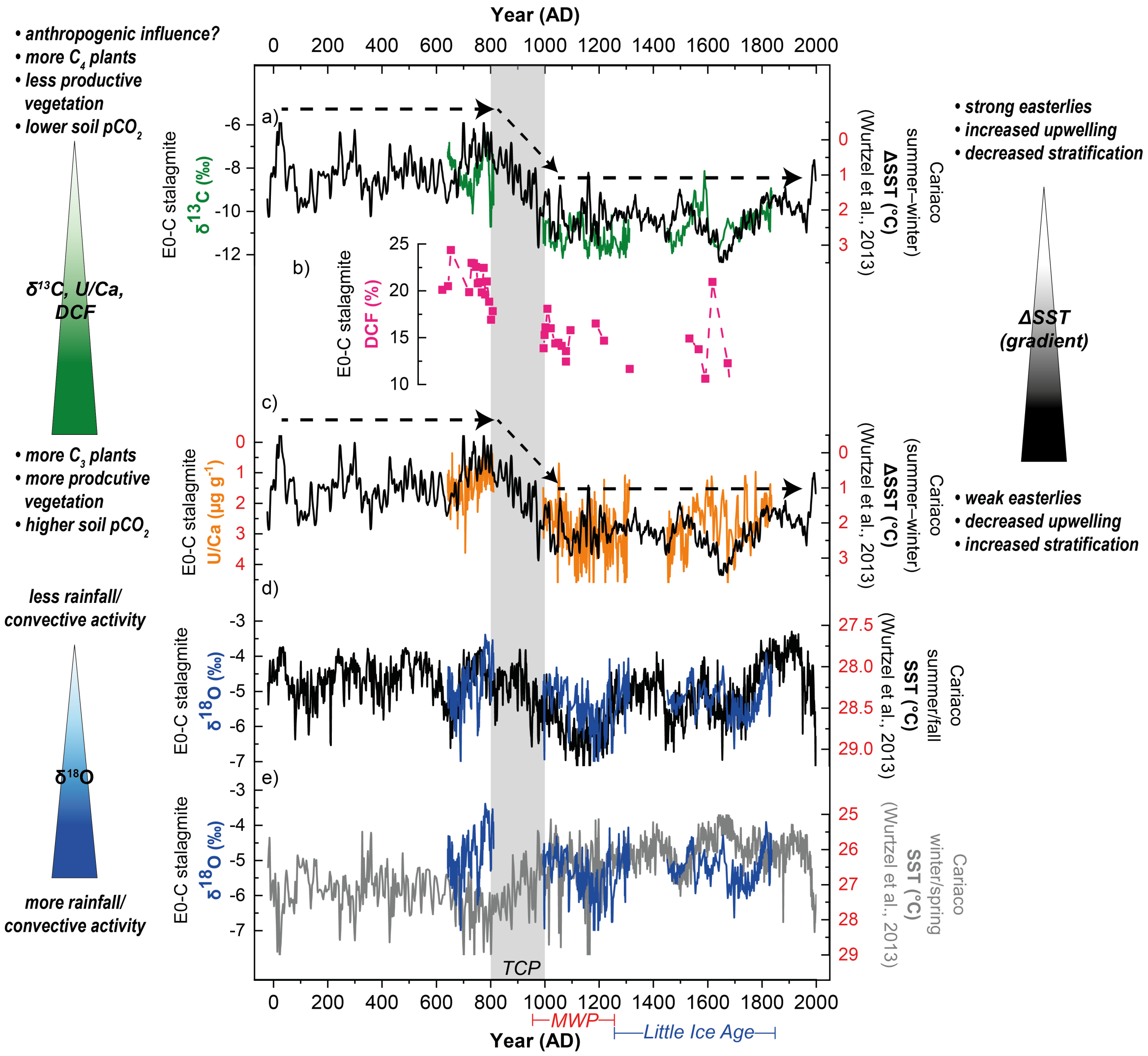

Figure V.7. Drivers of persistent environmental change across the Terminal Classic Period (TCP). Comparison of the E0-C record ($\delta^{13}C$, U/Ca, DCF) with SST reconstructions from the Cariaco Basin (Wurtzel et al., 2013) over the Common Era. From top to bottom: **(a)** $\delta^{13}C$ values of stalagmite E0-C plotted against ΔSST (the difference between summer/fall SSTs and winter/spring SSTs); **(b)** DCF of E0-C showing a similar shift across the TCP as $\delta^{13}C$ values and U/Ca ratios; **(c)** U/Ca ratios of E0-C plotted against ΔSST; **(d)** $\delta^{18}O$ values of stalagmite E0-C against summer/fall SSTs from the Cariaco Basin; **(e)** $\delta^{18}O$ values of stalagmite E0-C plotted against winter/spring SSTs from the Cariaco Basin. Notes on the side of the plots suggest potential drivers and forcings influencing the respective proxies, providing an explanation for the potential shift in the overall climate state (see discussion in the text). Grey shading marks the TCP. Colored bars indicate major historical periods: Medieval Warm Period (MWP), Little Ice Age.

V.8 Conclusions

This chapter explored the complex interplay of climatic and anthropogenic factors that influenced environmental changes in the Yucatán Peninsula (YP) across the Terminal Classic Period (TCP) and the onset of the Medieval Warm Period (MWP). The E0-C stalagmite record from Áaktun Kóopo Cave is the first from the northeastern YP to show that this region also experienced drier climatic conditions during the TCP, aligning with previous findings from lacustrine records. Multi-proxy analysis of E0-C revealed significant shifts in soil-sensitive proxies, such as δ^{13}C values, U/Ca ratios, and DCF, indicating a notable transition in vegetation and soil conditions above the cave around 900/1000 AD.

Lower DCF and δ^{13}C values, combined with higher U/Ca ratios, suggest increased vegetation productivity and elevated soil pCO_2 concentrations following the TCP. Results from combined *CaveCalc* and Rainforest reverse modeling, conducted as part of Celine Kolb's master thesis (Kolb, 2024), support the idea that changes in soil CO_2 levels, system openness, and vegetation composition (C3/C4 plants), contributed to variations in δ^{13}C and DCF values, highlighting the sensitivity of carbonate formation to small changes in soil CO_2 and openness.

Although, there is no direct evidence of past agriculture above the cave, human activities like deforestation and cultivation may have affected the soil environment above Áaktun Kóopo Cave, contributing to the shifts in DCF, δ^{13}C values, and U/Ca ratios observed across the TCP.

Given that multiple proxy records across the YP indicate a shift toward wetter conditions around 900–1000 AD, which was likely driven by broader atmospheric and oceanic processes, including changes in tropical Atlantic SSTs. The concurrent increase in temperature and rainfall could have further influenced vegetation composition and soil respiration rates. This broader atmospheric reorganization, which likely initiated during the MWP, appears to have played a critical role in reshaping regional hydroclimate patterns.

The persistence of the observed shifts in the E0-C proxies and other records from the YP suggest a major change in regional climate patterns. Although it is challenging to disentangle natural and human influences, both clearly shaped the landscape during this period.

VI A Composite δ^{18}O Stalagmite Record for the Northeastern YP

In this chapter, a composite stalagmite proxy record for Áaktun Kóopo Cave is constructed by combining the stable isotope records of stalagmites E0-C, E1, and E23-3, whose age models were developed in Chapter III.2. This process includes tuning the individual age models through *wiggle matching*, which will result in slight adjustments to the age models of stalagmites E0-C and E1. The composite record is constructed specifically for δ^{18}O, as this isotope predominantly reflects precipitation amount and convective activity. Unlike δ^{13}C, which is influenced by multiple processes—such as vegetation type and density, rainfall amount, moisture availability, and in-cave processes like prior carbonate precipitation (PCP)—δ^{18}O provides a more straightforward indicator of hydroclimatic conditions.

This composite δ^{18}O record represents the first stalagmite-based reconstruction of hydroclimate variability over the last 1400 years for the northeastern Yucatán Peninsula (YP). Furthermore, constructing a δ^{18}O composite enables a direct comparison with other records from across the YP to identify similarities in variability and patterns and to examine the timescales on which these occur. Following this, a brief comparison is made between the composite δ^{18}O record from Áaktun Kóopo Cave and other stalagmite records from both the northern and southern YP. The chapter concludes with an evaluation of the physical processes and potential forcing mechanisms that may explain the observed hydroclimatic shifts (dry/wet periods) in the stalagmites over multidecadal to centennial timescales. This evaluation includes time series analyses of the proxy records (δ^{18}O), which are conducted using spectral and wavelet analyses.

VI.1 Composite Proxy Record Construction – Stalagmite Age-Model Tuning

For the construction of a composite proxy record from Áaktun Kóopo Cave, stalagmites E0-C, E1, and E23-3 were selected. Stalagmite E8 was excluded from this process due to high uncertainties in the ^{230}Th/U dating and its relatively short growth period (see Chapter III.2). The chronology of stalagmite E23-3 is considered the most reliable compared to stalagmites E0-C and E1, owing to the continuous counting of seasonal Sr/Ca cycles and the ability to anchor the layer-counted chronology to the age of the stalagmite's top, which corresponds to the year of extraction in 2022 (see Chapter III.2). Consequently, the E23-3 stalagmite record serves as the reference for the composite proxy record.

The stable oxygen isotope (δ^{18}O) records of stalagmites E0-C and E1 were aligned with the most reliable δ^{18}O record from stalagmite E23-3 through a ”wiggle matching” process using *QAnalySeries* software (Kotov and Pälike) considering the uncertainty in the age models developed in Chapter III.2.
The upper section of the E1 δ^{18}O record (3–61 mm dft) was tuned to the δ^{18}O record of stalagmite E23-3, with a total of 10 tie points chosen to achieve optimal alignment. The age model for the lower section of E1 was left unchanged, as it does not overlap with the E23-3 record.
Similarly, the upper section of the E0-C δ^{18}O record (5–38.6 mm depth from top) was matched to both the upper and lower sections of stalagmite E1, using 11 tie points. The period between approximately 620 and 1310 AD is represented solely by the data from stalagmite E0-C, as it is the only stalagmite covering this interval.

Within the uncertainties of the individual age models, the δ^{18}O and δ^{13}C values of stalagmites E0-C, E1, and E23-3 exhibit the same pattern over the past 600 years (Fig. VI.1). This coherence suggests that the stalagmites from Áaktun Kóopo Cave record the same environmental signals, indicating that carbonate precipitation occurred under equilibrium conditions.

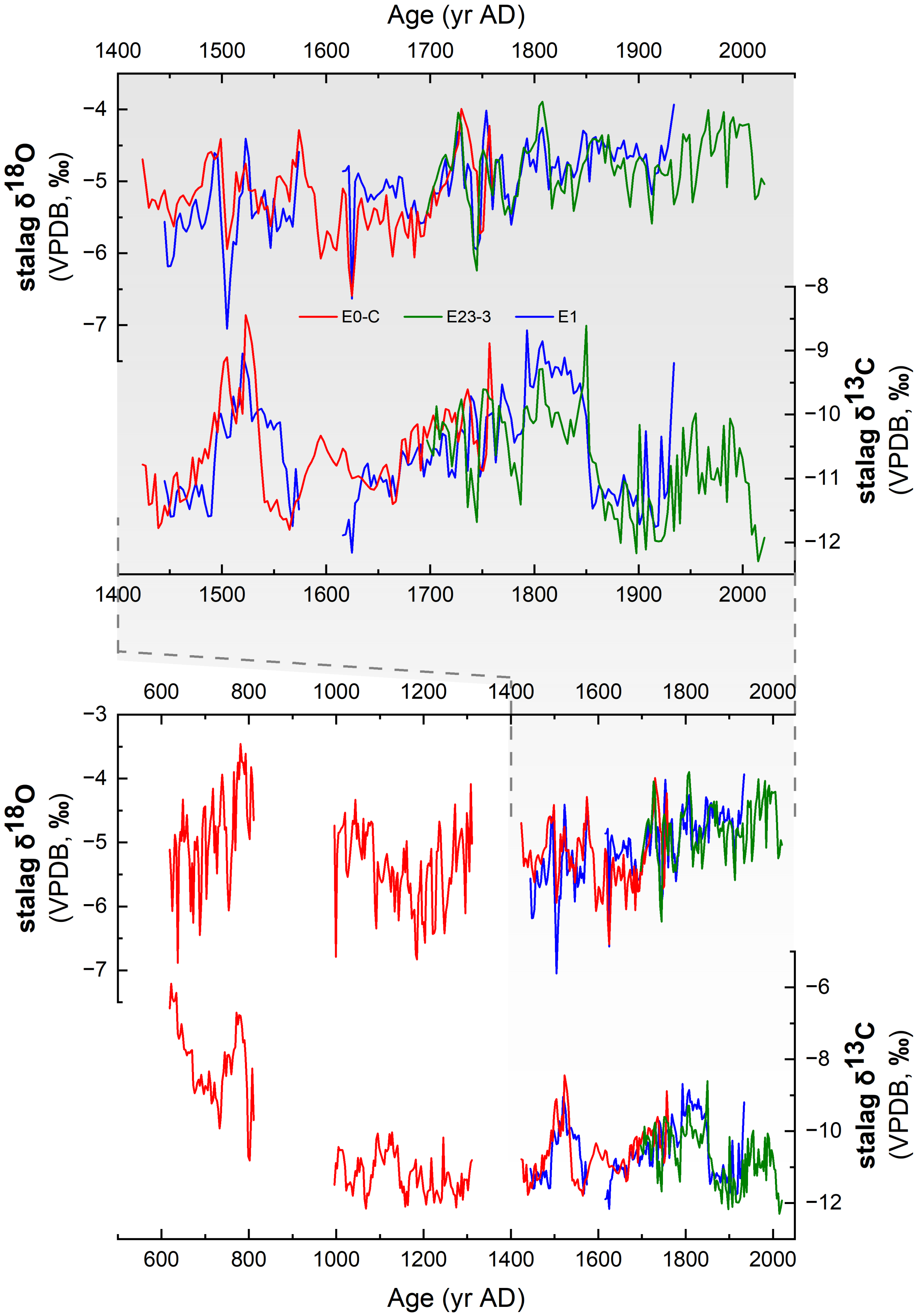

Figure VI.1. The composite δ^{18}O and δ^{13}C record, derived from stalagmites E0-C, E1, and E23-3, spans the last 1,400 years (bottom panel). A detailed view of the period from 1400 to 2022 AD is shown in the top panel.

VI.2 Normalization and Composite Record Calculation

In order to establish a single composite record out of the three individual records, each time series needs to be normalized. First the records were resampled using a spline algorithm implemented in Origin software to ensure a uniform temporal resolution. To achieve this, the step size (i.e., the time interval between consecutive data points) was selected based on the lowest temporal resolution among the three individual records, which resulted in a resampling interval of 3 years. Outliers were addressed by selecting a step size that retained 95% of the data within the sampling range. To standardize the records, z-scores were calculated for each proxy time series:

$$z = \frac{x - \overline{x}}{\sigma} \tag{VI.1}$$

where x represents the individual proxy measurement, $\overline{x}$ is the mean of the time series, and σ is the standard deviation. This transformation quantifies the deviation of each measurement from the mean, with positive z-scores indicating wetter conditions and negative z-scores indicating drier conditions relative to the average.

The resampled z-scores from each stalagmite record were then averaged to produce a composite paleoclimate proxy record for Áaktun Kóopo Cave, referred to as *AKC_comp* from this point forward (Fig. A13).

Stable oxygen isotopes (δ^{18}O) in stalagmites from the YP are typically interpreted as reflecting variations in rainfall amount, predominantly sourced from convective systems such as tropical cyclones and hurricanes (Lases-Hernández et al., 2020; Frappier, 2013; Vieten et al., 2018). More negative (positive) δ^{18}O values, and thus a negative (positive) z-score in the composite record, correspond to wetter (drier) conditions. Previous studies have been unsuccessful in correlating individual stalagmite δ^{18}O records across the YP, which is not unexpected given the spatial precipitation gradient that exists across the region today (De la Barreda et al., 2020). However, since all cave sites in the YP are subject to the same large-scale atmospheric and oceanographic processes, it is reasonable to assume that long-term hydrological changes, particularly those occurring on multidecadal to centennial timescales, may be recorded in these stalagmite records.

VI.3 Comparing Stalagmite δ^{18}O Records in the Yucatán Peninsula

To address this, I compare stalagmite δ^{18}O proxy records from the northern YP, specifically 'Chaac' (Medina-Elizalde et al., 2010), 'Tzab06-1' (James, 2023), and 'HOBO-5' (James, 2023), with the newly established composite record from Áaktun Kóopo Cave 'AKC_comp', all of which exhibit growth during some or all of the past 1,500 years. Additionally, I extend the comparison to records from the southern YP, including stalagmites YOK-I (Kennett et al., 2012) and YOK-G (Ridley et al., 2015; Asmerom et al., 2020).

Other existing stalagmite records, including VP-10-1 from Vaca Perdida Cave near the Maya site of Xcoch (Smyth et al., 2011, 2017a,b), stalagmite M1 from a cave beneath the central plaza of the Postclassic political center of Mayapan (Kennett et al., 2022), both in the northwestern YP, and MC-01 from Macal Chasm Cave on the Vaca Plateau in west-central Belize (Webster et al., 2007; Akers et al., 2016), were excluded from this comparison due to poor chronological control, low sampling resolution, or data unavailability.

The first part of this comparison focuses on examining the general range and variability of the individual δ^{18}O records. In the second part, a qualitative assessment of the normalized proxy records will be conducted to identify shared trends and differences in hydroclimate signals across the YP on multidecadal to centennial timescales.

Comparison with Northern YP Records

Stalagmite Chaac from Tzabnah Cave, near Tecoh located approximately 180 km west of Áaktun Kóopo Cave (Fig. 1), provided the first δ^{18}O record for the northern YP, covering the period between 478 and 2004 AD (Medina-Elizalde et al., 2010). Due to the stalagmite's low uranium content, the uncertainty of the U/Th-based age-depth model is ±70 years. However, Medina-Elizalde et al. (2010) claim to reduce this uncertainty to ±10 years for the period between 800 and 1000 AD by tuning the Chaac record to a high-resolution stalagmite record from Wanxiang Cave in subtropical China (Zhang et al., 2008), though no further explanation is provided regarding the teleconnections involved. With an average proxy resolution of 2.3 years (1 year between 800 and 940 AD), the Chaac stalagmite recorded eight positive δ^{18}O excursions between 810 and 938 AD. These excursions were interpreted as recurrent multi-year droughts (lasting between 3 and 18 years), with estimated precipitation reductions of approximately 36–52%, making them some of the most intense droughts of the last 1,500 years (Medina-Elizalde and Rohling, 2012; Medina-Elizalde et al., 2010).

Unfortunately, the period between 800 and 1000 AD (TCP), during which the Classic Maya civilization experienced profound changes, including a major population decline, is not captured within the stalagmites from Áaktun Kóopo Cave (AKC) analyzed so far. The composite record from AKC, which is based solely on stalagmite E0-C for the older period (~620–1440 AD), displays a hiatus between 811 ± 52 and 994 ± 29 AD (see III.2). However, just before this interruption in growth, the highest δ^{18}O values of the entire record (last 1,400 years) are observed (Fig. A15). The concurrent increase in Mg/Ca ratios, likely resulting from enhanced prior calcite precipitation (PCP) and/or water-rock interaction during this time (Fig. V.1), suggests severe dry conditions that may have also led to the cessation of growth. Although most of the TCP is absent in stalagmite E0-C, the pattern of hydroclimate proxies (δ^{18}O, Mg/Ca) at the onset of the TCP, immediately before stalagmite growth ceased and the hiatus itself, suggest that this period was among the driest recorded in the last 1,400 years.

The recently established paleoclimate record from stalagmite Tzab06-1, also from Tzabnah Cave, is the first to provide seasonal resolution spanning parts of the TCP (872–1103 AD) (James, 2023). The range in δ^{18}O values (−3.7 to −8.1‰) is similar to those of Chaac (−2.46 to −6.94‰) and AKC (−3.39 to −7.22‰). James (2023) detected ten wet-season (summer) droughts between 872 and 1103 AD, each lasting for three consecutive years or more, interspersed with equivalent intervals of years experiencing normal or enhanced wet-season precipitation.

Another recently established paleoclimate record comes from stalagmite HOBO-5, collected from Columnas Cave in the Puuc region, approximately 160 km southwest of Áaktun Kóopo Cave and 95 km southeast of Tzabnah Cave (James, 2023) (Fig. 1). Similar to the Chaac and AKC records, HOBO-5 spans the period from 544 to 2005 AD. The less variable and slightly more positive δ^{18}O values (−2.37 to −4.91‰) of HOBO-5, compared to both Chaac and AKC, may be attributed to a combination of Columnas Cave's location well above the water table, its thicker overburden, or a greater sampling interval (James, 2023). This could also explain why HOBO-5 records a single prolonged drought during the TCP, whereas Chaac and Tzab06-1 document a series of shorter, high-frequency droughts (James, 2023) (Fig. A15). The peak δ^{18}O values of HOBO-5 between 890 and 935 (±40) AD represent the most prominent excursion of the 1,500-year record, similar to the stable oxygen isotope records of both the Chaac stalagmite from Tzabnah Cave and the composite record from AKC.

These records indicate that the entire northern YP experienced the driest conditions of the past 1,500 years during the TCP (~800–1000 AD), a period during which some northern city centers, such as those in the Puuc region and other interior areas of the YP, experienced political collapse, while others, like the famous Chichén Itzá, continued to thrive until around 1000 to 1050 AD (Hoggarth et al., 2016).

The hiatus in the Tzab06-1 stalagmite from 1022 to 1067 AD, attributed to severe dry conditions (James, 2023), coincides with more positive δ^{18}O values in the Chaac stalagmite from the same cave (Medina-Elizalde et al., 2010). This period of extreme dry conditions also corresponds with a period of elevated δ^{18}O values in the stalagmites from Áaktun Kóopo Cave, although these values are not as pronounced as in periods before and after (Fig. A15).

Comparison with Southern YP Records

The stalagmites YOK-I and YOK-G from Yok Balum Cave in the southeastern YP, Belize, represent the stalagmite records with the best chronology and proxy resolution across the entire YP due to their aragonitic composition and high uranium content (Kennett et al., 2012; Ridley et al., 2015; Asmerom et al., 2020). However, these contemporaneously growing stalagmites do not show the same changes in δ^{18}O over the past 1,500 years, which usually indicates that the proxies are not solely driven by changes in the hydroclimate above the cave, and that kinetic effects might be at play as well. Nevertheless, they are among the most studied stalagmites of the Common Era in Central America (Kennett et al., 2012; Ridley et al., 2015; Asmerom et al., 2020; Jamieson et al., 2016; Lechleitner et al., 2016; Braun et al., 2023; Baldini et al., 2016; Lechleitner et al., 2019; Smirnov et al., 2017), though a clear explanation for the discrepancy in the paleoclimate proxies remains elusive. Therefore, I will briefly compare both stalagmites with the record from AKC in the following.

The δ^{18}O values of both YOK-I and YOK-G are slightly more positive (−3.8‰ on average) compared to those of AKC (−5.1‰ on average), except for the period leading into the TCP, when AKC exhibits its most positive values, and the period between roughly 1600 and 2000 AD, during which YOK-G shows similarly low δ^{18}O values and a slight long-term increase, mirroring the trend observed in AKC. The most prominent feature in the YOK-I record is the century-long dry period between approximately 1000 and 1100 AD, marked by a pronounced excursion to higher δ^{18}O values (A16) (Kennett et al., 2012), which aligns with the hiatus in Tzab06-1 (James, 2023), more positive δ^{18}O values in Chaac and elevated δ^{18}O values in the stalagmites from Áaktun Kóopo Cave (Fig. A15). These findings suggest that the 11th century may have experienced periods of drier conditions across large parts of the YP, with varying intensity and duration, despite a concurrent overall shift in hydroclimate toward wetter conditions (as discussed in Chapter V).

Normalization and Centennial-Scale Trends in Stalagmite δ^{18}O Records Across the Yucatán Peninsula

In order to qualitatively compare the previously mentioned stalagmite records from the northern and southern YP with the composite proxy record from Áaktun Kóopo Cave, the records were first normalized using the same method applied to the AKC composite record. To improve visualization of centennial-scale trends, I applied a 2nd order Savitzky-Golay filter with a window size of 50 points to the normalized records.

Plotting the z-scores of these records together reveals similar overall variance across stalagmites from both the northern and southern YP (Figs. VI.2 and VI.3), which is consistent on both multi-annual and centennial scales. This suggests that the climatic signals captured in these records may reflect regional-scale hydroclimate variability, while also allowing for site-specific influences.

The comparison highlights notable centennial-scale similarities, particularly between the HOBO-5 record from central northern Yucatán (James, 2023) and the 'AKC_comp' record, showing strong alignment in wet/dry fluctuations (Fig. VI.2a). In contrast, the 'Chaac' stalagmite from northwestern Yucatán exhibits different centennial-scale patterns (Fig. VI.2b). However, due to age model uncertainties, these records could potentially align if their chronologies were shifted within their respective uncertainty ranges.

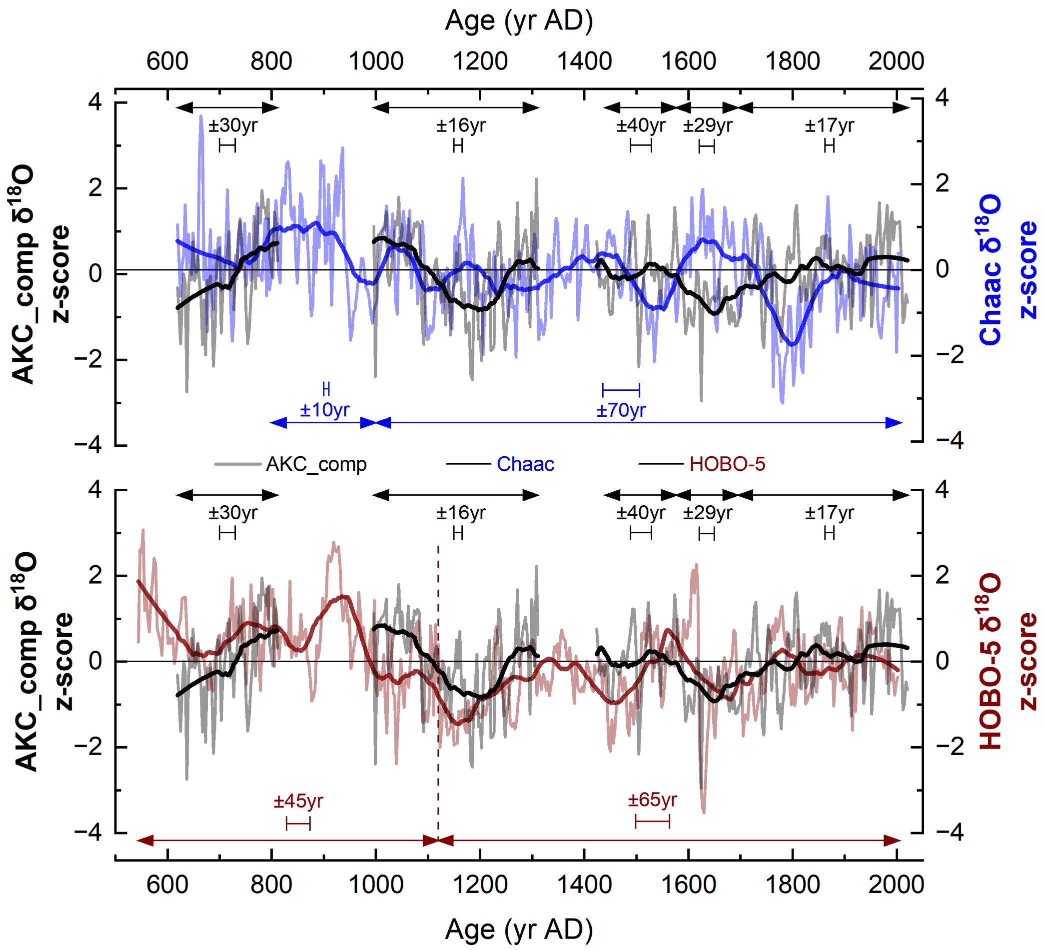

Figure VI.2. Z-score time series for δ^{18}O records of stalagmites from the northern Yucatán Peninsula over the past 1,400 years. The black line represents the δ^{18}O z-score record of 'AKC_comp' (this thesis), compared to the δ^{18}O z-score of stalagmite 'Chaac' in blue (top panel) (Medina-Elizalde et al., 2010) and 'HOBO-5' in brown (bottom panel) (James, 2023). Horizontal error bars indicate the uncertainty in the age model for each stalagmite record or for specific sections. To highlight centennial-scale trends, the normalized records were smoothed using a 2nd order Savitzky-Golay filter with a window size of 50 data points.

For stalagmite YOK-G from the southern YP, the centennial-scale wet/dry changes align more closely with the 'AKC_comp' record for the period between approximately 1400 and 2000 AD, suggesting that both sites experienced similar hydroclimatic conditions during this time. In contrast, stalagmite YOK-I exhibits similar long-term variability to the 'AKC_comp' record between 600 and 1300 AD but shows overall drier conditions from 1400 to 2000 AD, compared to both YOK-G and the 'AKC_comp' record, which indicate generally wetter conditions during this period. Although the two stalagmite records from Yok Balum Cave in Belize do not display identical changes in δ^{18}O over the past 1,500 years, they still share centennial-scale features with the records from the northern YP. This suggests that, despite some local variability, these records capture broad regional hydroclimate trends that appear consistent across the YP and surrounding areas on a centennial scale.

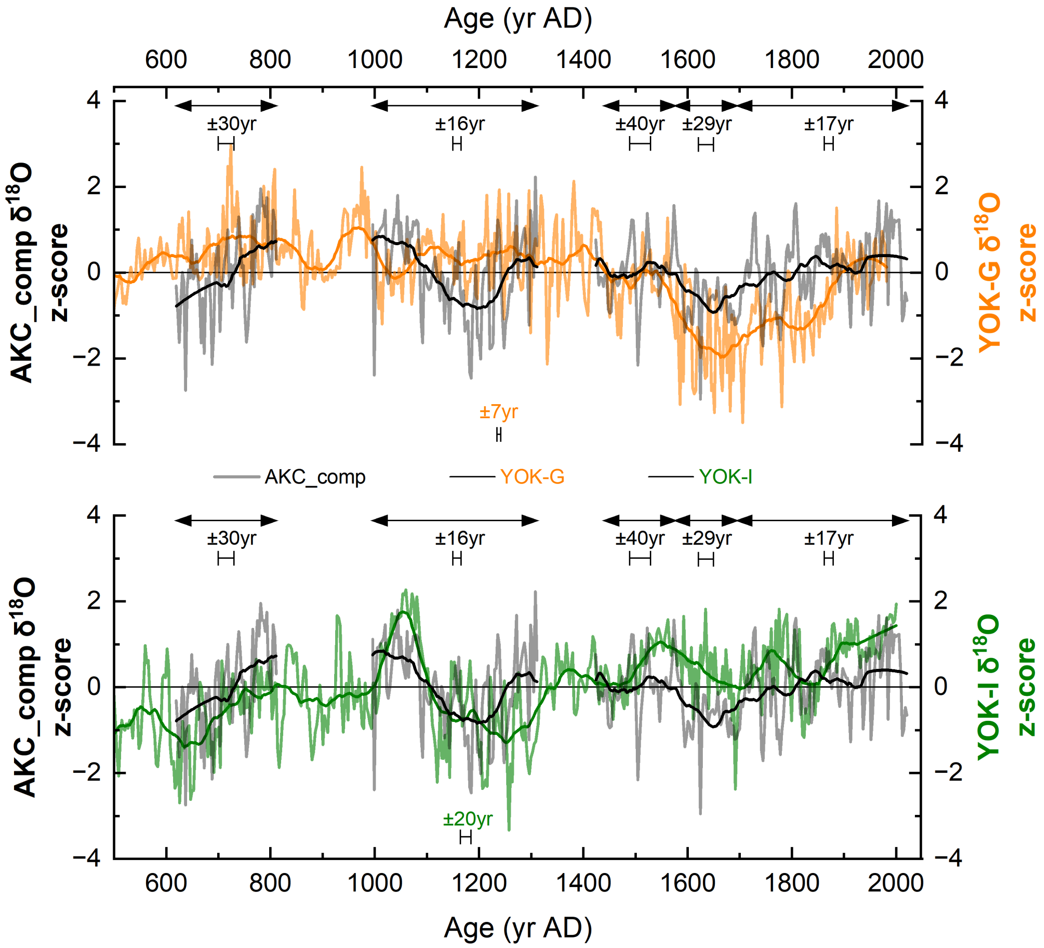

Figure VI.3. Z-score time series for δ^{18}O records of stalagmites from the southern Yucatán Peninsula over the past 1,400 years. The black line represents the δ^{18}O z-score record of 'AKC_comp' (this thesis), compared to the δ^{18}O z-score of stalagmite 'YOK-G' in orange (top panel) (Ridley et al., 2015; Asmerom et al., 2020) and 'YOK-I' in green (bottom panel) (Kennett et al., 2012). Horizontal error bars indicate the uncertainty in the age model for each stalagmite record or for specific sections. To highlight centennial-scale trends, the normalized records were smoothed using a 2nd order Savitzky-Golay filter with a window size of 50 data points.

One likely driver of these far-reaching changes in precipitation patterns over long time scales is the variation in sea surface temperatures (SSTs) of the tropical Atlantic, as discussed in Chapter V (Fig. A14), along with the associated latitudinal migration of the Intertropical Convergence Zone (ITCZ). These factors likely played a significant role in driving regional hydroclimate changes and influencing precipitation patterns across the YP and surrounding areas. This hypothesis is further supported by similar centennial-scale wet/dry fluctuations observed in a stalagmite record from Venezuela, located within the core region of the ITCZ (Medina et al., 2023)(Fig. VI.4). This is in contrast to the finding of Medina-Elizalde et al. (2010), who suggested that climate records from northern South America, such as the Cariaco Basin, Venezuela, may not serve as suitable analogs for the YP. However, the alignment of these patterns suggests a shared climatic driver, potentially related to tropical Atlantic SSTs and ITCZ shifts.

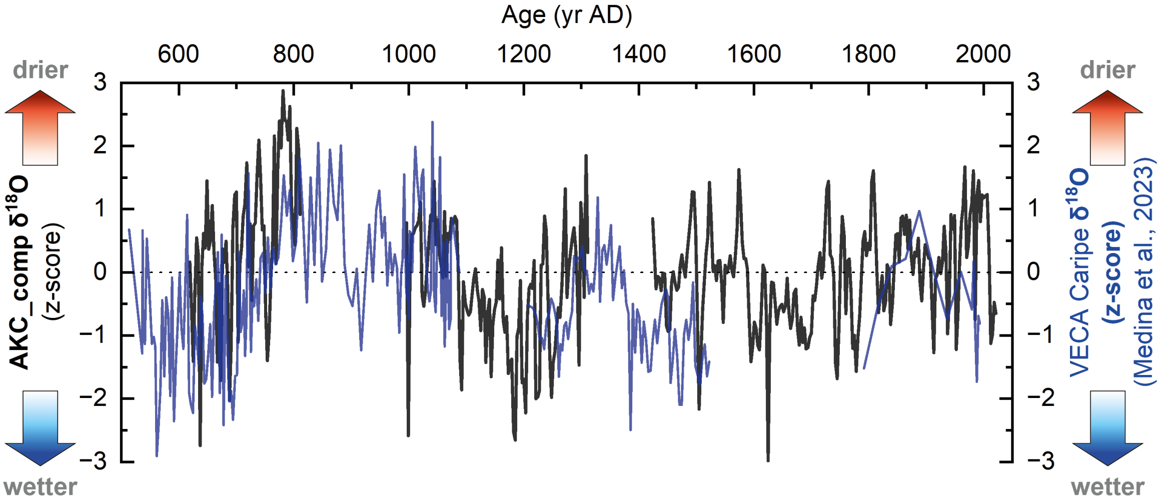

Figure VI.4. Z-score time series comparison of the δ^{18}O composite record from Áaktun Kóopo Cave (AKC) and the δ^{18}O record from stalagmite VECA Caripe, Venezuela (Medina et al., 2023) over the past 1,400 years. The black line represents the AKC δ^{18}O record, while the blue line shows the VECA Caripe δ^{18}O record. Positive z-scores in both records indicate drier conditions, while negative z-scores suggest wetter conditions. Both records exhibit a good alignment of centennial-scale hydroclimatic changes, suggesting a potential shared regional climatic driver influencing both the Yucatán Peninsula and northern South America.

VI.4 Spectral and Wavelet Analyses of the 'AKC_comp' Record

To further investigate the periodicities and time-frequency characteristics of the hydroclimatic signals observed in the 'AKC_comp' record, both spectral and wavelet analyses were applied. These methods provide insights into dominant periodicities over multiannual to centennial timescales and help to identify the temporal variability in the strength of these cycles.

The spectral power analysis of the 'AKC_comp' δ^{18}O record revealed significant periodicities on decadal (~13 years) and inter-decadal (~19 years) scales, as well as a centennial-scale periodicity (~250–300 years) (Fig. VI.5a). Results from the wavelet analysis show that decadal to inter-decadal periods are prominent throughout the past 1,400 years, except during gaps in the timeseries (Fig. VI.5b). In contrast, the centennial-scale variability is most pronounced between ~1000–1500 AD, which may partly result from edge effects that make variability less discernible outside this interval. These periodicities resemble known solar cycles, such as the 11-year Schwabe solar cycle (or sunspot cycle) and the 200–260-year de Vries/Suess solar cycle (Knudsen et al., 2009; Usoskin, 2017), suggesting a strong influence of solar forcing on the hydroclimate above Áaktun Kóopo Cave. Furthermore, these periodicities align with patterns typical of the El Niño–Southern Oscillation (ENSO), the Pacific Decadal Oscillation (PDO), and broader Pacific Decadal Variability (PDV) cycles (Hernández et al., 2020).

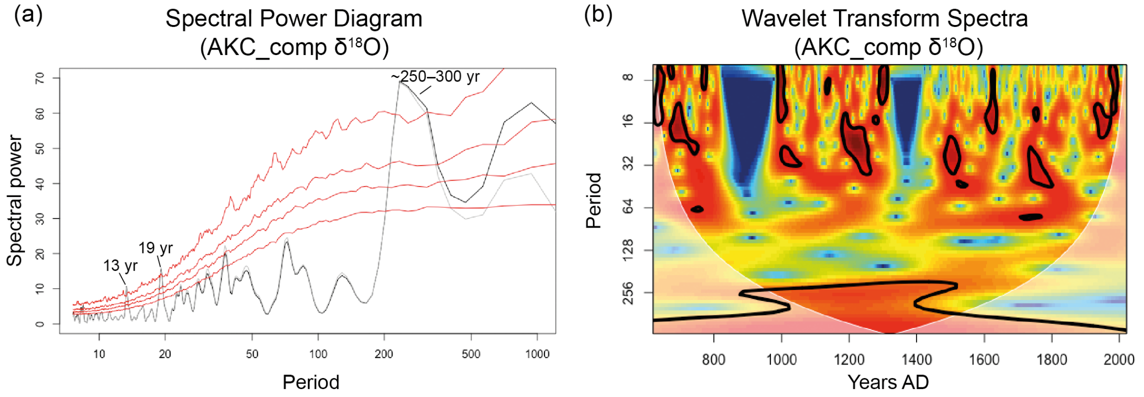

Figure VI.5. Time series analyses of the composite AKC δ^{18}O record. **(a)** Spectral power diagram of the AKC_comp δ^{18}O time series, down-sampled to a 3-year equidistant interval. The red lines indicate the calculated AR(1) false-alarm levels at 80%, 90%, 95%, and 99%, respectively. **(b)** Wavelet transform spectra for the AKC_comp δ^{18}O record, also down-sampled to a 3-year equidistant interval. Red (blue) colors correspond to high (low) transform coefficients (power). The blue areas between approximately 811–996 AD and 1311–1424 AD correspond to gaps in the AKC_comp δ^{18}O time series. Contour lines represent the 90% significance levels, while the white line marks the cone of influence, where edge effects become significant.

Solar activity, through the 'ocean dynamical thermostat' response, is known to influence SSTs in the Pacific, which in turn affect centennial-to-millennial scale shifts in the ENSO state (Clement et al., 1996; Marchitto et al., 2010). During periods of high solar activity, enhanced radiative forcing tends to promote La Niña-like conditions, resulting in cooler eastern Pacific SSTs and subsequently drier climatic conditions across Central America, including the YP (Marchitto et al., 2010). Consequently, episodes of increased solar activity may have driven prolonged drought periods in this region. This process may explain the observed connection between the 'AKC_comp' δ^{18}O record and reconstructed solar activity, reflected as changes in total solar irradiance (ΔTSI) (Steinhilber et al., 2009), over the period from ~1400–2000 AD (Fig. VI.6). However, this meachism does not appear to be stationary, and even reverses during the earlier MWP. Solar activity has also been suggested to influence Caribbean precipitation variability in a manner that could explain the observed reverse relationship between precipitation amount and solar activity. Specifically, this influence occurs through effects on tropical Atlantic SSTs and atmospheric circulation patterns (e.g., Bond et al., 2001; Jiang et al., 2015). Additionally, solar variability indirectly impacts the strength and position of the ITCZ and modulates the intensity of trade winds (Peterson et al., 1991). During times of weak (strong) solar activity, cooler (warmer) Atlantic SSTs and a southward (northward) shift of the ITCZ reduce (increase) rainfall across the YP and Caribbean realm.

With the stalagmites from Áaktun Kóopo Cave, there is now additional evidence of the potential influence of solar variability on Caribbean hydroclimate, as documented in numerous records from the late Holocene (e.g., Hodell et al., 2001; Medina-Elizalde et al., 2010; Vieten et al., 2024a) as well as from the early and mid-Holocene (Pollock et al., 2016; Warken et al., 2021; Stinnesbeck et al., 2017a; Tang et al., 2024). However, the connection appears to be non-stationary, as indicated by changes in the relationship between solar activity strength and precipitation amount.

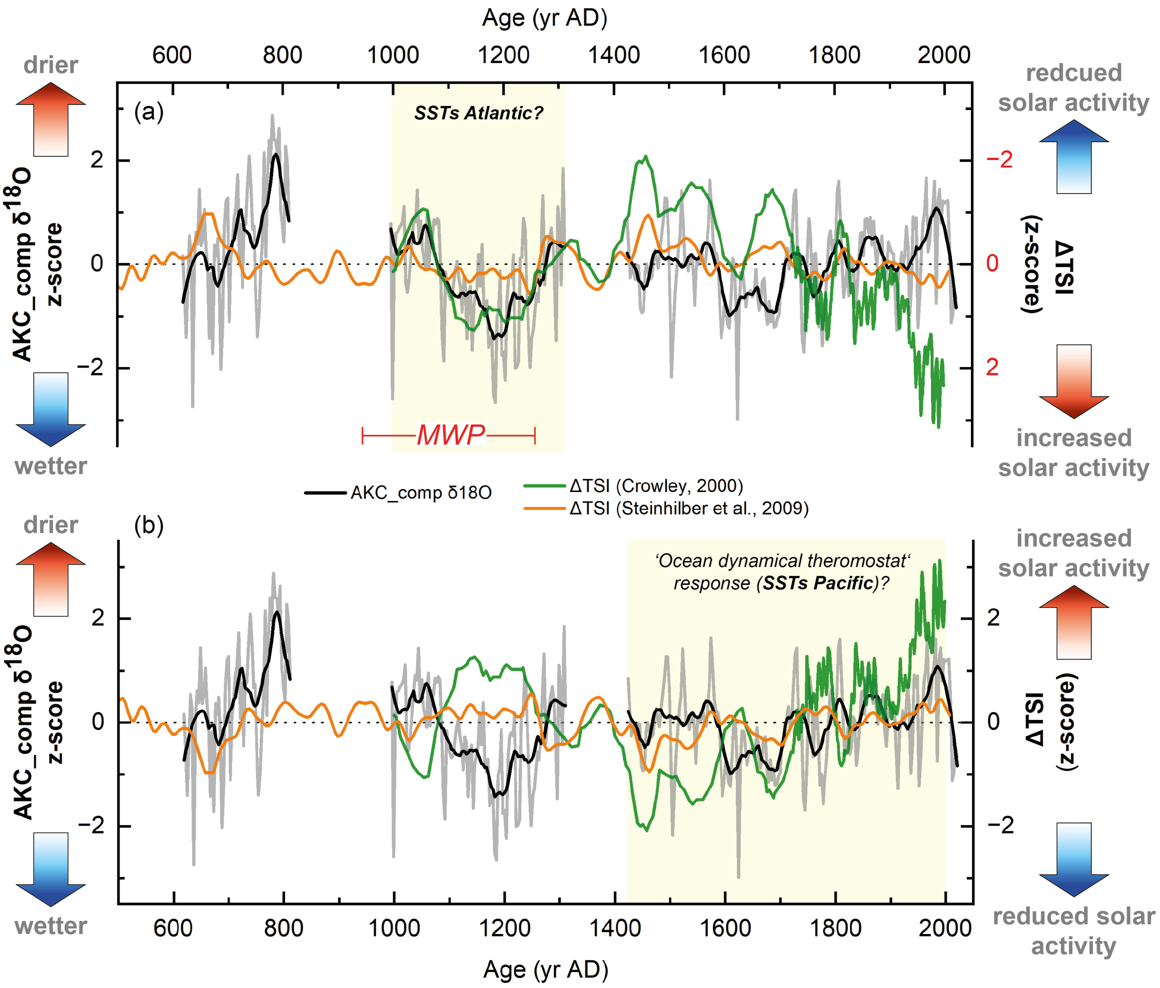

Figure VI.6. Z-score time series comparison of the $\delta^{18}O$ composite record from Áaktun Kóopo Cave (AKC) with different total solar irradiance (TSI) reconstructions based on ^{10}Be measurements from ice core records over the past 1,400 years (Steinhilber et al., 2009; Crowley, 2000) over the past 1,400 years. **(a)** The z-scores of the reconstructed TSIs are plotted inversely on the y-axis to highlight the contrasting relationship between solar activity strength and precipitation amount, as reflected by the AKC $\delta^{18}O$, during the Medieval Warm Period (MWP). **(b)** Same plot as in (a), but this time with both proxies aligned on the y-axis to highlight the direct relationship observed for the period between ~1400–2000 AD. This apparent shift in the connection between solar activity strength and precipitation amount suggests a non-stationary behavior, potentially driven by different influences of Atlantic and Pacific SSTs and their associated impacts on the ITCZ position and regional hydroclimate. For further explanation, see the text.

VI.5 Conclusions

The construction of a composite proxy record from Áaktun Kóopo Cave, based on stalagmites E0-C, E1, and E23-3, has provided a robust reconstruction of hydroclimate variability for the northeastern Yucatán Peninsula (YP) over the past 1,400 years. By aligning the individual δ^{18}O records of stalagmites E0-C and E1 with the well-dated and continuous record from E23-3, this study has produced a high-resolution proxy record of past rainfall variability. The strong coherence between the stable isotope records across the three stalagmites suggests these proxies reflect regional hydroclimate signals, with carbonate precipitation in the cave likely occurring under equilibrium conditions.

The analysis revealed prominent centennial-scale fluctuations in hydroclimate, such as the severe dry conditions leading to growth cessation in stalagmite E0-C around the onset of the Terminal Classic Period (TCP), as well as centennial-scale variability throughout the record. Additionally, the observed centennial-scale variability aligns with other paleoclimate records from the YP and Central America, indicating that these records likely respond to large-scale climatic drivers such as tropical Atlantic sea surface temperature (SST) variability and shifts in the Intertropical Convergence Zone (ITCZ). Spectral and wavelet analyses identified periodicities that match with known ENSO variability and solar cycles, including the 11-year Schwabe cycle and the 200–260-year de Vries/Suess cycle, supporting the idea that solar forcing may play a significant role in modulating Mesoamerican hydroclimate.

The findings also point to regional significance in these centennial-scale shifts, highlighted by the alignment with solar variability cycles that appear to exhibit non-stationary behavior. For instance, during the Medieval Warm Period (MWP), the relationship between solar activity and precipitation reverses, suggesting complex interactions between solar forcing, Atlantic SSTs, and ITCZ migration patterns. However, a longer, continuous record from the northern YP would be invaluable for better understanding broader climate patterns and distinguishing local effects from larger climate trends. Áaktun Kóopo Cave thus proves to be a highly sensitive site for recording hydroclimate variability over centuries to millennia, underscoring its importance for better understanding Mesoamerican climate patterns.

VII Conclusions and Outlook

This thesis provides new insights into the hydroclimatic and environmental history of the northeastern Yucatán Peninsula (YP) during the late Holocene through high-resolution, multi-proxy analysis of stalagmites from Áaktun Kóopo Cave. This site was selected for its unique location in an area of the peninsula that previously lacked high-resolution proxy records of hydroclimate and vegetation changes over the past 1,500 years, including the golden age of the Classic Maya Period, the political collapse during the Terminal Classic, and the Postclassic to Historic periods. Additionally, the cave contains significant Maya cultural remains, including multiple complete skeletons, making it an invaluable site for understanding the environmental context of human activity in the region.

Numerous ^{230}Th/U dates from these speleothems demonstrate continuous carbonate deposition over the past 2.7 kyr, encompassing the entire Maya era. High uranium concentrations in the stalagmites enabled precise dating, although the challenge of detrital contamination required careful correction, which was addressed by using high and variable (^{230}Th/^{232}Th) ratios, ranging between 3 and 68. The high growth rates of these stalagmites (averaging 200–300 µm a^{-1}) enabled the development of high-resolution multi-proxy records of past hydroclimate and vegetation changes. Using ultra-high resolution methods like trace element analysis with LA-ICP-MS and micromilled stable isotope sampling revealed clear seasonal cycles in element ratios, such as Sr/Ca, in some of the stalagmites, which helped to improve the accuracy of individual stalagmite chronologies.
The results from this study show that seasonal variations in trace element ratios (e.g., Sr/Ca, Na/Ca, U/Ca, P/Ca, and Cu/Ca) in the Áaktun Kóopo Cave stalagmites provide essential insights into how external climate conditions interact with internal cave processes. Prior calcite precipitation (PCP) and growth rate emerge as key drivers of speleothem geochemistry, as revealed through trace element and stable isotope analyses. Elements such as Sr, Ba, Na, and U are strongly coupled with growth rate on seasonal to interannual timescales, while Mg/Ca and δ^{13}C show an

inverse relationship with growth rate, highlighting the significant role of PCP. Stable oxygen isotopes ($\delta^{18}O$) in the analyzed stalagmites are interpreted as indicators of rainfall amount and the intensity of convective activity, consistent with findings from other stalagmite records across the YP and the broader Caribbean region. Moreover, these findings suggest that seasonal cave ventilation and precipitation patterns play a central role in controlling trace element incorporation.

Stalagmite E0-C makes an important contribution, as it provides the first multi-proxy stalagmite record from the northeastern YP. Although, much of the Terminal Classic Period (TCP; ∼800–1000 AD), during which the Classic Maya underwent profound societal changes and eventual collapse, is absent in this record due to a hiatus, hydroclimate-sensitive proxies ($\delta^{18}O$ and Mg/Ca) indicate peak aridity at the onset of the TCP, around 800 AD. These intense drought conditions may have led to the cessation in stalagmite growth, thus corroborating previous findings from lacustrine and speleothem records from other regions of the peninsula that indicate peak aridity during this period.

This research further demonstrated the potential of multi-proxy analysis in speleothem studies to track significant shifts in soil-sensitive proxies, including $\delta^{13}C$, U/Ca, and dead carbon fraction (DCF), which are thought to reflect changes in vegetation productivity, soil pCO_2 concentrations, and vegetation composition. A persistent shift in the mean values of these proxies in stalagmite E0-C across the TCP, indicates a pronounced transition in the vegetation and soil environment above Áaktun Kóopo Cave. Following the TCP, lower DCF and $\delta^{13}C$ values, combined with higher U/Ca ratios, suggest increased vegetation productivity and elevated soil pCO_2 concentrations at the onset of the Medieval Warm Period (MWP). Results from combined *CaveCalc* and Rainforest reverse modeling, conducted as part of Celine Kolb's master thesis (Kolb, 2024), support the idea that changes in soil CO_2 levels, system openness, and vegetation composition (C3/C4 plant ratios), contributed to the observed changes in stalagmite $\delta^{13}C$ and DCF values.

Although, there is no direct evidence of past agriculture above Áaktun Kóopo Cave, human activities like deforestation and cultivation may have affected the soil environment, potentially contributing to the observed shifts in DCF, $\delta^{13}C$ values, and U/Ca ratios across the TCP. The observation that multiple proxy records across the YP indicate a shift toward wetter conditions around 900–1000 AD, suggests a possible large-scale atmospheric reorganization, which was likely driven by changes in tropical Atlantic sea surface temperatures (SSTs) and trade wind patterns. The persistence of these shifts in the E0-C proxies, as well as in other YP records, reinforces the significance of this climatic transition.

In the last part of this thesis, I aligned the δ^{18}O records of stalagmites E0-C, E1, and E23-3 from Áaktun Kóopo Cave to produce a high-resolution composite record of past rainfall variability for the northeastern YP over the past 1,400 years. The consistency among these stable isotope records suggests that these proxies reliably reflect regional environmental signals and that carbonate precipitation in the cave likely occurred under equilibrium conditions, thus enhancing the robustness of this composite record. This composite record captures prominent centennial-scale fluctuations in hydroclimate, and shows variability consistent with other paleoclimate records from the YP and Central America. These findings indicate that Mesoamerican hydroclimate has been significantly influenced by large-scale climatic drivers, including tropical Atlantic (Pacific) SST variability and shifts in the Intertropical Convergence Zone (ITCZ). Spectral analysis further identified periodicities associated with ENSO variability and solar cycles, suggesting that solar forcing, through mechanisms like the 11-year Schwabe cycle and the 200–260-year de Vries/Suess cycle, may have influenced hydroclimatic conditions across the YP.

During periods such as the MWP, the record suggests complex interactions between solar activity, Atlantic SSTs, and ITCZ migration patterns, with evidence of non-stationary behavior in the relationship between solar activity and precipitation. This points to the importance of regional responses to global climate drivers, emphasizing the potential for Áaktun Kóopo Cave to serve as a sensitive archive for hydroclimatic variability over centennial to millennial timescales. Extending these analyses to a longer, continuous record would further enhance our understanding of Mesoamerican climate dynamics, allowing for greater distinction between local and regional climate influences within broader climate trends.

Outlook

The research presented in this thesis has provided new insights into hydroclimatic and environmental changes in the northeastern YP over the last ∼1,400 years. While the speleothems from Áaktun Kóopo Cave have demonstrated their suitability for reconstructing past hydrological and environmental conditions at high resolution, given their moderate uranium concentrations, challenges persist due to elevated and variable (^{230}Th/^{232}Th) activity ratios needed for correcting ^{230}Th/U ages. Over the past two decades, there has been a notable increase in studies acknowledging or addressing these elevated (^{230}Th/^{232}Th) activity ratios in speleothems, especially in tropical regions like the Caribbean. However, despite ratios being up to 80 times higher than the commonly applied value for the upper continental crust, a definitive explanation for these elevated levels remains elusive and is rarely directly addressed. The exact sources and mechanisms of detrital thorium and its variability within tropical carbonates are poorly understood, complicating efforts to produce highly accurate age models for tropical speleothems.

Future research should focus on enhancing the precision of detrital Th corrections to improve the reliability of age models, with a focus on isolating sources of thorium contamination within the cave environment. This may involve more detailed geochemical characterizations of the surrounding cave sediments, as well as systematic comparisons across regional cave systems to assess whether certain geologic or environmental factors correlate with the presence of elevated ^{230}Th.

As noted in this work, the stalagmite records analyzed from Áaktun Kóopo Cave currently do not capture the TCP. Given the significance of this period, it is crucial to fill this gap in order to gain a more comprehensive understanding of the hydroclimatic and environmental conditions during the TCP in the northeastern YP, as well as to assess how these conditions may have influenced the Classic Maya in this region. Adressing this gap would further improve interpretations of the observed shifts in soil-sensitive proxies across the TCP. Detailed knowledge of the timing and length of this transition is crucial to better understand the mechanisms driving these shifts and to separate human- from climate-related influences on the environment. There are still a few promising stalagmites in Áaktun Kóopo Cave that could potentially capture this significant period of interest.

As the constructed stalagmite chronologies from Áaktun Kóopo Cave reach back to the Early Preclassic Period (∼1000 BC), there is substantial potential to extend the current composite δ^{18}O record—which spans the last 1,400 years—further back in time. This would create the first high-resolution, single-cave composite δ^{18}O record from the northern YP, covering the last 3,000 years and, with it, the entire era of Maya cultural development. By including additional proxies such as δ^{13}C, DCF, and Mg/Ca alongside δ^{18}O, this extended record could serve as a benchmark for hydroclimate variability and environmental changes throughout Maya evolution in the region.

Furthermore, as variations in precipitation amount and/or convective activity appear to covary with other stalagmite records from the YP and beyond, particularly on centennial timescales, it may eventually be feasible to combine hydroclimate records from multiple locations. This would support the development of a regional hydroclimate synthesis for the YP, and potentially the broader Mesoamerican region, though this may be limited to centennial or millennial timescales.

List of Publications of the Author

- **Schorndorf, N.**, Frank, N., Ritter, S.M. et al. Mid- to late Holocene sea-level rise recorded in Hells Bells 234U/238U ratio and geochemical composition. Sci Rep 13, 10011 (2023). `https://doi.org/10.1038/s41598-023-36777-y`

- Ifrim C., Stinnesbeck W., González González A.H., **Schorndorf N.**, Gale A.S. (2021). Ontogeny, evolution and palaeogeographic distribution of the world's largest ammonite Parapuzosia (P.) seppenradensis (Landois, 1895). PLoS One 16(11): e0258510. `https://doi.org/10.1371/journal.pone.0258510`

- Steidle, S.D., Warken, S. F., **Schorndorf, N.**, Förstel, J., Schröder-Ritzrau, A., Moseley, G.E., et al. (2021). Reconstruction of Middle to Late Quaternary sea level using submerged speleothems from the northeastern Yucatán Peninsula. Journal of Quaternary Science, `https://doi.org/10.1002/jqs.3365`

- Warken, S. F., **Schorndorf, N.**, Stinnesbeck, W., Hennhoefer, D., Stinnesbeck, S., Förstel, J., Steidle, S.D., Avilés Olguin, J., and Frank, N. (2021). Solar Forcing of Early Holocene Droughts on the Yucatán Peninsula, Scientific Reports 11, 13885, `https://doi.org/10.1038/s41598-021-93417-z`

- Stinnesbeck, W., Rennie, S. R., Avilés Olguín, J., Stinnesbeck, S. R., Gonzalez, S., Frank, N., Warken, S.F., **Schorndorf, N.**, Krengel, T., Velázquez Morlet., A., González González, A. (2020). New evidence for an early settlement of the Yucatán Peninsula, Mexico: The Chan Hol 3 woman and her meaning for the Peopling of the Americas. PLoS One, 15(2), `https://doi.org/10.1371/journal.pone.0227984`

- Ritter S.M., Isenbeck-Schroter M., Scholz C., Keppler F., Gescher J., Klose L., **Schorndorf N.**, Olguín J.A., González-González A., Stinnesbeck W. (2019). Subaqueous speleothems (Hells Bells) formed by the interplay of pelagic redoxcline biogeochemistry and specific hydraulic conditions in the El Zapote sinkhole, Yucatan Peninsula, Mexico. Biogeosciences, 16(11), 2285-305. `https://doi.org/10.5194/bg-16-2285-2019`

- Zell, P., Stinnesbeck, W., Hennhoefer, D., Al Suwaidi, A., Brysch, S., Gruber, G., **Schorndorf, N.** (2019). Repeated turnovers in Late Jurassic faunal assemblages of the Gulf of Mexico: Correlation with cold ocean water. Journal of South American Earth Sciences, 91, 1-7. `https://doi.org/10.1016/j.jsames.2019.01.008`

Bibliography

William Cruse Ward. *Quaternary Geology of Northeastern Yucatan Peninsula*, page 1–19. NOGS Publication, New Orleans, 1985.

P. M. Douglas, M. Pagani, M. A. Canuto, M. Brenner, D. A. Hodell, T. I. Eglinton, and J. H. Curtis. Drought, agricultural adaptation, and sociopolitical collapse in the maya lowlands. *Proc Natl Acad Sci U S A*, 112(18):5607–12, 2015. ISSN 1091-6490 (Electronic) 0027-8424 (Linking). doi: 10.1073/pnas.1419133112.

Bertina J A. Arellano Hernández Olmedo Vera, Mexico: Consejo Nacional para la Cultura y las Artes . The Mayas of the Classic Period. Mexico City, and et al. The maya of the classic period. pages 9–99, 1997. (CONACULTA).

John WG Lowe. *The dynamics of apocalypse: a systems simulation of the classic Maya collapse.* University of New Mexico Press Albuquerque, 1985. ISBN 0826307655.

G. H. Haug, D. Gunther, L. C. Peterson, D. M. Sigman, K. A. Hughen, and B. Aeschlimann. Climate and the collapse of maya civilization. *Science*, 299 (5613):1731–5, 2003. ISSN 1095-9203 (Electronic) 0036-8075 (Linking). doi: 10.1126/science.1080444.

D. J. Kennett, S. F. Breitenbach, V. V. Aquino, Y. Asmerom, J. Awe, J. U. Baldini, P. Bartlein, B. J. Culleton, C. Ebert, C. Jazwa, M. J. Macri, N. Marwan, V. Polyak, K. M. Prufer, H. E. Ridley, H. Sodemann, B. Winterhalder, and G. H. Haug. Development and disintegration of maya political systems in response to climate change. *Science*, 338(6108):788–91, 2012. ISSN 1095-9203 (Electronic) 0036-8075 (Linking). doi: 10.1126/science.1226299.

J. H. Curtis, D. A. Hodell, and M. Brenner. Climate variability on the yucatan peninsula (mexico) during the past 3500 years, and implications for maya cultural evolution. *Quaternary Research*, 46(1):37–47, 1996. ISSN 0033-5894. doi: 10.1006/qres.1996.0042.

G. H. Haug, K. A. Hughen, D. M. Sigman, L. C. Peterson, and U. Rohl. Southward migration of the intertropical convergence zone through the holocene. *Science*, 293 (5533):1304–8, 2001. ISSN 0036-8075 (Print) 0036-8075 (Linking). doi: 10.1126/science.1059725.

M. Medina-Elizalde and E. J. Rohling. Collapse of classic maya civilization related to modest reduction in precipitation. *Science*, 335(6071):956–9, 2012. ISSN 1095-9203 (Electronic) 0036-8075 (Linking). doi: 10.1126/science.1216629.

P. M. J. Douglas, A. A. Demarest, M. Brenner, and M. A. Canuto. Impacts of climate change on the collapse of lowland maya civilization. *Annual Review of Earth and Planetary Sciences, Vol 44*, 44(1):613–645, 2016. ISSN 0084-6597. doi: 10.1146/annurev-earth-060115-012512.

Julie Hoggarth, Matthew Restall, James W. Wood, and Douglas J. Kennett. *Drought and Its Demographic Effects in the Maya Lowlands*, volume 58. 2017. doi: 10.1086/690046.

N. P. Evans, T. K. Bauska, F. Gazquez-Sanchez, M. Brenner, J. H. Curtis, and D. A. Hodell. Quantification of drought during the collapse of the classic maya civilization. *Science*, 361(6401):498–501, 2018. ISSN 1095-9203 (Electronic) 0036-8075 (Linking). doi: 10.1126/science.aas9871.

N. P. Dunning, T. P. Beach, and S. Luzzadder-Beach. Kax and kol: collapse and resilience in lowland maya civilization. *Proc Natl Acad Sci U S A*, 109(10):3652–7, 2012. ISSN 1091-6490 (Electronic) 0027-8424 (Print) 0027-8424 (Linking). doi: 10.1073/pnas.1114838109.

D. A. Hodell, M. Brenner, J. H. Curtis, and T. Guilderson. Solar forcing of drought frequency in the maya lowlands. *Science*, 292(5520):1367–70, 2001. ISSN 0036-8075 (Print) 0036-8075 (Linking). doi: 10.1126/science.1057759.

D. A. Hodell, M. Brenner, and J. H. Curtis. Terminal classic drought in the northern maya lowlands inferred from multiple sediment cores in lake chichancanab (mexico). *Quaternary Science Reviews*, 24(12-13):1413–1427, 2005. ISSN 0277-3791. doi: 10.1016/j.quascirev.2004.10.013.

D. A. Hodell, M. Brenner, and J. H. Curtis. Climate and cultural history of the northeastern yucatan peninsula, quintana roo, mexico. *Climatic Change*, 83(1-2): 215–240, 2007. ISSN 0165-0009. doi: 10.1007/s10584-006-9177-4.

M. F. Rosenmeier, D. A. Hodell, M. Brenner, J. H. Curtis, and T. P. Guilderson. A 4000-year lacustrine record of environmental change in the southern maya lowlands, peten, guatemala. *Quaternary Research*, 57(2):183–190, 2002. ISSN 0033-5894. doi: 10.1006/qres.2001.2305.

D. Wahl, R. Byrne, T. Schreiner, and R. Hansen. Palaeolimnological evidence of late-holocene settlement and abandonment in the mirador basin, peten, guatemala. *Holocene*, 17(6):813–820, 2007. ISSN 0959-6836. doi: 10.1177/0959683607080522.

J. W. Webster, G. A. Brook, L. B. Railsback, H. Cheng, R. L. Edwards, C. Alexander, and P. P. Reeder. Stalagmite evidence from belize indicating significant droughts at the time of preclassic abandonment, the maya hiatus, and the classic maya collapse. *Palaeogeography Palaeoclimatology Palaeoecology*, 250(1-4):1–17, 2007. ISSN 0031-0182. doi: 10.1016/j.palaeo.2007.02.022.

D. A. Hodell, J. H. Curtis, and M. Brenner. Possible role of climate in the collapse of classic maya civilization. *Nature*, 375(6530):391–394, 1995. ISSN 0028-0836. doi: 10.1038/375391a0.

Alejandro Antonio Aragón-Moreno, Gerald A. Islebe, and Nuria Torrescano-Valle. A 3800-yr, high-resolution record of vegetation and climate change on the north coast of the yucatan peninsula. *Review of Palaeobotany and Palynology*, 178:35–42, 2012. ISSN 00346667. doi: 10.1016/j.revpalbo.2012.04.002.

A. A. Vela-Pelaez, N. Torrescano-Valle, G. A. Islebe, J. F. Mas, and H. Weissenberger. Holocene precipitation changes in the maya forest, yucatan peninsula, mexico. *Palaeogeography Palaeoclimatology Palaeoecology*, 505:42–52, 2018. ISSN 0031-0182. doi: 10.1016/j.palaeo.2018.05.024.

Nathan D. Stansell, Byron A. Steinman, Matthew S. Lachniet, Jacob Feller, William Harvey, Alejandro Fernandez, Christopher J. Shea, Brittany Price, Jason Coenen, Maxwell Boes, and Stephen Perdziola. A lake sediment stable isotope record of late-middle to late holocene hydroclimate variability in the western guatemala highlands. *Earth and Planetary Science Letters*, 542:116327, 2020. ISSN 0012-821X. doi: https://doi.org/10.1016/j.epsl.2020.116327.

M. Medina-Elizalde, S. J. Burns, D. W. Lea, Y. Asmerom, L. von Gunten, V. Polyak, M. Vuille, and A. Karmalkar. High resolution stalagmite climate record from the yucatan peninsula spanning the maya terminal classic period. *Earth and Planetary Science Letters*, 298(1-2):255–262, 2010. ISSN 0012-821x. doi: 10.1016/j.epsl.2010.08.016.

Matthew S. Lachniet, Juan Pablo Bernal, Yemane Asmerom, Victor Polyak, and Dolores Piperno. A 2400 yr mesoamerican rainfall reconstruction links climate and cultural change. *Geology*, 40(3):259–262, 2012. ISSN 1943-2682 0091-7613. doi: 10.1130/g32471.1.

P. D. Akers, G. A. Brook, L. B. Railsback, F. Y. Liang, G. Iannone, J. W. Webster, P. P. Reeder, H. Cheng, and R. L. Edwards. An extended and higher-resolution record of climate and land use from stalagmite mc01 from macal chasm, belize, revealing connections between major dry events, overall climate variability, and maya sociopolitical changes. *Palaeogeography Palaeoclimatology Palaeoecology*, 459: 268–288, 2016. ISSN 0031-0182. doi: 10.1016/j.palaeo.2016.07.007.

H. C. Wu, T. Felis, D. Scholz, C. Giry, M. Kolling, K. P. Jochum, and S. R. Scheffers. Changes to yucatan peninsula precipitation associated with salinity and temperature extremes of the caribbean sea during the maya civilization collapse. *Sci Rep*, 7(1):15825, 2017. ISSN 2045-2322 (Electronic) 2045-2322 (Linking). doi: 10.1038/s41598-017-15942-0.

D. W. Stahle, J. V. Diaz, D. J. Burnette, J. C. Paredes, R. R. Heim, F. K. Fye, R. A. Soto, M. D. Therrell, M. K. Cleaveland, and D. K. Stahle. Major mesoamerican droughts of the past millennium. *Geophysical Research Letters*, 38(5), 2011. ISSN 0094-8276. doi: ArtnL0570310.1029/2010gl046472.

Daniel James. *Speleothem Palaeoclimatology in the Maya Lowlands of Northwestern Yucatán, Mexico.* Dissertation, Apollo - University of Cambridge Repository, 2023.

M. Medina-Elizalde, S. J. Burns, J. M. Polanco-Martínez, T. Beach, F. Lases-Hernández, C. C. Shen, and H. C. Wang. High-resolution speleothem record of precipitation from the yucatan peninsula spanning the maya preclassic period. *Global and Planetary Change*, 138:93–102, 2016a. ISSN 0921-8181. doi: 10.1016/j.gloplacha.2015.10.003.

H. E. Ridley, Y. Asmerom, J. U. L. Baldini, S. F. M. Breitenbach, V. V. Aquino, K. M. Prufer, B. J. Culleton, V. Polyak, F. A. Lechleitner, D. J. Kennett, M. H. Zhang, N. Marwan, C. G. Macpherson, L. M. Baldini, T. Y. Xiao, J. L. Peterkin, J. Awe, and G. H. Haug. Aerosol forcing of the position of the intertropical convergence zone since ad 1550. *Nature Geoscience*, 8(3):195–200, 2015. ISSN 1752-0894. doi: 10.1038/Ngeo2353.

Y. Asmerom, J. U. L. Baldini, K. M. Prufer, V. J. Polyak, H. E. Ridley, V. V. Aquino, L. M. Baldini, S. F. M. Breitenbach, C. G. Macpherson, and D. J. Kennett. Intertropical convergence zone variability in the neotropics during the common era.

Sci Adv, 6(7):eaax3644, 2020. ISSN 2375-2548 (Electronic) 2375-2548 (Linking). doi: 10.1126/sciadv.aax3644.

B. L. Turner and J. A. Sabloff. Classic period collapse of the central maya lowlands: insights about human-environment relationships for sustainability. *Proc Natl Acad Sci U S A*, 109(35):13908–14, 2012. ISSN 1091-6490 (Electronic) 0027-8424 (Print) 0027-8424 (Linking). doi: 10.1073/pnas.1210106109.

A. L. Pollock, P. E. van Beynen, K. L. DeLong, V. Polyak, Y. Asmerom, and P. P. Reeder. A mid-holocene paleoprecipitation record from belize. *Palaeogeography, Palaeoclimatology, Palaeoecology*, 463:103–111, 2016. ISSN 00310182. doi: 10.1016/j.palaeo.2016.09.021.

F. A. Lechleitner, S. F. Breitenbach, K. Rehfeld, H. E. Ridley, Y. Asmerom, K. M. Prufer, N. Marwan, B. Goswami, D. J. Kennett, V. V. Aquino, V. Polyak, G. H. Haug, T. I. Eglinton, and J. U. Baldini. Tropical rainfall over the last two millennia: evidence for a low-latitude hydrologic seesaw. *Sci Rep*, 7:45809, 2017. ISSN 2045-2322 (Electronic) 2045-2322 (Linking). doi: 10.1038/srep45809.

Jessica L Oster, Sophie F Warken, Natasha Sekhon, Monica M Arienzo, and Matthew Lachniet. Speleothem paleoclimatology for the caribbean, central america, and north america. *Quaternary*, 2(1):5, 2019.

K. Nooren, W. Z. Hoek, B. J. Dermody, D. Galop, S. Metcalfe, G. Islebe, and H. Middelkoop. Climate impact on the development of pre-classic maya civilisation. *Climate of the Past*, 14(8):1253–1273, 2018. ISSN 1814-9324. doi: 10.5194/cp-14-1253-2018.

V. L. Scarborough and G. G. Gallopin. A water storage adaptation in the maya lowlands. *Science*, 251(4994):658–62, 1991. ISSN 0036-8075 (Print) 0036-8075 (Linking). doi: 10.1126/science.251.4994.658.

Tripti Bhattacharya, Samantha Krause, Dan Penny, and David Wahl. Drought and water management in ancient maya society. *Progress in Physical Geography: Earth and Environment*, 47(2):189–204, 2022. ISSN 0309-1333 1477-0296. doi: 10.1177/03091333221129784.

S. F. Warken, J. Fohlmeister, A. Schröder-Ritzrauh, S. Constantin, C. Spötl, A. Gerdes, J. Esper, N. Frank, J. Arps, M. Terente, D. F. C. Riechelmann, A. Mangini, and D. Scholz. Reconstruction of late holocene autumn/winter precipitation variability in sw romania from a high-resolution speleothem trace element record. *Earth and Planetary Science Letters*, 499:122–133, 2018. ISSN 0012-821x. doi: 10.1016/j.epsl.2018.07.027.

Gabriela Serrato-Marks, Martín Medina-Elizalde, Stephen Burns, Syee Weldeab, Fernanda Lases-Hernandez, Gabriela Cazares, and David McGee. Evidence for decreased precipitation variability in the yucatán peninsula during the mid-holocene. *Paleoceanography and Paleoclimatology*, 36(5):e2021PA004219, 2021. ISSN 2572-4517. doi: 10.1029/2021PA004219.

Rolf Vieten, Sophie F. Warken, Davide Zanchettin, Amos Winter, Denis Scholz, David Black, Gabriella Koltai, and Christoph Spötl. Northeastern caribbean rainfall variability linked to solar and volcanic forcing. *Paleoceanography and Paleoclimatology*, 39(4):e2023PA004720, 2024a. ISSN 2572-4517 2572-4525. doi: 10.1029/2023pa004720.

R. A. Jamieson, J. U. L. Baldini, M. J. Brett, J. Taylor, H. E. Ridley, C. J. Ottley, K. M. Prufer, J. A. Wassenburg, D. Scholz, and S. F. M. Breitenbach. Intra- and inter-annual uranium concentration variability in a belizean stalagmite controlled by prior aragonite precipitation: A new tool for reconstructing hydro-climate using aragonitic speleothems. *Geochimica Et Cosmochimica Acta*, 190:332–346, 2016. ISSN 0016-7037. doi: 10.1016/j.gca.2016.06.037.

F. A. Lechleitner, J. U. L. Baldini, S. F. M. Breitenbach, J. Fohlmeister, C. McIntyre, B. Goswami, R. A. Jamieson, T. S. van der Voort, K. Prufer, N. Marwan, B. J. Culleton, D. J. Kennett, Y. Asmerom, V. Polyak, and T. I. Eglinton. Hydrological and climatological controls on radiocarbon concentrations in a tropical stalagmite. *Geochimica Et Cosmochimica Acta*, 194:233–252, 2016. ISSN 0016-7037. doi: 10.1016/j.gca.2016.08.039.

S. F. Warken, N. Schorndorf, W. Stinnesbeck, D. Hennhoefer, S. R. Stinnesbeck, J. Forstel, S. D. Steidle, J. Aviles Olguin, and N. Frank. Solar forcing of early holocene droughts on the yucatan peninsula. *Sci Rep*, 11(1):13885, 2021. ISSN 2045-2322 (Electronic) 2045-2322 (Linking). doi: 10.1038/s41598-021-93417-z.

P. Treble, J. M. G. Shelley, and J. Chappell. Comparison of high resolution sub-annual records of trace elements in a modern (1911-1992) speleothem with instrumental climate data from southwest australia. *Earth and Planetary Science Letters*, 216 (1-2):141–153, 2003. ISSN 0012-821x. doi: 10.1016/S0012-821x(03)00504-1.

A. Borsato, S. Frisia, I. J. Fairchild, A. Somogyi, and J. Susini. Trace element distribution in annual stalagmite laminae mapped by micrometer-resolution x-ray fluorescence: Implications for incorporation of environmentally significant species. *Geochimica Et Cosmochimica Acta*, 71(6):1494–1512, 2007. ISSN 0016-7037. doi: 10.1016/j.gca.2006.12.016.

Ian J. Fairchild and Pauline C. Treble. Trace elements in speleothems as recorders of environmental change. *Quaternary Science Reviews*, 28(5):449–468, 2009. ISSN 0277-3791. doi: https://doi.org/10.1016/j.quascirev.2008.11.007.

Jennifer Arps. *Towards -Precision of U-series Age Determinations of Secondary Carbonates*. Dissertation, Heidelberg University, 2017.

Inga Kristina Kerber, Jennifer Arps, René Eichstädter, Fabian Kontor, Christoph Dornick, Andrea Schröder-Ritzrau, Athulya Babu, Sophie Warken, and Norbert Frank. Simultaneous u and th isotope measurements for u-series dating using mcicpms. *Nuclear Instruments and Methods in Physics Research Section B: Beam Interactions with Materials and Atoms*, 539:169–178, 2023. ISSN 0168-583X. doi: 10.1016/j.nimb.2023.04.003.

Betsabé De la Barreda, Sarah E. Metcalfe, and Doreen S. Boyd. Precipitation regionalization, anomalies and drought occurrence in the yucatan peninsula, mexico. *International Journal of Climatology*, 40(10):4541–4555, 2020. ISSN 0899-8418 1097-0088. doi: 10.1002/joc.6474.

A.E. Weidie. *Geology of the Yucatán Plattform*, page 1–19. New Orleans Geological Society, New Orleans, Louisiana, USA, 1985.

W. C. Ward, G. Keller, W. Stinnesbeck, and T. Adatte. Yucatan subsurface stratigraphy - implications and constraints for the chicxulub impact. *Geology*, 23(10):873–876, 1995. ISSN 0091-7613. doi: 10.1130/0091-7613(1995)023<0873:Ynssia>2.3.Co;2.

E. Perry, A. Paytan, B. Pedersen, and G. Velazquez-Oliman. Groundwater geochemistry of the yucatan peninsula, mexico: Constraints on stratigraphy and hydrogeology. *Journal of Hydrology*, 367(1-2):27–40, 2009. ISSN 0022-1694. doi: 10.1016/j.jhydrol.2008.12.026.

Nuria Torrescano-Valle and William J Folan. Physical settings, environmental history with an outlook on global change. *Biodiversity and conservation of the Yucatan Peninsula*, pages 9–37, 2015. ISSN 3319065289.

Peter L. Smart, Patricia A. Beddows, Jim Coke, Stefan Doerr, Samantha Smith, and Fiona F. Whitaker. *Cave development on the Caribbean coast of the Yucatan*

Peninsula, Quintana Roo, Mexico, volume 404, page 105–128. Geological Society of America, 2006. ISBN 9780813724041. doi: 10.1130/2006.2404(10).

P. Bauer-Gottwein, B. R. N. Gondwe, G. Charvet, L. E. Marín, M. Rebolledo-Vieyra, and G. Merediz-Alonso. Review: The yucatan peninsula karst aquifer, mexico. *Hydrogeology Journal*, 19(3):507–524, 2011. ISSN 1431-2174. doi: 10.1007/s10040-010-0699-5.

Arturo González González, C. R. Sandoval, Alejandro Terrazas, M. B. Sanvicente, Wolfgang Stinnesbeck, O. Jerónimo-Avilés, María De Los Ríos, and E. Acevez. *The arrival of humans on the Yucatan Peninsula: Evidence from submerged caves in the state of Quintana Roo, Mexico*, volume 25. 2008.

Arturo H González, Alejandro Terrazas, Wolfgang Stinnesbeck, Martha E Benavente, Jerónimo Avilés, Carmen Rojas, José Manuel Padilla, Adriana Velásquez, Eugenio Acevez, and Orono Frey, Eberhard Center for the Study of the First Americans. The first human settlers on the yucatán peninsula: evidence from drowned caves in the state of quintana roo (south mexico). pages 323–337, 2013.

J. C. Chatters, D. J. Kennett, Y. Asmerom, B. M. Kemp, V. Polyak, A. N. Blank, P. A. Beddows, E. Reinhardt, J. Arroyo-Cabrales, D. A. Bolnick, R. S. Malhi, B. J. Culleton, P. L. Erreguerena, D. Rissolo, S. Morell-Hart, and Jr. Stafford, T. W. Late pleistocene human skeleton and mtdna link paleoamericans and modern native americans. *Science*, 344(6185):750–4, 2014. ISSN 1095-9203 (Electronic)0036-8075 (Linking). doi: 10.1126/science.1252619.

W. Stinnesbeck, J. Becker, F. Hering, E. Frey, A. G. Gonzalez, J. Fohlmeister, S. Stinnesbeck, N. Frank, A. Terrazas Mata, M. E. Benavente, J. Aviles Olguin, E. Aceves Nunez, P. Zell, and M. Deininger. The earliest settlers of mesoamerica date back to the late pleistocene. *PLoS One*, 12(8):e0183345, 2017a. ISSN 1932-6203 (Electronic) 1932-6203 (Linking). doi: 10.1371/journal.pone.0183345.

Sheryl Luzzadder-Beach. Water resources of the chunchucmil maya. *Geographical Review*, 90(4):493–510, 2000. ISSN 0016-7428.

Derek A. Smith and Miguel Sioui. *Chapter 6 - The evolving relationship between Maya communities and subterranean waters in the Yucatan Peninsula*, volume 4, pages 109–125. Elsevier, 2022. ISBN 2542-7946. doi: https://doi.org/10.1016/B978-0-12-824538-5.00006-6.

H. Gregory McDonald, James C. Chatters, and Timothy J. Gaudin. A new genus of megalonychid ground sloth (mammalia, xenarthra) from the late pleistocene of quintana roo, mexico. *Journal of Vertebrate Paleontology*, 37(3), 2017. ISSN 0272-4634 1937-2809. doi: 10.1080/02724634.2017.1307206.

S. R. Stinnesbeck, E. Frey, J. A. Olguin, W. Stinnesbeck, P. Zell, H. Mallison, A. G. Gonzalez, E. A. Nunez, A. V. Morlet, A. T. Mata, M. B. Sanvicente, F. Hering, and C. R. Sandoval. Xibalbaonyx oviceps, a new megalonychid ground sloth (folivora, xenarthra) from the late pleistocene of the yucatan peninsula, mexico, and its paleobiogeographic significance. *Palz*, 91(2):245–271, 2017b. ISSN 0031-0220. doi: 10.1007/s12542-017-0349-5.

Sarah R Stinnesbeck, Wolfgang Stinnesbeck, Eberhard Frey, Jerónimo Avilés Olguín, Carmen Rojas Sandoval, Adriana Velázquez Morlet, and Arturo Panthera balamoides and other pleistocene felids from the submerged caves of tulum, quintana roo, mexico. pages 1–10, 2018a. ISSN 0891-2963.

B. W. Schubert, J. C. Chatters, J. Arroyo-Cabrales, J. X. Samuels, L. H. Soibelzon, F. J. Prevosti, C. Widga, A. Nava, D. Rissolo, and P. L. Erreguerena. Yucatan carnivorans shed light on the great american biotic interchange. *Biol Lett*, 15 (5):20190148, 2019. ISSN 1744-957X (Electronic) 1744-9561 (Print) 1744-9561 (Linking). doi: 10.1098/rsbl.2019.0148.

W. Stinnesbeck, S. R. Rennie, J. Aviles Olguin, S. R. Stinnesbeck, S. Gonzalez, N. Frank, S. Warken, N. Schorndorf, T. Krengel, A. Velazquez Morlet, and A. Gonzalez Gonzalez. New evidence for an early settlement of the yucatan peninsula, mexico: The chan hol 3 woman and her meaning for the peopling of the americas. *PLoS One*, 15(2):e0227984, 2020. ISSN 1932-6203 (Electronic) 1932-6203 (Linking). doi: 10.1371/journal.pone.0227984.

Sarah R. Stinnesbeck, Wolfgang Stinnesbeck, Alejandro Terrazas Mata, Jerónimo Avilés Olguín, Martha Benavente Sanvicente, Patrick Zell, Eberhard Frey, Susanne Lindauer, Carmen Rojas Sandoval, Adriana Velázquez Morlet, Eugenio Acevez Nuñez, and Arturo González González. The muknal cave near tulum, mexico: An early-holocene funeral site on the yucatán peninsula. *The Holocene*, 28(12): 1992–2005, 2018b. ISSN 0959-6836 1477-0911. doi: 10.1177/0959683618798124.

Gabriel D. Wrobel, Julie A. Hoggarth, and Aubree Marshall. Before the maya: A review of paleoindian and archaic human skeletons found in the maya region. *Ancient Mesoamerica*, 32(3):475–485, 2021. ISSN 0956-5361 1469-1787. doi: 10.1017/s0956536121000250.

M. Medina-Elizalde, S. J. Burns, J. Polanco-Martinez, F. Lases-Hernandez, R. Bradley, H. C. Wang, and C. C. Shen. Synchronous precipitation reduction in the american tropics associated with heinrich 2. *Sci Rep*, 7(1):11216, 2017. ISSN 2045-2322 (Electronic) 2045-2322 (Linking). doi: 10.1038/s41598-017-11742-8.

M. Medina-Elizalde, J. M. Polanco-Martínez, F. Lases-Hernández, R. Bradley, and S. Burns. Testing the "tropical storm" hypothesis of yucatan peninsula climate variability during the maya terminal classic period. *Quaternary Research*, 86(2): 111–119, 2016b. ISSN 0033-5894. doi: 10.1016/j.yqres.2016.05.006.

F. Lases-Hernandez, M. Medina-Elizalde, S. Burns, and M. DeCesare. Long-term monitoring of drip water and groundwater stable isotopic variability in the yucatan peninsula: Implications for recharge and speleothem rainfall reconstruction. *Geochimica Et Cosmochimica Acta*, 246:41–59, 2019. ISSN 0016-7037. doi: 10.1016/j.gca.2018.11.028.

Ambarish V. Karmalkar, Raymond S. Bradley, and Henry F. Diaz. Climate change in central america and mexico: regional climate model validation and climate change projections. *Climate Dynamics*, 37(3-4):605–629, 2011. ISSN 0930-7575 1432-0894. doi: 10.1007/s00382-011-1099-9.

Victor Magaña, Jorge A. Amador, and Socorro Medina. The midsummer drought over mexico and central america. *Journal of Climate*, 12(6):1577–1588, 1999. ISSN 0894-8755-1520-0442. doi: 10.1175/1520-0442(1999)012<1577:Tmdoma>2.0.Co;2.

Talia G Anderson, Kevin J Anchukaitis, Diego Pons, and Matthew Taylor. Multiscale trends and precipitation extremes in the central american midsummer drought. *Environmental Research Letters*, 14(12):124016, 2019. ISSN 1748-9326.

Fernanda Lases-Hernández, Martín Medina-Elizalde, and Amy Benoit Frappier. Drip water 18o variability in the northeastern yucatán peninsula, mexico: Implications for tropical cyclone detection and rainfall reconstruction from speleothems. *Geochimica et Cosmochimica Acta*, 285:237–256, 2020. ISSN 00167037. doi: 10.1016/j.gca.2020.07.008.

Geoffrey J DiMego, Lance F Bosart, and G William Endersen. An examination of the frequency and mean conditions surrounding frontal incursions into the gulf of mexico and caribbean sea. *Monthly Weather Review*, 104(6):709–718, 1976. ISSN 1520-0493.

WK Henry. Some aspects of the fate of cold fronts in the gulf of mexico. *Monthly Weather Review*, 107(8):1078–1082, 1979. ISSN 1520-0493.

J. S. Singarayer, P. J. Valdes, and W. H. G. Roberts. Ocean dominated expansion and contraction of the late quaternary tropical rainbelt. *Sci Rep*, 7(1):9382, 2017. ISSN 2045-2322 (Electronic) 2045-2322 (Linking). doi: 10.1038/s41598-017-09816-8.

Amanda J Waite, Jeremy M Klavans, Amy C Clement, Lisa N Murphy, Volker Liebetrau, Anton Eisenhauer, Ralf J Weger, and Peter K Swart. Observational and model evidence for an important role for volcanic forcing driving atlantic multidecadal variability over the last 600 years. *Geophysical Research Letters*, 47 (23):e2020GL089428, 2020. ISSN 0094-8276.

B. A. Steinman, N. D. Stansell, M. E. Mann, C. A. Cooke, M. B. Abbott, M. Vuille, B. W. Bird, M. S. Lachniet, and A. Fernandez. Interhemispheric antiphasing of neotropical precipitation during the past millennium. *Proc Natl Acad Sci U S A*, 119 (17):e2120015119, 2022. ISSN 1091-6490 (Electronic) 0027-8424 (Print) 0027-8424 (Linking). doi: 10.1073/pnas.2120015119.

Marta Wojewódka-Przybył, Kim J Krahn, Ladislav Hamerlík, Laura Macario-González, Sergio Cohuo, Fernanda Charqueño-Celis, Anaís Cisneros, Philipp Hoelzmann, Handong Yang, and Neil L Rose. Imprints of the little ice age and the severe earthquake of ad 2001 on the aquatic ecosystem of a tropical maar lake in el salvador. *The Holocene*, 32(10):1065–1080, 2022. ISSN 0959-6836.

Jonathan Obrist-Farner, Byron A. Steinman, Nathan D. Stansell, and Jeremy Maurer. Incoherency in central american hydroclimate proxy records spanning the last millennium. *Paleoceanography and Paleoclimatology*, 38(3), 2023. ISSN 2572-4517 2572-4525. doi: 10.1029/2022pa004445.

National Oceanic and Atmospheric Administration. Historical hurricane tracks. `https://coast.noaa.gov/hurricanes/#map=4/32/-80`, 2023. Accessed: 2024-08-29.

O. P. Prat and B. R. Nelson. Mapping the world's tropical cyclone rainfall contribution over land using the trmm multi-satellite precipitation analysis. *Water Resources Research*, 49(11):7236–7254, 2013. ISSN 0043-1397. doi: 10.1002/wrcr.20527.

Aaron Donohoe, John Marshall, David Ferreira, and David Mcgee. The relationship between itcz location and cross-equatorial atmospheric heat transport: From the seasonal cycle to the last glacial maximum. *Journal of Climate*, 26(11):3597–3618, 2013. ISSN 0894-8755. doi: 10.1175/JCLI-D-12-00467.1.

T. Schneider, T. Bischoff, and G. H. Haug. Migrations and dynamics of the intertropical convergence zone. *Nature*, 513(7516):45–53, 2014. ISSN 1476-4687

(Electronic) 0028-0836 (Linking). doi: 10.1038/nature13636.

Michael P. Byrne, Angeline G. Pendergrass, Anita D. Rapp, and Kyle R. Wodzicki. Response of the intertropical convergence zone to climate change: Location, width, and strength. *Current Climate Change Reports*, 4(4):355–370, 2018. ISSN 2198-6061. doi: 10.1007/s40641-018-0110-5.

T. Bhattacharya, J. C. H. Chiang, and W. Cheng. Ocean-atmosphere dynamics linked to 800-1050 ce drying in mesoamerica. *Quaternary Science Reviews*, 169:263–277, 2017. ISSN 0277-3791. doi: 10.1016/j.quascirev.2017.06.005.

Dominik Schmitt, Eberhard Gischler, Daniel Birgel, Jörn Peckmann, Flavio S. Anselmetti, and Hendrik Vogel. Great blue hole (lighthouse reef, belize): A continuous, annually-resolved record of common era sea surface temperature, atlantic multidecadal oscillation and cyclone-controlled run-off. *Quaternary Science Reviews*, 247:106570, 2020. ISSN 0277-3791. doi: 10.1016/j.quascirev.2020.106570.

L. Travis-Taylor, M. Medina-Elizalde, A. V. Karmalkar, J. Polanco-Martinez, G. Serrato Marks, S. Burns, F. Lases-Hernandez, and D. McGee. Last glacial hydroclimate variability in the yucatan peninsula not just driven by itcz shifts. *Sci Rep*, 13(1):14356, 2023. ISSN 2045-2322 (Electronic) 2045-2322 (Linking). doi: 10.1038/s41598-023-40108-6.

Jorge Alberto Amador Astúa. A climate feature of the tropical americas: The trade wind easterly jet. 1998. ISSN 1409-2034.

A. M. Mestas-Nunez and D. B. Enfield. Water vapor fluxes over the intra-americas sea: Seasonal and interannual variability and associations with rainfall. *Journal of Climate*, 20(9):1910–1922, 2007. ISSN 0894-8755. doi: 10.1175/Jcl14096.1.

Ernesto Muñoz, Antonio J. Busalacchi, Sumant Nigam, and Alfredo Ruiz-Barradas. Winter and summer structure of the caribbean low-level jet. *Journal of Climate*, 21(6):1260–1276, 2008. ISSN 0894-8755 1520-0442. doi: 10.1175/2007jcli1855.1.

Chunzai Wang. Variability of the caribbean low-level jet and its relations to climate. *Climate Dynamics*, 29(4):411–422, 2007. ISSN 0930-7575. doi: 10.1007/s00382-007-0243-z.

A. Giannini, Y. Kushnir, and M. A. Cane. Interannual variability of caribbean rainfall, enso, and the atlantic ocean. *Journal of Climate*, 13(2):297–311, 2000. ISSN 0894-8755. doi: 10.1175/1520-0442(2000)013<0297:Ivocre>2.0.Co;2.

D. K. Gibson, J. Obrist-Farner, B. A. Birkett, J. H. Curtis, M. A. Berke, P. M. Douglas, P. M. Rice, and J. Maurer. The influence of tropical atlantic sea-surface temperatures and the north atlantic subtropical high during the maya droughts. *Holocene*, 0(0):09596836231211856, 2023. ISSN 0959-6836. doi: 10.1177/09596836231211856.

Matthew J Menne, Imke Durre, Russell S Vose, Byron E Gleason, and Tamara G Houston. An overview of the global historical climatology network-daily database. *Journal of atmospheric and oceanic technology*, 29(7):897–910, 2012. ISSN 0739-0572.

CONAGUA, Gobierno de México. Información Estadística Climatológica. `https://smn.conagua.gob.mx/es/climatologia/informacion-climatologica/informacion-estadistica-climatologica`, 2021. Resource Document, Accessed: October 7, 2024.

CA Hill and P Forti. *Cave minerals of the world.* National Speleological Society, Huntsville, Alabama. National Speleological Society, 2 edition, 1997. ISBN 1-879961-07-5.

F. McDermott. Palaeo-climate reconstruction from stable isotope variations in speleothems: a review. *Quaternary Science Reviews*, 23(7-8):901–918, 2004. ISSN 0277-3791. doi: 10.1016/j.quascirev.2003.06.021.

J. W. Raich and C. S. Potter. Global patterns of carbon-dioxide emissions from soils. *Global Biogeochemical Cycles*, 9(1):23–36, 1995. ISSN 0886-6236. doi: 10.1029/94gb02723.

R. Amundson, L. Stern, T. Baisden, and Y. Wang. The isotopic composition of soil and soil-respired co. *Geoderma*, 82(1-3):83–114, 1998. ISSN 0016-7061. doi: 10.1016/S0016-7061(97)00098-0.

Ben Bond-Lamberty, Chuankuan Wang, and Stith T Gower. A global relationship between the heterotrophic and autotrophic components of soil respiration? *Global Change Biology*, 10(10):1756–1766, 2004. ISSN 1354-1013.

Yakov Kuzyakov. Sources of co2 efflux from soil and review of partitioning methods. *Soil biology and biochemistry*, 38(3):425–448, 2006. ISSN 0038-0717.

Ian J Fairchild and Andy Baker. *Speleothem science: from process to past environments*, volume 3. John Wiley & Sons, 2012. ISBN 1444361074.

Chris H Hendy. The isotopic geochemistry of speleothems—i. the calculation of the effects of different modes of formation on the isotopic composition of speleothems and their applicability as palaeoclimatic indicators. *Geochimica et cosmochimica Acta*, 35(8):801–824, 1971. ISSN 0016-7037.

D. Genty, B. Vokal, B. Obelic, and M. Massault. Bomb c time history recorded in two modern stalagmites -: importance for soil organic matter dynamics and bomb c distribution over continents. *Earth and Planetary Science Letters*, 160(3-4):795–809, 1998. ISSN 0012-821x. doi: 10.1016/S0012-821x(98)00128-9.

D. Rudzka, F. McDermott, L. M. Baldini, D. Fleitmann, A. Moreno, and H. Stoll. The coupled c-radiocarbon systematics of three late glacial/early holocene speleothems; insights into soil and cave processes at climatic transitions. *Geochimica Et Cosmochimica Acta*, 75(15):4321–4339, 2011. ISSN 0016-7037. doi: 10.1016/j.gca.2011.05.022.

W. Dreybrodt and J. Fohlmeister. The impact of outgassing of co and prior calcium precipitation to the isotope composition of calcite precipitated on stalagmites. implications for reconstructing climate information from proxies. *Chemical Geology*, 589: 120676, 2022. ISSN 0009-2541. doi: ARTN12067610.1016/j.chemgeo.2021.120676.

K. R. Johnson. Tales from the underground: Speleothem records of past hydroclimate. *Elements*, 17(2):93–100, 2021. ISSN 1811-5209. doi: 10.2138/gselements.17.2.93.

H. Cheng, R. L. Edwards, C. C. Shen, V. J. Polyak, Y. Asmerom, J. Woodhead, J. Hellstrom, Y. J. Wang, X. G. Kong, C. Spötl, X. F. Wang, and E. C. Alexander. Improvements in th dating, th and u half-life values, and u-th isotopic measurements by multi-collector inductively coupled plasma mass spectrometry. *Earth and Planetary Science Letters*, 371:82–91, 2013. ISSN 0012-821x. doi: 10.1016/j.epsl.2013.04.006.

Denis Scholz and Dirk Hoffmann. 230th/u-dating of fossil corals and speleothems. *Quaternary Science Journal*, 57(1-2):52–76, 2008.

Miro Ivanovich and Russell S Harmon. Uranium-series disequilibrium: applications to earth, marine, and environmental sciences. 2. 1992.

D. A. Richards and J. A. Dorale. Uranium-series chronology and environmental applications of speleothems. *Uranium-Series Geochemistry*, 52(1):407–460, 2003. ISSN 1529-6466. doi: 10.2113/0520407.

Bernard Bourdon, Gideon M. Henderson, Craig C. Lundstrom, and Simon Turner. *Uranium-series Geochemistry.* Uranium-series Geochemistry. De Gruyter, Berlin, Boston, 2003. ISBN 9781501509308. doi: 10.1515/9781501509308.

D. Langmuir and J. S. Herman. The mobility of thorium in natural-waters at low-temperatures. *Geochimica Et Cosmochimica Acta*, 44(11):1753–1766, 1980. ISSN 0016-7037. doi: 10.1016/0016-7037(80)90226-4.

M. Ivanovich. Uranium series disequilibrium - concepts and applications. *Radiochimica Acta*, 64(2):81–94, 1994. ISSN 0033-8230.

A. H. Jaffey, K. F. Flynn, L. E. Glendenin, W. C. Bentley, and A. M. Essling. Precision measurement of half-lives and specific activities of u-235 and u-238. *Physical Review C*, 4(5):1889–+, 1971. ISSN 0556-2813. doi: 10.1103/PhysRevC.4.1889.

B Duchemin, N Coursol, and MM Be. The re-evaluation of decay data for the u-238 chain. *Nuclear Instruments and Methods in Physics Research Section A: Accelerators, Spectrometers, Detectors and Associated Equipment*, 339(1-2): 146–150, 1994. ISSN 0168-9002.

M. Gascoyne. *Geochemistry of the actinides and their daughters.* Clarendon Press, United Kingdom, 1992. ISBN 0 19 854278 X.

A. Kaufman, G. J. Wasserburg, D. Porcelli, M. Bar-Matthews, A. Ayalon, and L. Halicz. U-th isotope systematics from the soreq cave, israel and climatic correlations. *Earth and Planetary Science Letters*, 156(3-4):141–155, 1998. ISSN 0012-821x. doi: 10.1016/S0012-821x(98)00002-8.

Jeffrey A. Dorale, R. Lawrence Edwards, E. Calvin Alexander, Chuan-Chou Shen, David A. Richards, and Hai Cheng. *Uranium-Series Dating of Speleothems: Current Techniques, Limits, & Applications*, book section Chapter 10, pages 177–197. Springer US, 2004. ISBN 978-1-4613-4799-6 978-1-4419-9118-8. doi: 10.1007/978-1-4419-9118-8_10.

L. S. Morton, C. V. Evans, G. Harbottle, and G. O. Estes. Pedogenic fractionation and bioavailability of uranium and thorium in naturally radioactive spodosols. *Soil Science Society of America Journal*, 65(4):1197–1203, 2001. ISSN 0361-5995. doi: https://doi.org/10.2136/sssaj2001.6541197x.

Pascal Reiller, Valérie Moulin, Florence Casanova, and Christian Dautel. Retention behaviour of humic substances onto mineral surfaces and consequences upon thorium (iv) mobility: case of iron oxides. *Applied Geochemistry*, 17(12):1551–1562, 2002. ISSN 0883-2927. doi: https://doi.org/10.1016/S0883-2927(02)00045-8.

Rennan Cabral Nascimento, Yuri Jacques Agra Bezerra da Silva, Clístenes Williams Araújo do Nascimento, Ygor Jacques Agra Bezerra da Silva, Rayanna Jacques Agra Bezerra da Silva, and Adrian L Collins. Thorium content in soil, water and sediment samples and fluvial sediment-associated transport in a catchment system with a semiarid-coastal interface, brazil. *Environmental Science and Pollution Research*, 26:33532–33540, 2019. ISSN 0944-1344.

B. E. Wortham, J. L. Banner, E. W. James, R. L. Edwards, and S. Loewy. Application of cave monitoring to constrain the value and source of detrital 230th/232th in speleothem calcite: Implications for u-series geochronology of speleothems. *Palaeogeography Palaeoclimatology Palaeoecology*, 596:110978, 2022. ISSN 0031-0182. doi: ARTN11097810.1016/j.palaeo.2022.110978.

Henry P. Schwarcz. Uranium series dating of quaternary deposits. *Quaternary International*, 1:7–17, 1989. ISSN 10406182. doi: 10.1016/1040-6182(89)90005-0.

J. L. Bischoff and J. A. Fitzpatrick. U-series dating of impure carbonates - an isochron technique using total-sample dissolution. *Geochimica Et Cosmochimica Acta*, 55(2): 543–554, 1991. ISSN 0016-7037. doi: 10.1016/0016-7037(91)90011-S.

J. Hellstrom. U–th dating of speleothems with high initial 230th using stratigraphical constraint. *Quaternary Geochronology*, 1(4):289–295, 2006. ISSN 18711014. doi: 10.1016/j.quageo.2007.01.004.

Stuart Ross Taylor and Scott M McLennan. The continental crust: its composition and evolution. 1985.

KR Ludwig and JB Paces. Uranium-series dating of pedogenic silica and carbonate, crater flat, nevada. *Geochimica et Cosmochimica Acta*, 66(3):487–506, 2002. ISSN 0016-7037.

K. H. Wedepohl. The composition of the continental-crust. *Geochimica Et Cosmochimica Acta*, 59(7):1217–1232, 1995. ISSN 0016-7037. doi: 10.1016/0016-7037(95)00038-2.

J. W. Beck, D. A. Richards, R. L. Edwards, B. W. Silverman, P. L. Smart, D. J. Donahue, S. Hererra-Osterheld, G. S. Burr, L. Calsoyas, A. J. Jull, and D. Biddulph. Extremely large variations of atmospheric 14c concentration during the last glacial period. *Science*, 292(5526):2453–8, 2001. ISSN 0036-8075 (Print) 0036-8075 (Linking). doi: 10.1126/science.1056649.

J. W. Partin, K. M. Cobb, J. F. Adkins, B. Clark, and D. P. Fernandez. Millennial-scale trends in west pacific warm pool hydrology since the last glacial maximum. *Nature*, 449(7161):452–U3, 2007. ISSN 0028-0836. doi: 10.1038/nature06164.

Dirk L. Hoffmann, J. Warren Beck, David A. Richards, Peter L. Smart, Joy S. Singarayer, Tricia Ketchmark, and Chris J. Hawkesworth. Towards radiocarbon calibration beyond 28ka using speleothems from the bahamas. *Earth and Planetary Science Letters*, 289(1-2):1–10, 2010. ISSN 0012821X. doi: 10.1016/j.epsl.2009.10.004.

S. A. Carolin, K. M. Cobb, J. F. Adkins, B. Clark, J. L. Conroy, S. Lejau, J. Malang, and A. A. Tuen. Varied response of western pacific hydrology to climate forcings over the last glacial period. *Science*, 340(6140):1564–6, 2013. ISSN 1095-9203 (Electronic) 0036-8075 (Linking). doi: 10.1126/science.1233797.

M. M. Arienzo, P. K. Swart, A. Pourmand, K. Broad, A. C. Clement, L. N. Murphy, H. B. Vonhof, and B. Kakuk. Bahamian speleothem reveals temperature decrease associated with heinrich stadials. *Earth and Planetary Science Letters*, 430:377–386, 2015. ISSN 0012-821x. doi: 10.1016/j.epsl.2015.08.035.

G. E. Moseley, D. A. Richards, P. L. Smart, C. D. Standish, D. L. Hoffmann, H. ten Hove, and O. Vinn. Early-middle holocene relative sea-level oscillation events recorded in a submerged speleothem from the yucatan peninsula, mexico. *Holocene*, 25(9):1511–1521, 2015. ISSN 0959-6836. doi: 10.1177/0959683615585832.

S. D. Steidle, S. F. Warken, N. Schorndorf, J. Förstel, A. Schröder-Ritzrau, G. E. Moseley, C. Spötl, J. Aviles, W. Stinnesbeck, and N. Frank. Reconstruction of middle to late quaternary sea level using submerged speleothems from the northeastern yucatan peninsula. *Journal of Quaternary Science*, 36(7):1190–1200, 2021. ISSN 0267-8179. doi: 10.1002/jqs.3365.

Rolf Vieten, Sophie F Warken, Amos Winter, Denis Scholz, Davide Zanchettin, David Black, and Matthew Lachniet. A sequence of abrupt climatic fluctuations in the north-eastern caribbean related to the 8.2 ka event. *The Holocene*, 34(3):325–337, 2024b. ISSN 0959-6836.

L. F. Robinson, N. S. Belshaw, and G. M. Henderson. U and th concentrations and isotope ratios in modern carbonates and waters from the bahamas. *Geochimica Et Cosmochimica Acta*, 68(8):1777–1789, 2004. ISSN 0016-7037. doi: 10.1016/j.gca.2003.10.005.

Ting-Yong Li, Xuefeng Wang, Chao-Jun Chen, Ming Tan, and Yao Wu. Testing the initial 230th/232th for "known age carbonate" and its significance for 230th dating and paleoclimate research. *Quaternary International*, 607:113–119, 2022. ISSN 10406182. doi: 10.1016/j.quaint.2021.07.020.

Claudia Fensterer, Denis Scholz, Derik Hoffmann, Augusta Mangini, and Jesus M Pajón. 230th/u-dating of a late holocene low uranium speleothem from cuba. In *IOP Conference Series: Earth and Environmental Science*, volume 9, page 012015. IOP Publishing, 2010. ISBN 1755-1315.

C. Fensterer, D. Scholz, D. Hoffmann, C. Spötl, J. M. Pajón, and A. Mangini. Cuban stalagmite suggests relationship between caribbean precipitation and the atlantic multidecadal oscillation during the past 1.3 ka. *Holocene*, 22(12):1405–1412, 2012. ISSN 0959-6836. doi: 10.1177/0959683612449759.

Sophie F Warken, Denis Scholz, Christoph Spötl, Klaus P Jochum, Jesús M Pajón, André Bahr, and Augusto Mangini. Caribbean hydroclimate and vegetation history across the last glacial period. *Quaternary Science Reviews*, 218:75–90, 2019. ISSN 0277-3791.

Isabel Rivera-Collazo, Amos Winter, Denis Scholz, Augusto Mangini, Thomas Miller, Yochanan Kushnir, and David Black. Human adaptation strategies to abrupt climate change in puerto rico ca. 3.5 ka. *The Holocene*, 25(4):627–640, 2015. ISSN 0959-6836. doi: 10.1177/0959683614565951.

S. F. Warken, R. Vieten, A. Winter, C. Spötl, T. E. Miller, K. P. Jochum, A. Schröder-Ritzrau, A. Mangini, and D. Scholz. Persistent link between caribbean precipitation and atlantic ocean circulation during the last glacial revealed by a speleothem record from puerto rico. *Paleoceanography and Paleoclimatology*, 35(11), 2020. ISSN 2572-4517. doi: ARTNe2020PA00394410.1029/2020PA003944.

Douglas J. Kennett, Marilyn Masson, Carlos Peraza Lope, Stanley Serafin, Richard J. George, Tom C. Spencer, Julie A. Hoggarth, Brendan J. Culleton, Thomas K. Harper, Keith M. Prufer, Susan Milbrath, Bradley W. Russell, Eunice Uc González, Weston C. McCool, Valorie V. Aquino, Elizabeth H. Paris, Jason H. Curtis, Norbert Marwan, Mingua Zhang, Yemane Asmerom, Victor J. Polyak, Stacy A. Carolin, Daniel H. James, Andrew J. Mason, Gideon M. Henderson, Mark Brenner, James U. L. Baldini, Sebastian F. M. Breitenbach, and David A. Hodell. Drought-induced civil conflict among the ancient maya. *Nature Communications*, 13(1), 2022. ISSN 2041-1723. doi: 10.1038/s41467-022-31522-x.

KS Heier and JL Carter. Uranium, thorium and potassium contents in basic rocks. In *Proceedings of the International Symposium on The Natural Radiation Environment*. University of Chicago Press, 1963.

KS Heier and John JW Rogers. Radiometric determination of thorium, uranium and potassium in basalts and in two magmatic differentiation series. *Geochimica et Cosmochimica acta*, 27(2):137–154, 1963. ISSN 0016-7037.

Chaoyong Hu, Gideon M. Henderson, Junhua Huang, Shucheng Xie, Ying Sun, and Kathleen R. Johnson. Quantification of holocene asian monsoon rainfall from spatially separated cave records. *Earth and Planetary Science Letters*, 266(3-4): 221–232, 2008. ISSN 0012-821X. doi: 10.1016/j.epsl.2007.10.015.

K. R. Ludwig and D. M. Titterington. Calculation of isochrons, ages, and errors. *Geochimica et Cosmochimica Acta*, 58(22):5031–5042, 1994. ISSN 00167037. doi: 10.1016/0016-7037(94)90229-1.

J. C. Lin, W. S. Broecker, R. F. Anderson, S. Hemming, J. L. Rubenstone, and G. Bonani. New 230th/u and 14c ages from lake lahontan carbonates, nevada, usa, and a discussion of the origin of initial thorium. *Geochimica et Cosmochimica Acta*, 60(15):2817–2832, 1996. ISSN 00167037. doi: 10.1016/0016-7037(96)00136-6.

R. F. Denniston, K. H. Wyrwoll, Y. Asmerom, V. J. Polyak, W. F. Humphreys, J. Cugley, D. Woods, Z. LaPointe, J. Peota, and E. Greaves. North atlantic forcing of millennial-scale indo-australian monsoon dynamics during the last glacial period. *Quaternary Science Reviews*, 72:159–168, 2013a. ISSN 0277-3791. doi: 10.1016/j.quascirev.2013.04.012.

M. Lomitschka and A. Mangini. Precise th/u-dating of small and heavily coated samples of deep sea corals. *Earth and Planetary Science Letters*, 170(4):391–401, 1999. ISSN 0012-821x. doi: 10.1016/S0012-821x(99)00117-X.

H. Cheng, J. Adkins, R. L. Edwards, and E. A. Boyle. U-th dating of deep-sea corals. *Geochimica Et Cosmochimica Acta*, 64(14):2401–2416, 2000. ISSN 0016-7037. doi: 10.1016/S0016-7037(99)00422-6.

Andrea Schröder-Ritzrau, Augusto Mangini, and Michael Lomitschka. Deep-sea corals evidence periodic reduced ventilation in the north atlantic during the lgm/holocene transition. *Earth and Planetary Science Letters*, 216(3):399–410, 2003. ISSN 0012-821X.

N. Frank, M. Paterne, L. Ayliffe, T. van Weering, J. P. Henriet, and D. Blamart. Eastern north atlantic deep-sea corals:: tracing upper intermediate water Δ c during the holocene. *Earth and Planetary Science Letters*, 219(3-4):297–309, 2004. ISSN 0012-821x. doi: 10.1016/S0012-821x(03)00721-0.

Chuan-Chou Shen, Kuei-Shu Li, Kerry Sieh, Danny Natawidjaja, Hai Cheng, Xianfeng Wang, R Lawrence Edwards, Doan Dinh Lam, Yu-Te Hsieh, and Tung-Yung Fan. Variation of initial 230th/232th and limits of high precision u–th dating of shallow-water corals. *Geochimica et Cosmochimica Acta*, 72(17):4201–4223, 2008. ISSN 0016-7037.

H. Godwin. Half-life of radiocarbon. *Nature*, 195(4845):984, 1962. ISSN 0028-0836. doi: 10.1038/195984a0.

E. C. Anderson, W. F. Libby, S. Weinhouse, A. F. Reid, A. D. Kirshenbaum, and A. V. Grosse. Radiocarbon from cosmic radiation. *Science*, 105(2735):576–7, 1947. ISSN 0036-8075 (Print) 0036-8075 (Linking). doi: 10.1126/science.105.2735.576.

Christopher Bronk Ramsey. Radiocarbon dating: revolutions in understanding. *Archaeometry*, 50(2):249–275, 2008. ISSN 0003-813X.

A. Burke and L. F. Robinson. The southern ocean's role in carbon exchange during the last deglaciation. *Science*, 335(6068):557–61, 2012. ISSN 1095-9203 (Electronic) 0036-8075 (Linking). doi: 10.1126/science.1208163.

Willem Gerrit Mook. Environmental isotopes in the hydrological cycle: principles and applications. 2000.

J. R. Arnold and W. F. Libby. Radiocarbon dates. *Science*, 113(2927):111–120, 1951. ISSN 0036-8075. doi: 10.1126/science.113.2927.111.

W. F. Libby. Atmospheric helium three and radiocarbon from cosmic radiation. *Physical Review*, 69(11-1):671–672, 1946. ISSN 0031-899x. doi: 10.1103/PhysRev.69.671.2.

P. J. Reimer, W. E. N. Austin, E. Bard, A. Bayliss, P. G. Blackwell, C. B. Ramsey, M. Butzin, H. Cheng, R. L. Edwards, M. Friedrich, P. M. Grootes, T. P. Guilderson, I. Hajdas, T. J. Heaton, A. G. Hogg, K. A. Hughen, B. Kromer, S. W. Manning, R. Muscheler, J. G. Palmer, C. Pearson, J. van der Plicht, R. W. Reimer, D. A. Richards, E. M. Scott, J. R. Southon, C. S. M. Turney, L. Wacker, F. Adolphi, U. Büntgen, M. Capano, S. M. Fahrni, A. Fogtmann-Schulz, R. Friedrich, P. Köhler, S. Kudsk, F. Miyake, J. Olsen, F. Reinig, M. Sakamoto, A. Sookdeo, and S. Talamo. The intcal20 northern hemisphere radiocarbon age calibration curve (0-55 cal kbp). *Radiocarbon*, 62(4):725–757, 2020. ISSN 0033-8222. doi: 10.1017/Rdc.2020.41.

Christopher Bronk Ramsey, Florian Adolphi, William Austin, Edouard Bard, Alex Bayliss, Maarten Blaauw, Hai Cheng, R. Lawrence Edwards, Michael Friedrich, Timothy Heaton, Alan Hogg, Quan Hua, Konrad Hughen, Bernd Kromer, Sturt Manning, Raimund Muscheler, Jonathan Palmer, Charlotte Pearson, Paula Reimer, Ron Reimer, David Richards, Marian Scott, John Southon, Chris Turney, and Lukas Wacker. Development of the intcal database. *Radiocarbon*, pages 1–17, 2023. ISSN 0033-8222 1945-5755. doi: 10.1017/rdc.2023.53.

M. Schaub, U. Büntgen, K. F. Kaiser, B. Kromer, S. Talamo, K. K. Andersen, and S. O. Rasmussen. Lateglacial environmental variability from swiss tree rings. *Quaternary Science Reviews*, 27(1-2):29–41, 2008. ISSN 0277-3791. doi: 10.1016/j.quascirev.2007.01.017.

Q. Hua, M. Barbetti, D. Fink, K. F. Kaiser, M. Friedrich, B. Kromer, V. A. Levchenko, U. Zoppi, A. M. Smith, and F. Bertuch. Atmospheric c variations derived from tree rings during the early younger dryas. *Quaternary Science Reviews*, 28(25-26): 2982–2990, 2009. ISSN 0277-3791. doi: 10.1016/j.quascirev.2009.08.013.

P. J. Reimer, E. Bard, A. Bayliss, J. W. Beck, P. G. Blackwell, C. B. Ramsey, C. E. Buck, H. Cheng, R. L. Edwards, M. Friedrich, P. M. Grootes, T. P. Guilderson, H. Haflidason, I. Hajdas, C. Hatté, T. J. Heaton, D. L. Hoffmann, A. G. Hogg, K. A. Hughen, K. F. Kaiser, B. Kromer, S. W. Manning, M. Niu, R. W. Reimer, D. A. Richards, E. M. Scott, J. R. Southon, R. A. Staff, C. S. M. Turney, and J. van der Plicht. Intcal13 and marine13 radiocarbon age calibration curves 0-50,000 years cal bp. *Radiocarbon*, 55(4):1869–1887, 2013. ISSN 0033-8222. doi: 10.2458/azu_js_rc.55.16947.

J. Southon, A. L. Noronha, H. Cheng, R. L. Edwards, and Y. J. Wang. A high-resolution record of atmospheric c based on hulu cave speleothem h82. *Quaternary Science Reviews*, 33:32–41, 2012. ISSN 0277-3791. doi: 10.1016/j.quascirev.2011.11.022.

Christopher Bronk Ramsey, Richard A Staff, Charlotte L Bryant, Fiona Brock, Hiroyuki Kitagawa, Johannes Van Der Plicht, Gordon Schlolaut, Michael H Marshall, Achim Brauer, and Henry F Lamb. A complete terrestrial radiocarbon record for 11.2 to 52.8 kyr bp. *Science*, 338(6105):370–374, 2012. ISSN 0036-8075.

K. Hughen, J. Southon, S. Lehman, C. Bertrand, and J. Turnbull. Marine-derived c calibration and activity record for the past 50,000 years updated from the cariaco basin. *Quaternary Science Reviews*, 25(23-24):3216–3227, 2006. ISSN 0277-3791. doi: 10.1016/j.quascirev.2006.03.014.

E. Bard, G. Ménot, F. Rostek, L. Licari, P. Böning, R. L. Edwards, H. Cheng, Y. J. Wang, and T. J. Heaton. Radiocarbon calibration/comparison records based on marine sediments from the pakistan and iberian margins. *Radiocarbon*, 55(4):1999–2019, 2013. ISSN 0033-8222. doi: 10.2458/azu_js_rc.55.17114.

Nicolas Durand, Pierre Deschamps, Edouard Bard, Bruno Hamelin, Gilbert Camoin, Alexander L Thomas, Gideon M Henderson, Yusuke Yokoyama, and Hiroyuki Matsuzaki. Comparison of 14c and u-th ages in corals from iodp# 310 cores offshore tahiti. *Radiocarbon*, 55(4):1947–1974, 2013. ISSN 0033-8222.

T. J. Heaton, E. Bard, and K. A. Hughen. Elastic tie-pointing-transferring chronologies between records via a gaussian process. *Radiocarbon*, 55(4):1975–1997, 2013. ISSN 0033-8222. doi: 10.2458/azu_js_rc.55.17777.

A. A. Burchuladze, S. V. Pagava, P. Povinec, G. I. Togonidze, and S. Usacev. Radiocarbon variations with the 11-year solar-cycle during the last century. *Nature*, 287(5780):320–322, 1980. ISSN 0028-0836. doi: 10.1038/287320a0.

R. Muscheler, J. Beer, G. Wagner, C. Laj, C. Kissel, G. M. Raisbeck, F. Yiou, and P. W. Kubik. Changes in the carbon cycle during the last deglaciation as indicated by the comparison of be and c records. *Earth and Planetary Science Letters*, 219 (3-4):325–340, 2004. ISSN 0012-821x. doi: 10.1016/S0012-821x(03)00722-2.

R. Muscheler, R. Beer, P. W. Kubik, and H. A. Synal. Geomagnetic field intensity during the last 60,000 years based on be and cl from the summit ice cores and c. *Quaternary Science Reviews*, 24(16-17):1849–1860, 2005. ISSN 0277-3791. doi: 10.1016/j.quascirev.2005.01.012.

Peter Köhler, Raimund Muscheler, and Hubertus Fischer. A model-based interpretation of low-frequency changes in the carbon cycle during the last 120,000 years and its implications for the reconstruction of atmospheric Δ14c. *Geochemistry, Geophysics, Geosystems*, 7(11), 2006. ISSN 1525-2027.

A. Scifo, M. Kuitems, A. Neocleous, B. J. S. Pope, D. Miles, E. Jansma, P. Doeve, A. M. Smith, F. Miyake, and M. W. Dee. Radiocarbon production events and their potential relationship with the schwabe cycle. *Scientific Reports*, 9(1):17056, 2019. ISSN 2045-2322. doi: ARTN1705610.1038/s41598-019-53296-x.

P. P. Tans, A. F. M. De Jong, and W. G. Mook. Natural atmospheric 14c variation and the suess effect. *Nature*, 280(5725):826–828, 1979. ISSN 0028-0836 1476-4687. doi: 10.1038/280826a0.

Ingeborg Levin, Tobias Naegler, Bernd Kromer, Moritz Diehl, Roger J. Francey, Angel J. Gomez-Pelaez, L. Paul Steele, Dietmar Wagenbach, Rolf Weller, and Douglas E. Worthy. Observations and modelling of the global distribution and long-term trend of atmospheric ¹⁴co₂. *Tellus B: Chemical and Physical Meteorology*, 62(1):26–46, 2010. ISSN 1600-0889 0280-6509. doi: 10.1111/j.1600-0889.2009.00446.x.

M. Stuiver. International agreements and the use of the new oxalic-acid standard. *Radiocarbon*, 25(2):793–795, 1983. ISSN 0033-8222. doi: 10.1017/S0033822200006159.

Kristina Stenström, Göran Skog, Elisavet Georgiadou, Johan Genberg, and Anette Mellström. A guide to radiocarbon units and calculations. 2011.

L. Comas-Bru, K. Rehfeld, C. Roesch, S. Amirnezhad-Mozhdehi, S. P. Harrison, K. Atsawawaranunt, S. M. Ahmad, Y. A. Brahim, A. Baker, M. Bosomworth, S. F. M. Breitenbach, Y. Burstyn, A. Columbu, M. Deininger, A. Demény, B. Dixon, J. Fohlmeister, I. G. Hatvani, J. Hu, N. Kaushal, Z. Kern, I. Labuhn, F. A. Lechleitner, A. Lorrey, B. Martrat, V. F. Novello, J. Oster, C. Pérez-Mejías, D. Scholz, N. Scroxton, N. Sinha, B. M. Ward, S. Warken, H. W. Zhang, and SISAL Working Grp Members. Sisalv2: a comprehensive speleothem isotope database with multiple age-depth models. *Earth System Science Data*, 12(4):2579–2606, 2020. ISSN 1866-3508. doi: 10.5194/essd-12-2579-2020.

M. S. Lachniet. Climatic and environmental controls on speleothem oxygen-isotope values. *Quaternary Science Reviews*, 28(5-6):412–432, 2009. ISSN 0277-3791. doi: 10.1016/j.quascirev.2008.10.021.

Tyler B Coplen. New guidelines for reporting stable hydrogen, carbon, and oxygen isotope-ratio data. *Geochimica et Cosmochimica Acta*, 60(17):3359–3360, 1996. ISSN 0016-7037.

R. Gonfiantini. Standards for stable isotope measurements in natural compounds. *Nature*, 271(5645):534–536, 1978. ISSN 0028-0836. doi: 10.1038/271534a0.

W. Dansgaard. Stable isotopes in precipitation. *Tellus*, 16(4):436–468, 1964. ISSN 0040-2826.

F. Zaucker and W. S. Broecker. The influence of atmospheric moisture transport on the fresh-water balance of the atlantic drainage-basin - general-circulation model simulations and observations. *Journal of Geophysical Research-Atmospheres*, 97 (D3):2765–2773, 1992. ISSN 2169-897x. doi: 10.1029/91jd01699.

G. A. Schmidt, A. N. LeGrande, and G. Hoffmann. Water isotope expressions of intrinsic and forced variability in a coupled ocean-atmosphere model. *Journal of Geophysical Research-Atmospheres*, 112(D10), 2007. ISSN 2169-897x. doi: ArtnD1010310.1029/2006jd007781.

ID Clark and P Fritz. Environmental isotopes in hydrology lewis publishers. *Boca Raton, New York*, 1997.

Daniel P. Schrag, Jess F. Adkins, Katherine McIntyre, Jane L. Alexander, David A. Hodell, Christopher D. Charles, and Jerry F. McManus. The oxygen isotopic composition of seawater during the last glacial maximum. *Quaternary Science Reviews*, 21(1):331–342, 2002. ISSN 0277-3791. doi: 10.1016/S0277-3791(01)00110-X.

David W. Lea, Pamela A. Martin, Dorothy K. Pak, and Howard J. Spero. Reconstructing a 350ky history of sea level using planktonic mg/ca and oxygen isotope records from a cocos ridge core. *Quaternary Science Reviews*, 21(1):283–293, 2002. ISSN 0277-3791. doi: 10.1016/S0277-3791(01)00081-6.

Zachary Sharp. *Principles of Stable Isotope Geochemistry*. 2007. ISBN 0130091391.

Kazimierz Rozanski, Luis Araguás-Araguás, and Roberto Gonfiantini. Isotopic patterns in modern global precipitation. *GMS*, 78:1–36, 1993.

M. Vuille, R. S. Bradley, M. Werner, R. Healy, and F. Keimig. Modeling o in precipitation over the tropical americas:: 1.: Interannual variability and climatic controls -: art. no. 4174. *Journal of Geophysical Research-Atmospheres*, 108(D6), 2003. ISSN 2169-897x. doi: Artn417410.1029/2001jd002038.

M. S. Lachniet and W. P. Patterson. Oxygen isotope values of precipitation and surface waters in northern central america (belize and guatemala) are dominated by temperature and amount effects. *Earth and Planetary Science Letters*, 284(3-4): 435–446, 2009. ISSN 0012-821x. doi: 10.1016/j.epsl.2009.05.010.

A. B. Frappier. Masking of interannual climate proxy signals by residual tropical cyclone rainwater: Evidence and challenges for low-latitude speleothem paleoclimatology. *Geochemistry Geophysics Geosystems*, 14(9):3632–3647, 2013. ISSN 1525-2027. doi: 10.1002/ggge.20218.

R. Vieten, S. Warken, A. Winter, A. Schröder-Ritzrau, D. Scholz, and C. Spötl. Hurricane impact on seepage water in larga cave, puerto rico. *Journal of Geophysical Research-Biogeosciences*, 123(3):879–888, 2018. ISSN 2169-8953. doi: 10.1002/2017jg004218.

O. Escolero, L. E. Marin, E. Domínguez-Mariani, and S. Torres-Onofre. Dynamic of the freshwater-saltwater interface in a karstic aquifer under extraordinary recharge action:: the merida yucatan case study. *Environmental Geology*, 51(5):719–723, 2007. ISSN 0943-0105. doi: 10.1007/s00254-006-0383-1.

Kuilian Tang and Xiahong Feng. The effect of soil hydrology on the oxygen and hydrogen isotopic compositions of plants' source water. *Earth and Planetary Science Letters*, 185(3-4):355–367, 2001. ISSN 0012-821X.

D. Gillieson. *Caves: Processes, Development and Management.* Wiley, 1996. ISBN 9780631178194.

AB Klimchouk. The formation of epikarst and its role in vadose speleogenesis. *Speleogenesis: Evolution of karst aquifers. Huntsville: Natl. Speleol. Soc*, pages 91–99, 2000.

Miryam Bar-Matthews, Avner Ayalon, Alan Matthews, Eytan Sass, and Ludwik Halicz. Carbon and oxygen isotope study of the active water-carbonate system in a karstic mediterranean cave: Implications for paleoclimate research in semiarid regions. *Geochimica et Cosmochimica Acta*, 60(2):337–347, 1996. ISSN 0016-7037.

Miryam Bar-Matthews, Avner Ayalon, Mabs Gilmour, Alan Matthews, and Chris J Hawkesworth. Sea–land oxygen isotopic relationships from planktonic foraminifera and speleothems in the eastern mediterranean region and their implication for paleorainfall during interglacial intervals. *Geochimica et cosmochimica acta*, 67 (17):3181–3199, 2003. ISSN 0016-7037.

Francisco Carrasco, Bartolomé Andreo, Cristina Liñán, and Jacques Mudry. Contribution of stable isotopes to the understanding of the unsaturated zone of a carbonate aquifer (nerja cave, southern spain). *Comptes rendus. Géoscience*, 338 (16):1203–1212, 2006. ISSN 1778-7025.

Andrew J Long and Larry D Putnam. Linear model describing three components of flow in karst aquifers using 18o data. *Journal of hydrology*, 296(1-4):254–270, 2004. ISSN 0022-1694.

Pauline C. Treble, Andy Baker, Nerilie J. Abram, John C. Hellstrom, Jagoda Crawford, Michael K. Gagan, Andrea Borsato, Alan D. Griffiths, Petra Bajo, Monika Markowska, Stacey C. Priestley, Stuart Hankin, and David Paterson. Ubiquitous karst hydrological control on speleothem oxygen isotope variability in a global study. *Communications Earth & Environment*, 3(1), 2022. ISSN 2662-4435. doi: 10.1038/s43247-022-00347-3.

J. Fohlmeister, N. R. G. Voarintsoa, F. A. Lechleitner, M. Boyd, S. Brandtstätter, M. J. Jacobson, and J. L. Oster. Main controls on the stable carbon isotope composition of speleothems. *Geochimica Et Cosmochimica Acta*, 279:67–87, 2020. ISSN 0016-7037. doi: 10.1016/j.gca.2020.03.042.

V. Skiba and J. Fohlmeister. Contemporaneously growing speleothems and their value to decipher in-cave processes – a modelling approach. *Geochimica et Cosmochimica Acta*, 348:381–396, 2023. ISSN 0016-7037. doi: 10.1016/j.gca.2023.03.016.

S. A. Mischel, D. Scholz, C. Spötl, K. P. Jochum, A. Schröder-Ritzrau, and S. Fiedler. Holocene climate variability in central germany and a potential link to the polar north atlantic: A replicated record from three coeval speleothems. *Holocene*, 27(4): 509–525, 2017. ISSN 0959-6836. doi: 10.1177/0959683616670246.

D. Scholz, S. Frisia, A. Borsato, C. Spötl, J. Fohlmeister, M. Mudelsee, R. Miorandi, and A. Mangini. Holocene climate variability in north-eastern italy: potential influence of the nao and solar activity recorded by speleothem data. *Clim. Past*, 8 (4):1367–1383, 2012. ISSN 1814-9332. doi: 10.5194/cp-8-1367-2012.

F. A. Lechleitner, C. C. Day, O. Kost, M. Wilhelm, N. Haghipour, G. M. Henderson, and H. M. Stoll. Stalagmite carbon isotopes suggest deglacial increase in soil respiration in western europe driven by temperature change. *Climate of the Past*, 17(5):1903–1918, 2021. ISSN 1814-9324. doi: 10.5194/cp-17-1903-2021.

Daniel O. Breecker, Ashley E. Payne, Jay Quade, Jay L. Banner, Carolyn E. Ball, Kyle W. Meyer, and Brian D. Cowan. The sources and sinks of co2 in caves under mixed woodland and grassland vegetation. *Geochimica et Cosmochimica Acta*, 96: 230–246, 2012. ISSN 0016-7037. doi: 10.1016/j.gca.2012.08.023.

Alexandra L. Noronha, Kathleen R. Johnson, John R. Southon, Chaoyong Hu, Jiaoyang Ruan, and Staryl McCabe-Glynn. Radiocarbon evidence for decomposition of aged organic matter in the vadose zone as the main source of speleothem carbon. *Quaternary Science Reviews*, 127:37–47, 2015. ISSN 0277-3791. doi: 10.1016/j.quascirev.2015.05.021.

D. P. Mattey, T. C. Atkinson, J. A. Barker, R. Fisher, J. P. Latin, R. Durrell, and M. Ainsworth. Carbon dioxide, ground air and carbon cycling in gibraltar karst. *Geochimica et Cosmochimica Acta*, 184:88–113, 2016. ISSN 0016-7037. doi: 10.1016/j.gca.2016.01.041.

Shelly J. Bergel, Peter E. Carlson, Toti E. Larson, Chris T. Wood, Kathleen R. Johnson, Jay L. Banner, and Daniel O. Breecker. Constraining the subsoil carbon source to cave-air co2and speleothem calcite in central texas. *Geochimica et Cosmochimica Acta*, 217:112–127, 2017. ISSN 0016-7037. doi: https://doi.org/10.1016/j.gca.2017.08.017.

Joachim Elsig, Jochen Schmitt, Daiana Leuenberger, Robert Schneider, Marc Eyer, Markus Leuenberger, Fortunat Joos, Hubertus Fischer, and Thomas F. Stocker. Stable isotope constraints on holocene carbon cycle changes from an antarctic ice core. *Nature*, 461(7263):507–510, 2009. ISSN 1476-4687. doi: 10.1038/nature08393.

Jochen Schmitt, Robert Schneider, Joachim Elsig, Daiana Leuenberger, Anna Lourantou, Jérôme Chappellaz, Peter Köhler, Fortunat Joos, Thomas F. Stocker, Markus Leuenberger, and Hubertus Fischer. Carbon isotope constraints on the deglacial co₂ rise from ice cores. *Science*, 336(6082):711–714, 2012. doi: 10.1126/science.1217161.

S. Eggleston, J. Schmitt, B. Bereiter, R. Schneider, and H. Fischer. Evolution of the stable carbon isotope composition of atmospheric co2 over the last glacial cycle. *Paleoceanography*, 31(3):434–452, 2016. ISSN 0883-8305. doi: 10.1002/2015PA002874.

H. Graven, C. E. Allison, D. M. Etheridge, S. Hammer, R. F. Keeling, I. Levin, H. A. J. Meijer, M. Rubino, P. P. Tans, C. M. Trudinger, B. H. Vaughn, and J. W. C. White. Compiled records of carbon isotopes in atmospheric co2 for historical simulations in cmip6. *Geosci. Model Dev.*, 10(12):4405–4417, 2017. ISSN 1991-9603. doi: 10.5194/gmd-10-4405-2017.

Thure E. Cerling. The stable isotopic composition of modern soil carbonate and its relationship to climate. *Earth and Planetary Science Letters*, 71(2):229–240, 1984. ISSN 0012-821X. doi: 10.1016/0012-821X(84)90089-X.

Corinne I. Wong and Daniel O. Breecker. Advancements in the use of speleothems as climate archives. *Quaternary Science Reviews*, 127:1–18, 2015. ISSN 0277-3791. doi: 10.1016/j.quascirev.2015.07.019.

Dominique Genty, Andy Baker, Marc Massault, Chris Proctor, Mabs Gilmour, Edwige Pons-Branchu, and Bruno Hamelin. Dead carbon in stalagmites: carbonate bedrock paleodissolution vs. ageing of soil organic matter. implications for 13c variations in speleothems. *Geochimica et Cosmochimica Acta*, 65(20):3443–3457, 2001. ISSN 0016-7037. doi: 10.1016/S0016-7037(01)00697-4.

J. U. L. Baldini, F. McDermott, A. Baker, L. M. Baldini, D. P. Mattey, and L. Bruce Railsback. Biomass effects on stalagmite growth and isotope ratios: A 20th century analogue from wiltshire, england. *Earth and Planetary Science Letters*, 240(2): 486–494, 2005. ISSN 0012-821X. doi: 10.1016/j.epsl.2005.09.022.

Francisco W. Cruz, Stephen J. Burns, Ivo Karmann, Warren D. Sharp, Mathias Vuille, and José A. Ferrari. A stalagmite record of changes in atmospheric circulation and soil processes in the brazilian subtropics during the late pleistocene. *Quaternary Science Reviews*, 25(21):2749–2761, 2006. ISSN 0277-3791. doi: 10.1016/j.quascirev.2006.02.019.

Ana Moreno, Heather Stoll, Montserrat Jiménez-Sánchez, Isabel Cacho, Blas Valero-Garcés, Emi Ito, and R. Lawrence Edwards. A speleothem record of glacial (25–11.6kyr bp) rapid climatic changes from northern iberian peninsula. *Global and Planetary Change*, 71(3):218–231, 2010. ISSN 0921-8181. doi: 10.1016/j.gloplacha.2009.10.002.

Rhawn F. Denniston, Yemane Asmerom, Matthew Lachniet, Victor J. Polyak, Pandora Hope, Ni An, Kristyn Rodzinyak, and William F. Humphreys. A last glacial maximum through middle holocene stalagmite record of coastal western australia climate. *Quaternary Science Reviews*, 77:101–112, 2013b. ISSN 0277-3791. doi: 10.1016/j.quascirev.2013.07.002.

Harmon Craig. The geochemistry of the stable carbon isotopes. *Geochimica et Cosmochimica Acta*, 3(2):53–92, 1953. ISSN 0016-7037. doi: https://doi.org/10.1016/0016-7037(53)90001-5.

Kerstin Braun, Miryam Bar-Matthews, Alan Matthews, Avner Ayalon, Richard M. Cowling, Panagiotis Karkanas, Erich C. Fisher, Kelsey Dyez, Tami Zilberman, and Curtis W. Marean. Late pleistocene records of speleothem stable isotopic compositions from pinnacle point on the south african south coast. *Quaternary Research*, 91(1):265–288, 2019. ISSN 0033-5894. doi: 10.1017/qua.2018.61.

D. Genty, D. Blamart, R. Ouahdi, M. Gilmour, A. Baker, J. Jouzel, and Sandra Van-Exter. Precise dating of dansgaard–oeschger climate oscillations in western europe from stalagmite data. *Nature*, 421:833, 2003. doi: 10.1038/nature01391https://www.nature.com/articles/nature01391#supplementary-information.

Jessica L. Oster, Isabel P. Montañez, Thomas P. Guilderson, Warren D. Sharp, and Jay L. Banner. Modeling speleothem 13c variability in a central sierra nevada cave using 14c and 87sr/86sr. *Geochimica et Cosmochimica Acta*, 74(18):5228–5242, 2010. ISSN 0016-7037. doi: 10.1016/j.gca.2010.06.030.

M. L. Griffiths, J. Fohlmeister, R. N. Drysdale, Q. Hua, K. R. Johnson, J. C. Hellstrom, M. K. Gagan, and J. X. Zhao. Hydrological control of the dead carbon fraction in a holocene tropical speleothem. *Quaternary Geochronology*, 14:81–93, 2012. ISSN 1871-1014. doi: 10.1016/j.quageo.2012.04.001.

Jens Fohlmeister, Birgit Plessen, Alexey Sergeevich Dudashvili, Rik Tjallingii, Christian Wolff, Abror Gafurov, and Hai Cheng. Winter precipitation changes during the medieval climate anomaly and the little ice age in arid central asia. *Quaternary Science Reviews*, 178:24–36, 2017. ISSN 0277-3791. doi: 10.1016/j.quascirev.2017.10.026.

S. Therre, J. Fohlmeister, D. Fleitmann, A. Matter, S. J. Burns, J. Arps, A. Schröder-Ritzrau, R. Friedrich, and N. Frank. Climate-induced speleothem radiocarbon variability on socotra island from the last glacial maximum to the younger dryas. *Clim. Past*, 16(1):409–421, 2020. ISSN 1814-9332. doi: 10.5194/cp-16-409-2020.

T. Braun, S. F. M. Breitenbach, V. Skiba, F. A. Lechleitner, E. E. Ray, L. M. Baldini, V. J. Polyak, J. U. L. Baldini, D. J. Kennett, K. M. Prufer, and N. Marwan. Decline in seasonal predictability potentially destabilized classic maya societies. *Communications Earth & Environment*, 4(1):82, 2023. ISSN 2662-4435. doi: ARTN8210.1038/s43247-023-00717-5.

A. Frappier, D. Sahagian, L. A. Gonzalez, and S. J. Carpenter. El nino events recorded by stalagmite carbon isotopes. *Science*, 298(5593):565, 2002. ISSN 1095-9203 (Electronic) 0036-8075 (Linking). doi: 10.1126/science.1076446.

L. M. Baldini, J. U. Baldini, J. N. McElwaine, A. B. Frappier, Y. Asmerom, K. B. Liu, K. M. Prufer, H. E. Ridley, V. Polyak, D. J. Kennett, C. G. Macpherson, V. V. Aquino, J. Awe, and S. F. Breitenbach. Persistent northward north atlantic tropical cyclone track migration over the past five centuries. *Sci Rep*, 6(1):37522, 2016. ISSN 2045-2322 (Electronic) 2045-2322 (Linking). doi: 10.1038/srep37522.

D. Fleitmann, H. Cheng, S. Badertscher, R. L. Edwards, M. Mudelsee, O. M. Göktürk, A. Fankhauser, R. Pickering, C. C. Raible, A. Matter, J. Kramers, and O. Tüysüz. Timing and climatic impact of greenland interstadials recorded in stalagmites from northern turkey. *Geophysical Research Letters*, 36(19), 2009. ISSN 0094-8276. doi: ArtnL1970710.1029/2009gl040050.

E. A. Webb, H. P. Schwarcz, and P. F. Healy. Detection of ancient maize in lowland maya soils using stable carbon isotopes: evidence from caracol, belize. *Journal of*

Archaeological Science, 31(8):1039–1052, 2004. ISSN 0305-4403. doi: 10.1016/j.jas.2004.01.001.

Scott L. Fedick and Louis S. Santiago. Large variation in availability of maya food plant sources during ancient droughts. *Proceedings of the National Academy of Sciences*, 119(1):e2115657118, 2022. doi: 10.1073/pnas.2115657118.

G. A. Islebe, N. Torrescano-Valle, M. Valdez-Hernandez, A. Carrillo-Bastos, and A. A. Aragon-Moreno. Maize and ancient maya droughts. *Sci Rep*, 12(1): 22272, 2022. ISSN 2045-2322 (Electronic) 2045-2322 (Linking). doi: 10.1038/s41598-022-26761-3.

Dominique Genty and Marc Massault. Bomb 14c recorded in laminated speleothems: calculation of dead carbon proportion. *Radiocarbon*, 39(1):33–48, 1997. ISSN 0033-8222.

Christoph Spötl, Jens Fohlmeister, Hai Cheng, and Ronny Boch. Modern aragonite formation at near-freezing conditions in an alpine cave, carnic alps, austria. *Chemical Geology*, 435:60–70, 2016. ISSN 0009-2541.

P. Bajo, A. Borsato, R. Drysdale, Q. Hua, S. Frisia, G. Zanchetta, J. Hellstrom, and J. Woodhead. Stalagmite carbon isotopes and dead carbon proportion (dcp) in a near-closed-system situation: An interplay between sulphuric and carbonic acid dissolution. *Geochimica Et Cosmochimica Acta*, 210:208–227, 2017. ISSN 0016-7037. doi: 10.1016/j.gca.2017.04.038.

Olga Y. Chervyatsova, Sergey S. Potapov, Lyudmila Y. Kuzmina, Yuri V. Dublyansky, Sergey A. Sadykov, Daria V. Kiseleva, Tatyana G. Okuneva, Said-Emin Dzhabrailov, and Gennady V. Samokhin. Sulfuric acid speleogenesis in the north caucasus: Sharo-argun valley caves (chechen republic, russia). *Geomorphology*, 369: 107346, 2020. ISSN 0169-555X. doi: 10.1016/j.geomorph.2020.107346.

Annabel Wolf, Jonathan Lloyd Baker, Rik Tjallingii, Yanjun Cai, Alexander Osinzev, Mariya Antonosyan, Noel Amano, Kathleen Rose Johnson, Vanessa Skiba, Jeremy McCormack, Ola Kwiecien, Olga Yakovlevna Chervyatsova, Yuri Viktorovich Dublyansky, Roman Saidovich Dbar, Hai Cheng, and Sebastian Franz Martin Breitenbach. Western caucasus regional hydroclimate controlled by cold-season temperature variability since the last glacial maximum. *Communications Earth & Environment*, 5(1):66, 2024. ISSN 2662-4435. doi: 10.1038/s43247-023-01151-3.

J. Fohlmeister, D. Scholz, B. Kromer, and A. Mangini. Modelling carbon isotopes of carbonates in cave drip water. *Geochimica Et Cosmochimica Acta*, 75(18):5219–

5228, 2011. ISSN 0016-7037. doi: 10.1016/j.gca.2011.06.023.

A. L. Noronha, K. R. Johnson, C. Y. Hu, J. Y. Ruan, J. R. Southon, and J. E. Ferguson. Assessing influences on speleothem dead carbon variability over the holocene: Implications for speleothem-based radiocarbon calibration. *Earth and Planetary Science Letters*, 394:20–29, 2014. ISSN 0012-821x. doi: 10.1016/j.epsl.2014.03.015.

Quan Hua, Duncan Cook, Jens Fohlmeister, Dan Penny, Paul Bishop, and Solomon Buckman. Radiocarbon dating of a speleothem record of paleoclimate for angkor, cambodia. *Radiocarbon*, 59(6):1873–1890, 2017. ISSN 0033-8222. doi: 10.1017/RDC.2017.115.

Susan Trumbore. Radiocarbon and soil carbon dynamics. *Annual review of earth and planetary sciences*, 37:47–66, 2009. ISSN 0084-6597.

Steffen Therre. *Radiocarbon in Stalagmites: Indicator of Climate Variability and Key to Atmospheric Radiocarbon Reconstruction.* Dissertation, Heidelberg University, 2020.

I. J. Fairchild, A. Borsato, A. F. Tooth, S. Frisia, C. J. Hawkesworth, Y. M. Huang, F. McDermott, and B. Spiro. Controls on trace element (sr-mg) compositions of carbonate cave waters: implications for speleothem climatic records. *Chemical Geology*, 166(3-4):255–269, 2000. ISSN 0009-2541. doi: 10.1016/S0009-2541(99)00216-8.

Michael L. Griffiths, Russell N. Drysdale, Michael K. Gagan, Silvia Frisia, Jian-xin Zhao, Linda K. Ayliffe, Wahyoe S. Hantoro, John C. Hellstrom, Matthew J. Fischer, Yue-Xing Feng, and Bambang W. Suwargadi. Evidence for holocene changes in australian–indonesian monsoon rainfall from stalagmite trace element and stable isotope ratios. *Earth and Planetary Science Letters*, 292(1):27–38, 2010. ISSN 0012-821X. doi: https://doi.org/10.1016/j.epsl.2010.01.002.

J. T. Sliwinski, O. Kost, L. Endres, M. Iglesias, N. Haghipour, S. González-Lemos, and H. M. Stoll. Exploring soluble and colloidally transported trace elements in stalagmites: The strontium-yttrium connection. *Geochimica et Cosmochimica Acta*, 343:64–83, 2023. ISSN 0016-7037. doi: https://doi.org/10.1016/j.gca.2022.12.023.

Mohammadali Faraji, Andrea Borsato, Silvia Frisia, Adam Hartland, John C. Hellstrom, and Alan Greig. High-resolution reconstruction of infiltration in the southern cook islands based on trace elements in speleothems. *Quaternary Research*, pages 1–21, 2023. ISSN 0033-5894. doi: 10.1017/qua.2023.51.

N. Kaushal, F. A. Lechleitner, M. Wilhelm, K. Azennoud, J. C. Bühler, K. Braun, Y. Ait Brahim, A. Baker, Y. Burstyn, L. Comas-Bru, J. Fohlmeister, Y. Goldsmith, S. P. Harrison, I. G. Hatvani, K. Rehfeld, M. Ritzau, V. Skiba, H. M. Stoll, J. G. Szűcs, P. Tanos, P. C. Treble, V. Azevedo, J. L. Baker, A. Borsato, S. Chawchai, A. Columbu, L. Endres, J. Hu, Z. Kern, A. Kimbrough, K. Koç, M. Markowska, B. Martrat, S. Masood Ahmad, C. Nehme, V. F. Novello, C. Pérez-Mejías, J. Ruan, N. Sekhon, N. Sinha, C. V. Tadros, B. H. Tiger, S. Warken, A. Wolf, H. Zhang, and Sisal Working Group members. Sisalv3: a global speleothem stable isotope and trace element database. *Earth Syst. Sci. Data*, 16(4):1933–1963, 2024. ISSN 1866-3516. doi: 10.5194/essd-16-1933-2024. ESSD.

C. C. Day and G. M. Henderson. Controls on trace-element partitioning in cave-analogue calcite. *Geochimica Et Cosmochimica Acta*, 120:612–627, 2013. ISSN 0016-7037. doi: 10.1016/j.gca.2013.05.044.

Darrel M. Tremaine and Philip N. Froelich. Speleothem trace element signatures: A hydrologic geochemical study of modern cave dripwaters and farmed calcite. *Geochimica et Cosmochimica Acta*, 121:522–545, 2013. ISSN 00167037. doi: 10.1016/j.gca.2013.07.026.

Andrea Borsato, Silvia Frisia, Peter M. Wynn, Ian J. Fairchild, and Renza Miorandi. Sulphate concentration in cave dripwater and speleothems: long-term trends and overview of its significance as proxy for environmental processes and climate changes. *Quaternary Science Reviews*, 127:48–60, 2015. ISSN 0277-3791. doi: https://doi.org/10.1016/j.quascirev.2015.05.016.

R. N. Drysdale, G. Zanchetta, I. Baneschi, M. Guidi, I. Isola, I. Couchoud, L. Piccini, A. Greig, H. Wong, J. D. Woodhead, E. Regattieri, E. Corrick, B. Paul, C. Spötl, E. Denson, J. Gordon, S. Jaillet, F. Dux, and J. C. Hellstrom. Partitioning of mg, sr, ba and u into a subaqueous calcite speleothem. *Geochimica Et Cosmochimica Acta*, 264:67–91, 2019. ISSN 0016-7037. doi: 10.1016/j.gca.2019.08.001.

Oliver Kost, Jakub Sliwinski, Nils Gies, Mona Lueder, and Heather Stoll. The influence of fluid inclusions, organics, and calcite fabric on trace element distributions in stalagmites. *Frontiers in Earth Science*, 11:1240888, 2023. ISSN 2296-6463.

I. J. Fairchild, C. L. Smith, A. Baker, L. Fuller, C. Spötl, D. Mattey, F. McDermott, and Eimp. Modification and preservation of environmental signals in speleothems. *Earth-Science Reviews*, 75(1-4):105–153, 2006. ISSN 0012-8252. doi: 10.1016/j.earscirev.2005.08.003.

K. R. Johnson, C. Y. Hu, N. S. Belshaw, and G. M. Henderson. Seasonal trace-element and stable-isotope variations in a chinese speleothem: The potential for high-resolution paleomonsoon reconstruction. *Earth and Planetary Science Letters*, 244(1-2):394–407, 2006. ISSN 0012-821x. doi: 10.1016/j.epsl.2006.01.064.

D. J. Sinclair, J. L. Banner, F. W. Taylor, J. Partin, J. Jenson, J. Mylroie, E. Goddard, T. Quinn, J. Jocson, and B. Miklavic. Magnesium and strontium systematics in tropical speleothems from the western pacific. *Chemical Geology*, 294:1–17, 2012. ISSN 0009-2541. doi: 10.1016/j.chemgeo.2011.10.008.

S. E. Rodriguez-Cruz, R. A. Jockusch, and E. R. Williams. Hydration energies and structures of alkaline earth metal ions, m2+(h2o)n, n = 5-7, m = mg, ca, sr, and ba. *J Am Chem Soc*, 121(38):8898–906, 1999. ISSN 0002-7863 (Print) 1520-5126 (Electronic) 0002-7863 (Linking). doi: 10.1021/ja9911871.

Heather M. Stoll, Wolfgang Müller, and Manolo Prieto. I-stal, a model for interpretation of mg/ca, sr/ca and ba/ca variations in speleothems and its forward and inverse application on seasonal to millennial scales. *Geochemistry, Geophysics, Geosystems*, 13(9), 2012. ISSN 1525-2027. doi: 10.1029/2012gc004183.

Y. M. Huang and I. J. Fairchild. Partitioning of sr and mg into calcite under karst-analogue experimental conditions. *Geochimica Et Cosmochimica Acta*, 65(1):47–62, 2001. ISSN 0016-7037. doi: 10.1016/S0016-7037(00)00513-5.

D. J. Sinclair. Two mathematical models of mg and sr partitioning into solution during incongruent calcite dissolution implications for dripwater and speleothem studies. *Chemical Geology*, 283(3-4):119–133, 2011. ISSN 0009-2541. doi: 10.1016/j.chemgeo.2010.05.022.

Darrel M Tremaine, Daniel J Sinclair, Heather M Stoll, Maria Lagerström, Carlos P Carvajal, and Robert M Sherrell. A two-year automated dripwater chemistry study in a remote cave in the tropical south pacific: Using [cl−] as a conservative tracer for seasalt contribution of major cations. *Geochimica et Cosmochimica Acta*, 184: 289–310, 2016. ISSN 0016-7037.

J. A. Wassenburg, S. Riechelmann, A. Schröder-Ritzrau, D. F. C. Riechelmann, D. K. Richter, A. Immenhauser, M. Terente, S. Constantin, A. Hachenberg, M. Hansen, and D. Scholz. Calcite mg and sr partition coefficients in cave environments: Implications for interpreting prior calcite precipitation in speleothems. *Geochimica Et Cosmochimica Acta*, 269:581–596, 2020. ISSN 0016-7037. doi: 10.1016/j.gca.2019.11.011.

R. Belli, A. Borsato, S. Frisia, R. Drysdale, R. Maas, and A. Greig. Investigating the hydrological significance of stalagmite geochemistry (mg, sr) using sr isotope and particulate element records across the late glacial-to-holocene transition. *Geochimica et Cosmochimica Acta*, 199:247–263, 2017. ISSN 0016-7037. doi: 10.1016/j.gca.2016.10.024.

Clément Bourdin, Eric Douville, and Dominique Genty. Alkaline-earth metal and rare-earth element incorporation control by ionic radius and growth rate on a stalagmite from the chauvet cave, southeastern france. *Chemical Geology*, 290(1-2):1–11, 2011. ISSN 00092541. doi: 10.1016/j.chemgeo.2011.08.006.

P. L. Smedley and D. G. Kinniburgh. Uranium in natural waters and the environment: Distribution, speciation and impact. *Applied Geochemistry*, 148:105534, 2023. ISSN 0883-2927. doi: https://doi.org/10.1016/j.apgeochem.2022.105534.

Amos Frumkin and Mordechai Stein. The sahara–east mediterranean dust and climate connection revealed by strontium and uranium isotopes in a jerusalem speleothem. *Earth and Planetary Science Letters*, 217(3-4):451–464, 2004. ISSN 0012821X. doi: 10.1016/s0012-821x(03)00589-2.

J. C. Hellstrom and M. T. McCulloch. Multi-proxy constraints on the climatic significance of trace element records from a new zealand speleothem. *Earth and Planetary Science Letters*, 179(2):287–297, 2000. ISSN 0012-821x. doi: 10.1016/S0012-821x(00)00115-1.

L. Chen, J. Y. Huang, S. H. Liu, Q. Chen, L. Yang, Iven He, X. J. Mi, Y. Yang, and H. Y. Zhou. Variation of u/ca ratio in the stalagmite si3 from ne siehuan. central china and its cliniatie significance. *Bulletin of Mineralogy Petrology and Geochemistry*, 35:183–187, 2016. doi: 10.3969/j.issn.1007-2802.2016.01.022.

Q. Chen, S. H. Liu, H. B. He, J. Tang, J. X. Zhao, Y. X. Feng, X. Q. Yang, and H. Y. Zhou. Seasonal variations of uranium in karst waters from northeastern sichuan, central china and controlling mechanisms. *Geochemistry International*, 58 (1):103–112, 2020. ISSN 0016-7029. doi: 10.1134/S0016702920010048.

D. Langmuir. Uranium solution-mineral equilibria at low-temperatures with applications to sedimentary ore-deposits. *Geochimica Et Cosmochimica Acta*, 42(6): 547–569, 1978. ISSN 0016-7037. doi: 10.1016/0016-7037(78)90001-7.

Heather M. Stoll, Chris Day, Franziska Lechleitner, Oliver Kost, Laura Endres, Jakub Sliwinski, Carlos Pérez-Mejías, Hai Cheng, and Denis Scholz. Distinguishing the combined vegetation and soil component of 13c variation in speleothem records from subsequent degassing and prior calcite precipitation effects. *Climate of the Past*, 19(12):2423–2444, 2023. ISSN 1814-9332. doi: 10.5194/cp-19-2423-2023.

J. T. Sliwinski and H. M. Stoll. Combined fluorescence imaging and la-icp-ms trace element mapping of stalagmites: Microfabric identification and interpretation. *Chemical Geology*, 581:120397, 2021. ISSN 0009-2541. doi: 10.1016/j.chemgeo.2021.120397.

Valentina Vanghi, Andrea Borsato, Silvia Frisia, Daryl L. Howard, Gertruida Gloy, John Hellstrom, and Petra Bajo. High-resolution synchrotron x-ray fluorescence investigation of calcite coralloid speleothems: Elemental incorporation and their potential as environmental archives. *Sedimentology*, 66(7):2661–2685, 2019. ISSN 0037-0746. doi: 10.1111/sed.12607.

F. Adrian. *Saisonalität in Stalagmiten der Estrella Höhle, Mexiko: Spurenelementuntersuchung mittels LA-ICP-MS.* Bachelor's thesis, Heidelberg University, 2023.

M. Stange. *Einfluss von Saisonalitäten und Starkregenereignissen auf Spurenelemente in einem Stalagmiten aus Yucatán, Mexiko.* Bachelor's thesis, Heidelberg University, 2024.

C. Kolb. *Modeling Past Environmental Conditions Through Speleothem Carbon Isotope Analysis: A Case Study From Yucatán.* Master's thesis, Heidelberg University, 2024.

F. Tec. *Centro de Interpretación Biocultural en Áaktun Kóopo, una Caverna del Complejo Santa Rita, Yucatán, México.* Master's thesis, UNIVERSIDAD AUTÓNOMA DE YUCATÁN, 2021.

Karl Sigismund Kunth, Alexander von Humboldt, and Aimé Bonpland. *Nova genera et species plantarum.* Whaddon & Wesley, 1976.

Christian Thomas, Carlos Evia Cervantes, Yan Thomas, and Fatima Tec Pool. *Las cuevas de Yucatán: la région de Valladolid.* Xibalba, 2011.

M. Gómez. *Práctica Mortuoria Maya Prehispánica En Una Cueva En El Oriente De Yucatán: Áaktun Kóopo.* Master's thesis, Escuela Nacional de Antropología e Historia (ENAH), Ciudad de México, 2020.

Silvia Frisia, Andrea Borsato, Ian J Fairchild, Frank McDermott, and Enrico M Selmo. Aragonite-calcite relationships in speleothems (grotte de clamouse, france): environment, fabrics, and carbonate geochemistry. *Journal of Sedimentary Research*, 72(5):687–699, 2002. ISSN 1938-3681.

Christine Perrin, Laurent Prestimonaco, Guilhem Servelle, Romain Tilhac, Marion Maury, and Patrick Cabrol. Aragonite–calcite speleothems: identifying original and diagenetic features. *Journal of Sedimentary Research*, 84(4):245–269, 2014. ISSN 1938-3681.

S. Frisia. Microstratigraphic logging of calcite fabrics in speleothems as tool for palaeoclimate studies. *International Journal of Speleology*, 44(1):1–16, 2015. ISSN 0392-6672. doi: 10.5038/1827-806x.44.1.1.

Eric Douville, Eline Sallé, Norbert Frank, Markus Eisele, Edwige Pons-Branchu, and Sophie Ayrault. Rapid and accurate u–th dating of ancient carbonates using inductively coupled plasma-quadrupole mass spectrometry. *Chemical Geology*, 272 (1-4):1–11, 2010. ISSN 00092541. doi: 10.1016/j.chemgeo.2010.01.007.

Lélia Matos, Furu Mienis, Claudia Wienberg, Norbert Frank, Cornelia Kwiatkowski, Jeroen Groeneveld, François Thil, Fatima Abrantes, Marina R Cunha, and Dierk Hebbeln. Interglacial occurrence of cold-water corals off cape lookout (nw atlantic): First evidence of the gulf stream influence. *Deep sea research part I: oceanographic research papers*, 105:158–170, 2015. ISSN 0967-0637.

A. M. Wefing, J. Arps, P. Blaser, C. Wienberg, D. Hebbeln, and N. Frank. High precision u-series dating of scleractinian cold-water corals using an automated chromatographic u and th extraction. *Chemical Geology*, 475:140–148, 2017. ISSN 0009-2541. doi: 10.1016/j.chemgeo.2017.10.036.

S. Therre, L. Pross, R. Friedrich, M. Trüssel, and N. Frank. Heidelberg radiocarbon lab - establishing a new carbon dioxide extraction line for carbonate samples. *Radiocarbon*, 63(3):915–924, 2021. ISSN 0033-8222. doi: 10.1017/Rdc.2021.28.

H. A. Synal, M. Stocker, and M. Suter. Micadas: A new compact radiocarbon ams system. *Nuclear Instruments & Methods in Physics Research Section B-Beam Interactions with Materials and Atoms*, 259(1):7–13, 2007. ISSN 0168-583x. doi: 10.1016/j.nimb.2007.01.138.

B. Kromer, S. Lindauer, H. A. Synal, and L. Wacker. Mams - a new ams facility at the curt-engelhorn-centre for achaeometry, mannheim, germany. *Nuclear Instruments & Methods in Physics Research Section B-Beam Interactions with Materials and Atoms*, 294:11–13, 2013. ISSN 0168-583x. doi: 10.1016/j.nimb.2012.01.015.

Elvira Beisel. *Radiocarbon in Cold-Water Corals of the Eastern Atlantic Thermocline Over the Last 38,000 Years.* Dissertation, Heidelberg University, 2024.

Kazimierz Rozanski, Willibald Stichler, Roberto Gonfiantini, EM Scott, RP Beukens, Bernd Kromer, and Johannes Van Der Plicht. The iaea 14c intercomparison exercise 1990. *Radiocarbon*, 34(3):506–519, 1992. ISSN 0033-8222.

Matthias Ruff, Lukas Wacker, Heinz W Gäggeler, Martin Suter, Hans-Arno Synal, and Sönke Szidat. A gas ion source for radiocarbon measurements at 200 kv. *Radiocarbon*, 49(2):307–314, 2007. ISSN 0033-8222.

Negar Haghipour, Blanca Ausin, Muhammed O Usman, N Ishikawa, Lukas Wacker, Caroline Welte, Kosuke Ueda, and Timothy I Eglinton. Compound-specific radiocarbon analysis by elemental analyzer–accelerator mass spectrometry: Precision and limitations. *Analytical Chemistry*, 91(3):2042–2049, 2018. ISSN 0003-2700.

Andy Baker, Gregoire Mariethoz, Laia Comas-Bru, Andreas Hartmann, Silvia Frisia, Andrea Borsato, Pauline C Treble, and Asfawossen Asrat. The properties of annually laminated stalagmites-a global synthesis. *Reviews of Geophysics*, 59(2): e2020RG000722, 2021. ISSN 8755-1209.

A. Borsato, S. Frisia, D. Howard, and A. Greig. A guide to synchrotron hard x-ray fluorescence mapping of annually laminated stalagmites: Sample preparation, analysis and evaluation. *Spectrochimica Acta Part B-Atomic Spectroscopy*, 185: 106308, 2021. ISSN 0584-8547. doi: ARTN10630810.1016/j.sab.2021.106308.

Ian J. Orland, Yuval Burstyn, Miryam Bar-Matthews, Reinhard Kozdon, Avner Ayalon, Alan Matthews, and John W. Valley. Seasonal climate signals (1990–2008) in a modern soreq cave stalagmite as revealed by high-resolution geochemical analysis. *Chemical Geology*, 363:322–333, 2014. ISSN 0009-2541. doi: https://doi.org/10.1016/j.chemgeo.2013.11.011.

Mark S Roberts, Peter L Smart, and Andy Baker. Annual trace element variations in a holocene speleothem. *Earth and Planetary Science Letters*, 154(1-4):237–246, 1998. ISSN 0012-821X.

Jessica K. Wang, Kathleen R. Johnson, Andrea Borsato, Dillon J. Amaya, Michael L. Griffiths, Gideon M. Henderson, Silvia Frisia, and Andrew Mason. Hydroclimatic variability in southeast asia over the past two millennia. *Earth and Planetary Science Letters*, 525:115737, 2019. ISSN 0012-821X. doi: https://doi.org/10.1016/j.epsl.2019.115737.

Silvia Frisia, Andrea Borsato, Ian J Fairchild, and Frank McDermott. Calcite fabrics, growth mechanisms, and environments of formation in speleothems from the italian alps and southwestern ireland. *Journal of Sedimentary Research*, 70(5):1183–1196, 2000. ISSN 1938-3681.

K. P. Jochum, U. Weis, B. Stoll, D. Kuzmin, Q. C. Yang, I. Raczek, D. E. Jacob, A. Stracke, K. Birbaum, D. A. Frick, D. Günther, and J. Enzweiler. Determination of reference values for nist srm 610-617 glasses following iso guidelines. *Geostandards and Geoanalytical Research*, 35(4):397–429, 2011. ISSN 1639-4488. doi: 10.1111/j.1751-908X.2011.00120.x.

Michael Schulz and Manfred Mudelsee. Redfit: estimating red-noise spectra directly from unevenly spaced paleoclimatic time series. *Computers & Geosciences*, 28 (3):421–426, 2002. ISSN 0098-3004. doi: https://doi.org/10.1016/S0098-3004(01)00044-9.

Andy Bunn, Mikko Korpela, Franco Biondi, Filipe Campelo, Pierre Mérian, Fares Qeadan, and Christian Zang. dplr: dendrochronology program library in r. *R package version*, 1(1), 2020.

Tarik C Gouhier, Aslak Grinsted, and Viliam Simko. R package biwavelet: conduct univariate and bivariate wavelet analyses (version 0.20. 19), 2019.

KR Ludwig. Mathematical–statistical treatment of data and errors for 230th/u geochronology. *Reviews in Mineralogy and Geochemistry*, 52(1):631–656, 2003. ISSN 1529-6466.

K Ludwig. Isoplot version 4.15: a geochronological toolkit for microsoft excel. *Berkeley Geochronology Center, Special Publication*, 4:247–270, 2008.

P. Vermeesch. Isoplotr: A free and open toolbox for geochronology. *Geoscience Frontiers*, 9(5):1479–1493, 2018. ISSN 1674-9871. doi: 10.1016/j.gsf.2018.04.001.

Chao-Jun Chen and Ting-Yong Li. Geochemical characteristics of cave drip water respond to enso based on a 6-year monitoring work in yangkou cave, southwest china. *Journal of Hydrology*, 561:896–907, 2018. ISSN 0022-1694. doi: https://doi.org/10.1016/j.jhydrol.2018.04.061.

S. M. Mclennan, W. B. Nance, and S. R. Taylor. Rare-earth element-thorium correlations in sedimentary-rocks, and the composition of the continental crust. *Geochimica Et Cosmochimica Acta*, 44(11):1833–1839, 1980. ISSN 0016-7037. doi: 10.1016/0016-7037(80)90232-X.

Lorraine E. Lisiecki and Maureen E. Raymo. A pliocene-pleistocene stack of 57 globally distributed benthic 18o records. *Paleoceanography*, 20(1):n/a–n/a, 2005. ISSN 08838305. doi: 10.1029/2004pa001071.

Daniel Marcos Bonotto and JN Andrews. The mechanism of 234u238u activity ratio enhancement in karstic limestone groundwater. *Chemical geology*, 103(1-4):193–206, 1993. ISSN 0009-2541. doi: 10.1016/0009-2541(93)90301-X.

James B. Paces, Kenneth R. Ludwig, Zell E. Peterman, and Leonid A. Neymark. 234u/238u evidence for local recharge and patterns of ground-water flow in the vicinity of yucca mountain, nevada, usa. *Applied Geochemistry*, 17(6):751–779, 2002. ISSN 08832927. doi: 10.1016/s0883-2927(02)00037-9.

K. Maher, D. E. Ibarra, J. L. Oster, D. M. Miller, J. L. Redwine, M. C. Reheis, and J. W. Harden. Uranium isotopes in soils as a proxy for past infiltration and precipitation across the western united states. *American Journal of Science*, 314 (4):821–857, 2014. ISSN 0002-9599. doi: 10.2475/04.2014.01.

S. C. Priestley, T. E. Payne, J. J. Harrison, V. E. A. Post, P. Shand, A. J. Love, and D. L. Wohling. Use of u-isotopes in exploring groundwater flow and inter-aquifer leakage in the south-western margin of the great artesian basin and arckaringa basin, central australia. *Applied Geochemistry*, 98:331–344, 2018. ISSN 0883-2927. doi: 10.1016/j.apgeochem.2018.10.002.

Michael Smyth, Ezra Zubrow, David Ortegón Zapata, Nicholas P Dunning, Eric M Weaver, Jane E Slater, and Philip van Beynen. Exploratory research into arctic climate change and ancient maya response: Paleoclimate reconstruction and archaeological investigation at the puuc region of yucatan, mexico. 2011.

M. P. Smyth, N. P. Dunning, E. M. Weaver, P. van Beynen, and D. O. Zapata. The perfect storm: climate change and ancient maya response in the puuc hills region of yucatan. *Antiquity*, 91(356):490–509, 2017a. ISSN 0003-598x. doi: 10.15184/aqy.2016.266.

Amy Benoit Frappier, James Pyburn, Aurora D. Pinkey-Drobnis, Xianfeng Wang, D. Reide Corbett, and Bruce H. Dahlin. Two millennia of tropical cyclone-induced mud layers in a northern yucatán stalagmite: Multiple overlapping climatic hazards during the maya terminal classic "megadroughts". *Geophysical Research Letters*, 41 (14):5148–5157, 2014. ISSN 00948276. doi: 10.1002/2014gl059882.

Aviva Intveld, Sebastian FM Breitenbach, Stacy A Carolin, Daniel H James, Ola Kwiecien, Mark Brenner, Carlos Peraza Lope, and David A Hodell. Comparison of historical and speleothem (paleo) climate records from northwest yucatán (mexico). In *EGU General Assembly Conference Abstracts*, page 18659.

Catherine M Sherwin and James UL Baldini. Cave air and hydrological controls on prior calcite precipitation and stalagmite growth rates: Implications for palaeoclimate reconstructions using speleothems. *Geochimica et Cosmochimica Acta*, 75(14): 3915–3929, 2011. ISSN 0016-7037.

Corinne I. Wong, Jay L. Banner, and Marylynn Musgrove. Seasonal dripwater mg/ca and sr/ca variations driven by cave ventilation: Implications for and modeling of speleothem paleoclimate records. *Geochimica et Cosmochimica Acta*, 75(12): 3514–3529, 2011. ISSN 0016-7037. doi: 10.1016/j.gca.2011.03.025.

Rolf Vieten, Amos Winter, Sophie Warken, Andrea Schröder-Ritzrau, Thomas Miller, and Denis Scholz. Seasonal temperature variations controlling cave ventilation processes in cueva larga, puerto rico. *International Journal of Speleology*, 45: 259–273, 2016. doi: 10.5038/1827-806X.45.3.1983.

Natasha Sekhon, Valdir F. Novello, Francisco W. Cruz, Barbara E. Wortham, Tulio G. R. Ribeiro, and Daniel O. Breecker. Diurnal to seasonal ventilation in brazilian caves. *Global and Planetary Change*, 197:103378, 2021. ISSN 0921-8181. doi: https://doi.org/10.1016/j.gloplacha.2020.103378.

Franci Gabrovšek. How do caves breathe: The airflow patterns in karst underground. *Plos one*, 18(4):e0283767, 2023. ISSN 1932-6203.

Adam Hartland, Ian J. Fairchild, Jamie R. Lead, Andrea Borsato, Andy Baker, Silvia Frisia, and Mohammed Baalousha. From soil to cave: Transport of trace metals by natural organic matter in karst dripwaters. *Chemical Geology*, 304-305:68–82, 2012. ISSN 0009-2541. doi: https://doi.org/10.1016/j.chemgeo.2012.01.032.

Mohammadali Faraji, Andrea Borsato, Silvia Frisia, John C Hellstrom, Andrew Lorrey, Adam Hartland, Alan Greig, and David P Mattey. Accurate dating of stalagmites from low seasonal contrast tropical pacific climate using sr 2d maps, fabrics and annual hydrological cycles. *Scientific reports*, 11(1):1–16, 2021. ISSN 2045-2322.

A. R. Atwood, D. S. Battisti, E. Wu, D. M. W. Frierson, and J. P. Sachs. Data-model comparisons of tropical hydroclimate changes over the common era. *Paleoceanography and Paleoclimatology*, 36(7):e2020PA003934, 2021. ISSN 2572-4517. doi: ARTNe2020PA00393410.1029/2020PA003934.

David L Webster. *The fall of the ancient Maya: solving the mystery of the Maya collapse*. Thames & Hudson London, 2002. ISBN 0500051135.

Richardson B. Gill, Paul A. Mayewski, Johan Nyberg, Gerald H. Haug, and Larry C. Peterson. Drought and the maya collapse. *Ancient Mesoamerica*, 18(2):283–302, 2007. ISSN 0956-5361. doi: 10.1017/S0956536107000193.

Claire E. Ebert, Keith M. Prufer, Martha J. Macri, Bruce Winterhalder, and Douglas J. Kennett. Terminal long count dates and the disintegration of classic period maya polities. *Ancient Mesoamerica*, 25(2):337–356, 2015. ISSN 0956-5361 1469-1787. doi: 10.1017/s0956536114000248.

Claudia Fensterer, Denis Scholz, Dirk L. Hoffmann, Christoph Spötl, Andrea Schröder-Ritzrau, Christian Horn, Jesus M. Pajón, and Augusto Mangini. Millennial-scale climate variability during the last 12.5 ka recorded in a caribbean speleothem. *Earth and Planetary Science Letters*, 361:143–151, 2013. ISSN 0012821X. doi: 10.1016/j.epsl.2012.11.019.

Jiaying Wu, David F. Porinchu, and Sally P. Horn. Late holocene hydroclimate variability in costa rica: Signature of the terminal classic drought and the medieval climate anomaly in the northern tropical americas. *Quaternary Science Reviews*, 215:144–159, 2019. ISSN 0277-3791. doi: https://doi.org/10.1016/j.quascirev.2019.04.023.

F. W. Cruz, S. J. Burns, M. Jercinovic, I. Karmann, W. D. Sharp, and M. Vuille. Evidence of rainfall variations in southern brazil from trace element ratios (mg/ca and sr/ca) in a late pleistocene stalagmite. *Geochimica Et Cosmochimica Acta*, 71 (9):2250–2263, 2007. ISSN 0016-7037. doi: 10.1016/j.gca.2007.02.005.

A. Carrillo-Bastos, G. A. Islebe, N. Torrescano-Valle, and N. E. González. Holocene vegetation and climate history of central quintana roo, yucatan peninsula, mexico. *Review of Palaeobotany and Palynology*, 160(3-4):189–196, 2010. ISSN 0034-6667. doi: 10.1016/j.revpalbo.2010.02.013.

Rodrigo Vargas and Michael F Allen. Environmental controls and the influence of vegetation type, fine roots and rhizomorphs on diel and seasonal variation in soil respiration. *New Phytologist*, 179(2):460–471, 2008. ISSN 0028-646X.

Tim Beach, Sheryl Luzzadder-Beach, Duncan Cook, Nicholas Dunning, Douglas J. Kennett, Samantha Krause, Richard Terry, Debora Trein, and Fred Valdez. Ancient maya impacts on the earth's surface: An early anthropocene analog? *Quaternary*

Science Reviews, 124:1–30, 2015. ISSN 02773791. doi: 10.1016/j.quascirev.2015.05.028.

Robert Owen, Christopher C. Day, and Gideon M. Henderson. Cavecalc: A new model for speleothem chemistry & isotopes. *Computers & Geosciences*, 119:115–122, 2018. ISSN 0098-3004. doi: https://doi.org/10.1016/j.cageo.2018.06.011.

Johannes Gehrke, Raghu Ramakrishnan, and Venkatesh Ganti. Rainforest—a framework for fast decision tree construction of large datasets. *Data Mining and Knowledge Discovery*, 4:127–162, 2000. ISSN 1384-5810.

Daniel Wolfensberger, Marco Gabella, Marco Boscacci, Urs Germann, and Alexis Berne. Rainforest: a random forest algorithm for quantitative precipitation estimation over switzerland. *Atmospheric Measurement Techniques*, 14(4):3169–3193, 2021. ISSN 1867-1381.

S. Morell-Hart, L. Dussol, and S. L. Fedick. Agriculture in the ancient maya lowlands (part 1): Paleoethnobotanical residues and new perspectives on plant management. *Journal of Archaeological Research*, 31(4):561–615, 2023. ISSN 1059-0161. doi: 10.1007/s10814-022-09180-w.

Robert J. Oglesby, Thomas L. Sever, William Saturno, David J. Erickson, and Jayanthi Srikishen. Collapse of the maya: Could deforestation have contributed? *Journal of Geophysical Research: Atmospheres*, 115(D12), 2010. ISSN 0148-0227. doi: 10.1029/2009jd011942.

B. I. Cook, K. J. Anchukaitis, J. O. Kaplan, M. J. Puma, M. Kelley, and D. Gueyffier. Pre-columbian deforestation as an amplifier of drought in mesoamerica. *Geophysical Research Letters*, 39(16):n/a–n/a, 2012. ISSN 0094-8276. doi: ArtnL1670610.1029/2012gl052565.

G. A. Islebe, H. Hooghiemstra, M. Brenner, J. H. Curtis, and D. A. Hodell. A holocene vegetation history from lowland guatemala. *Holocene*, 6(3):265–271, 1996. ISSN 0959-6836. doi: 10.1177/095968369600600302.

J. H. Curtis, M. Brenner, D. A. Hodell, R. A. Balser, G. A. Islebe, and H. Hooghiemstra. A multi-proxy study of holocene environmental change in the maya lowlands of peten, guatemala. *Journal of Paleolimnology*, 19(2):139–159, 1998. ISSN 0921-2728. doi: 10.1023/A:1007968508262.

D. Wahl, R. Byrne, T. Schreiner, and R. Hansen. Holocene vegetation change in the northern peten and its implications for maya prehistory. *Quaternary Research*, 65 (3):380–389, 2006. ISSN 0033-5894. doi: 10.1016/j.yqres.2005.10.004.

F. S. Anselmetti, D. A. Hodell, D. Ariztegui, M. Brenner, and M. F. Rosenmeier. Quantification of soil erosion rates related to ancient maya deforestation. *Geology*, 35(10):915–918, 2007. ISSN 0091-7613. doi: 10.1130/G23834a.1.

A. D. Mueller, G. A. Islebe, F. S. Anselmetti, D. Ariztegui, M. Brenner, D. A. Hodell, I. Hajdas, Y. Hamann, G. H. Haug, and D. J. Kennett. Recovery of the forest ecosystem in the tropical lowlands of northern guatemala after disintegration of classic maya polities. *Geology*, 38(6):523–526, 2010. ISSN 0091-7613. doi: 10.1130/G30797.1.

D. Battistel, M. Roman, A. Marchetti, N. M. Kehrwald, M. Radaelli, E. Balliana, G. Toscano, and C. Barbante. Anthropogenic impact in the maya lowlands of peten, guatemala, during the last 5500 years. *Journal of Quaternary Science*, 33 (2):166–176, 2018. ISSN 0267-8179. doi: 10.1002/jqs.3013.

William J Folan, Armando Anaya Hernandez, Ellen R Kintz, Laraine A Fletcher, Raymundo Gonzalez Heredia, Jacinto May Hau, and Nicolas Caamal Canche. Coba, quintana roo, mexico: a recent analysis of the social, economic and political organization of a major maya urban center. *Ancient Mesoamerica*, pages 59–70, 2009. ISSN 0956-5361.

Sarah Kurnick, David Rogoff, and Iliana Ancona Aragón. A preliminary revised life history of punta laguna, yucatan, mexico: A persistent place. *Ancient Mesoamerica*, 35(1):278–303, 2023. ISSN 0956-5361 1469-1787. doi: 10.1017/s0956536123000093.

Adán Pacheco Benítez and Ana María Parrilla Albuerne. El naranjal, quintana roo (méxico): un sitio megalítico en las tierras bajas del norte. *Mayab*, (17):5–19, 2004. ISSN 1130-6157.

Leticia Vargas De la Peña, Alejandra Alonso Olvera, Víctor R Castillo Borges, and Alfonso Lacadena García-Gallo. *Ek'BalamA Maya city in the urban landscape of Yucatan*, pages 364–383. Routledge, 2020. ISBN 1351029584.

Lingli Liu, Xin Wang, Marc J. Lajeunesse, Guofang Miao, Shilong Piao, Shiqiang Wan, Yuxin Wu, Zhenhua Wang, Sen Yang, Ping Li, and Meifeng Deng. A cross-biome synthesis of soil respiration and its determinants under simulated precipitation changes. *Global Change Biology*, 22(4):1394–1405, 2016. ISSN 1354-1013. doi: https://doi.org/10.1111/gcb.13156.

Yue Du, Ying-Ping Wang, Fanglong Su, Jun Jiang, Chen Wang, Mengxiao Yu, and Junhua Yan. The response of soil respiration to precipitation change is asymmetric and differs between grasslands and forests. *Global Change Biology*, 26(10):6015–6024, 2020. ISSN 1354-1013. doi: https://doi.org/10.1111/gcb.15270.

Kristiina Karhu, Marc D. Auffret, Jennifer A. J. Dungait, David W. Hopkins, James I. Prosser, Brajesh K. Singh, Jens-Arne Subke, Philip A. Wookey, Göran I. Ågren, Maria-Teresa Sebastià, Fabrice Gouriveau, Göran Bergkvist, Patrick Meir, Andrew T. Nottingham, Norma Salinas, and Iain P. Hartley. Temperature sensitivity of soil respiration rates enhanced by microbial community response. *Nature*, 513 (7516):81–84, 2014. ISSN 1476-4687. doi: 10.1038/nature13604.

D. Wahl, F. Estrada-Belli, and L. Anderson. A 3400 year paleolimnological record of prehispanic human-environment interactions in the holmul region of the southern maya lowlands. *Palaeogeography Palaeoclimatology Palaeoecology*, 379:17–31, 2013. ISSN 0031-0182. doi: 10.1016/j.palaeo.2013.03.006.

D. Wahl, R. Byrne, and L. Anderson. An 8700 year paleoclimate reconstruction from the southern maya lowlands. *Quaternary Science Reviews*, 103:19–25, 2014. ISSN 0277-3791. doi: 10.1016/j.quascirev.2014.08.004.

Marie-Alexandrine Sicre, Jérémy Jacob, Ullah Ezat, Sonia Rousse, Catherine Kissel, Pascal Yiou, Jón Eiríksson, Karen Luise Knudsen, Eystein Jansen, and Jean-Louis Turon. Decadal variability of sea surface temperatures off north iceland over the last 2000 years. *Earth and Planetary Science Letters*, 268(1):137–142, 2008. ISSN 0012-821X. doi: https://doi.org/10.1016/j.epsl.2008.01.011.

J. B. Wurtzel, D. E. Black, R. C. Thunell, L. C. Peterson, E. J. Tappa, and S. Rahman. Mechanisms of southern caribbean sst variability over the last two millennia. *Geophysical Research Letters*, 40(22):5954–5958, 2013. ISSN 0094-8276. doi: 10.1002/2013gl058458.

A. Zhuravleva, H. A. Bauch, M. Mohtadi, K. Fahl, and M. Kienast. Caribbean salinity anomalies contributed to variable north atlantic circulation and climate during the common era. *Sci Adv*, 9(44):eadg2639, 2023. ISSN 2375-2548 (Electronic) 2375-2548 (Linking). doi: 10.1126/sciadv.adg2639.

N. E. Graham, C. M. Ammann, D. Fleitmann, K. M. Cobb, and J. Luterbacher. Support for global climate reorganization during the ”medieval climate anomaly”. *Climate Dynamics*, 37(5-6):1217–1245, 2011. ISSN 0930-7575. doi: 10.1007/s00382-010-0914-z.

M. C. Peros, S. Collins, J. G. Martínez-López, L. W. V. López, M. A. P. Sosa, L. F. Brisson, F. Hardy, M. Lamothe, P. J. van Hengstum, B. Phillips, K. Broad, J. Heinerth, E. Bermúdez, E. L. Cabrera, Z. Masson, G. Deole, F. Oliva, C. Jaskolski, and F. E. Amador. Multi-proxy paleohydrological and paleoecological reconstruction of a subaquatic cave in western cuba. *Palaeogeography Palaeoclimatology Palaeoecology*, 627:111725, 2023. ISSN 0031-0182. doi: ARTN11172510.1016/j.palaeo.2023.111725.

Arnaud Czaja. Why is north tropical atlantic sst variability stronger in boreal spring? *Journal of Climate*, 17(15):3017–3025, 2004. ISSN 0894-8755.

W. Yang, E. Wallace, G. A. Vecchi, J. P. Donnelly, J. Emile-Geay, G. J. Hakim, L. W. Horowitz, R. M. Sullivan, R. Tardif, P. J. van Hengstum, and T. S. Winkler. Last millennium hurricane activity linked to endogenous climate variability. *Nat Commun*, 15(1):816, 2024. ISSN 2041-1723 (Electronic) 2041-1723 (Linking). doi: 10.1038/s41467-024-45112-6.

Thomas K Bauska, Fortunat Joos, Alan C Mix, Raphael Roth, Jinho Ahn, and Edward J Brook. Links between atmospheric carbon dioxide, the land carbon reservoir and climate over the past millennium. *Nature Geoscience*, 8(5):383–387, 2015. ISSN 1752-0894.

M Rubino, DM Etheridge, CM Trudinger, CE Allison, PJ Rayner, I Enting, R Mulvaney, LP Steele, RL Langenfelds, and WT Sturges. Low atmospheric co2 levels during the little ice age due to cooling-induced terrestrial uptake. *Nature Geoscience*, 9(9):691–694, 2016. ISSN 1752-0894.

Owen K. Atkin, Dan Bruhn, Vaughan M. Hurry, and Mark G. Tjoelker. Evans review no. 2: The hot and the cold: unravelling the variable response of plant respiration to temperature. *Functional Plant Biology*, 32(2):87–105, 2005. doi: https://doi.org/10.1071/FP03176.

T. Cai, L. B. Flanagan, and K. H. Syed. Warmer and drier conditions stimulate respiration more than photosynthesis in a boreal peatland ecosystem: analysis of automatic chambers and eddy covariance measurements. *Plant Cell Environ*, 33(3):394–407, 2010. ISSN 1365-3040 (Electronic) 0140-7791 (Linking). doi: 10.1111/j.1365-3040.2009.02089.x.

P. Köhler, C. Nehrbass-Ahles, J. Schmitt, T. F. Stocker, and H. Fischer. A 156 kyr smoothed history of the atmospheric greenhouse gases co2, ch4, and n2o and their radiative forcing. *Earth Syst. Sci. Data*, 9(1):363–387, 2017. ISSN 1866-3516. doi: 10.5194/essd-9-363-2017.

D. Genty, D. Blamart, B. Ghaleb, V. Plagnes, C. Causse, M. Bakalowicz, K. Zouari, N. Chkir, J. Hellstrom, K. Wainer, and F. Bourges. Timing and dynamics of the last deglaciation from european and north african c stalagmite profiles -: comparison with chinese and south hemisphere stalagmites. *Quaternary Science Reviews*, 25 (17-18):2118–2142, 2006. ISSN 0277-3791. doi: 10.1016/j.quascirev.2006.01.030.

DE Black, RC Thunell, A Kaplan, K Tedesco, EJ Tappa, and LC Peterson. Late holocene tropical atlantic climate variability: records from the cariaco basin. In *AGU Fall Meeting Abstracts*, volume 2001, pages PP22B–01, 2001.

Sergey Kotov and Heiko Pälike. Qanalyseries-a cross-platform time series tuning and analysis tool. In *AGU Fall Meeting Abstracts*, volume 2018, pages PP53D–1230.

Michael P Smyth, Nicholas P Dunning, Eric M Weaver, Philip van Beynen, D Ortegón Zapata, and Meghan Rubenstein. An enigmatic maya center: Climate change, settlement systems, and water adaptations at xcoch, puuc region, yucatán. *Recent Investigations in the Puuc Region of Yucatán. Archaeopress Precolumbian Archaeology*, 8:3–24, 2017b.

Pingzhong Zhang, Hai Cheng, R Lawrence Edwards, Fahu Chen, Yongjin Wang, Xunlin Yang, Jian Liu, Ming Tan, Xianfeng Wang, and Jinghua Liu. A test of climate, sun, and culture relationships from an 1810-year chinese cave record. *science*, 322(5903):940–942, 2008. ISSN 0036-8075.

J. A. Hoggarth, S. F. M. Breitenbach, B. J. Culleton, C. E. Ebert, M. A. Mason, and D. J. Kennett. The political collapse of chichen itza in climatic and cultural context. *Global and Planetary Change*, 138:25–42, 2016. ISSN 0921-8181. doi: 10.1016/j.gloplacha.2015.12.007.

Franziska A. Lechleitner, Susan Q. Lang, Negar Haghipour, Cameron McIntyre, James U. L. Baldini, Keith M. Prufer, and Timothy I. Eglinton. Towards organic carbon isotope records from stalagmites: Coupled 13c and 14c analysis using wet chemical oxidation. *Radiocarbon*, 61(03):749–764, 2019. ISSN 0033-8222. doi: 10.1017/rdc.2019.35.

D. A. Smirnov, S. F. M. Breitenbach, G. Feulner, F. A. Lechleitner, K. M. Prufer, J. U. L. Baldini, N. Marwan, and J. Kurths. A regime shift in the sun-climate connection with the end of the medieval climate anomaly. *Scientific Reports*, 7(1): 11131, 2017. ISSN 2045-2322. doi: 10.1038/s41598-017-11340-8.

N. Melissa M. Medina, Francisco W. Cruz, Amos Winter, Haiwei Zhang, Angela Ampuero, Mathias Vuille, Víctor C. Mayta, Marília C. Campos, Verónica Marcela

Rámirez, Giselle Utida, Andrés Camilo Zúñiga, and Hai Cheng. Atlantic itcz variability during the holocene based on high-resolution speleothem isotope records from northern venezuela. *Quaternary Science Reviews*, 307:108056, 2023. ISSN 0277-3791. doi: https://doi.org/10.1016/j.quascirev.2023.108056.

Mads Faurschou Knudsen, Peter Riisager, Bo Holm Jacobsen, Raimund Muscheler, Ian Snowball, and Marit-Solveig Seidenkrantz. Taking the pulse of the sun during the holocene by joint analysis of 14c and 10be. *Geophysical Research Letters*, 36 (16), 2009. ISSN 0094-8276.

Ilya G Usoskin. A history of solar activity over millennia. *Living Reviews in Solar Physics*, 14(1):3, 2017. ISSN 2367-3648.

Armand Hernández, Celia Martin-Puertas, Paola Moffa-Sánchez, Eduardo Moreno-Chamarro, Pablo Ortega, Simon Blockley, Kim M. Cobb, Laia Comas-Bru, Santiago Giralt, Hugues Goosse, Jürg Luterbacher, Belen Martrat, Raimund Muscheler, Andrew Parnell, Sergi Pla-Rabes, Jesper Sjolte, Adam A. Scaife, Didier Swingedouw, Erika Wise, and Guobao Xu. Modes of climate variability: Synthesis and review of proxy-based reconstructions through the holocene. *Earth-Science Reviews*, page 103286, 2020. ISSN 0012-8252. doi: https://doi.org/10.1016/j.earscirev.2020.103286.

Amy C Clement, Richard Seager, Mark A Cane, and Stephen E Zebiak. An ocean dynamical thermostat. *Journal of Climate*, 9(9):2190–2196, 1996. ISSN 1520-0442.

Thomas M. Marchitto, Raimund Muscheler, Joseph D. Ortiz, Jose D. Carriquiry, and Alexander van Geen. Dynamical response of the tropical pacific ocean to solar forcing during the early holocene. *Science*, 330(6009):1378, 2010. doi: 10.1126/science.1194887.

F. Steinhilber, J. Beer, and C. Fröhlich. Total solar irradiance during the holocene. *Geophysical Research Letters*, 36(19), 2009. ISSN 0094-8276. doi: 10.1029/2009gl040142.

Gerard Bond, Bernd Kromer, Juerg Beer, Raimund Muscheler, Michael N. Evans, William Showers, Sharon Hoffmann, Rusty Lotti-Bond, Irka Hajdas, and Georges Bonani. Persistent solar influence on north atlantic climate during the holocene. *Science*, 294(5549):2130, 2001. doi: 10.1126/science.1065680.

Hui Jiang, Raimund Muscheler, Svante Björck, Marit-Solveig Seidenkrantz, Jesper Olsen, Longbin Sha, Jesper Sjolte, Jón Eiríksson, Lihua Ran, and Karen-Luise

Knudsen. Solar forcing of holocene summer sea-surface temperatures in the northern north atlantic. *Geology*, 43(3):203–206, 2015. ISSN 1943-2682.

L. C. Peterson, J. T. Overpeck, N. G. Kipp, and J. Imbrie. A high-resolution late quaternary upwelling record from the anoxic cariaco basin, venezuela. *Paleoceanography*, 6(1):99–119, 1991. ISSN 0883-8305. doi: https://doi.org/10.1029/90PA02497.

Huiru Tang, Liangcheng Tan, Yongli Gao, Jingjie Zang, Le Ma, Yanzhen Li, R. Lawrence Edwards, Hai Cheng, Ashish Sinha, Xiqian Wang, Xing Cheng, Ángel A. Garcia, and E. Calvin Alexander. Mid-holocene hydroclimatic change and hurricane activity in central america recorded by an isla de mona stalagmite. *Marine Geology*, 471:107289, 2024. ISSN 0025-3227. doi: https://doi.org/10.1016/j.margeo.2024.107289.

Thomas J. Crowley. Causes of climate change over the past 1000 years. *Science*, 289 (5477):270–277, 2000. doi: doi:10.1126/science.289.5477.270.

DM Shaw, GA Reilly, JR Muysson, GE Pattenden, and FE Campbell. An estimate of the chemical composition of the canadian precambrian shield. *Canadian Journal of Earth Sciences*, 4(5):829–853, 1967. ISSN 0008-4077.

D. M. Shaw, J. Dostal, and R. R. Keays. Additional estimates of continental surface precambrian shield composition in canada. *Geochimica Et Cosmochimica Acta*, 40 (1):73–83, 1976. ISSN 0016-7037. doi: 10.1016/0016-7037(76)90195-2.

DM Shaw. *Radioactive elements in the Canadian Precambrian shield and the interior of the earth*, pages 855–870. Elsevier, 1968.

S. R. Taylor. Trace element abundances and the chondritic earth model. *Geochimica Et Cosmochimica Acta*, 28(Dec):1989–1998, 1964a. ISSN 0016-7037. doi: 10.1016/0016-7037(64)90142-5.

S. R. Taylor. Abundance of chemical elements in the continental crust - a new table. *Geochimica Et Cosmochimica Acta*, 28(Aug):1273–1285, 1964b. ISSN 0016-7037. doi: 10.1016/0016-7037(64)90129-2.

S. M. McLennan and S. R. Taylor. Heat flow and the chemical composition of continental crust. *The Journal of Geology*, 104(4):369–377, 1995. doi: 10.1086/629834.

D. Leinfelder. *Cavity Ring-Down Spectroscopy for stable water isotope analysis An instrument characterisation study.* Thesis, Heidelberg University, 2014.

F. Lases-Hernandez. *Characterization of geochemical and environmental processes controling the stable isotope and trace element composition of drip water and* *farmed calcite in río secreto karst cave, located in the Yucatán Península, México.* Dissertation, Universidad Nacional Autónoma de México (UNAM), 2020.

Walter RT Witschey and Clifford T Brown. The electronic atlas of ancient maya sites. *Mayagis. smv. org*, 2010.

List of Figures

List of Appendix Figures

List of Tables

List of Appendix Tables

Appendix

Supplementary Material for Chapters I–VI

Chapter I – Introduction

Untangling the Th/U Ratio of the Upper Continental Crust: A Muddle of False Citations

At present, for a geological material in ^{238}U–^{234}U–^{230}Th secular equilibrium, assuming a crustal Th/U ratio of 3.8 (Taylor and McLennan, 1985), which approximates the ratio of ^{232}Th to ^{238}U due to their abundance as the most prevalent isotopes of their respective elements, and with an assumed error of 50%, the ^{230}Th/^{232}Th ratio of $4.4 \pm 2.2 \times 10^{-6}$ is commonly utilized. This ratio is used for deducing the initial ^{230}Th and for correcting calculated ^{230}Th/U ages. It should be noted that many studies wrongly cite the study by Wedepohl (1995) when they use an average ^{232}Th/^{238}U value of 3.8 for the upper continental crust. Actually, the values Wedepohl (1995) provides are not his own, and he references them to Shaw et al. (1967, 1976) (see Fig. A1). However, those references are again wrongly cited. Shaw et al. (1967) does not report on U or Th data at all, while Shaw (1968) states that *"[...] these elements have been discussed elsewhere (Shaw et al., 1967; Shaw, 1968) and are included here for the sake of completeness.*" The corresponding values he provides, however, are referenced with Taylor (1964a,b) and yield a different Th/U ratio of 3.55. Again, these values are recited and trace back to Heier and Carter (1963) and Heier and Rogers (1963). The values Wedepohl (1995) shows in his table are from the study of Shaw (1968) in which he analyzed surface exposures of the Canadian Precambrian Shield, resulting in mean values of 10.3±4.2 ppm Th and mean values of 2.45±1.3 ppm for U, yielding a Th/U ratio of 4.2 (4.1 if rounded). One reason for this confusion could be attributed to the frequently cited review paper by Richards and Dorale (2003) regarding the uranium-series chronology and environmental applications of speleothems, which erroneously referenced the study by Wedepohl (1995) in discussing a crustal ^{232}Th/^{238}U ratio of 3.6–3.8. At the same time, Richards and Dorale (2003) cite the study by McLennan and Taylor (1995), which is the more appropriate citation here as it provides mean concentrations of 10.7 ppm for Th and 2.8 ppm for U in the upper continental crust, resulting in a Th/U ratio of 3.8. However, these values were derived from the study by (Taylor and McLennan, 1985), which is the correct reference to cite when using a Th/U ratio of 3.8 for the upper continental crust.

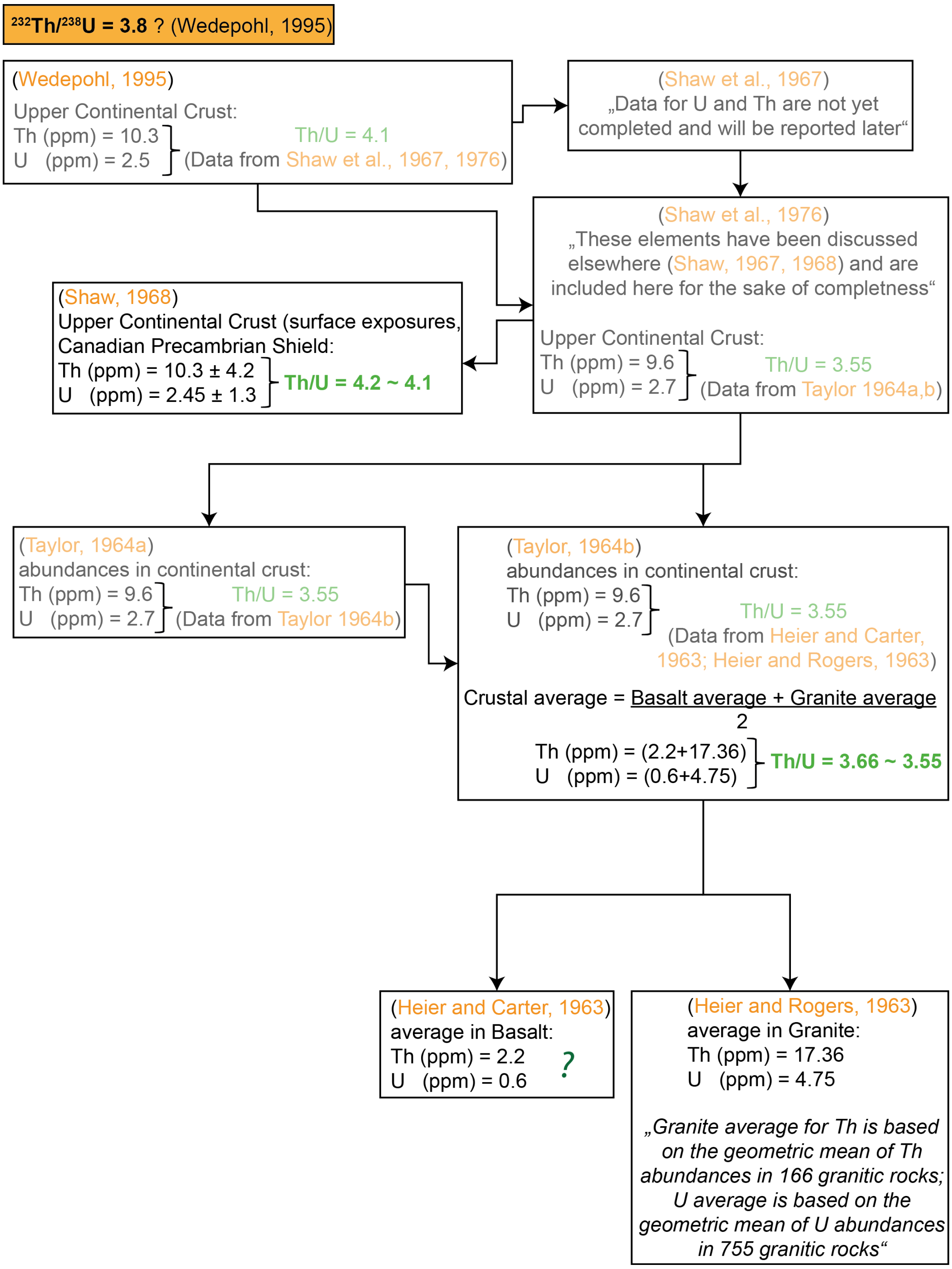

Figure A1. Untangling the Th/U Ratio of the Upper Continental Crust. Most speleothem studies use an average ^{232}Th/^{238}U value of 3.8 from the upper continental crust to correct for initial ^{230}Th, citing the study by Wedepohl (1995). However, the values he provides yield a different ratio and are derived from various studies, as shown in this flow chart. The correct reference to cite when using a Th/U ratio of 3.8 for the upper continental crust is (Taylor and McLennan, 1985).

Supporting Information for Chapter II – Material and Methods

Monitoring Áaktun Kóopo Cave: First Insights into Climate and Hydrology

As detailed in Chapter II.1, comprehensive and continuous monitoring of cave parameters in Áaktun Kóopo Cave was not feasible due to various complications. Nevertheless, some data were collected during two field trips, aided by loggers placed inside the cave, providing initial insights into the cave's climate and hydrology.

The following section presents the results of the monitored cave parameters, including temperature, CO_2 concentration, and the stable isotopic composition of the drip water.

Temperature, CO_2 Concentration, and Drip Rate

The temperature and humidity logger (THL 1) placed inside the cave during the exploratory field trip in May 2018 (see Chapter II.2.1) recorded data every 30 minutes for almost one year until its capacity was exhausted (02.06.2018–30.04.2019). The logger was extracted from the cave in May 2021 by Dr. Jeronimo Avilés Olguín, one of our project partners from Yucatán, Mexico (Grupo Espeleológico AJAU, Mérida).
The recorded temperatures showed only slight changes throughout the year, with minimum values of around 25.6°C in June 2018 and April 2019, and maximum values up to 25.9°C in December 2018, averaging 25.74°C. This mean annual cave temperature closely matches the mean surface annual temperature of 26.1°C, recorded during the same period at a nearby weather station in Ideal, Quintana Roo (CONAGUA, 2021), approximately 20 km northeast of Áaktun Kóopo Cave.
The two loggers (THL 2 and THL 3) placed inside the cave during the field trip in March 2022 recorded data every 60 minutes for one year (17.03.2022–01.04.2023) until I returned to the cave to retrieve the data and restart the loggers (see Chapter II.2.1).
Plotting the temperature patterns of these two loggers alongside that of the 2018/2019 logger reveals that all three loggers exhibit varying degrees of seasonal change (Fig. A2A). The humidity recorded by THL 1 remained at 100% throughout the entire monitoring period, while the two other loggers (THL 2 and THL 3) also maintained a constant humidity of 100% until their sensors malfunctioned at the end of November 2022 and the beginning of December 2022, respectively.

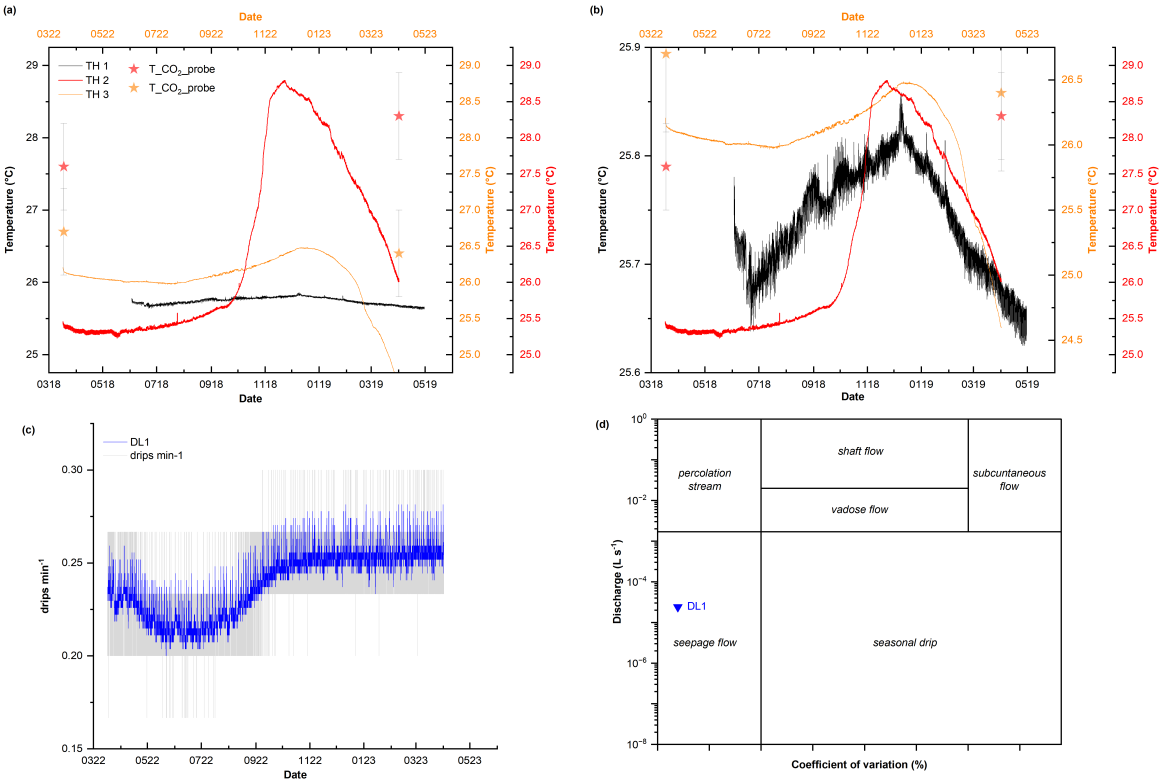

Figure A2. Recorded temperature and drip rates in Áaktun Kóopo Cave. The location of each logger (THL 1 to THL 3) within the cave is shown in Fig. A5. Note that the temperature of THL 1 is shown for the same months but different years (2018/2019) than the temperatures of THL 2 and TH3 (2022/2023). **(a)** Recorded temperature against time. The scale of the temperature axes is the same for all. **(b)** Same as in (a), but with different temperature axes, allowing for a more detailed comparison of changing temperatures throughout the year. **(c)** Drips per minute plotted against time. A moving average of 9 was applied for better visualization (blue curve). **(d)** Characterization of the drip site as seepage flow (blue triangle), according to Smart and Friederich (1986)Reference.

The drip logger (DL1) that was placed inside the cave during our cave visit in March 2022 exhibits nearly constant drip rates throughout the monitoring period (17.03.2022–01.04.2023), with slightly elevated rates observed between September 2022 and March 2023 compared to the period from May to August 2022 (Fig. A2a). Drip rates can be further quantified as discharge (L s^{-1}), assuming an approximate drip volume of 0.1 ml per drip, which is a common volume for a drip. According to Smart and Friederich (1986) (*Reference not available!*), determining the mean (annual) discharge rate over the monitoring period and the associated relative standard deviation (known as the ”coefficient of variation”) facilitates the characterization of the drip site into different flow regimes. Given the minimal seasonal fluctuations, with a coefficient of variation of 9.8% and a mean annual discharge of $< 10^{-3}$ L s^{1}, the drip site is classified as seepage flow (Fig. A2b).

During the cave visit on March 16th, 2022, the CO_2 concentration in eleven different parts of the cave (Fig. A5) was measured using a handheld CO_2 probe (Amprobe, usable up to 5000 ppm with ± 30 ppm). The same parts of the cave were measured again during the 2023 field trip. Although CO_2 data from different seasons is lacking, comparing the data from the two different years remains valuable. Based on the measured CO_2 concentrations, three distinct areas within the cave can be identified. The area encompassing stations 1–5, nearest to the cave entrance, exhibited relatively constant CO_2 concentrations, with mean values of 1,687±115 ppm (1σ std). Station 6 (2,240±142 ppm) marks a transition to the western part of the cave (stations 7–11), where CO_2 concentrations are more than double, averaging 4,741±620 ppm (1σ std). One year later, on the 1st of April 2023, CO_2 concentrations at the stations close to the entrance (stations 1–3) were similar to those from the year before, with a mean of 1,743±68 ppm (1σ std). However, this time, stations 4 and 5 showed higher CO_2 concentrations of 2,600±113 ppm (1σ std). At the same time, station 6 also showed a higher concentration of 3,059±183 ppm. Additionally, for the western part of the cave (stations 7–11), CO_2 concentrations were significantly higher this time, with mean values of *6,260 ppm*. It should be noted here that, although the CO_2 probe provides data for concentrations up to 9,999 ppm, it is only specified for values between 0–5,000 ppm with an accuracy of ±30 ppm ±5% reading error. The CO_2 device also measures temperature (±0.6°C), allowing for a rough comparison with the temperatures recorded by the THLs. With the exception of the cave entrance, which acts as a sinkhole and is therefore open to the surface, the temperature, measured concurrently with CO_2 concentrations, remained relatively constant throughout the cave, with a mean of 26.8±0.4 °C. A slightly elevated temperature of 27.6±0.6°C was recorded immediately after, and approximately 2 meters above, a body of water traversed upon entering this section of the cave (station 3), which is only a few meters away from THL 2. One year later, temperatures were again quite constant throughout the cave (stations 2–11), with a mean of 26.6±0.7°C. As in the previous year, the highest temperatures were measured at station 2 (28.3±0.6°C), this time 0.7°C warmer. When comparing the temperatures measured with the CO_2 device at station 3 (close to THL 2) and station 8 (close to THL 3) during both cave visits with the temperatures recorded on those days by the THL 2 and THL 3, slight differences were observed. In both years, the temperatures measured by the CO_2 probe were slightly higher (up to 2.3°C) compared to those recorded by the loggers (Fig. A2). Since the CO_2 probe was repeatedly enclosed in a dry bag while crawling and wading through the cave and its pools, where temperatures were presumably slightly elevated, the device may not have had enough time to fully acclimatize to the ambient temperature in the cave. In addition to measurements of CO_2 concentration and temperature, the CO_2 probe also provides data on the relative humidity with an accuracy of ±5% (Table A1). As expected, the relative humidity within the doline at the cave entrance (station 1) shows the lowest measured values during both cave visits in 2022 and 2023, with 72±5% and 57±5%, respectively. For stations 4–11, the relative humidity during both cave visits was 100±5%, indicating minimal to no ventilation of air inside these parts of the cave.

station (#)	**CO_2 (ppm)**		**T (°C)**		**RH (%)**	
	16.03.2022	01.04.2023	16.03.2022	01.04.2023	16.03.2022	01.04.2023
1	1,841±122	1,700±115	29.1±0.6	32.0±0.6	72±5	57±5
2	1,694±115	1,730±117	27.2±0.6	27.5±0.6	89±5	89±5
3	1,623±111	1,800±120	27.6±0.6	28.3±0.6	89±5	82±5
4	1,642±112	2,494±155	26.3±0.6	26.1±0.6	100±5	100±5
5	1,635±112	2,705±165	26.2±0.6	26.0±0.6	100±5	100±5
6	2,240±142	3,059±183	26.6±0.6	26.1±0.6	100±5	100±5
7	5,220	6,880	26.6±0.6	26.3±0.6	100±5	100±5
8	4,201±241	7,321	26.7±0.6	26.4±0.6	100±5	100±5
9	4,220±241	5,437	26.7±0.6	26.3±0.6	100±5	100±5
10	5,725	5,510	27.1±0.6	26.3±0.6	100±5	100±5
11	4,337±247	6,150	26.9±0.6	26.6±0.6	100±5	100±5

Table A1. Temperature, relative humidity, and CO_2 concentration were measured at various stations within Áaktun Kóopo Cave during field trips conducted in 2022 and 2023. The CO_2 probe used in the measurements provides data for concentrations up to 10,000 ppm. However, it is specified only for values between 0–5,000 ppm, with an accuracy of ±30 ppm ±5% reading error. Values exceeding 5,000 ppm are highlighted in red to denote their range beyond the specified accuracy.

Drip Water Analysis

Treatment of drip water samples

After the collection of the drip water, the plastic bottles (125 ml) were immediately sealed with Parafilm for transportation. A few hours later, back in the hotel room, the samples were divided into different containers, adequately sealed again with Parafilm, and stored inside the fridge until returning to Germany.

Stable Water Isotopes

Stable water isotopes were analyzed with a Picarro CRDS (Cavity Ring-Down Spectrometer) at the Institute of Environmental Physics, Heidelberg University. For δD and δ^{18}O a repeatability of <0.2‰ and <0.06‰, respectively was reached. With the established measuring routine, a long-term reproducibility better than 0.6‰ for δD and better than 0.09‰ for δ^{18}O are achieved (Leinfelder, 2014).

A total of seven dripwater samples from three different drip sites inside Áaktun Kóopo Cave, collected during visits in March 2022 and April 2023, have been analyzed for δD and δ^{18}O (Fig. A3). The two drip sites, EDW-1 and EDW-2, were sampled during both visits. Since drip site EDW-2 provided sufficient water, aliquot samples could be taken in both years, allowing for a reproducibility check. Sample EDW-3, which was collected in 2022, differs from the other samples in that it consists of water collected from multiple drip sites (soda straws) within an area of roughly one square meter, instead of a single drip. This approach was necessary due to the low drip rates in this part of the cave during the visit.

The analyzed dripwater from Áaktun Kóopo Cave yielded δ^{18}O values ranging between −5.35 to −4.03 ‰, while δD values are ranging between −34.67 to −26.86 ‰.

All drip water samples plot close to the Global Meteoric Water Line (GMWL) and also close to the Local Meteoric Water Line (LMWL) and Drip Water Line (DWL) that have been established during four years of monitoring at the nearby Río Secreto reserve (Lases-Hernandez, 2020).Compared to the >900 drip water samples from the nearby Río Secreto Cave system, collected during four hydrological years from 16 different drip sites, the dripwater from Áaktun Kóopo Cave shows rather low δ^{18}O and δD values and plots at the lower left corner of a δD vs. δ^{18}O plot (Fig. A3).

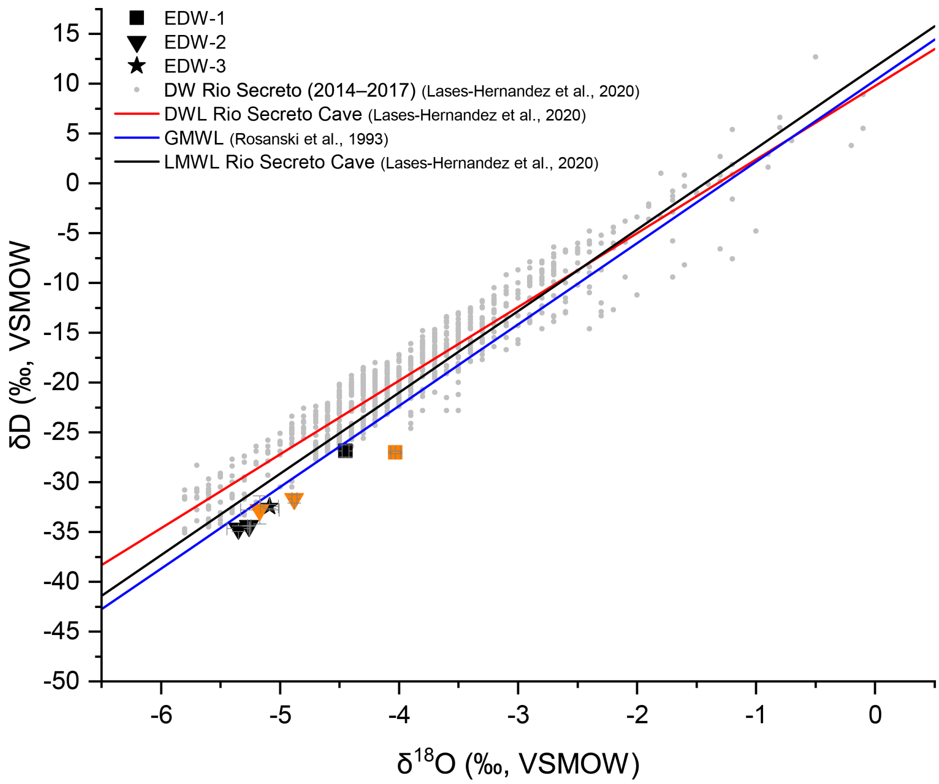

Figure A3. **δD vs. δ^{18}O of dripwater samples from Áaktun Kóopo Cave.** Comparison of the linear relationship between δ^{18}O and δD of dripwater samples from Áaktun Kóopo Cave, collected during cave visits in 2022 (black symbols) and 2023 (orange symbols). For comparison, the local meteoric water line (LMWL), comprised of 66 rainfall samples, and the drip water line (DWL), consisting of >900 drip water samples collected during four hydrological years (2014–2017) at the nearby Río Secreto reserve (Lases-Hernandez, 2020), are included. The global meteoric water line (GMWL) (Rozanski et al., 1993) is also shown.

Uranium and Thorium Isotopes

Some of the drip water samples were further processed using ^{230}Th/U dating to analyze uranium and thorium isotopes, with the goal of evaluating the initial (^{230}Th/^{232}Th) activity ratio in the drip water. The water samples underwent the same chemical procedures as the carbonate samples (see Chapter II.3.2).

^{230}Th/U-dating of three drip water samples from Àaktun Kóopo Cave yielded U concentrations ranging from 1571.204 ± 0.132 to 3274.631 ± 0.191 ng g^{-1} (Table A2). The measured δ^{234}U values ranging between 5.66 ± 0.96 and 12.5 ± 1.7 ‰, are close to secular equilibrium. (^{230}Th/^{232}Th) activity ratios vary between 1.659 ± 0.046 and 8.9 ± 1.0 (n=3), indicating at least a two-component system, such as detrital Th versus hydrogenous Th (see chapter III.1 for further discussion).

Sample label	Lab. Nr.	Cave	^{238}U (ng g^{-1})	Error 2σ (abso.)	^{232}Th (ng g^{-1})	Error 2σ (abso.)	^{230}Th/^{238}U (Act.rat.)	Error 2σ (abso.)	^{230}Th/^{232}Th (Act.rat.)	Error (abso.)	δ^{234}U (‰)	Error 2σ (abso.)	Age (uncorr.) (ka)	Error 2σ (ka)	δ^{234}U (init.) (‰)	Error 2σ (abso.)
11565	Actun Ha	Actun Ha	1.582297	0.00011	0.0012468	0.0000027	0.00345	0.00012	13.40	0.45	2.0	1.2	0.376	0.013	2.0	1.2
11566	MC Pool	Madre Cristallina	2.375551	0.00016	0.00016105	0.00000051	0.000253	0.000031	11.4	1.4	−2.2	1.0	0.0277	0.0033	−2.2	1.0
11567	multiple dripsites	Áaktun Koópo	3.274631	0.00019	0.00046562	0.00000082	0.000281	0.000034	6.04	0.74	5.66	0.96	0.0304	0.0037	5.66	0.96
11568	EDW 1	Áaktun Kóopo	2.349388	0.00019	0.017490	0.000027	0.00404	0.00011	1.659	0.046	7.5	2.2	0.4382	0.012	7.5	2.2
11569	EDW 2	Àaktun Kóopo	1.571204	0.00013	0.00023727	0.00000059	0.000443	0.000050	8.9	1.0	12.5	1.7	0.0477	0.0055	12.5	1.7

Table A2. ^{230}Th/U dating results of drip water from Áaktun Kóopo Cave, Aactun Ha Cave, and Madre Cristallina Cave. Errors are reported as 2σ analytical uncertainties.

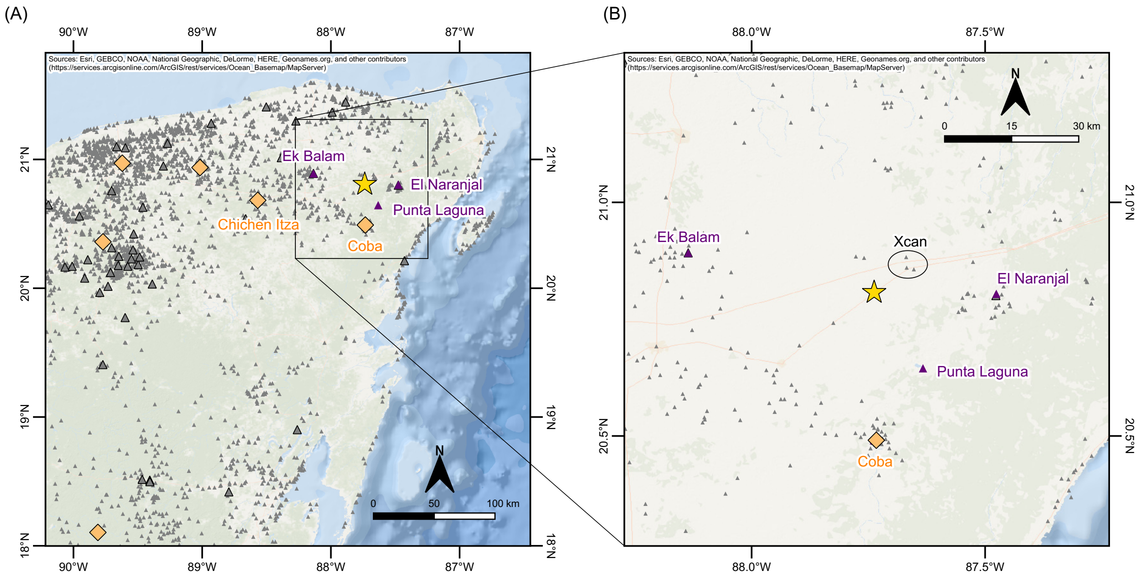

Figure A4. **(A)** Location of the Áaktun Kóopo Cave (yellow asterisk) in the northeastern Yucatán Peninsula, Mexico, relative to other Maya archaeological settlements in the area. **(B)** Zoom-in showing the settlement density around Áaktun Kóopo Cave, with well-known settlements such as Coba, Punta Laguna, El Naranjal, and Ek Balam, all within 20–40 km distance, and the closest settlement, Xcan, less than 10 km to the northeast. Orange diamonds represent large settlements, large triangles represent intermediate ones, and small triangles represent the smallest ones, based on Witschey and Brown (2010).

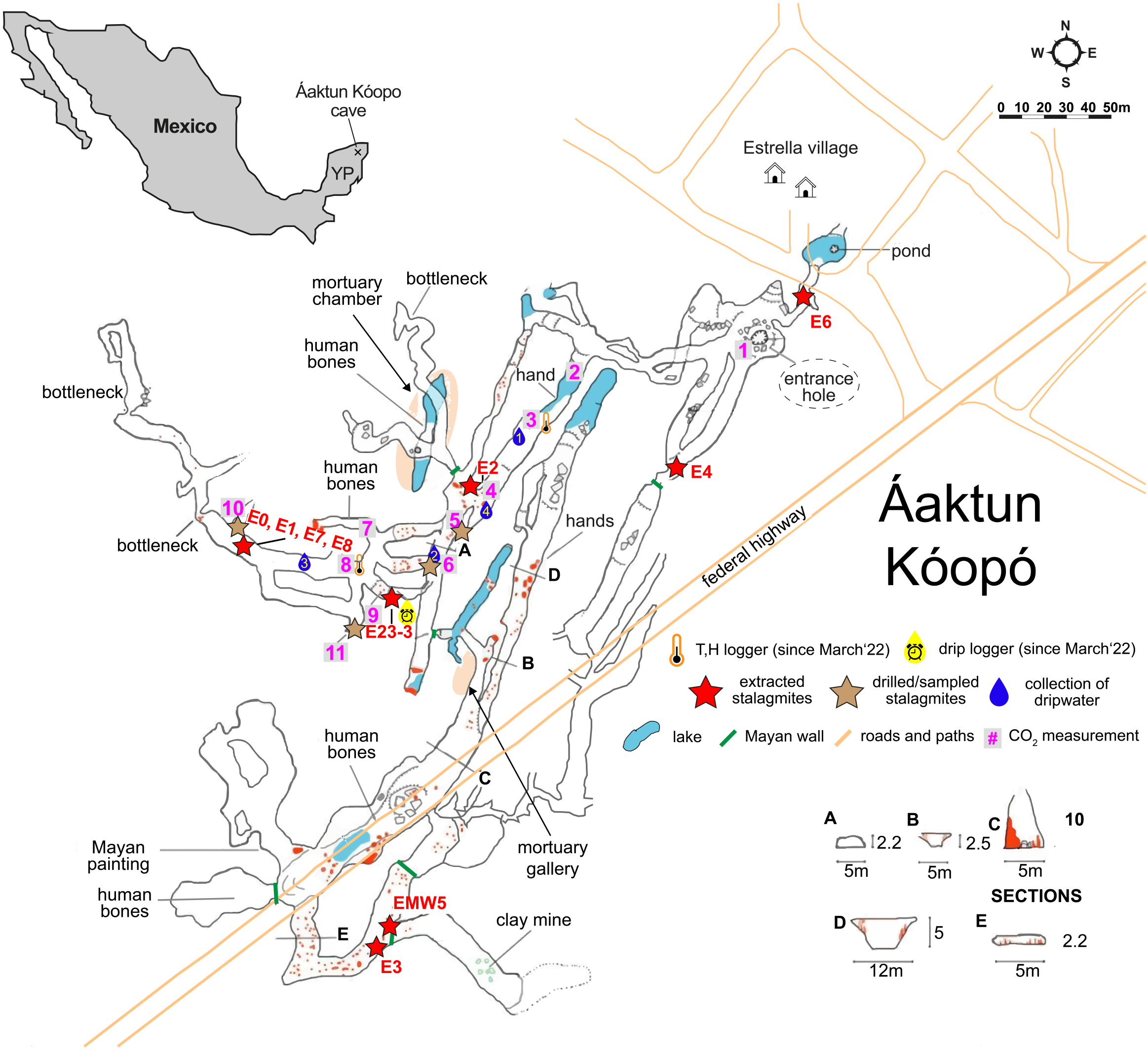

Figure A5. Map of Áaktun Kóopo Cave showing the locations where samples were taken or measurements performed during field trips in 2018, 2022, and 2023. Red stars show locations of stalagmites that have been extracted from the cave, while brown stars represent locations where samples were drilled or scraped from stalagmites. Blue drop symbols mark the sites of drip water collection, and pink numbers correspond to CO$_2$ measurements conducted during the 2022 and 2023 field trips (see Table A1). Map was taken from Thomas et al. (2011) and modified after Gómez (2020) and Tec (2021).

Table A3. Stalagmites collected during Field Trip 1: The locations of the samples collected inside Áaktun Kóopo Cave are shown in Figure A5.

Sample	Material	Info	Length (mm)
E0	Calcite	• 3 individual stalagmites (E0-A, E0-B, E0-C) • E0-B and E0-C are connected forming an L-shape • extracted from the northwestern part of the cave (Fig. A5) • drip site appeared active at time of collection	E0-A = 66 E0-B = 226 E0-C = 221
E1	Calcite/ Aragonite	• stalagmite extracted from the northwestern part of the cave • drip site appeared still active at time of collection	186
E2	Calcite	• stalagmite extracted from the central part of the cave • drip site appeared still active at time of collection	262
E3	Calcite	• stalagmite extracted from the southern part of the cave in front of a large Maya wall	274
E4	Calcite	• stalagmite extracted from the northeastern part of the cave	89
EMW-5	Calcite	• stalagmite extracted from the southern part of the cave • this little stalagmite detached from a Maya wall during the collection of stalagmite E3	62
E6	Calcite	• stalagmite extracted from the northeastern part close to the cave entrance	230
E7	Calcite/ Aragonite	• 2 stalagmites (E7-A, E7-B) are connected forming an L-shape • extracted from the northwestern part of the cave • drip site appeared still active at time of collection	E7-A = 127 E7-B = 65
E8	Calcite	• stalagmite extracted from the northwestern part of the cave • drip site appeared still active at time of collection	81

Additional Notes: 1 T/H-logger was placed during the collection.

Table A4. Samples collected during Field Trip 2: The locations of the samples collected inside Áaktun Kóopo Cave are shown in Figure A5.

Sample	Material	Info
Estrella Loc. 5	Calcite	• Small carbonate fragment collected from a flowstone in the central part of the cave; located near station 5 of the CO_2 mapping (Fig. A5)
Estrella drip site 1	Calcite	• Modern calcite precipitates scraped from the floor below drip site EDW-1; located near station 6 of the CO_2 mapping
EDW-1	Drip water	• Drip water collected from the drip site above the sampled calcite precipitates
EDW-2	Drip water	• Drip water collected near station 3 of the CO_2 mapping • A temperature and humidity (T/H) logger was also installed at this location
EDW-3	Drip water	• Drip water collected from multiple drip sites (soda straws) within an area of approximately 1 m^2 in the western part of the cave, within the same chamber where most of the analyzed stalagmites were extracted

Additional Notes: 2 T/H-loggers + 1 drip logger (placed in 2022) were read out and restarted; CO_2 monitoring was performed in 11 different parts of the cave.

Table A5. Samples collected during Field Trip 3: The locations of the samples collected inside Áaktun Kóopo Cave are shown in Figure A5.

Sample	Material	Info
E23-1-B	Calcite	• Small core drilled from the bottom of stalagmite E23-1; located near station 10 of the CO_2 mapping
E23-1-T	Calcite	• Small core drilled from the top of stalagmite E23-1; located near station 10 of the CO_2 mapping
E23-2-B	Calcite	• Small core drilled from the bottom of stalagmite E23-2; located near station 11 of the CO_2 mapping
E23-2-T	Calcite	• Small core drilled from the top of stalagmite E23-2; located near station 11 of the CO_2 mapping
E23-3	Calcite	• Stalagmite extracted from the northwestern part of the cave • A drip logger was placed below the drip that fed this stalagmite during the previous field trip
EDW-23-1	Drip water	• Drip water collected from the same drip site as the previous year
EDW-23-2	Drip water	• Drip water collected from the same drip site as the previous year
EDW-23-3	Drip water	• Drip water collected from the same multiple drip sites as the previous year
EDW-23-4	Drip water	• Drip water collected from the northern part of the cave, located between EDW-23-1 and EDW-23-2

Additional Notes: 2 T/H-loggers + 1 drip logger (placed in 2022) were read out and restarted; CO_2 monitoring was performed in 11 different parts of the cave.

(a)

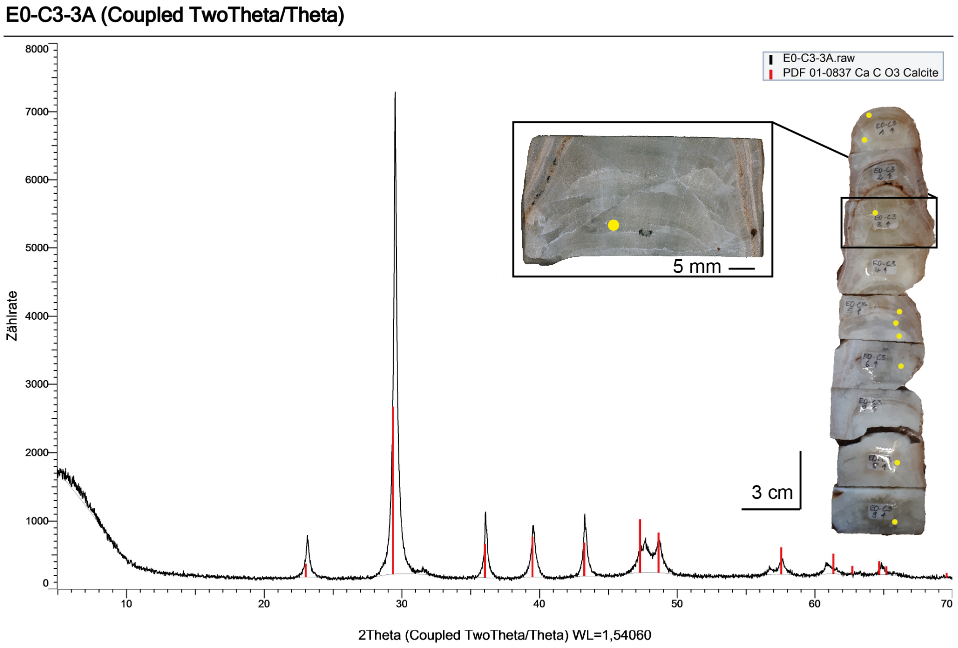

(b)

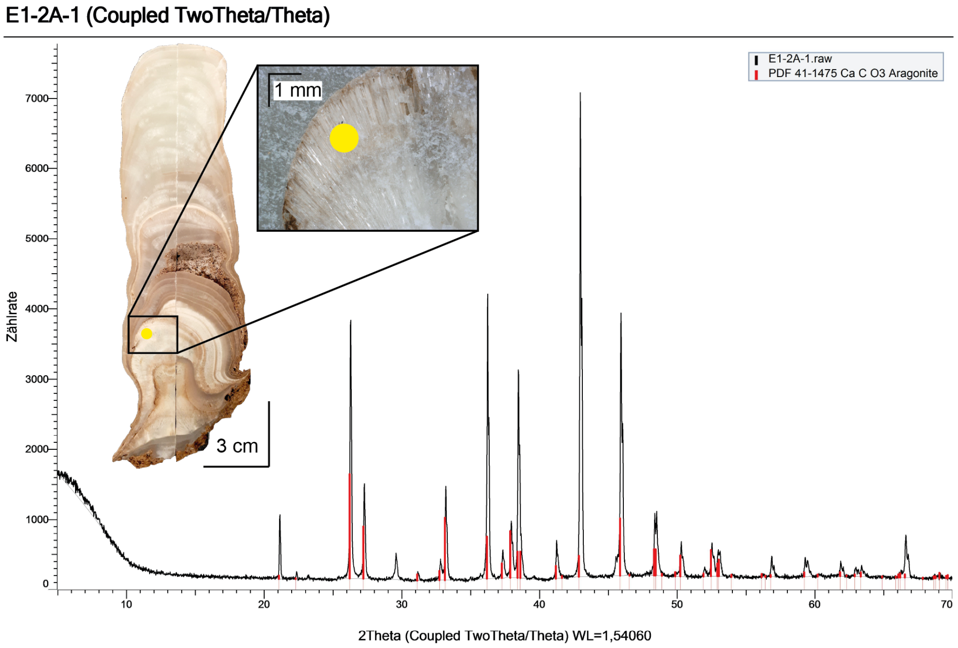

Figure A6. **(a)** X-ray diffraction (XRD) pattern showing the characteristic diffraction peaks (2θ) of calcite for a sample from stalagmite E0-C. The image on the right displays the remaining stalagmite cubes from the thin section preparation, from which sample powder was drilled for XRD analysis (yellow dots). The inset indicates the location of the sample corresponding to the presented diffraction pattern. All eight additional samples analyzed from stalagmite E0-C exhibited the same calcite pattern and are therefore not shown. **(b)** XRD pattern showing the characteristic diffraction peaks (2θ) of aragonite for a sample from the bottom part of stalagmite E1 (yellow dot on the scan). The presence of millimeter-sized needle-like crystals with a silky luster suggested an aragonitic phase, which was confirmed by XRD analysis. Peak positions and intensity data were analyzed using Diffrac.Suite EVA software (Bruker).

Stalagmite	measured distance (dft) [mm]	line scans [#]	spot size [μm]	scan speed (measurement) [μm s^{-1}]	analyzed isotopes	standard material	Project/ Thesis
E0-C	2.62–170.39	4	50 x 50	20	^{25}Mg, ^{26}Mg, ^{27}Al, ^{31}P, ^{43}Ca, ^{44}Ca, ^{88}Sr, ^{138}Ba, ^{232}Th, ^{238}U	NIST SRM 612	this study
E0-C (top remeasured)	0–39.52	1	25 x 100	10	^{25}Mg, ^{27}Al, ^{31}P, ^{32}S, ^{43}Ca, ^{44}Ca, ^{59}Co, ^{60}Ni, ^{63}Cu, ^{66}Zn, ^{88}Sr, ^{89}Y, ^{137}Ba, ^{232}Th, ^{238}U	NIST SRM 612	this study
E1	0–96.93 0–25.41	5 + 1	25 x 100	5	^{25}Mg, ^{27}Al, ^{31}P, ^{43}Ca, ^{44}Ca, ^{59}Co, ^{60}Ni, ^{63}Cu, ^{66}Zn, ^{88}Sr, ^{138}Ba, ^{232}Th, ^{238}U	NIST SRM 612	Adrian (2023)
E4	0.32–72.25	3	25 x 100	10	^{25}Mg, ^{27}Al, ^{31}P, ^{43}Ca, ^{44}Ca, ^{59}Co, ^{60}Ni, ^{63}Cu, ^{66}Zn, ^{88}Sr, ^{138}Ba, ^{232}Th, ^{238}U	NIST SRM 612	this study
E8	0–71.57	3	25 x 100	5	^{25}Mg, ^{27}Al, ^{31}P, ^{43}Ca, ^{44}Ca, ^{59}Co, ^{60}Ni, ^{63}Cu, ^{66}Zn, ^{88}Sr, ^{138}Ba, ^{232}Th, ^{238}U	NIST SRM 612	Adrian (2023)
E-23-3	0–84.46	2 x 4	25 x 100	10	^{23}Na, ^{25}Mg, ^{27}Al, ^{31}P, ^{43}Ca, ^{44}Ca, ^{60}Ni, ^{63}Cu, ^{66}Zn, ^{88}Sr, ^{89}Y, ^{138}Ba, ^{232}Th, ^{238}U	NIST SRM 612	Stange (2024)

Table A6. Settings for individual LA-ICP-MS measurements on stalagmites from Áaktun Kóopo Cave. The repetition rate was set to 20 Hz for all measurements. To avoid potential surface contamination, the scan path was pre-ablated using a circular spot with a diameter of 150 μm, at a scan speed of 100 μm s^{-1} and a repetition rate of 10 Hz. Some of the measurements were conducted as part of several Bachelor theses, contributing to this PhD project.

Supporting Information for Chapter III – Chronology And Stalagmite Age Modeling

Radiocarbon Evidence for Modern Stalagmite Growth

A total of four ^{14}C measurements were performed on three different stalagmite tips (E0-C, E1, and E8), with one duplicate measurement taken from the E0-C sample. The measured ^{14}C activities ($a^{14}C_{meas}$) ranged from 97.54 ± 0.20 pmC to 94.95 ± 0.19 pmC. Assuming only a minor contribution of ”dead carbon” (5–10%) to the carbonate in the stalagmite would result in $a^{14}C_{meas}$ values >100 pmC, which suggests modern growth (post-1950 AD) for the stalagmite tips.

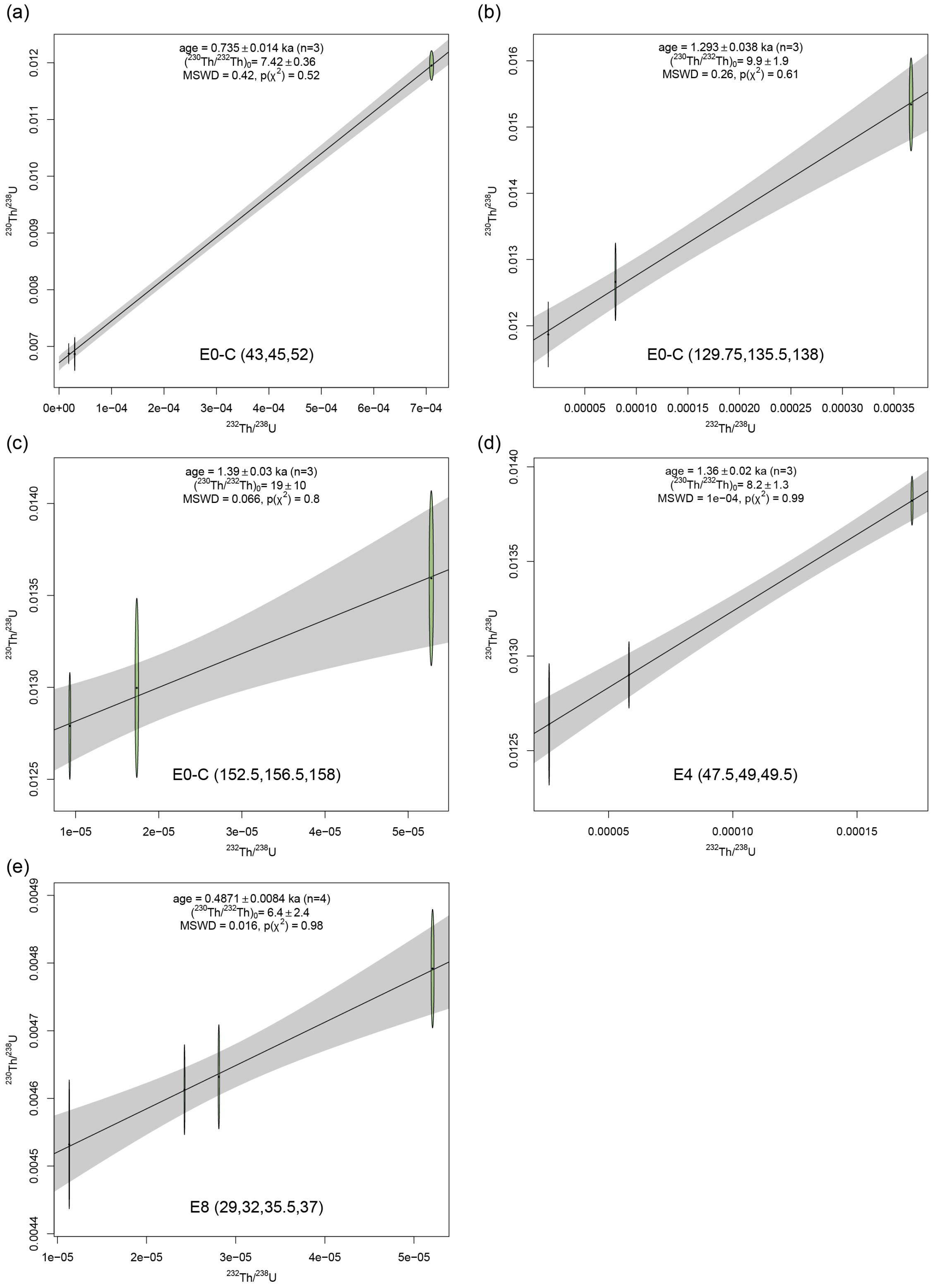

Figure A7. Five isochrons from three different stalagmites (E0-C, E4, and E8), with fit probabilities >0.05 and mean squared weighted deviation (MSWD) values <1, were derived using ISOPLOT software (Vermeesch, 2018). **(a–c)** Isochrons from stalagmite E0-C. **(d)** Isochron from stalagmite E4. **(e)** Isochron from stalagmite E8. The numbers in brackets next to the stalagmite's name indicate the distance in millimeters (mm) from the top of the stalagmite of the samples that comprise the individual isochrons.

Supporting Information for Chapter IV – Stalagmite Proxies – Results And Interpretation

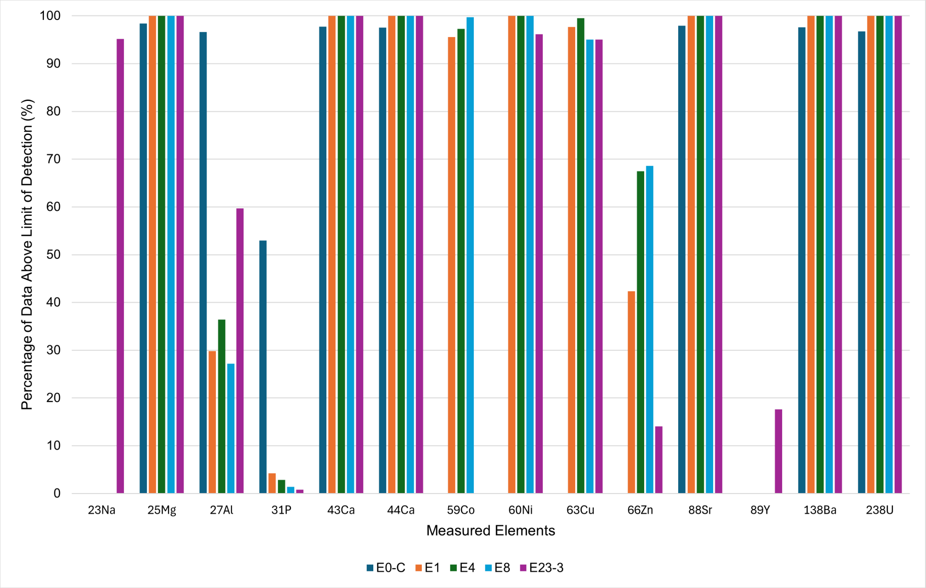

Figure A8. A bar plot showing the percentage of data above the limit of detection (LOD), defined as the signal-to-noise ratio where SNR ≤ 3, for various trace elements measured by LA-ICP-MS in stalagmites E0-C, E1, E4, E8, and E23-3 from Áaktun Kóopo Cave. Isotopes are displayed along the x-axis, with colors corresponding to individual stalagmites.

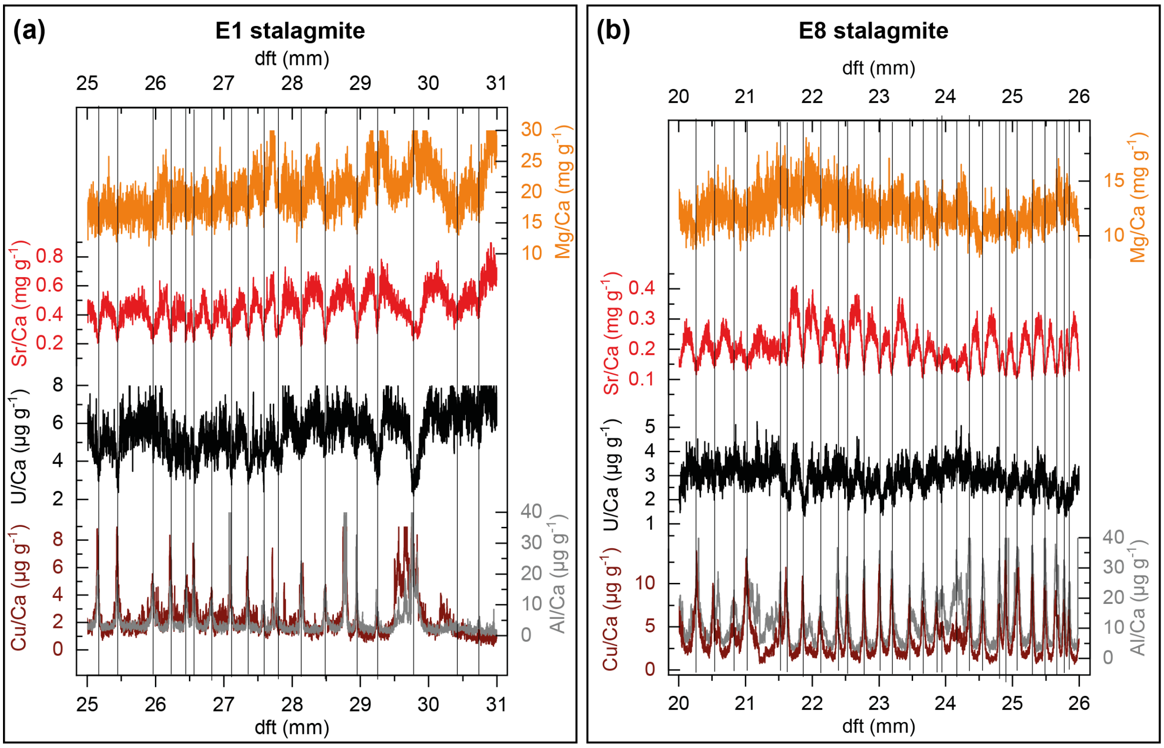

Figure A9. Seasonal variations in trace Elements of stalagmites E1 and E8 from Áaktun Kóopo Cave.

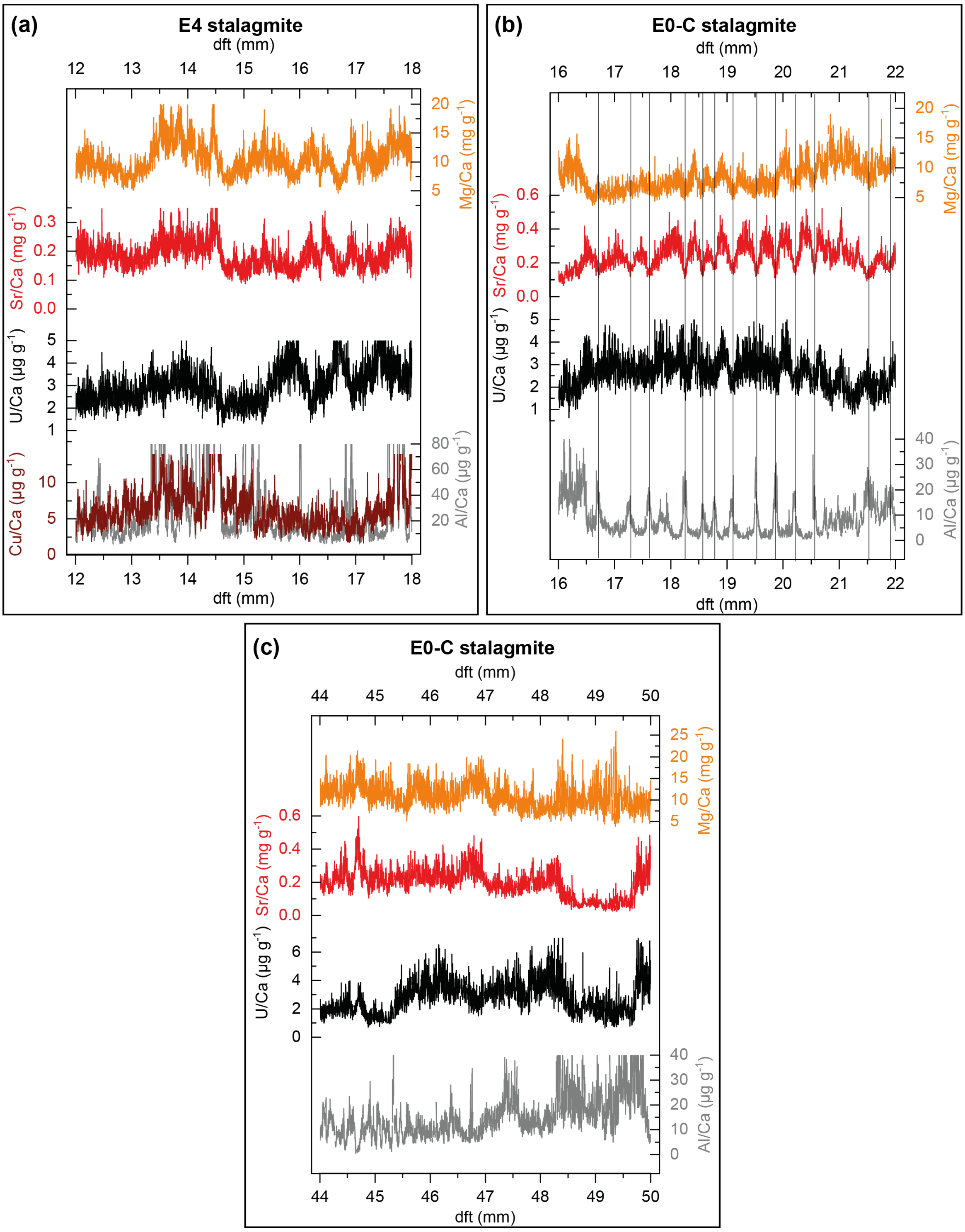

Figure A10. Seasonal variations in trace Elements of stalagmites E4 and E0-C from Áaktun Kóopo Cave.

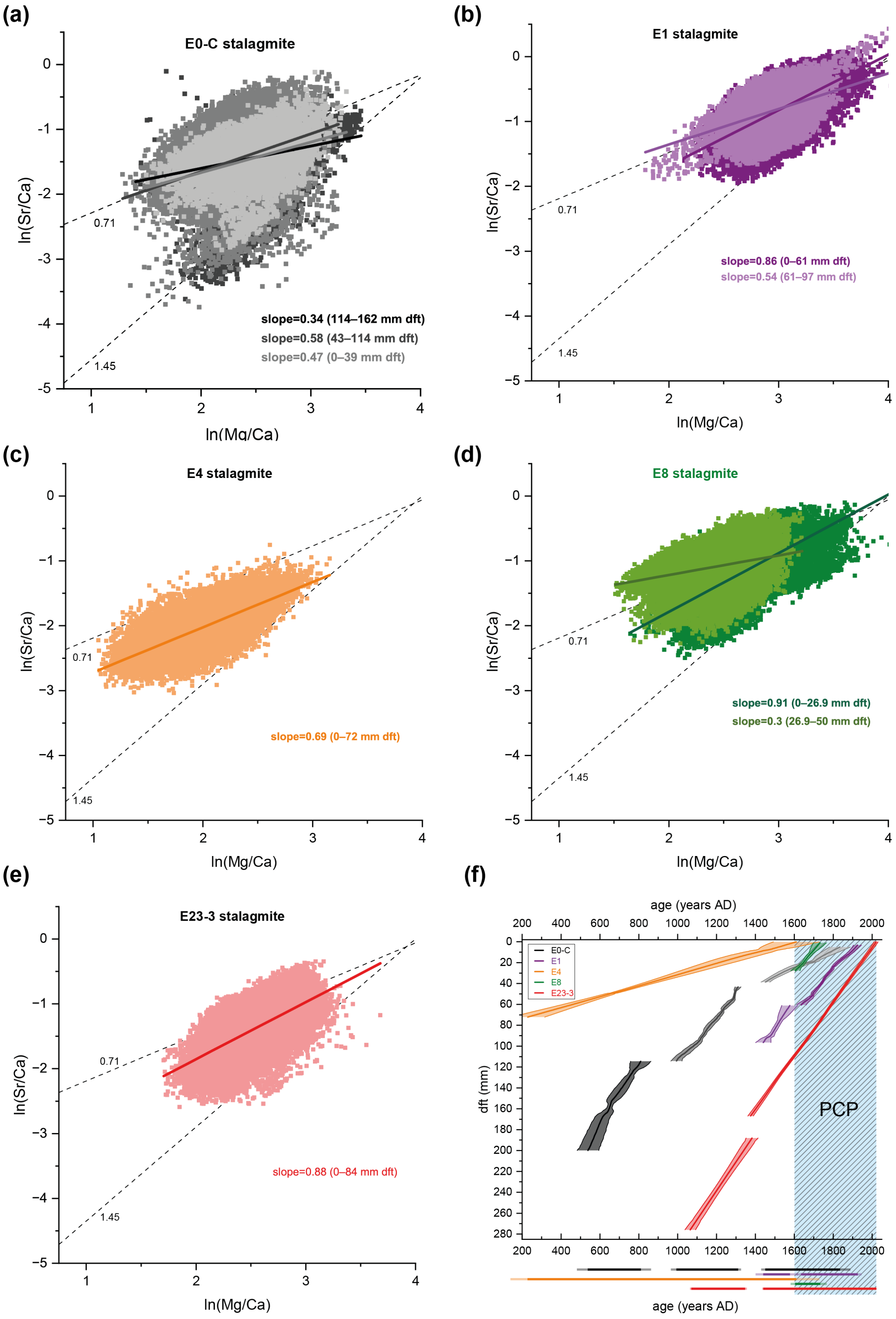
(a)
E0-C stalagmite
ln(Sr/Ca)
ln(Mg/Ca)
0.71
1.45
slope=0.34 (114–162 mm dft)
slope=0.58 (43–114 mm dft)
slope=0.47 (0–39 mm dft)
(b)
E1 stalagmite
ln(Sr/Ca)
ln(Mg/Ca)
0.71
1.45
slope=0.86 (0–61 mm dft)
slope=0.54 (61–97 mm dft)
(c)
E4 stalagmite
ln(Sr/Ca)
ln(Mg/Ca)
0.71
1.45
slope=0.69 (0–72 mm dft)
(d)
E8 stalagmite
ln(Sr/Ca)
ln(Mg/Ca)
0.71
1.45
slope=0.91 (0–26.9 mm dft)
slope=0.3 (26.9–50 mm dft)
(e)
E23-3 stalagmite
ln(Sr/Ca)
ln(Mg/Ca)
0.71
1.45
slope=0.88 (0–84 mm dft)
(f)
age (years AD)
dft (mm)
E0-C
E1
E4
E8
E23-3
PCP
age (years AD)

Figure A11. (From previous page:) **(a–e)** Relationships between ln(Sr/Ca) and ln(Mg/Ca) for different stalagmites from Áaktun Kóopo Cave. For stalagmites with known growth interruptions (hiatuses), distinct sections are analyzed separately, as indicated by the different colors for both the plotted data points and the fitted regression slopes (solid lines). The dashed lines represent the theoretical range of slopes, between 0.71 and 1.45, associated with prior calcite precipitation (PCP) and/or incongruent calcite dissolution (ICD), based on the models of Sinclair et al. (2012) and Wassenburg et al. (2020). dft = distance from top. **(f)** Stalagmite age-depth models presented in Chapter III.1, showing the age of the distinct sections considered in the regression plots (a–e). The regression slopes of ln(Mg/Ca) versus ln(Sr/Ca) in stalagmites E1, E8, and E23-3 (b, d, e) suggest significant influence of PCP on Mg and Sr incorporation for the last 400 years, as highlighted by the dashed blue shaded area.

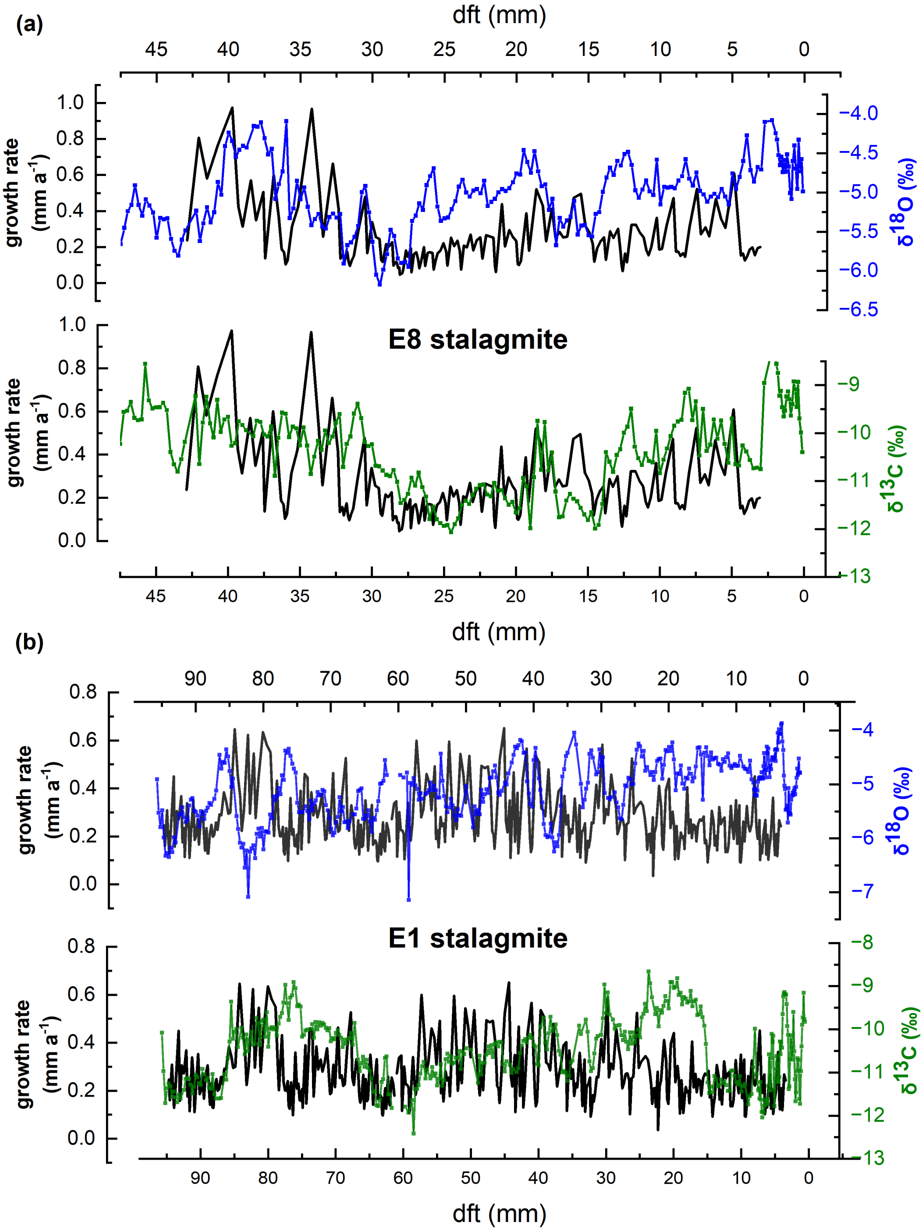

Figure A12. (From previous page:) Stable isotopes (δ^{18}O, δ^{13}C) compared to the growth rates of **(a)** stalagmite E8 and **(b)** stalagmite E1. While δ^{13}C values generally follow changes in growth rates, δ^{18}O values do not show such a connection. Growth rates were estimated based on the distance between consecutive Sr/Ca minima, determined through LA-ICP-MS measurements (see Methods II.3.2).

Supporting Information for Chapter VI – Composite Proxy Record for the Northeastern YP and Evaluation of Stalagmite δ^{18}O

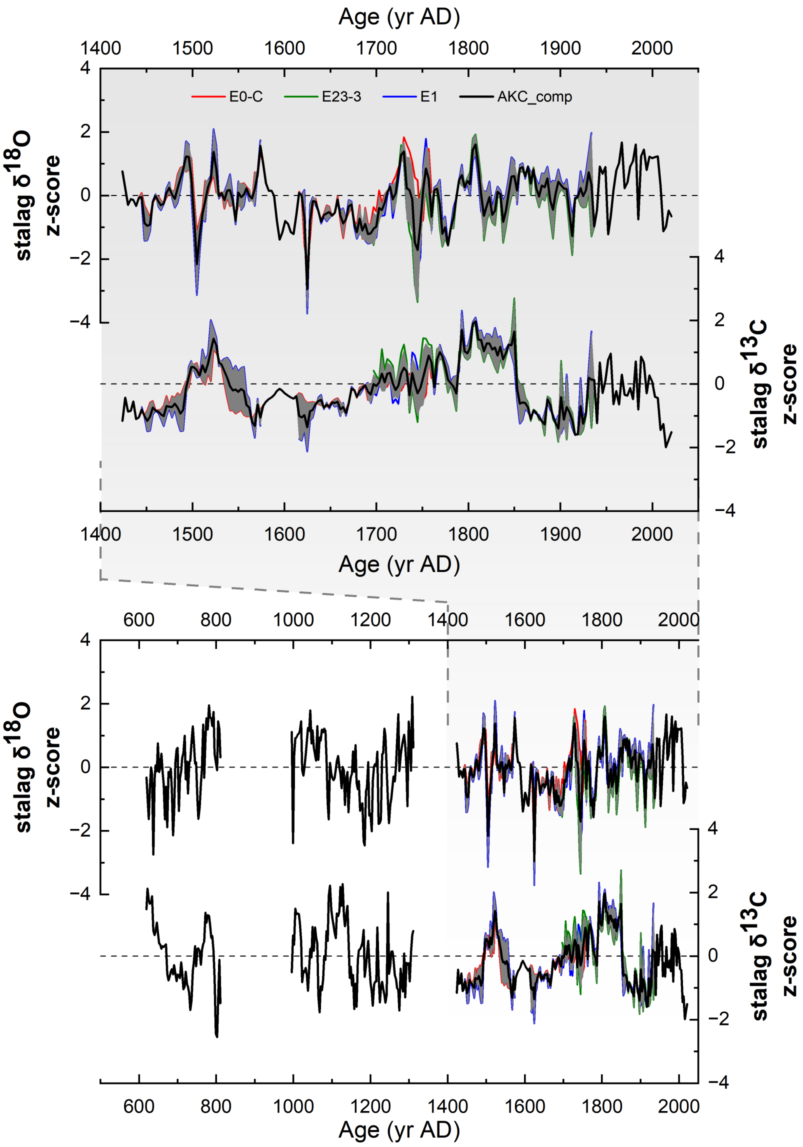

Figure A13. Z-score time series for stable oxygen (δ^{18}O) and stable carbon (δ^{13}C) isotopes from Áaktun Kóopo Cave stalagmites E0-C, E1, and E23-3 over the past 1,400 years (bottom), with a detailed view of the period from 1400 to 2022 AD (top). The black curve represents the mean z-score, while the grey envelope denotes the standard error of the mean.

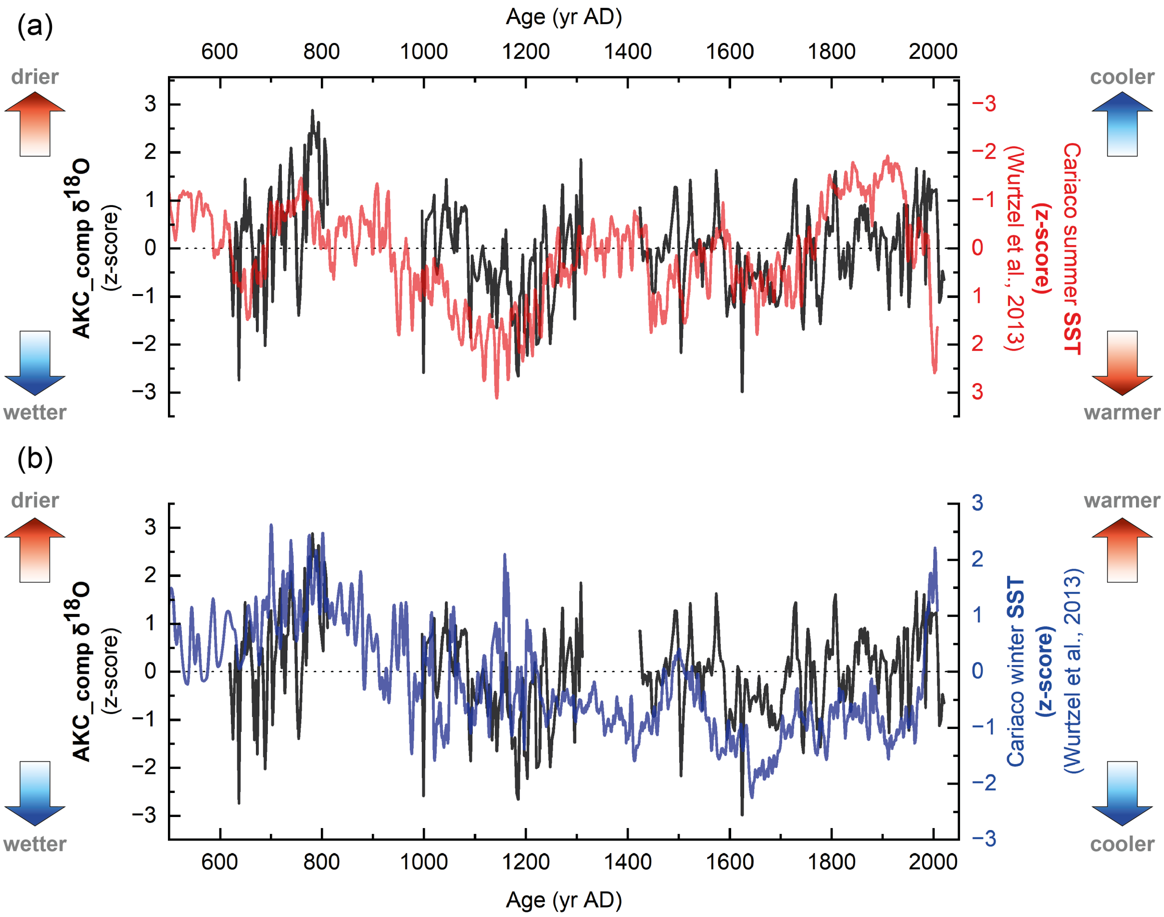

Figure A14. Z-score time series comparison of the δ^{18}O composite record from Áaktun Kóopo Cave (AKC) and reconstructed sea surface temperatures (SSTs) from the Cariaco Basin (Wurtzel et al., 2013). **(a)** Shows the comparison between AKC δ^{18}O (black line) and summer/fall SSTs (red line), while **(b)** shows the comparison between AKC δ^{18}O (black line) and winter/spring SSTs (blue line) over the past 1,400 years. Positive z-scores in the AKC δ^{18}O record indicate drier conditions, while negative values indicate wetter conditions. Warmer SSTs in the Cariaco Basin correspond to positive z-scores, while cooler SSTs correspond to negative z-scores. The alignment of the records illustrates the relationship between hydroclimatic variability in the Yucatán Peninsula and SST changes in the tropical Atlantic.

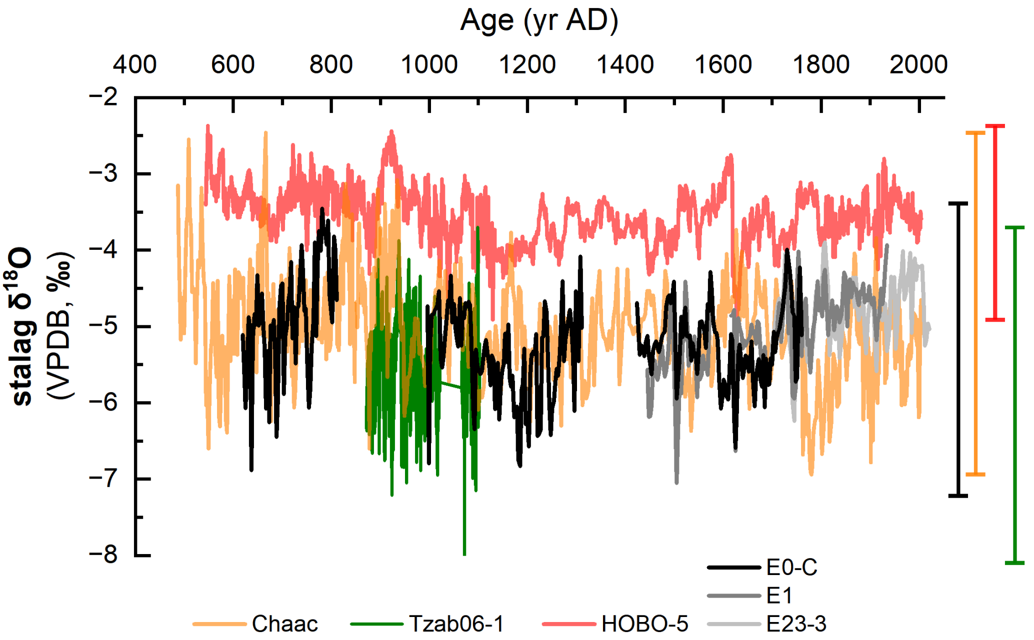

Figure A15. Stalagmite δ^{18}O records from the northern Yucatán Peninsula (YP) spanning the past 1500 years. The composite record from Áaktun Kóopo Cave (*AKC_comp*) is compared with two existing records from Tzabnah Cave in Tecoh, northwestern YP, *Chaac* (Medina-Elizalde et al., 2010) and *Tzab06-1* (James, 2023), as well as a record from Columnas Cave in the Puuc region, northern YP, *HOBO-5* (James, 2023).

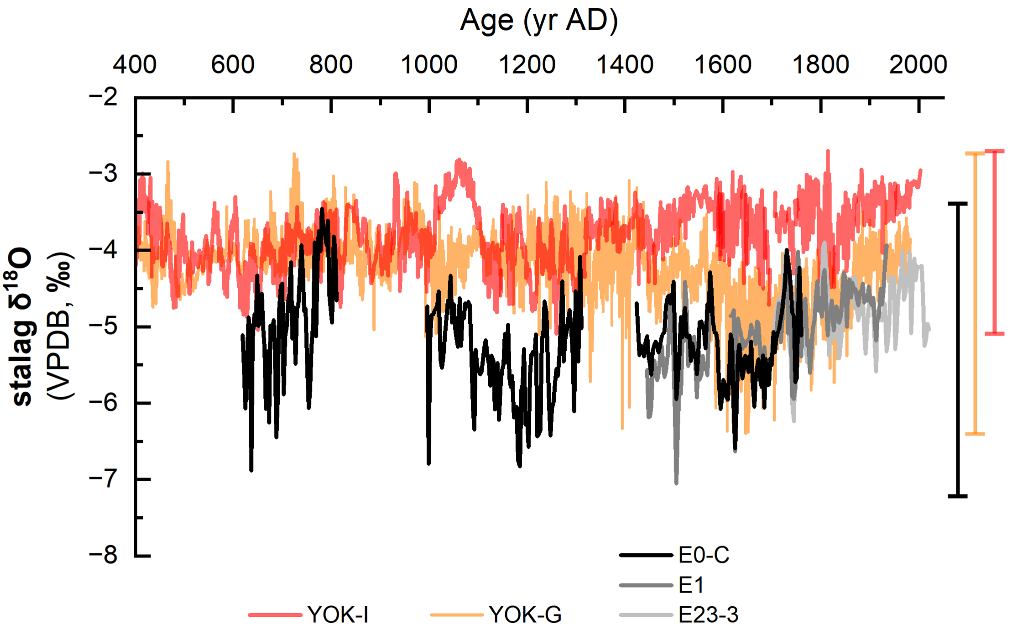

Figure A16. Stalagmite δ^{18}O records from the southern Yucatán Peninsula spanning the past 1500 years. The composite record from Áaktun Kóopo Cave (*AKC_comp*) is compared with the two records from YOK Balum Cave in Belize, southeastern YP, *YOK-I* (Kennett et al., 2012) and *YOK-G* (Ridley et al., 2015; Asmerom et al., 2020)

Supplementary Data

Supplementary Tables for Chapter III

Table A7. ^{230}Th/U data of speleothems from Áaktun Kóopo Cave. Errors are 2σ analytical errors. Corrected ^{230}Th ages assume variable (^{230}Th/^{232}Th) activity ratios ranging between 3 and 67. Those ratios have been estimated by using different approaches, such as isochron techniques (i), stratigraphic constrain (s), zero-age carbonate (zac) or layer counting (lc). For samples for which the initial (^{230}Th/^{232}Th) activity ratio couldn't be estimated, a mean value (m) of 35.5±32.5 was used to account for the high range.

Sample label	Lab. Nr.	dft (mm)	^{238}U (ng/g)	Error 2σ (abso.)	^{232}Th (ng/g)	Error 2σ (abso.)	^{230}Th/ ^{238}U (Act.rat.)	Error 2σ (abso.)	^{230}Th/ ^{232}Th (Act.rat)	Error (abso.)	δ^{234}U (‰)	Error 2σ (abso.)	Age (uncorr.) (ka)	Error 2σ (ka)	Age (corr.) (ka)	Error 2σ (ka)	Age (corr.) (a AD)	Error 2σ (a)	δ^{234}U (init.) (‰)	Error 2σ (abso.)	^{230}Th/^{232}Th (init.) (Act.rat.)	Error (abso.)	method
E0-A-49	9602	49	645.397	0.035	0.01935	0.00017	0.01952	0.00031	1997	36	38.6	1.5	2.068	0.033	2.032	0.046	-14	46	38.9	1.5	35.5	32.5	m
E0-A-8	9603	8	530.436	0.035	0.07321	0.0004	0.0163	0.00035	362.8	8	38.2	1.6	1.725	0.037	1.56	0.16	461	159	38.4	1.7	35.5	32.5	m
E0-B-5	9553	5	476.15	0.045			0.01525	0.00039			19.3	2.5	1.643	0.043	1.643	0.043	375	43	19.4	2.5	35.5	32.5	m
E0-B-35	11221	35	529.677	0.084	0.0746	0.0012	0.01801	0.00064	392	15	18.7	2.3	1.945	0.072	1.73	0.14	292	137	18.8	2.3	43.75	24.25	s,m
E0-B-59	9756	59	479.457	0.039	0.01293	0.00017	0.01675	0.00031	1909	44	16.2	1.9	1.812	0.035	1.778	0.047	240	47	16.3	1.9	35.5	32.5	m
EO-B-85,5	10986	85.5	560.886	0.042	0.20982	0.00078	0.01977	0.00029	161.3	2.5	16.9	1.7	2.141	0.032							15	12	s,m
E0-B-110	11222	110	591.414	0.031	0.06447	0.00029	0.01943	0.00019	547	5.8	15.3	1.5	2.107	0.021	1.97	0.13	50	131	15.4	1.5	35.5	32.5	m
E0-B-152	9755	152	655.593	0.061	0.28205	0.0008	0.02041	0.00033	145.5	2.4	14.6	1.9	2.215	0.036							16	13	s,m
EO-B-177	10987	177	601.345	0.047	0.19689	0.0006	0.02123	0.00027	197.6	2.6	20.4	1.4	2.292	0.03							23.5	20.5	s,m
E0-B-212	9552	212	549.821	0.047	0.14486	0.00074	0.0273	0.00045	317.9	5.5	18.5	3	2.962	0.05	2.63	0.31	-616	308	18.6	3	35.5	32.5	m
EO-C-Top	10521	2	926.114	0.05	1.2732	0.0028	0.01338	0.00015	29.73	0.34	19.2	1.2	1.441	0.016							26	3.7	s
E0-C-7	9555	7	769.553	0.047	0.04864	0.00018	0.00326	0.0001	158.1	4.9	13.6	1.2	0.352	0.011							36.5	31.5	s,m
EO-C-10,5	11232	10.5	935.652	0.059	0.05312	0.00035	0.00326	0.00013	175.9	7	11.9	1.1	0.352	0.014							36.25	31.75	s,m
EO-C-15,5	11233	15.5	1165.767	0.056	0.04018	0.00017	0.00329	0.000073	293.3	6.7	10.68	0.79	0.3556	0.0079	0.308	0.036	1713	36	10.69	0.79	39	29	s,m
EO-C-19	10973	19	1186.315	0.046	0.02106	0.00011	0.003113	0.000064	536	11	12.82	0.67	0.3357	0.0069	0.314	0.022	1708	22	12.83	0.67	35.5	32.5	m
E0-C-20	12136	20	1014.64	0.39	0.02751	0.000081	0.003377	0.000037	380.6	4.4	13.53	0.38	0.3639	0.0057	0.33	0.031	1693	31	13.54	0.38	35.5	32.5	m
EO-C-21,5	11234	21.5	832.906	0.044	0.10012	0.00027	0.004181	0.000079	106.7	2	11.05	0.63	0.4519	0.0087							35.5	32.5	m
EO-C-23.5	10520	23.5	804.089	0.053	0.05268	0.00018	0.005042	0.000099	234.8	4.7	14.4	1.1	0.543	0.011	0.462	0.074	1559	74	14.4	1.1	35.5	32.5	m
EO-C-24,5	11235	24.5	838.226	0.042	0.17535	0.00052	0.00608	0.00013	89.4	2	11.7	1.2	0.658	0.015							35.5	32.5	m
E0-C-37,5	9759	37.5	1105.866	0.073			0.00507	0.00014			13.3	1.1	0.547	0.015	0.555	0.017	1463	17	13.4	1.1	35.5	32.5	m
EO-C-43	11236	43	774.849	0.044	1.6817	0.0035	0.01195	0.00011	17	0.2	14.9	1.1	1.292	0.012							7.42	0.36	i
E0-C-45	9758	45	843.683	0.055	0.07688	0.00042	0.00687	0.00012	231.6	4.2	11.4	1	0.743	0.013	0.719	0.013	1299	13	11.4	1	7.42	0.36	i
EO-C-52	10974	52	980.159	0.049	0.05544	0.00016	0.006874	0.000073	371.4	4.1	10.55	0.85	0.7443	0.0078	0.73	0.008	1292	8	10.57	0.85	7.42	0.36	i
E0-C-57,5	11220	57.5	1076.86	0.3	0.022908	0.00008	0.006964	0.000083	1002	12	11.51	0.77	0.7533	0.009	0.727	0.026	1294	26	11.54	0.77	35.5	32.5	m
EO-C-63	10519	63	1113.238	0.066			0.007233	0.000076			11.42	0.61	0.7826	0.0082	0.785	0.009	1235	9	11.44	0.61	35.5	32.5	m
EO-C-69	10975	69	1050.387	0.06	0.06055	0.00016	0.007541	0.000082	399.8	4.5	10.3	0.66	0.817	0.009	0.794	0.02	1228	20	10.33	0.66	11.5	8.5	s,m
E0-C-69,5	12137	69.5	920.76	0.3	0.06441	0.00025	0.00831	0.00012	363.3	5.3	12.52	0.67	0.898	0.013	0.811	0.085	1212	85	12.55	0.67	35.5	32.5	m
EO-C-73	11237	73	933.81	0.043	0.05407	0.00016	0.008442	0.000099	448.9	5.5	12.77	0.67	0.913	0.011	0.828	0.054	1193	54	12.8	0.67	41.5	26.5	s,m
E0-C-75	11062	75	922.315	0.044	0.06312	0.00027	0.008285	0.000095	369.8	4.5	12.92	0.89	0.896	0.01	0.806	0.076	1215	76	12.95	0.9	37	31	s,m
E0-C-76	12138	76	921.68	0.2	0.021804	0.000085	0.008253	0.000084	1063	12	12.48	0.42	0.893	0.01	0.86	0.026	1163	26	12.51	0.42	39	29	s,m
EO-C-77	11238	77	994.05	0.05	0.04919	0.0002	0.008065	0.000091	498.6	5.9	11.6	1.1	0.873	0.01	0.811	0.057	1210	57	11.7	1.1	35.5	32.5	m
EO-C-81.5	10518	81.5	1087.077	0.068	0.00013409	0.00000072	0.008675	0.000085	213749	2386	12.5	1	0.9383	0.0093	0.938	0.009	1082	9	12.5	1	35.5	32.5	m

Continued on next page

Table A7 – *Continuation of* ^{230}*Th/U data of speleothems from Áaktun Kóopo Cave*

Sample label	**Lab. Nr.**	**dft (mm)**	^{238}**U (ng/g)**	**Error 2σ (abso.)**	^{232}**Th (ng/g)**	**Error 2σ (abso.)**	^{230}**Th/**^{238}**U (Act.rat.)**	**Error 2σ (abso.)**	^{230}**Th/**^{232}**Th (Act.rat)**	**Error (abso.)**	δ^{234}**U (‰)**	**Error 2σ (abso.)**	**Age (uncorr.) (ka)**	**Error 2σ (ka)**	**Age (corr.) (ka)**	**Error 2σ (ka)**	**Age (corr.) (a AD)**	**Error 2σ (a)**	δ^{234}**U (init.) (‰)**	**Error 2σ (abso.)**	^{230}**Th/**^{232}**Th (init.) (Act.rat.)**	**Error (abso.)**	**method**
EO-C-84,5	11239	84.5	1231.992	0.064	0.06069	0.00029	0.00885	0.00013	549.9	8.4	12.16	0.82	0.957	0.014	0.875	0.037	1146	37	12.19	0.82	47.5	20.5	s,m
EO-C-88,5	11266	88.5	1273.923	0.072	0.015025	0.000091	0.00829	0.00012	2168	34	10.2	1.2	0.898	0.013	0.883	0.019	1138	19	10.3	1.2	35.5	32.5	m
EO-C-92.5	10517	92.5	1323.557	0.064			0.008327	0.000079			12.94	0.93	0.9001	0.0085	0.904	0.009	1116	9	12.97	0.93	35.5	32.5	m
EO-C-96,5	11267	96.5	1195.955	0.079	0.03813	0.00022	0.00846	0.00015	817	15	10.2	1.5	0.917	0.016	0.903	0.019	1118	19	10.2	1.5	12.5	9.5	s,m
E0-C-99,5	11063	99.5	1185.693	0.063	0.08613	0.0003	0.00937	0.00011	393.4	4.6	12	1	1.014	0.012	0.941	0.048	1080	48	12	1	28.5	19	s
E0-C-100,5	12139	100.5	1041.81	0.23	0.013372	0.000048	0.009084	0.000086	2160	22	13.25	0.59	0.982	0.01	0.966	0.018	1057	18	13.28	0.59	35.5	32.5	m
EO-C-102	11240	102	1099.32	0.072	0.04319	0.00029	0.009	0.00016	703	13	11.2	1.1	0.975	0.017	0.925	0.05	1096	50	11.2	1.1	35.5	32.5	m
EO-C-105,5	10976	105.5	1131.861	0.057	0.03114	0.0001	0.009367	0.000079	1041.3	9.4	12.27	0.63	1.0137	0.0085	0.979	0.033	1042	33	12.31	0.63	35.5	32.5	m
EO-C-108,5	11241	108.5	1112.965	0.066	0.16815	0.00048	0.01095	0.00014	222.9	2.9	13.4	1.2	1.184	0.015	1.03	0.14	990	140	13.5	1.2	28.75	25.75	s,m
EO-C-112	11268	112	1021.202	0.066	0.09948	0.00054	0.01068	0.00025	336.7	8.1	14.9	2.4	1.154	0.027	1.03	0.11	989	114	15	2.4	35.5	32.5	m
EO-C-113	10516	113	1117.696	0.06	0.14679	0.00022	0.01073	0.0001	249.1	2.4	13.53	0.7	1.161	0.011	1.02	0.13	1000	128	13.57	0.7	30.5	27.5	s,m
EO-C-115,5	11269	115.5	523.807	0.035	0.33368	0.00078	0.01689	0.00025	81.6	1.2	17.5	1.7	1.825	0.028							33.25	8.25	s
EO-C-116,75	11270	116.75	490.803	0.028	0.09853	0.00034	0.0115	0.00026	176.8	4	16.3	2	1.241	0.028							26	23	s,m
EO-C-117	10977	117	526.817	0.032	0.9144	0.0024	0.01455	0.00032	25.6	0.6	16.1	1.7	1.572	0.035							8	3	s,m
EO-C-119,5	11271	119.5	481.611	0.025	0.02899	0.00016	0.01225	0.00018	626.7	9.8	14.1	1.3	1.325	0.02	1.224	0.049	797	49	14.2	1.3	47.5	20.5	s,m
E0-C-120	9757	120	410.434	0.036	0.01817	0.00018	0.01137	0.00033	790	24	15.5	2.2	1.228	0.037	1.173	0.065	845	65	15.5	2.2	35.5	32.5	m
E0-C-120,75	12140	120.75	416.21	0.12	0.03035	0.00012	0.01276	0.00021	529.3	8.9	16.6	1	1.377	0.023	1.265	0.065	758	65	16.6	1	44	24	s,m
EO-C-122	11272	122	354.898	0.022	0.02883	0.00014	0.01249	0.0002	471.5	7.8	12.5	1.9	1.354	0.022	1.241	0.087	780	87	12.5	1.9	39.25	28.75	s,m
E0-C-122	12141	122	366.19	0.18	0.03441	0.00015	0.01315	0.00031	424	10	14.8	1.8	1.423	0.034	1.261	0.073	762	73	14.8	1.8	48.75	19.25	s,m
E0-C-124,75	12142	124.75	550.69	0.15	0.02739	0.00013	0.01215	0.00016	747	10	18.3	1.3	1.309	0.017	1.247	0.057	776	57	18.3	1.3	35.5	32.5	m
EO-C-129,75	11273	129.75	636.94	0.04	0.02816	0.00011	0.01187	0.0002	823	14	11.8	1.8	1.287	0.022	1.271	0.022	750	22	11.9	1.8	9.9	1.9	i
E0-C-135,5	12143	135.5	587.65	0.23	0.14321	0.00041	0.01266	0.00024	159.7	3.1	16.8	1.5	1.366	0.026							9.9	1.9	i
E0-C-138	12144	138	528.94	0.2	0.5926	0.0011	0.01534	0.00029	42.1	0.8	16.6	1.2	1.658	0.032							9.9	1.9	i
EO-C-152,5	11274	152.5	572.494	0.026	0.01628	0.000079	0.01279	0.00012	1380	14	14.2	1.2	1.384	0.013	1.365	0.017	656	17	14.2	1.2	19	10	i
E0-C-156,5	12145	156.5	560.93	0.16	0.09047	0.00018	0.01359	0.00019	259.2	3.7	16.15	0.92	1.469	0.021	1.361	0.06	662	60	16.21	0.92	19	10	i
EO-C-158	11275	158	598.252	0.036	0.03174	0.00016	0.013	0.0002	752	12	15.5	1.5	1.405	0.022	1.369	0.029	652	29	15.5	1.5	19	10	i
EO-C-162,5	10978	162.5	632.411	0.032	0.04017	0.00011	0.0133	0.00016	641.2	8.1	16.8	1.2	1.435	0.018	1.356	0.075	665	75	16.9	1.2	35.5	32.5	m
E0-C-166	11064	166	371.477	0.02	0.05432	0.00021	0.01499	0.00022	312.5	4.8	18	2.1	1.618	0.024	1.44	0.17	586	165	18	2.1	35.5	32.5	m
E0-C-200	9554	200	544.975	0.045	0.10513	0.00051	0.01585	0.00029	251.4	4.8	17.4	1.9	1.712	0.032	1.47	0.22	547	220	17.5	1.9	35.5	32.5	m
E1-Top	10979	1	1771.328	0.089	0.51392	0.0009	0.005344	0.000057	56.5	0.6	9.23	0.63	0.5789	0.0061							52.1	4.1	s
E1-3,5	11223	3.5	1836.087	0.078	0.07911	0.00025	0.000765	0.000038	54.5	2.7	8.11	0.84	0.0828	0.0041							27	24	s,m
E1-7	11224	7	1743.306	0.097	0.07268	0.00023	0.001802	0.000037	132.3	2.8	8.49	0.61	0.195	0.0041							51	17	s,m
E1 - 11	11946	11	2237.344	0.088	0.02562	0.00011	0.00132	0.000025	350.9	6.9	10.01	0.66	0.1426	0.0039	0.128	0.013	1895	13	10.01	0.66	35.5	32.5	m
E1 - 16	11947	16	1551.859	0.055	0.11735	0.00037	0.002977	0.000046	120.2	1.9	10.22	0.63	0.3218	0.0053							50	18	s,m
E1-22	11225	22	1797.401	0.091	0.017469	0.000063	0.00217	0.000041	681	13	10.62	0.62	0.2343	0.0044	0.222	0.012	1799	12	10.63	0.62	35.5	32.5	m
E1 - 26,5	11948	26.5	1543.853	0.055	0.03103	0.0001	0.002362	0.000045	361.8	7	13.87	0.65	0.2544	0.0067	0.229	0.024	1794	24	13.88	0.65	35.5	32.5	m
E1 - 31	11949	31	1930.797	0.049	0.03077	0.00012	0.002563	0.00004	493.9	7.9	15.09	0.58	0.2757	0.0059	0.256	0.019	1767	19	15.1	0.58	35.5	32.5	m
E1-35	11058	35	1473.198	0.075	0.017711	0.000075	0.002671	0.000045	679	12	12.47	0.67	0.288	0.0049	0.267	0.009	1754	9	12.48	0.67	49	19	s,m
E1 - 39	11950	39	1745.56	0.077			0.002577	0.000051			14.7	0.9	0.2773	0.0059	0.2773	0.0059	1746	6	14.7	0.9	0	0	
E1 - 44	11951	44	1728.205	0.06	0.09521	0.00033	0.003532	0.000046	197.6	2.7	13.11	0.56	0.3808	0.0051							38.5	14.5	s
E1-48,5	11226	48.5	1726.966	0.083	0.014962	0.000064	0.003087	0.000042	1087	16	12.61	0.5	0.333	0.0046	0.322	0.011	1699	11	12.63	0.5	35.5	32.5	m
E1 - 54	11952	54	1715.401	0.08	0.05117	0.00015	0.003389	0.000043	350	4.5	14.25	0.82	0.3649	0.0066	0.328	0.034	1695	34	14.26	0.82	35.5	32.5	m

Continued on next page

Table A7 – *Continuation of ^{230}Th/U data of speleothems from Áaktun Kóopo Cave*

Sample label	**Lab. Nr.**	**dft (mm)**	**^{238}U (ng/g)**	**Error 2σ (abso.)**	**^{232}Th (ng/g)**	**Error 2σ (abso.)**	**^{230}Th/ ^{238}U (Act.rat.)**	**Error 2σ (abso.)**	**^{230}Th/ ^{232}Th (Act.rat)**	**Error (abso.)**	**δ^{234}U (‰)**	**Error 2σ (abso.)**	**Age (uncorr.) (ka)**	**Error 2σ (ka)**	**Age (corr.) (ka)**	**Error 2σ (ka)**	**Age (corr.) (a AD)**	**Error 2σ (a)**	**δ^{234}U (init.) (‰)**	**Error 2σ (abso.)**	**^{230}Th/^{232}Th (init.) (Act.rat.)**	**Error (abso.)**	**method**
E1-59,5	10980	59.5	1523.231	0.082	0.05646	0.00013	0.003989	0.000042	329.3	3.5	17.06	0.49	0.4285	0.0046	0.382	0.043	1639	43	17.08	0.49	35.5	32.5	m
E1-62	11059	62	1313.74	0.58	0.2305	0.0022	0.00555	0.00015	96.8	2.7	15.95	0.95	0.597	0.016							35.75	16.25	s
E1-63,5	11674	63.5	1354.252	0.055	0.23936	0.00027	0.004845	0.000053	84.1	0.9	16.03	0.41	0.5213	0.0057							23.25	16.25	s
E1 - 70	11953	70	1242.043	0.079	0.17828	0.00051	0.004473	0.000065	95.9	1.4	17.71	0.85	0.4803	0.0071							21.5	18.5	s,m
E1-73,5	11227	73.5	1735.97	0.088	0.03627	0.00015	0.004784	0.00006	698	9.3	12.19	0.57	0.5166	0.0065	0.491	0.025	1531	25	12.2	0.57	35.5	32.5	m
E1-75	11060	75	1202.21	0.061	0.14117	0.00039	0.007591	0.000087	198.3	2.3	14.89	0.93	0.819	0.01							68	0	s
E1-78,5	11061	78.5	1512.197	0.095	0.2912	0.0011	0.00765	0.00019	122	3.1	13.4	1.2	0.827	0.021							55.25	12.75	s,m
E1-80,5	11675	80.5	1434.68	0.046	0.11122	0.00014	0.005014	0.000043	198.3	1.7	14.43	0.4	0.5403	0.0046							35.5	32.5	m
E1 - 84	11954	84	1541.23	0.065	0.03422	0.0002	0.00514	0.00013	714	18	17.58	0.71	0.552	0.014	0.525	0.029	1498	29	17.6	0.71	35.5	32.5	m
E1 - 87	11955	87	1515.484	0.076	0.18074	0.00061	0.00702	0.00017	181.7	4.5	15.28	0.69	0.756	0.02							54	14	s,m
E1-90,5	11228	90.5	1621.764	0.089	0.06072	0.00023	0.005437	0.000056	443.5	4.9	14.58	0.66	0.5859	0.0061	0.539	0.043	1482	43	14.6	0.66	35.5	32.5	m
E1-92	10981	92	1695.43	0.1	0.03719	0.00012	0.005474	0.000061	764.8	8.8	18.04	0.58	0.5879	0.0065	0.561	0.026	1460	26	18.07	0.58	35.5	32.5	m
E2-6	9629	6	762.897	0.072	0.09972	0.00059	0.00099	0.00014	23.3	3.3	10.6	1.5	0.107	0.015							35.5	32.5	m
E2-262,5	9628	262.5	509.779	0.044	0.17169	0.00059	0.02049	0.00034	186.6	3.1	7.4	2.2	2.241	0.037							35.5	32.5	m
E3-5,5	9631	5.5	970.698	0.076	0.26381	0.00074	0.00137	0.00011	15.5	1.3	7.2	1.6	0.149	0.012							9.2	6.2	s,m
E3-2B-22	12146	22	633.16	0.15	0.33474	0.00071	0.002339	0.000054	13.6	0.3	8.23	0.66	0.2532	0.0068							8.1	5.1	s,m
E3-2B-70	12147	70	575.55	0.17	0.025897	0.000091	0.005241	0.00009	356.8	6.2	5.01	0.74	0.57	0.01	0.513	0.054	1510	54	5.01	0.74	35.5	32.5	m
E3-2B-130	12148	130	325.44	0.24	0.012097	0.000081	0.01255	0.0003	1028	25	9.1	1.6	1.365	0.033	1.318	0.053	705	53	9.1	1.6	35.5	32.5	m
E3-2B-155	12149	155	440.53	0.24	0.09521	0.00031	0.01379	0.00017	193.2	2.5	10.7	0.94	1.498	0.018							35.5	32.5	m
E3-215	9630	215	331.193	0.042	0.06848	0.00068	0.02208	0.00063	328	10	17.8	4.1	2.391	0.07	2.13	0.25	-116	247	17.9	4.1	35.5	32.5	m
E4-Top	11051	1	1126.134	0.061	8.657	0.018	0.02142	0.00017	8.53	0.07	8.2	1.1	2.342	0.019							7.3	1.2	s
E4-4,5	11141	4.5	1065.393	0.077	0.8496	0.0025	0.007237	0.000087	27.74	0.34	9.4	1	0.785	0.01							15.9	11.7	s
E4-6	9550	6	1140.565	0.067	2.0224	0.0046	0.0094	0.00016	16.23	0.28	7.63	0.86	1.022	0.018							10.9	5.2	s
E4-7,5	11142	7.5	1237.376	0.072	0.09626	0.00022	0.006081	0.000065	239	2.6	8.49	0.77	0.6595	0.0071	0.562	0.088	1459	88	8.5	0.77	35.5	32.5	m
E4-9	11143	9	1254.572	0.06	0.11964	0.00025	0.006362	0.000081	204.2	2.6	7.7	1	0.6906	0.009	0.57	0.11	1450	108	7.7	1	35.5	32.5	m
E4-10	11052	10	1153.243	0.076	2.2986	0.0042	0.01109	0.00011	17.01	0.18	8.27	0.89	1.206	0.013							10	6.5	s
E4-11,5	11144	11.5	1130.282	0.068	4.456	0.012	0.01418	0.00016	11.03	0.13	10.4	1	1.541	0.018							7.65	3.3	s
E4-13	11145	13	1202.259	0.092	1.0409	0.0025	0.00861	0.00012	30.51	0.44	12.5	1.6	0.931	0.014							9.15	6.15	s,m
E4-15	11146	15	1365.197	0.079	26.473	0.059	0.05088	0.00024	8.065	0.042	11.23	0.81	5.629	0.027							7.36	0.64	s
E4-16	11147	16	1473.913	0.079	2.7839	0.0056	0.012427	0.000097	20.2	0.16	6.54	0.68	1.355	0.011							13.15	6.85	s
E4-18	10982	18	1740.17	0.11	0.32014	0.00065	0.0085	0.000095	141.6	1.6	7.03	0.63	0.924	0.011							35.5	32.5	m
E4-19,5	11152	19.5	1645.78	0.1	15.62	0.046	0.0313	0.00019	10.095	0.067	9.46	0.81	3.435	0.021							7.45	1.3	s
E4-20,5	11153	20.5	1326.155	0.062	3.5764	0.0088	0.015155	0.000099	17.21	0.12	8.9	0.81	1.65	0.011							7.8	4.7	s
E4-21,5	11154	21.5	997.112	0.055	9.369	0.022	0.0318	0.00016	10.328	0.057	8.62	0.77	3.493	0.018							7.7	1.3	s
E4-23	11155	23	869.915	0.041	3.7221	0.0092	0.01734	0.00014	12.4	0.11	7.4	1.1	1.893	0.016							6.5	2.9	s
E4-24,5	11156	24.5	885.362	0.052	7.593	0.019	0.03917	0.00024	13.99	0.092	8.9	1.1	4.318	0.027							11	1.5	s
E4-25,5	11157	25.5	740.474	0.038	1.8107	0.0033	0.01629	0.00015	20.41	0.19	8.5	1	1.776	0.016							10	5.1	s
E4-28	10983	28	853.239	0.055	1.3851	0.0022	0.01227	0.00014	23.17	0.27	9	1.2	1.334	0.016							9.1	6.1	s,m
E4-29,5	11158	29.5	823.449	0.034	0.8976	0.0023	0.01432	0.00013	40.12	0.39	8.15	0.69	1.56	0.015							16.5	11.8	s
E4-37	11053	37	744.671	0.032	1.1892	0.003	0.01494	0.00015	28.59	0.3	5.9	0.9	1.631	0.017							12.5	8.1	s

Continued on next page

Table A7 – *Continuation of ^{230}Th/U data of speleothems from Áaktun Kóopo Cave*

Sample label	Lab. Nr.	dft (mm)	^{238}U (ng/g)	Error 2σ (abso.)	^{232}Th (ng/g)	Error 2σ (abso.)	^{230}Th/ ^{238}U (Act.rat.)	Error 2σ (abso.)	^{230}Th/ ^{232}Th (Act.rat)	Error (abso.)	δ^{234}U (‰)	Error 2σ (abso.)	Age (uncorr.) (ka)	Error 2σ (ka)	Age (corr.) (ka)	Error 2σ (ka)	Age (corr.) (a AD)	Error 2σ (a)	δ^{234}U (init.) (‰)	Error 2σ (abso.)	^{230}Th/^{232}Th (init.) (Act.rat.)	Error (abso.)	method
E4-40	11054	40	659.002	0.036	1.1814	0.0021	0.01697	0.00014	28.94	0.24	6.7	1	1.853	0.015							14.6	7.2	s
E4-42	11148	42	623.639	0.033	1.3714	0.0026	0.02015	0.00017	28.07	0.25	7.1	1.3	2.204	0.019							16.3	5.8	s
E4-43,5	11149	43.5	666.473	0.04	0.4339	0.0011	0.01411	0.00014	66.58	0.67	9	1.2	1.536	0.015							26.6	19.9	s
E4-44,5	11150	44.5	604.009	0.039	0.12745	0.00029	0.01301	0.00011	189.6	1.7	5.2	1.4	1.421	0.012							36.5	31.5	s,m
E4-46	11161	46	659.711	0.029	0.2563	0.00057	0.01376	0.00013	107.8	1.1	5.1	1.1	1.503	0.015							26	17	s
E4-47,5	11160	47.5	635.883	0.024	0.33454	0.00067	0.01382	0.0001	80.42	0.63	6.43	0.89	1.508	0.012							8.2	1.3	i
E4-49	11159	49	715.499	0.04	0.12728	0.00031	0.0129	0.00014	221.8	2.5	8	1.2	1.405	0.016	1.353	0.018	668	18	8	1.2	8.2	1.3	i
E4-49,5	9551	49.5	671.6	0.054	0.05352	0.00033	0.01264	0.00026	487	10	10.4	1.5	1.373	0.028	1.349	0.028	669	28	10.5	1.5	8.2	1.3	i
EMW5-28,5	9686	28.5	377.813	0.035	0.17431	0.00056	0.018491	0.000376	123.4	2.5	11.8	2.2	2.011	0.041							35.5	32.5	m
E6-7,5	9752	7.5	877.43	0.39			0.9110	0.0034			2.0	2.7	261.0	5.5	261.0	5.5	-258952	5495	4.1	5.7	35.5	32.5	m
E6-31,5	9751	31.5	106.068	0.071			0.981	0.013			17.1	2.7	347	46	347	46	-345265	45665	45.7	8.4	35.5	32.5	m
E6-220	9750	220	320.176	0.098	0.02666	0.00063	0.9788	0.0052	36054	867	14.1	2.2	353	17	353	16	-350578	15754	38.2	6.3	35.5	32.5	m
E7-A-108	9753	108	1253.11	0.10			0.01967	0.00017			70.4	1.4	2.025	0.016	2.025	0.016	-6.6	15.6	70.8	1.4	35.5	32.5	m
E7-B-21,5	9754	21.5	887.647	0.091	0.07604	0.00073	0.011399	0.000197	411.1	8.1	39	1.8	1.203	0.021	1.1	0.1	920	96	39.2	1.8	35.5	32.5	m
E8-Top	10984	0	1221.09	0.068	2.4599	0.0046	0.022375	0.000184	34.05	0.29	9.93	0.91	2.443	0.021							31.6	2.3	s
E8-8,5	11340	8.5	1176.211	0.049	0.03538	0.00011	0.003085	0.000044	313.7	4.5	12.64	0.83	0.3327	0.0047	0.295	0.035	1726	35	12.65	0.84	35.5	32.5	m
E8-14,5	11229	14.5	948.936	0.046	0.01924	0.000081	0.003505	0.000068	527	10	12.04	0.68	0.3783	0.0074	0.353	0.024	1668	24	12.05	0.68	35.5	32.5	m
E8-21	11341	21	1082.946	0.042	0.029229	0.000079	0.003795	0.000072	430.5	8.3	14.15	0.56	0.4088	0.0078	0.375	0.031	1646	31	14.17	0.56	35.5	32.5	m
E8-26	11055	26	882.458	0.054	0.0518	0.00018	0.003951	0.000089	205.6	4.7	12.98	0.87	0.426	0.01	0.353	0.07	1668	70	12.99	0.87	35.5	32.5	m
E8-29	11056	29	1026.913	0.053	0.03556	0.00011	0.004532	0.000078	399.8	7	15.3	0.92	0.4878	0.0084	0.48	0.009	1541	9	15.32	0.92	6.4	2.4	i
E8-32	11676	32	1116.095	0.039	0.08274	0.00015	0.004613	0.000054	190.5	2.3	13.5	0.82	0.4974	0.006							6.4	2.4	i
E8-35,5	11677	35.5	1058.437	0.055	0.09093	0.00023	0.004632	0.000063	165.4	2.3	15.77	0.79	0.4984	0.0068							6.4	2.4	i
E8-37	11342	37	1100.165	0.064	0.17512	0.00047	0.004792	0.000072	92.1	1.4	15.35	0.74	0.5158	0.0077							6.4	2.4	i
E8-42	11678	42	1341.937	0.056	0.11717	0.00041	0.00455	0.000079	159.9	2.8	16.2	1	0.4894	0.0085							4	1	s,m
E8-46,5	11679	46.5	1367.938	0.07	0.10724	0.00031	0.004584	0.000078	178.9	3.1	15.3	0.76	0.4935	0.0085							5.25	2.25	s,m
E8-48	10985	48	1310.124	0.077	0.08031	0.00027	0.004577	0.00008	228.5	4.1	14.73	0.95	0.4929	0.0087	0.48	0.011	1542	11	14.75	0.95	6.25	3.25	s,m
E8-55	11231	55	596.551	0.027	0.09265	0.00034	0.013494	0.000194	264.7	3.9	7.5	1	1.47	0.022	1.27	0.18	746	181	7.5	1	35.5	32.5	m
E8-60,5	11057	60.5	523.577	0.04	0.06993	0.00029	0.013166	0.000207	301.7	4.9	7.1	1.4	1.435	0.023	1.27	0.15	754	148	7.1	1.4	35.5	32.5	m
E8-67	9633	67	597.658	0.057	0.598	0.0015	0.016261	0.000334	50	1	9.9	1.9	1.77	0.036							35.5	32.5	m
E-23-1-B	12454	0	874.48	0.32	0.05694	0.00094	0.509867	0.000888	24283	405	23.79	0.55	74.9	0.2	74.82	0.21	-72799	206	29.38	0.68	35.5	32.5	m
E-23-1-T	12459	0	680.29	0.34	3.624	0.0057	0.146284	0.00048	85.25	0.31	27.53	0.85	16.735	0.061							35.5	32.5	m
E-23-2-B	12455	0	535.299	0.038	0.12051	0.00025	0.020089	0.000121	276.7	1.8	22.22	0.53	2.164	0.013	1.88	0.26	138	259	22.34	0.53	35.5	32.5	m
E-23-2-T	12460	0	899.094	0.033	0.04017	0.00014	0.002021	0.000032	140.2	2.3	15.01	0.35	0.2173	0.0034							35.5	32.5	m
E-23-3B-7,5	12464	7.5	1309.574	0.061	0.04209	0.00013	0.000583	0.000023	55.9	2.2	21.77	0.63	0.0622	0.0025							26	7	lc
E-23-3B-29	12465	29	1133.958	0.091	0.04686	0.00014	0.001476	0.000049	110.1	3.7	22.6	0.73	0.1575	0.0052							26	7	lc

Continued on next page

Table A7 – *Continuation of* ^{230}*Th/U data of speleothems from Áaktun Kóopo Cave*

Sample label	Lab. Nr.	dft (mm)	^{238}U (ng/g)	Error 2σ (abso.)	^{232}Th (ng/g)	Error 2σ (abso.)	^{230}Th/^{238}U (Act.rat.)	Error 2σ (abso.)	^{230}Th/^{232}Th (Act.rat)	Error (abso.)	δ^{234}U (‰)	Error 2σ (abso.)	Age (uncorr.) (ka)	Error 2σ (ka)	Age (corr.) (ka)	Error 2σ (ka)	Age (corr.) (a AD)	Error 2σ (a)	δ^{234}U (init.) (‰)	Error 2σ (abso.)	^{230}Th/^{232}Th (init.) (Act.rat.)	Error (abso.)	method
E-23-3B-60	12825	60	1264.36	0.59	0.027192	0.000093	0.002369	0.000036	344.2	5.4	19.63	0.55	0.2537	0.0053	0.234	0.006	1790	6	19.64	0.55	26	7	lc
E-23-3B-92	12824	92	1261.47	0.39	0.03349	0.00016	0.003411	0.000058	400.8	7.1	20.16	0.4	0.3652	0.0078	0.341	0.009	1683	9	20.18	0.4	26	7	lc
E-23-3B-125	12467	125	1422.348	0.065	0.022633	0.000066	0.00479	0.000034	937.1	7.1	20.72	0.47	0.513	0.0036	0.499	0.005	1526	5	20.74	0.47	26	7	lc
E-23-3B-146	12468	146	1501.446	0.054	0.04257	0.00011	0.005505	0.000045	603.5	5.2	21.12	0.48	0.5895	0.0049	0.564	0.008	1460	8	21.16	0.48	26	7	lc
E-23-3A-190	12462	190	1273.973	0.078	0.05294	0.00015	0.00641	0.000083	476.4	6.3	21.85	0.68	0.6861	0.0089	0.648	0.013	1376	13	21.89	0.68	26	7	lc
E-23-3A-268	12463	268	1362.189	0.058	0.0454	0.00012	0.008981	0.000061	830.7	6.1	23.47	0.39	0.961	0.0066	0.931	0.011	1093	11	23.54	0.39	26	7	lc
Estrella Loc.5	11705	-	925.727	0.048	4.7348	0.0073	0.983	0.0017	593.3	1.4	15.76	0.62	358.3	5.3	351.9	8.1	-349878	8085	42.6	1.9	35.5	32.5	m
Estrella drip site 1	11706	-	1325.237	0.06	24.42	0.043	0.03924	0.00017	6.571	0.03	3.11	0.65	4.352	0.02	0.01	1.38	2016	1378	3.11	0.65	6.5	3.25	zac

Table A8. Stable Isotopes (δ^{13}C, δ^{18}O) for stalagmite E0-C. The age of each sample corresponds to the chronology discussed in Chapter III.2.

Sample ID	**Analyzing laboratory**	**Distance [mm] (from top)**	**Age [a BP]**	**Age [a AD]**	**Age error [a]**	**$\delta^{13}C_{carb}$ [‰ VPDB]**	**$\delta^{18}O_{carb}$ [‰ VPDB]**
E0-C-704	Earth Sciences, Heidelberg University	0.3				-10.4	-4.8
E0-C-703	Earth Sciences, Heidelberg University	0.4				-11.33	-4.98
E0-C-702	Earth Sciences, Heidelberg University	0.5				-11.04	-4.72
E0-C-700	Earth Sciences, Heidelberg University	0.7				-11.91	-5.16
E0-C-699	Earth Sciences, Heidelberg University	0.8				-10.49	-4.98
E0-C-698	Earth Sciences, Heidelberg University	0.9				-11.57	-5.28
E0-C-697	Earth Sciences, Heidelberg University	1				-11.47	-5.34
E0-C-696	Earth Sciences, Heidelberg University	1.1				-11.63	-5.46
E0-C-695	Earth Sciences, Heidelberg University	1.2				-12.23	-5.39
E0-C-694	Earth Sciences, Heidelberg University	1.3				-11.73	-5.17
E0-C-693	Earth Sciences, Heidelberg University	1.4				-12.55	-5.33
E0-C-692	Earth Sciences, Heidelberg University	1.5				-11.93	-4.96
E0-C-691	Earth Sciences, Heidelberg University	1.6				-11.33	-4.38
E0-C-689	Earth Sciences, Heidelberg University	1.8				-11.19	-4.12
E0-C-688	Earth Sciences, Heidelberg University	1.9				-10.86	-4.19
E0-C-687	Earth Sciences, Heidelberg University	2				-11.31	-4.05
E0-C-686	Earth Sciences, Heidelberg University	2.1				-12.09	-4.26
E0-C-685	Earth Sciences, Heidelberg University	2.2				-11.51	-4.34
E0-C-684	Earth Sciences, Heidelberg University	2.3				-11.26	-4.16
E0-C-683	Earth Sciences, Heidelberg University	2.4				-11.38	-4.24
E0-C-682	Earth Sciences, Heidelberg University	2.5				-11.69	-4.33
E0-C-681	Earth Sciences, Heidelberg University	2.6				-12.02	-4.25
E0-C-679	Earth Sciences, Heidelberg University	2.8				-11.88	-4.5
E0-C-678	Earth Sciences, Heidelberg University	2.9				-11.53	-4.43
E0-C-677	Earth Sciences, Heidelberg University	3				-11.24	-4.37
E0-C-676	Earth Sciences, Heidelberg University	3.1				-11.1	-4.3
E0-C-674	Earth Sciences, Heidelberg University	3.3				-12.61	-4.56
E0-C-673	Earth Sciences, Heidelberg University	3.4				-12.75	-4.55
E0-C-672	Earth Sciences, Heidelberg University	3.5				-11.88	-4.51
E0-C-671	Earth Sciences, Heidelberg University	3.6				-11.61	-4.37
E0-C-670	Earth Sciences, Heidelberg University	3.7				-11.31	-4.4
E0-C-669	Earth Sciences, Heidelberg University	3.8				-11	-4.15
E0-C-668	Earth Sciences, Heidelberg University	3.9				-10.51	-4.07
E0-C-667	Earth Sciences, Heidelberg University	4				-11.06	-4.11
E0-C-666	Earth Sciences, Heidelberg University	4.1				-11.2	-4.14
E0-C-665	Earth Sciences, Heidelberg University	4.2				-11.6	-4.17
E0-C-664	Earth Sciences, Heidelberg University	4.3				-10.14	-4.03
E0-C-663	Earth Sciences, Heidelberg University	4.4				-9.06	-3.83
E0-C-662	Earth Sciences, Heidelberg University	4.5				-9.39	-4.01
E0-C-661	Earth Sciences, Heidelberg University	4.6				-10.44	-4.27
E0-C-660	Earth Sciences, Heidelberg University	4.7				-10.14	-4.39
E0-C-659	Earth Sciences, Heidelberg University	4.8				-9.25	-4.7
E0-C-658	Earth Sciences, Heidelberg University	4.9				-8.84	-4.84
E0-C-657	Earth Sciences, Heidelberg University	5				-9.08	-4.72
E0-C-656	Earth Sciences, Heidelberg University	5.1	115.8	1834.2	52.8	-9.84	-5.13
E0-C-655	Earth Sciences, Heidelberg University	5.2	116.9	1833.1	52.6	-8.93	-4.26
E0-C-654	Earth Sciences, Heidelberg University	5.3	117.9	1832.1	52.4	-9.07	-4.24
E0-C-653	Earth Sciences, Heidelberg University	5.4	118.9	1831.1	52.3	-10.09	-4.37
E0-C-652	Earth Sciences, Heidelberg University	5.5	119.8	1830.2	52.2	-10.93	-5.2

Continued on next page

Table A8 – *Continuation of Stable Isotopes ($\delta^{13}C$, $\delta^{18}O$) for stalagmite E0-C*

Sample ID	**Analyzing laboratory**	**Distance [mm] (from top)**	**Age [a BP]**	**Age [a AD]**	**Age error [a]**	**$\delta^{13}C_{carb}$ [‰ VPDB]**	**$\delta^{18}O_{carb}$ [‰ VPDB]**
E0-C-651	Earth Sciences, Heidelberg University	5.6	120.9	1829.1	52.1	-10.88	-5.63
E0-C-649	Earth Sciences, Heidelberg University	5.8	123	1827	51.9	-10.84	-5.7
E0-C-648	Earth Sciences, Heidelberg University	5.9	124.1	1825.9	51.9	-10.82	-4.99
E0-C-647	Earth Sciences, Heidelberg University	6	125.2	1824.8	51.8	-10.11	-4.82
E0-C-624	Elemtex Ltd., Cornwall, Cornwall	6.1	126.5	1823.5	51.4	-10.45	-4.8
E0-C-623	Elemtex Ltd., Cornwall, Cornwall	6.35	129.4	1820.6	50.8	-9.59	-4.32
E0-C-622	Elemtex Ltd., Cornwall, Cornwall	6.6	131.9	1818.1	50.3	-9.79	-4.13
E0-C-621	Elemtex Ltd., Cornwall, Cornwall	6.85	134.6	1815.4	49.9	-10.38	-3.91
E0-C-620	Earth Sciences, Heidelberg University	7.1	137.6	1812.4	49.4	-10.4	-4.65
E0-C-619	Elemtex Ltd., Cornwall	7.35	140.2	1809.8	48.9	-10.03	-4.32
E0-C-618	Earth Sciences, Heidelberg University	7.6	142.7	1807.3	48.5	-9.98	-4.77
E0-C-617	Elemtex Ltd., Cornwall	7.85	145.2	1804.8	48.2	-10.08	-4.57
E0-C-616	Earth Sciences, Heidelberg University	8.1	147.6	1802.4	47.8	-10.14	-4.93
E0-C-615	Elemtex Ltd., Cornwall	8.35	150.3	1799.7	47.2	-9.74	-4.48
E0-C-614	Earth Sciences, Heidelberg University	8.6	152.6	1797.4	46.7	-10.08	-5.23
E0-C-613	Elemtex Ltd., Cornwall	8.85	155.1	1794.9	46.2	-9.82	-4.69
E0-C-612	Earth Sciences, Heidelberg University	9.1	157.9	1792.1	45.7	-10.01	-5.35
E0-C-611	Elemtex Ltd., Cornwall	9.35	160.5	1789.5	45.2	-10.19	-4.9
E0-C-610	Earth Sciences, Heidelberg University	9.6	163.2	1786.8	44.7	-10.29	-5.56
E0-C-609	Elemtex Ltd., Cornwall	9.85	165.8	1784.2	44.3	-10.25	-5.08
E0-C-608	Earth Sciences, Heidelberg University	10.1	168.5	1781.5	43.8	-10.33	-5.66
E0-C-607	Elemtex Ltd., Cornwall	10.35	171.2	1778.8	43	-10.19	-5.34
E0-C-606	Earth Sciences, Heidelberg University	10.6	173.8	1776.2	42.5	-10.31	-5.56
E0-C-605	Elemtex Ltd., Cornwall	10.85	176.6	1773.4	41.7	-9.99	-5.04
E0-C-604	Earth Sciences, Heidelberg University	11.1	179.3	1770.7	40.9	-10.82	-5.87
E0-C-603	Elemtex Ltd., Cornwall	11.35	181.8	1768.2	40.3	-10.09	-5.43
E0-C-602	Earth Sciences, Heidelberg University	11.6	184.4	1765.6	39.7	-10.22	-5.78
E0-C-601	Elemtex Ltd., Cornwall	11.85	187	1763	39.2	-10.42	-5.29
E0-C-600	Earth Sciences, Heidelberg University	12.1	189.4	1760.6	38.7	-10.21	-5.86
E0-C-599	Elemtex Ltd., Cornwall	12.35	191.8	1758.2	37.9	-10.23	-5.73
E0-C-598	Earth Sciences, Heidelberg University	12.6	194.4	1755.6	37.1	-10.85	-6
E0-C-597	Elemtex Ltd., Cornwall	12.85	196.9	1753.1	36.3	-10.81	-5.63
E0-C-596	Earth Sciences, Heidelberg University	13.1	199.2	1750.8	35.7	-10.5	-5.82
E0-C-595	Elemtex Ltd., Cornwall	13.35	201.6	1748.4	35.1	-10.01	-5.34
E0-C-594	Earth Sciences, Heidelberg University	13.6	203.9	1746.1	34.3	-10.47	-5.84
E0-C-593	Elemtex Ltd., Cornwall	13.85	206.2	1743.8	33.5	-10.18	-6.09
E0-C-592	Earth Sciences, Heidelberg University	14.1	208.6	1741.4	32.6	-10.54	-5.96
E0-C-591	Elemtex Ltd., Cornwall	14.35	210.8	1739.2	31.6	-10.27	-5.36
E0-C-590	Earth Sciences, Heidelberg University	14.6	213.2	1736.8	30.5	-10.45	-5.94
E0-C-589	Elemtex Ltd., Cornwall	14.85	215.4	1734.6	29.4	-10.77	-5.78
E0-C-588	Earth Sciences, Heidelberg University	15.1	217.6	1732.4	28.4	-10.42	-5.89
E0-C-587	Elemtex Ltd., Cornwall	15.35	220.1	1729.9	27	-10.37	-5.69
E0-C-586	Earth Sciences, Heidelberg University	15.6	222.4	1727.6	25.7	-10.46	-5.83
E0-C-585	Elemtex Ltd., Cornwall	15.85	224.3	1725.7	24.7	-10.68	-5.16
E0-C-584	Earth Sciences, Heidelberg University	16.1	226.4	1723.6	23.5	-10.29	-5.58
E0-C-583	Elemtex Ltd., Cornwall	16.35	228.3	1721.7	22.5	-10.66	-5.1
E0-C-582	Earth Sciences, Heidelberg University	16.6	230.3	1719.7	21.7	-11.22	-5.88
E0-C-581	Elemtex Ltd., Cornwall	16.85	232.6	1717.4	20.3	-11.39	-5.6
E0-C-580	Earth Sciences, Heidelberg University	17.1	234.4	1715.6	19.6	-11.4	-6.06
E0-C-579	Elemtex Ltd., Cornwall	17.35	236.3	1713.7	19.1	-10.94	-5.49
E0-C-578	Earth Sciences, Heidelberg University	17.6	237.7	1712.3	19.7	-11.14	-6.07
E0-C-577	Elemtex Ltd., Cornwall	17.85	239.2	1710.8	20.6	-10.78	-5.19

Continued on next page

Table A8 – *Continuation of Stable Isotopes ($\delta^{13}C$, $\delta^{18}O$) for stalagmite E0-C*

Sample ID	**Analyzing laboratory**	**Distance [mm] (from top)**	**Age [a BP]**	**Age [a AD]**	**Age error [a]**	**$\delta^{13}C_{carb}$ [‰ VPDB]**	**$\delta^{18}O_{carb}$ [‰ VPDB]**
E0-C-576	Earth Sciences, Heidelberg University	18.1	241.1	1708.9	21.3	-10.89	-5.65
E0-C-575	Elemtex Ltd., Cornwall	18.35	243.5	1706.5	21.7	-11.17	-5.35
E0-C-574	Earth Sciences, Heidelberg University	18.6	246.2	1703.8	21.9	-11.12	-5.67
E0-C-573	Elemtex Ltd., Cornwall	18.85	249	1701	22.2	-10.98	-5.2
E0-C-572	Earth Sciences, Heidelberg University	19.1	252.4	1697.6	22	-10.99	-6.62
E0-C-571	Elemtex Ltd., Cornwall	19.35	257.9	1692.1	21.5	-10.52	-4.99
E0-C-570	Earth Sciences, Heidelberg University	19.6	264.7	1685.3	22.6	-10.79	-5.98
E0-C-569	Elemtex Ltd., Cornwall	19.85	270.9	1679.1	24.5	-10.57	-5.68
E0-C-568	Earth Sciences, Heidelberg University	20.1	276.3	1673.7	25.4	-10.33	-6.07
E0-C-567	Elemtex Ltd., Cornwall	20.35	281.5	1668.5	25.5	-10.66	-5.14
E0-C-566	Earth Sciences, Heidelberg University	20.6	287.2	1662.8	25.7	-10.88	-5.04
E0-C-565	Elemtex Ltd., Cornwall	20.85	293.2	1656.8	26.1	-11.31	-4.29
E0-C-564	Earth Sciences, Heidelberg University	21.1	298.8	1651.2	26.9	-11.37	-4.82
E0-C-563	Elemtex Ltd., Cornwall	21.35	304	1646	27.9	-11.56	-4.71
E0-C-562	Earth Sciences, Heidelberg University	21.6	309	1641	29	-11.83	-5.3
E0-C-561	Elemtex Ltd., Cornwall	21.85	313.8	1636.2	30.1	-11.62	-5.06
E0-C-560	Earth Sciences, Heidelberg University	22.1	317.9	1632.1	30.9	-11.65	-5.01
E0-C-559	Elemtex Ltd., Cornwall	22.35	321.6	1628.4	31.6	-11.57	-4.82
E0-C-558	Earth Sciences, Heidelberg University	22.6	325.4	1624.6	32	-11.62	-5.15
E0-C-557	Elemtex Ltd., Cornwall	22.85	328.9	1621.1	32.4	-11.3	-4.93
E0-C-556	Earth Sciences, Heidelberg University	23.1	332.4	1617.6	32.7	-11.43	-5.38
E0-C-555	Elemtex Ltd., Cornwall	23.35	335.6	1614.4	33.1	-11.41	-5.14
E0-C-554	Earth Sciences, Heidelberg University	23.6	339.2	1610.8	33	-11.53	-5.73
E0-C-553	Elemtex Ltd., Cornwall	23.85	342.6	1607.4	32.8	-11.27	-5.24
E0-C-552	Earth Sciences, Heidelberg University	24.1	345.7	1604.3	32.5	-11.33	-5.44
E0-C-551	Elemtex Ltd., Cornwall	24.35	348.5	1601.5	32.3	-10.56	-5.15
E0-C-550	Earth Sciences, Heidelberg University	24.6	351.6	1598.4	32.1	-9.92	-5.53
E0-C-549	Elemtex Ltd., Cornwall	24.85	354.9	1595.1	31.8	-9.02	-4.91
E0-C-548	Elemtex Ltd., Cornwall	25.1	358.7	1591.3	31.3	-8.89	-5.36
E0-C-547	Elemtex Ltd., Cornwall	25.35	361.8	1588.2	31	-8.13	-4.7
E0-C-545	Elemtex Ltd., Cornwall	25.85	368.3	1581.7	30.1	-9.95	-4.9
E0-C-544	Elemtex Ltd., Cornwall	26.1	371.7	1578.3	29.7	-9.96	-5.02
E0-C-543	Elemtex Ltd., Cornwall	26.35	374.4	1575.6	29.6	-9.57	-5.15
E0-C-542	Earth Sciences, Heidelberg University	26.6	377.2	1572.8	29.3	-9.73	-5.05
E0-C-541	Elemtex Ltd., Cornwall	26.85	380.6	1569.4	28.8	-10.3	-4.8
E0-C-540	Earth Sciences, Heidelberg University	27.1	383.7	1566.3	28.3	-10.19	-5.5
E0-C-539	Elemtex Ltd., Cornwall	27.35	386.6	1563.4	28.1	-9.62	-5.36
E0-C-538	Earth Sciences, Heidelberg University	27.6	389.4	1560.6	28	-9.63	-5.67
E0-C-537	Elemtex Ltd., Cornwall	27.85	392.3	1557.7	28.1	-9.81	-5.62
E0-C-536	Earth Sciences, Heidelberg University	28.1	395.5	1554.5	27.8	-9.09	-5.94
E0-C-535	Elemtex Ltd., Cornwall	28.35	398.5	1551.5	27.5	-9.04	-5.3
E0-C-534	Earth Sciences, Heidelberg University	28.6	401.2	1548.8	27.4	-9.4	-5.1
E0-C-533	Elemtex Ltd., Cornwall	28.85	404.1	1545.9	27.2	-9.61	-4.36
E0-C-532	Earth Sciences, Heidelberg University	29.1	406.9	1543.1	27.1	-10.59	-4.83
E0-C-531	Elemtex Ltd., Cornwall	29.35	409.6	1540.4	26.7	-9.64	-4.33
E0-C-530	Earth Sciences, Heidelberg University	29.6	412.1	1537.9	26.6	-9.99	-4.7
E0-C-529	Elemtex Ltd., Cornwall	29.85	414.8	1535.2	26.3	-10.24	-4.45
E0-C-528	Earth Sciences, Heidelberg University	30.1	417.2	1532.8	26.1	-10.43	-4.76
E0-C-527	Elemtex Ltd., Cornwall	30.35	419.9	1530.1	25.9	-10.69	-4.61
E0-C-526	Earth Sciences, Heidelberg University	30.6	422.4	1527.6	25.7	-10.51	-4.9
E0-C-525	Elemtex Ltd., Cornwall	30.85	424.8	1525.2	25.5	-10.58	-4.63
E0-C-524	Earth Sciences, Heidelberg University	31.1	427.4	1522.6	25.3	-10.76	-5.07

Continued on next page

Table A8 – *Continuation of Stable Isotopes ($\delta^{13}C$, $\delta^{18}O$) for stalagmite E0-C*

Sample ID	**Analyzing laboratory**	**Distance [mm] (from top)**	**Age [a BP]**	**Age [a AD]**	**Age error [a]**	**$\delta^{13}C_{carb}$ [‰ VPDB]**	**$\delta^{18}O_{carb}$ [‰ VPDB]**
E0-C-523	Elemtex Ltd., Cornwall	31.35	430.1	1519.9	25.1	-10.69	-5.08
E0-C-522	Earth Sciences, Heidelberg University	31.6	432.7	1517.3	24.9	-10.69	-5.1
E0-C-521	Elemtex Ltd., Cornwall	31.85	435.3	1514.7	24.6	-11.11	-5.13
E0-C-520	Earth Sciences, Heidelberg University	32.1	437.9	1512.1	24.3	-10.83	-5.3
E0-C-519	Elemtex Ltd., Cornwall	32.35	440.6	1509.4	23.9	-10.67	-5.14
E0-C-518	Earth Sciences, Heidelberg University	32.6	443.2	1506.8	23.6	-11.13	-5.34
E0-C-517	Elemtex Ltd., Cornwall	32.85	445.6	1504.4	23.2	-11.58	-5.09
E0-C-516	Earth Sciences, Heidelberg University	33.1	448.2	1501.8	22.8	-11.13	-5.38
E0-C-515	Elemtex Ltd., Cornwall	33.35	450.7	1499.3	22.5	-11.33	-5.17
E0-C-514	Earth Sciences, Heidelberg University	33.6	453.2	1496.8	22.1	-11.37	-5.48
E0-C-513	Elemtex Ltd., Cornwall	33.85	455.7	1494.3	21.8	-11.36	-5.17
E0-C-512	Earth Sciences, Heidelberg University	34.1	458.2	1491.8	21.3	-10.87	-5.37
E0-C-511	Elemtex Ltd., Cornwall	34.35	460.6	1489.4	20.9	-11.09	-5.11
E0-C-510	Earth Sciences, Heidelberg University	34.6	463.1	1486.9	20.6	-10.97	-5.65
E0-C-509	Elemtex Ltd., Cornwall	34.85	465.6	1484.4	20.5	-11.13	-5.35
E0-C-508	Earth Sciences, Heidelberg University	35.1	468.1	1481.9	20.3	-11.63	-5.66
E0-C-507	Elemtex Ltd., Cornwall	35.35	470.5	1479.5	20.2	-11.59	-5.38
E0-C-506	Earth Sciences, Heidelberg University	35.6	472.9	1477.1	20.1	-11.51	-5.5
E0-C-505	Elemtex Ltd., Cornwall	35.85	475.1	1474.9	20.1	-11.39	-5.04
E0-C-504	Earth Sciences, Heidelberg University	36.1	477.3	1472.7	20	-11.86	-5.39
E0-C-503	Elemtex Ltd., Cornwall	36.35	479.4	1470.6	19.9	-11.57	-5.1
E0-C-502	Earth Sciences, Heidelberg University	36.6	481.5	1468.5	20	-11.94	-5.59
E0-C-501	Elemtex Ltd., Cornwall	36.85	483.5	1466.5	20.1	-11.52	-5.14
E0-C-500	Elemtex Ltd., Cornwall	37.1	485.5	1464.5	20.4	-10.99	-5.22
E0-C-499	Elemtex Ltd., Cornwall	37.35	487.4	1462.6	20.6	-11.03	-5.34
E0-C-498	Elemtex Ltd., Cornwall	37.6	489.5	1460.5	20.9	-11.38	-5.25
E0-C-497	Elemtex Ltd., Cornwall	37.85	491.7	1458.3	21.2	-11.4	-5.28
E0-C-496	Elemtex Ltd., Cornwall	38.1	494	1456	21.6	-11.42	-5.38
E0-C-495	Elemtex Ltd., Cornwall	38.35	496.3	1453.7	22	-10.82	-5.18
E0-C-494	Elemtex Ltd., Cornwall	38.6	498.5	1451.5	22.4	-10.8	-4.98
E0-C-493	Elemtex Ltd., Cornwall	43.25	639	1311	15	-10.8	-5.02
E0-C-492	Elemtex Ltd., Cornwall	43.5	640	1310	14.7	-11.42	-5.27
E0-C-491	Elemtex Ltd., Cornwall	43.75	640.9	1309.1	14.3	-11.26	-4.76
E0-C-490	Elemtex Ltd., Cornwall	44	641.9	1308.1	13.9	-10.89	-4.1
E0-C-489	Elemtex Ltd., Cornwall	44.25	642.8	1307.2	13.7	-10.4	-4.06
E0-C-488	Elemtex Ltd., Cornwall	44.5	643.7	1306.3	13.3	-11.07	-4.47
E0-C-487	Elemtex Ltd., Cornwall	44.75	644.7	1305.3	12.9	-11.2	-5.3
E0-C-486	Elemtex Ltd., Cornwall	45	645.4	1304.6	12.6	-11.12	-5.49
E0-C-485	Elemtex Ltd., Cornwall	45.25	646.5	1303.5	12	-11.13	-5.08
E0-C-484	Earth Sciences, Heidelberg University	45.5	647.4	1302.6	11.6	-11.69	-4.92
E0-C-483	Elemtex Ltd., Cornwall	45.75	648.4	1301.6	11	-11.61	-4.7
E0-C-482	Earth Sciences, Heidelberg University	46	649.4	1300.6	10	-11.78	-4.64
E0-C-481	Elemtex Ltd., Cornwall	46.25	650.3	1299.7	9	-11.6	-4.58
E0-C-480	Earth Sciences, Heidelberg University	46.5	651.1	1298.9	7.9	-11.31	-4.53
E0-C-479	Elemtex Ltd., Cornwall	46.75	651.9	1298.1	6.6	-11.64	-4.54
E0-C-478	Earth Sciences, Heidelberg University	47	652.3	1297.7	5.6	-12.13	-5.28
E0-C-477	Elemtex Ltd., Cornwall	47.25	652.8	1297.2	5.1	-10.8	-4.7
E0-C-476	Earth Sciences, Heidelberg University	47.5	653.2	1296.8	4.8	-11.91	-5.28
E0-C-475	Elemtex Ltd., Cornwall	47.75	653.5	1296.5	4.6	-11.62	-5.47
E0-C-474	Earth Sciences, Heidelberg University	48	653.8	1296.2	4.6	-11.47	-6.19
E0-C-473	Elemtex Ltd., Cornwall	48.25	654.2	1295.8	4.5	-11.15	-5.9
E0-C-472	Earth Sciences, Heidelberg University	48.5	654.5	1295.5	4.4	-11.68	-6

Continued on next page

Table A8 – *Continuation of Stable Isotopes ($\delta^{13}C$, $\delta^{18}O$) for stalagmite E0-C*

Sample ID	**Analyzing laboratory**	**Distance [mm] (from top)**	**Age [a BP]**	**Age [a AD]**	**Age error [a]**	**$\delta^{13}C_{carb}$ [‰ VPDB]**	**$\delta^{18}O_{carb}$ [‰ VPDB]**
E0-C-471	Elemtex Ltd., Cornwall	48.75	654.8	1295.2	4.4	-10.99	-5.61
E0-C-470	Earth Sciences, Heidelberg University	49	655.2	1294.8	4.5	-11.27	-6.01
E0-C-469	Elemtex Ltd., Cornwall	49.25	655.5	1294.5	4.5	-11.43	-5.65
E0-C-468	Earth Sciences, Heidelberg University	49.5	655.8	1294.2	4.5	-11.23	-5.74
E0-C-467	Elemtex Ltd., Cornwall	49.75	656.1	1293.9	4.6	-10.77	-5.25
E0-C-466	Earth Sciences, Heidelberg University	50	656.3	1293.7	4.6	-11.33	-5.51
E0-C-465	Elemtex Ltd., Cornwall	50.25	656.7	1293.3	4.7	-11.49	-5
E0-C-464	Earth Sciences, Heidelberg University	50.5	657	1293	4.7	-11.34	-5.39
E0-C-463	Elemtex Ltd., Cornwall	50.75	657.3	1292.7	4.8	-11.54	-4.71
E0-C-462	Earth Sciences, Heidelberg University	51	657.6	1292.4	4.8	-11.47	-5.23
E0-C-461	Elemtex Ltd., Cornwall	51.25	657.8	1292.2	4.8	-11.94	-4.95
E0-C-459	Elemtex Ltd., Cornwall	51.75	658.4	1291.6	5.1	-11.2	-4.87
E0-C-457	Elemtex Ltd., Cornwall	52.25	658.9	1291.1	5.2	-11.1	-4.36
E0-C-455	Elemtex Ltd., Cornwall	52.75	659.4	1290.6	5.4	-10.4	-4.17
E0-C-453	Elemtex Ltd., Cornwall	53.25	659.9	1290.1	5.7	-11.99	-4.92
E0-C-451	Elemtex Ltd., Cornwall	53.75	660.5	1289.5	6.1	-11.46	-5.07
E0-C-449	Elemtex Ltd., Cornwall	54.25	661.4	1288.6	7.2	-10.74	-4.62
E0-C-447	Elemtex Ltd., Cornwall	54.75	662.6	1287.4	8.4	-10.99	-4.77
E0-C-445	Elemtex Ltd., Cornwall	55.25	664.4	1285.6	10.4	-11.78	-4.83
E0-C-443	Elemtex Ltd., Cornwall	55.75	668	1282	13.6	-11.71	-4.98
E0-C-441	Elemtex Ltd., Cornwall	56.25	671.6	1278.4	15.9	-11.41	-5.16
E0-C-439	Elemtex Ltd., Cornwall	56.75	674.6	1275.4	17.1	-12.15	-5.52
E0-C-437	Elemtex Ltd., Cornwall	57.25	677.2	1272.8	17.7	-11.73	-4.25
E0-C-435	Elemtex Ltd., Cornwall	57.75	679.5	1270.5	17.7	-11.88	-4.79
E0-C-433	Elemtex Ltd., Cornwall	58.25	681.9	1268.1	17.4	-11.69	-5
E0-C-431	Elemtex Ltd., Cornwall	58.75	684.5	1265.5	17.2	-11.59	-5.41
E0-C-429	Elemtex Ltd., Cornwall	59.25	687.3	1262.7	17.1	-11.53	-5.66
E0-C-427	Elemtex Ltd., Cornwall	59.75	690.2	1259.8	17.1	-11.26	-5.56
E0-C-423	Elemtex Ltd., Cornwall	60.75	696.5	1253.5	16.7	-11.17	-6.01
E0-C-421	Elemtex Ltd., Cornwall	61.25	699.6	1250.4	16.4	-11.45	-6.1
E0-C-420	Earth Sciences, Heidelberg University	61.5	701.1	1248.9	16.4	-11.7	-6.75
E0-C-419	Elemtex Ltd., Cornwall	61.75	702.4	1247.6	16.2	-11.37	-6.32
E0-C-418	Earth Sciences, Heidelberg University	62	703.7	1246.3	16.2	-10.8	-6.76
E0-C-417	Elemtex Ltd., Cornwall	62.25	704.9	1245.1	16.1	-10.18	-6.05
E0-C-416	Earth Sciences, Heidelberg University	62.5	706.2	1243.8	16	-11.92	-5.8
E0-C-415	Elemtex Ltd., Cornwall	62.75	707.5	1242.5	15.9	-11.71	-5.29
E0-C-414	Earth Sciences, Heidelberg University	63	708.6	1241.4	15.6	-12.05	-5.7
E0-C-413	Elemtex Ltd., Cornwall	63.25	709.8	1240.2	15.2	-11.51	-4.89
E0-C-412	Earth Sciences, Heidelberg University	63.5	710.9	1239.1	14.8	-12.01	-4.84
E0-C-411	Elemtex Ltd., Cornwall	63.75	711.9	1238.1	14.5	-11.78	-4.08
E0-C-410	Earth Sciences, Heidelberg University	64	712.8	1237.2	14.2	-11.76	-4.87
E0-C-409	Elemtex Ltd., Cornwall	64.25	714	1236	13.2	-11.86	-4.68
E0-C-408	Earth Sciences, Heidelberg University	64.5	715.2	1234.8	11.7	-11.71	-5.1
E0-C-407	Elemtex Ltd., Cornwall	64.75	716.3	1233.7	9.6	-11.56	-4.9
E0-C-406	Earth Sciences, Heidelberg University	65	717.2	1232.8	7.6	-11.79	-5.17
E0-C-405	Elemtex Ltd., Cornwall	65.25	717.7	1232.3	6.9	-11.5	-4.75
E0-C-404	Earth Sciences, Heidelberg University	65.5	718.2	1231.8	6.8	-11.59	-5.06
E0-C-403	Elemtex Ltd., Cornwall	66	719.1	1230.9	7.1	-11.36	-4.81
E0-C-402	Earth Sciences, Heidelberg University	66.25	719.6	1230.4	7.6	-11.96	-5.38
E0-C-401	Elemtex Ltd., Cornwall	66.5	720.2	1229.8	7.9	-11.54	-5.09
E0-C-400	Earth Sciences, Heidelberg University	66.75	720.8	1229.2	8.6	-11.83	-5.92
E0-C-398	Earth Sciences, Heidelberg University	67.25	722.3	1227.7	10.1	-11.82	-6.3

Continued on next page

Table A8 – *Continuation of Stable Isotopes ($\delta^{13}C$, $\delta^{18}O$) for stalagmite E0-C*

Sample ID	**Analyzing laboratory**	**Distance [mm] (from top)**	**Age [a BP]**	**Age [a AD]**	**Age error [a]**	**$\delta^{13}C_{carb}$ [‰ VPDB]**	**$\delta^{18}O_{carb}$ [‰ VPDB]**
E0-C-396	Earth Sciences, Heidelberg University	67.75	724.3	1225.7	12.3	-11.64	-6.43
E0-C-394	Earth Sciences, Heidelberg University	68.25	726.3	1223.7	13.1	-11.97	-6.4
E0-C-393	Elemtex Ltd., Cornwall	68.5	727.3	1222.7	13.3	-11.77	-5.76
E0-C-392	Earth Sciences, Heidelberg University	68.75	728.6	1221.4	13.8	-11.51	-6.61
E0-C-391	Elemtex Ltd., Cornwall	69	729.5	1220.5	13.7	-11.53	-6.16
E0-C-390	Earth Sciences, Heidelberg University	69.25	730.6	1219.4	13.8	-11.11	-6.26
E0-C-389	Elemtex Ltd., Cornwall	69.5	731.6	1218.4	13.8	-10.75	-5.06
E0-C-388	Earth Sciences, Heidelberg University	70	733.8	1216.2	14	-11.41	-5.26
E0-C-386	Earth Sciences, Heidelberg University	70.5	736.1	1213.9	14.2	-11.79	-5.47
E0-C-384	Earth Sciences, Heidelberg University	71	739	1211	14.8	-11.59	-5.26
E0-C-382	Earth Sciences, Heidelberg University	71.5	741.3	1208.7	14.6	-11.72	-5.39
E0-C-380	Earth Sciences, Heidelberg University	72	743.7	1206.3	14.7	-12.06	-5.62
E0-C-378	Earth Sciences, Heidelberg University	72.5	746.1	1203.9	15.3	-12.2	-6.67
E0-C-376	Earth Sciences, Heidelberg University	73	747.3	1202.7	15.9	-11.91	-6.71
E0-C-374	Earth Sciences, Heidelberg University	73.5	748.4	1201.6	16.5	-11.74	-6.68
E0-C-373	Elemtex Ltd., Cornwall	73.75	750.2	1199.8	16.7	-11.64	-6.2
E0-C-372	Earth Sciences, Heidelberg University	74	752.2	1197.8	17	-11.07	-7.15
E0-C-371	Elemtex Ltd., Cornwall	74.25	753.4	1196.6	17.2	-11.44	-5.93
E0-C-370	Earth Sciences, Heidelberg University	74.5	754.6	1195.4	17.4	-11.6	-6.07
E0-C-369	Elemtex Ltd., Cornwall	74.75	755.8	1194.2	17.5	-10.92	-5.27
E0-C-368	Earth Sciences, Heidelberg University	75	757	1193	17.5	-11.71	-5.77
E0-C-367	Elemtex Ltd., Cornwall	75.25	758.3	1191.7	17.6	-11.16	-5.35
E0-C-366	Earth Sciences, Heidelberg University	75.5	759.7	1190.3	17.7	-11.25	-6.19
E0-C-365	Elemtex Ltd., Cornwall	75.75	761.1	1188.9	17.8	-11.04	-5.51
E0-C-364	Earth Sciences, Heidelberg University	76	762.4	1187.6	17.8	-11.49	-5.95
E0-C-363	Elemtex Ltd., Cornwall	76.25	763.9	1186.1	17.8	-11.53	-5.96
E0-C-362	Earth Sciences, Heidelberg University	76.5	765.5	1184.5	17.8	-11.58	-7.15
E0-C-361	Elemtex Ltd., Cornwall	76.75	767.1	1182.9	17.9	-10.85	-6.19
E0-C-360	Earth Sciences, Heidelberg University	77	768.6	1181.4	18	-10.79	-7.02
E0-C-359	Elemtex Ltd., Cornwall	77.25	770.1	1179.9	18.1	-10.87	-5.77
E0-C-358	Earth Sciences, Heidelberg University	77.5	771.5	1178.5	18.1	-11.07	-6.16
E0-C-357	Elemtex Ltd., Cornwall	77.75	772.9	1177.1	18.2	-10.95	-5.39
E0-C-356	Earth Sciences, Heidelberg University	78	774.2	1175.8	18.3	-11.08	-6.17
E0-C-355	Elemtex Ltd., Cornwall	78.25	775.6	1174.4	18.4	-10.58	-5.67
E0-C-354	Earth Sciences, Heidelberg University	78.5	776.8	1173.2	18.4	-11.11	-6.23
E0-C-353	Elemtex Ltd., Cornwall	78.75	778	1172	18.4	-10.91	-5.36
E0-C-352	Earth Sciences, Heidelberg University	79	779.1	1170.9	18.4	-11.29	-6.28
E0-C-351	Elemtex Ltd., Cornwall	79.25	780.3	1169.7	18.3	-11.11	-5.51
E0-C-350	Earth Sciences, Heidelberg University	79.5	781.5	1168.5	18.2	-11.22	-6.46
E0-C-349	Elemtex Ltd., Cornwall	79.75	782.7	1167.3	18.2	-11.21	-5.66
E0-C-348	Earth Sciences, Heidelberg University	80	783.7	1166.3	18.2	-11.58	-6.21
E0-C-347	Elemtex Ltd., Cornwall	80.25	784.8	1165.2	18.1	-11.43	-5.45
E0-C-346	Earth Sciences, Heidelberg University	80.5	785.9	1164.1	17.9	-12.06	-5.68
E0-C-345	Elemtex Ltd., Cornwall	80.75	787	1163	17.8	-11.7	-5.36
E0-C-344	Earth Sciences, Heidelberg University	81	788	1162	17.8	-12	-5.47
E0-C-343	Elemtex Ltd., Cornwall	81.25	789	1161	17.7	-11.68	-4.97
E0-C-342	Earth Sciences, Heidelberg University	81.5	790.1	1159.9	17.6	-12.17	-5.39
E0-C-341	Elemtex Ltd., Cornwall	81.75	791	1159	17.5	-11.96	-4.7
E0-C-340	Earth Sciences, Heidelberg University	82	792.1	1157.9	17.5	-12.1	-5.49
E0-C-339	Elemtex Ltd., Cornwall	82.25	793.2	1156.8	17.5	-11.7	-5.18
E0-C-338	Earth Sciences, Heidelberg University	82.5	794.2	1155.8	17.3	-11.77	-5.7
E0-C-337	Elemtex Ltd., Cornwall	82.75	795.3	1154.7	17.1	-11.47	-4.93

Continued on next page

Table A8 – *Continuation of Stable Isotopes ($\delta^{13}C$, $\delta^{18}O$) for stalagmite E0-C*

Sample ID	**Analyzing laboratory**	**Distance [mm] (from top)**	**Age [a BP]**	**Age [a AD]**	**Age error [a]**	**$\delta^{13}C_{carb}$ [‰ VPDB]**	**$\delta^{18}O_{carb}$ [‰ VPDB]**
E0-C-336	Earth Sciences, Heidelberg University	83	796.2	1153.8	17.1	-11.7	-5.69
E0-C-335	Elemtex Ltd., Cornwall	83.25	797.1	1152.9	16.9	-11.38	-5.21
E0-C-334	Earth Sciences, Heidelberg University	83.5	798.2	1151.8	16.7	-11.73	-5.53
E0-C-333	Elemtex Ltd., Cornwall	83.75	799.1	1150.9	16.4	-11.35	-5.38
E0-C-332	Earth Sciences, Heidelberg University	84	800.1	1149.9	15.8	-11.52	-5.8
E0-C-331	Elemtex Ltd., Cornwall	84.25	801	1149	15.6	-11.4	-5.57
E0-C-330	Earth Sciences, Heidelberg University	84.5	801.9	1148.1	15.1	-11.51	-5.83
E0-C-329	Elemtex Ltd., Cornwall	84.75	802.8	1147.2	14.1	-11.35	-5.41
E0-C-328	Earth Sciences, Heidelberg University	85	803.7	1146.3	13.9	-11.7	-5.91
E0-C-327	Elemtex Ltd., Cornwall	85.25	804.4	1145.6	12.9	-11.36	-5.35
E0-C-326	Earth Sciences, Heidelberg University	85.5	805.2	1144.8	12	-11.37	-6.07
E0-C-325	Elemtex Ltd., Cornwall	85.75	806	1144	11.6	-10.98	-5.71
E0-C-324	Earth Sciences, Heidelberg University	86	806.8	1143.2	11.1	-11.02	-6.35
E0-C-323	Elemtex Ltd., Cornwall	86.25	807.5	1142.5	10.7	-10.63	-5.61
E0-C-322	Earth Sciences, Heidelberg University	86.5	808.3	1141.7	10.7	-10.55	-5.96
E0-C-321	Elemtex Ltd., Cornwall	86.75	809.1	1140.9	10.6	-10.33	-5.27
E0-C-320	Earth Sciences, Heidelberg University	87	809.8	1140.2	10.5	-10.42	-5.54
E0-C-319	Elemtex Ltd., Cornwall	87.25	810.6	1139.4	10.8	-10.19	-5.09
E0-C-318	Earth Sciences, Heidelberg University	87.5	811.3	1138.7	11.2	-10.65	-5.31
E0-C-317	Elemtex Ltd., Cornwall	87.75	812.1	1137.9	11.4	-10.09	-4.63
E0-C-316	Earth Sciences, Heidelberg University	88	812.8	1137.2	11.6	-10.54	-5.49
E0-C-314	Earth Sciences, Heidelberg University	88.5	814.3	1135.7	11.8	-10.61	-6.03
E0-C-313	Elemtex Ltd., Cornwall	88.75	815.1	1134.9	11.7	-10.56	-5.56
E0-C-312	Earth Sciences, Heidelberg University	89	816.1	1133.9	11.8	-10.74	-6.11
E0-C-311	Elemtex Ltd., Cornwall	89.25	817.2	1132.8	11.7	-10.19	-5.43
E0-C-310	Earth Sciences, Heidelberg University	89.5	818.2	1131.8	11.6	-10.41	-5.8
E0-C-309	Elemtex Ltd., Cornwall	89.75	819.3	1130.7	11.7	-10.57	-5.36
E0-C-308	Earth Sciences, Heidelberg University	90	820.6	1129.4	11.8	-10.22	-5.93
E0-C-307	Elemtex Ltd., Cornwall	90.25	821.9	1128.1	11.9	-10.03	-5.36
E0-C-306	Earth Sciences, Heidelberg University	90.5	823.1	1126.9	11.7	-10.37	-6.19
E0-C-305	Elemtex Ltd., Cornwall	90.75	824.3	1125.7	11.4	-10.4	-5.52
E0-C-304	Earth Sciences, Heidelberg University	91	825.4	1124.6	11.1	-10.39	-5.88
E0-C-303	Elemtex Ltd., Cornwall	91.25	826.4	1123.6	10.8	-10.56	-5.13
E0-C-302	Earth Sciences, Heidelberg University	91.5	827.3	1122.7	10.7	-10.36	-5.78
E0-C-301	Elemtex Ltd., Cornwall	91.75	828.2	1121.8	10.6	-10.06	-5.47
E0-C-300	Earth Sciences, Heidelberg University	92	829.1	1120.9	10.4	-10.32	-5.83
E0-C-299	Elemtex Ltd., Cornwall	92.25	830.1	1119.9	10.6	-10.48	-5.2
E0-C-298	Earth Sciences, Heidelberg University	92.5	830.8	1119.2	10.5	-10.52	-5.61
E0-C-297	Elemtex Ltd., Cornwall	92.75	831.4	1118.6	10.6	-10.43	-4.79
E0-C-296	Earth Sciences, Heidelberg University	93	832	1118	10.7	-10.39	-5.29
E0-C-295	Elemtex Ltd., Cornwall	93.25	832.5	1117.5	10.7	-10.39	-4.96
E0-C-294	Earth Sciences, Heidelberg University	93.5	832.9	1117.1	10.6	-10.46	-5.33
E0-C-293	Elemtex Ltd., Cornwall	93.75	833.5	1116.5	10.8	-10.58	-4.88
E0-C-292	Earth Sciences, Heidelberg University	94	834.3	1115.7	11.4	-10.51	-5.3
E0-C-291	Elemtex Ltd., Cornwall	94.25	835.1	1114.9	12.2	-10.35	-4.85
E0-C-290	Earth Sciences, Heidelberg University	94.5	836.4	1113.6	13.4	-10.41	-5.24
E0-C-288	Earth Sciences, Heidelberg University	95	839.3	1110.7	15.8	-10.94	-5.37
E0-C-286	Earth Sciences, Heidelberg University	95.5	841.4	1108.6	17	-10.89	-5.53
E0-C-285	Elemtex Ltd., Cornwall	97.75	852.6	1097.4	20.2	-10.42	-5.49
E0-C-284	Elemtex Ltd., Cornwall	98	854.7	1095.3	20.5	-10.08	-5.29
E0-C-283	Elemtex Ltd., Cornwall	98.25	858.3	1091.7	21.1	-10.28	-6.43
E0-C-282	Elemtex Ltd., Cornwall	98.5	860.2	1089.8	21.7	-11.06	-6.46

Continued on next page

Table A8 – *Continuation of Stable Isotopes ($\delta^{13}C$, $\delta^{18}O$) for stalagmite E0-C*

Sample ID	**Analyzing laboratory**	**Distance [mm] (from top)**	**Age [a BP]**	**Age [a AD]**	**Age error [a]**	**$\delta^{13}C_{carb}$ [‰ VPDB]**	**$\delta^{18}O_{carb}$ [‰ VPDB]**
E0-C-281	Elemtex Ltd., Cornwall	98.75	862.1	1087.9	22.2	-10.81	-5.34
E0-C-280	Elemtex Ltd., Cornwall	99	863.5	1086.5	22	-10.71	-5.41
E0-C-279	Elemtex Ltd., Cornwall	99.25	865	1085	22.2	-11.13	-4.8
E0-C-278	Elemtex Ltd., Cornwall	99.5	866.5	1083.5	22.3	-11.27	-4.59
E0-C-277	Elemtex Ltd., Cornwall	99.75	867.9	1082.1	22.5	-11.3	-4.97
E0-C-276	Elemtex Ltd., Cornwall	100	869.5	1080.5	22.7	-11.2	-4.66
E0-C-274	Elemtex Ltd., Cornwall	100.5	872.4	1077.6	23	-11.49	-4.73
E0-C-273	Elemtex Ltd., Cornwall	100.75	874.1	1075.9	23.2	-11.79	-4.75
E0-C-272	Elemtex Ltd., Cornwall	101	876	1074	23.3	-11.79	-4.69
E0-C-271	Elemtex Ltd., Cornwall	101.25	878	1072	23.1	-11.59	-4.74
E0-C-270	Elemtex Ltd., Cornwall	101.5	880.2	1069.8	23.4	-11.92	-5.11
E0-C-269	Elemtex Ltd., Cornwall	101.75	882.1	1067.9	23.4	-12.16	-4.84
E0-C-268	Elemtex Ltd., Cornwall	102	884.2	1065.8	23.4	-11.93	-5.1
E0-C-267	Elemtex Ltd., Cornwall	102.25	886	1064	23.5	-11.81	-5.45
E0-C-266	Elemtex Ltd., Cornwall	102.5	887.8	1062.2	23.9	-11.03	-4.6
E0-C-265	Elemtex Ltd., Cornwall	102.75	889.5	1060.5	24.1	-11.38	-5.05
E0-C-263	Elemtex Ltd., Cornwall	103.25	892	1058	24.7	-10.63	-5.34
E0-C-262	Elemtex Ltd., Cornwall	103.5	893.5	1056.5	24.7	-10.63	-5.08
E0-C-261	Elemtex Ltd., Cornwall	103.75	895.2	1054.8	25.2	-11.16	-5.48
E0-C-260	Elemtex Ltd., Cornwall	104	896.7	1053.3	25.6	-11.26	-5.03
E0-C-259	Elemtex Ltd., Cornwall	104.25	898.2	1051.8	25.5	-10.41	-5.03
E0-C-257	Elemtex Ltd., Cornwall	104.75	901.2	1048.8	24.8	-10.95	-4.52
E0-C-256	Elemtex Ltd., Cornwall	105	902.8	1047.2	24.7	-11.2	-4.99
E0-C-255	Elemtex Ltd., Cornwall	105.25	904.4	1045.6	24.7	-11.65	-4.55
E0-C-254	Elemtex Ltd., Cornwall	105.5	905.8	1044.2	24.8	-11.09	-4.32
E0-C-253	Elemtex Ltd., Cornwall	105.75	907.3	1042.7	24.8	-11.23	-4.94
E0-C-252	Elemtex Ltd., Cornwall	106	908.8	1041.2	25.2	-11.41	-4.7
E0-C-251	Elemtex Ltd., Cornwall	106.25	910.3	1039.7	25.6	-11.04	-4.84
E0-C-250	Elemtex Ltd., Cornwall	106.5	911.6	1038.4	26.4	-11.82	-4.62
E0-C-249	Elemtex Ltd., Cornwall	106.75	913.5	1036.5	26.6	-11.69	-4.94
E0-C-248	Elemtex Ltd., Cornwall	107	915.7	1034.3	26.4	-11.49	-4.89
E0-C-247	Elemtex Ltd., Cornwall	107.25	918	1032	26.4	-11.42	-5.16
E0-C-246	Elemtex Ltd., Cornwall	107.5	920.2	1029.8	26.4	-11.49	-5.29
E0-C-245	Elemtex Ltd., Cornwall	107.75	922.6	1027.4	26.3	-11.48	-5.63
E0-C-244	Elemtex Ltd., Cornwall	108	924.9	1025.1	25.6	-11.46	-5.45
E0-C-243	Elemtex Ltd., Cornwall	108.25	926.9	1023.1	25.1	-11.66	-5.44
E0-C-242	Elemtex Ltd., Cornwall	108.5	928.4	1021.6	25.1	-10.84	-4.63
E0-C-241	Elemtex Ltd., Cornwall	108.75	930.1	1019.9	25.2	-11	-4.53
E0-C-240	Elemtex Ltd., Cornwall	109	931.7	1018.3	25	-11.4	-4.51
E0-C-239	Elemtex Ltd., Cornwall	109.25	933.2	1016.8	25	-10.57	-4.76
E0-C-238	Elemtex Ltd., Cornwall	109.5	934.8	1015.2	24.9	-10.36	-5.11
E0-C-237	Elemtex Ltd., Cornwall	109.75	936.1	1013.9	24.9	-10.53	-4.75
E0-C-234	Elemtex Ltd., Cornwall	110.5	940.4	1009.6	24.9	-10.52	-4.81
E0-C-233	Elemtex Ltd., Cornwall	110.75	942	1008	24.4	-10.53	-4.84
E0-C-231	Elemtex Ltd., Cornwall	111.25	945.4	1004.6	23.6	-10.44	-4.86
E0-C-230	Elemtex Ltd., Cornwall	111.5	946.6	1003.4	23.6	-10.58	-5.05
E0-C-229	Earth Sciences, Heidelberg University	111.75	947.7	1002.3	23.9	-10.79	-5.19
E0-C-228	Earth Sciences, Heidelberg University	112	948.6	1001.4	24.8	-11.57	-5.15
E0-C-227	Earth Sciences, Heidelberg University	112.25	949.5	1000.5	25.2	-11.15	-4.85
E0-C-226	Earth Sciences, Heidelberg University	112.5	950.5	999.5	25	-10.87	-6.94
E0-C-225	Earth Sciences, Heidelberg University	112.75	951.3	998.7	25.5	-10.9	-6.43
E0-C-217	Elemtex Ltd., Cornwall	113	952.2	997.8	25.7	-10.57	-4.53

Continued on next page

Table A8 – *Continuation of Stable Isotopes ($\delta^{13}C$, $\delta^{18}O$) for stalagmite E0-C*

Sample ID	**Analyzing laboratory**	**Distance [mm] (from top)**	**Age [a BP]**	**Age [a AD]**	**Age error [a]**	**$\delta^{13}C_{carb}$ [‰ VPDB]**	**$\delta^{18}O_{carb}$ [‰ VPDB]**
E0-C-224	Earth Sciences, Heidelberg University	113.25	953	997	26.5	-10.9	-5.18
E0-C-223	Earth Sciences, Heidelberg University	113.5	953.9	996.1	27.1	-11.46	-4.72
E0-C-214	Elemtex Ltd., Cornwall	113.75	954.8	995.2	27.9	-11.13	-4.87
E0-C-213	Elemtex Ltd., Cornwall	114	955.6	994.4	28.2	-9.76	-5.11
E0-C-212	Elemtex Ltd., Cornwall	114.25	956.4	993.6	28.5	-9.7	-4.65
E0-C-211	Elemtex Ltd., Cornwall	114.5	1139.9	810.1	52.1	-8.14	-3.91
E0-C-210	Elemtex Ltd., Cornwall	114.75	1140.8	809.2	52	-7.37	-3.92
E0-C-209	Elemtex Ltd., Cornwall	115	1141.6	808.4	50.9	-8.22	-4.06
E0-C-207	Elemtex Ltd., Cornwall	115.5	1143.1	806.9	49.8	-8.06	-3.54
E0-C-206	Elemtex Ltd., Cornwall	115.75	1143.7	806.3	49.8	-7.6	-3.92
E0-C-205	Elemtex Ltd., Cornwall	116	1144.4	805.6	49.7	-8.57	-3.69
E0-C-204	Elemtex Ltd., Cornwall	116.25	1145.1	804.9	49.8	-9.85	-3.85
E0-C-203	Elemtex Ltd., Cornwall	116.5	1145.9	804.1	49.6	-9.09	-4.02
E0-C-202	Elemtex Ltd., Cornwall	116.75	1146.8	803.2	49.4	-9.42	-4.27
E0-C-201	Elemtex Ltd., Cornwall	117	1147.7	802.3	49	-10.71	-4.77
E0-C-200	Elemtex Ltd., Cornwall	117.25	1148.4	801.6	47.9	-10.69	-5.24
E0-C-199	Elemtex Ltd., Cornwall	117.5	1149.1	800.9	47.2	-9.81	-5.19
E0-C-198	Elemtex Ltd., Cornwall	117.75	1149.8	800.2	45.4	-10.02	-5.3
E0-C-197	Elemtex Ltd., Cornwall	118	1150.7	799.3	44.5	-10.72	-4.85
E0-C-196	Elemtex Ltd., Cornwall	118.25	1151.6	798.4	44.2	-10.39	-4.6
E0-C-195	Elemtex Ltd., Cornwall	118.5	1152.7	797.3	43.7	-9.56	-4.38
E0-C-194	Elemtex Ltd., Cornwall	118.75	1153.7	796.3	42.7	-9.13	-4.71
E0-C-193	Elemtex Ltd., Cornwall	119	1154.6	795.4	41.4	-8.31	-4.25
E0-C-192	Elemtex Ltd., Cornwall	119.25	1155.7	794.3	41.1	-8.35	-3.79
E0-C-191	Elemtex Ltd., Cornwall	119.5	1156.9	793.1	39.9	-8.06	-3.6
E0-C-190	Elemtex Ltd., Cornwall	119.75	1157.9	792.1	38.7	-7.12	-3.73
E0-C-189	Elemtex Ltd., Cornwall	120	1159.3	790.7	38.5	-7.19	-3.89
E0-C-188	Elemtex Ltd., Cornwall	120.25	1160.3	789.7	37.2	-7.58	-3.93
E0-C-187	Elemtex Ltd., Cornwall	120.5	1161.5	788.5	36.1	-7.68	-3.69
E0-C-186	Elemtex Ltd., Cornwall	120.75	1162.9	787.1	35.8	-7.54	-3.75
E0-C-185	Elemtex Ltd., Cornwall	121	1164.3	785.7	32.9	-7.23	-3.55
E0-C-184	Elemtex Ltd., Cornwall	121.25	1165.7	784.3	30.2	-7.07	-3.77
E0-C-183	Elemtex Ltd., Cornwall	121.5	1167.2	782.8	28.8	-7.26	-3.63
E0-C-182	Elemtex Ltd., Cornwall	121.75	1168.5	781.5	26.9	-7.04	-3.5
E0-C-181	Elemtex Ltd., Cornwall	122	1169.9	780.1	25	-6.34	-3.39
E0-C-180	Elemtex Ltd., Cornwall	122.25	1171.4	778.6	23	-6.55	-3.7
E0-C-179	Elemtex Ltd., Cornwall	122.5	1172.8	777.2	22.3	-7.04	-4.46
E0-C-177	Elemtex Ltd., Cornwall	123	1175.3	774.7	21.8	-7	-3.74
E0-C-176	Elemtex Ltd., Cornwall	123.25	1176.2	773.8	21.4	-6.89	-4.04
E0-C-175	Elemtex Ltd., Cornwall	123.5	1177.2	772.8	20.9	-6.86	-4.04
E0-C-174	Elemtex Ltd., Cornwall	123.75	1178	772	20.1	-6.7	-4.22
E0-C-173	Elemtex Ltd., Cornwall	124	1178.8	771.2	19.8	-6.99	-4.69
E0-C-172	Elemtex Ltd., Cornwall	124.25	1179.7	770.3	19.7	-7.65	-4.57
E0-C-171	Elemtex Ltd., Cornwall	124.5	1180.7	769.3	19	-7.54	-5.12
E0-C-170	Elemtex Ltd., Cornwall	124.75	1181.5	768.5	18.4	-7.9	-5.12
E0-C-169	Elemtex Ltd., Cornwall	125	1182.4	767.6	18	-8.06	-5.1
E0-C-168	Elemtex Ltd., Cornwall	125.25	1183.1	766.9	18.1	-7.66	-4.39
E0-C-167	Elemtex Ltd., Cornwall	125.5	1184	766	18.1	-7.73	-3.89
E0-C-166	Elemtex Ltd., Cornwall	125.75	1184.8	765.2	18.2	-8.07	-4.66
E0-C-165	Elemtex Ltd., Cornwall	126	1185.6	764.4	18.1	-7.99	-4.73
E0-C-163	Elemtex Ltd., Cornwall	126.5	1187.5	762.5	17.7	-7.92	-5.01
E0-C-162	Elemtex Ltd., Cornwall	126.75	1188.5	761.5	17.3	-7.86	-5.22

Continued on next page

Table A8 – *Continuation of Stable Isotopes ($\delta^{13}C$, $\delta^{18}O$) for stalagmite E0-C*

Sample ID	**Analyzing laboratory**	**Distance [mm] (from top)**	**Age [a BP]**	**Age [a AD]**	**Age error [a]**	**$\delta^{13}C_{carb}$ [‰ VPDB]**	**$\delta^{18}O_{carb}$ [‰ VPDB]**
E0-C-161	Elemtex Ltd., Cornwall	127	1189.6	760.4	17.2	-8.41	-5.18
E0-C-160	Elemtex Ltd., Cornwall	127.25	1190.7	759.3	17.1	-8.35	-5.51
E0-C-159	Elemtex Ltd., Cornwall	127.5	1191.9	758.1	17.5	-8.09	-5.48
E0-C-158	Elemtex Ltd., Cornwall	127.75	1192.6	757.4	18.2	-7.89	-6.01
E0-C-157	Elemtex Ltd., Cornwall	128	1193.6	756.4	18.9	-8.27	-5.34
E0-C-156	Elemtex Ltd., Cornwall	128.25	1194.5	755.5	20	-8.53	-5.64
E0-C-155	Elemtex Ltd., Cornwall	128.5	1195.4	754.6	20.7	-8.69	-6.11
E0-C-154	Elemtex Ltd., Cornwall	128.75	1196.1	753.9	22.3	-7.76	-6.06
E0-C-152	Elemtex Ltd., Cornwall	129.25	1197.6	752.4	23.7	-7.45	-6.25
E0-C-151	Elemtex Ltd., Cornwall	129.5	1198.3	751.7	24.8	-8.44	-5.85
E0-C-150	Elemtex Ltd., Cornwall	129.75	1199.1	750.9	25.4	-7.88	-5.55
E0-C-149	Elemtex Ltd., Cornwall	130	1199.9	750.1	25.6	-8.8	-5.12
E0-C-148	Elemtex Ltd., Cornwall	130.25	1200.7	749.3	26	-8.42	-4.61
E0-C-147	Elemtex Ltd., Cornwall	130.5	1201.4	748.6	26.3	-8.61	-4.76
E0-C-144	Elemtex Ltd., Cornwall	131.25	1204	746	27.1	-7.78	-4.74
E0-C-142	Elemtex Ltd., Cornwall	131.75	1206.2	743.8	26.9	-7.98	-4.84
E0-C-141	Elemtex Ltd., Cornwall	132	1207.4	742.6	27.5	-8.4	-4.44
E0-C-139	Elemtex Ltd., Cornwall	132.5	1209.3	740.7	27.8	-8	-3.99
E0-C-136	Elemtex Ltd., Cornwall	133.25	1212	738	28.4	-9.03	-4.02
E0-C-131	Elemtex Ltd., Cornwall	134.5	1216.6	733.4	29.1	-10.11	-4.71
E0-C-130	Elemtex Ltd., Cornwall	134.75	1217.5	732.5	29.1	-9.48	-4.73
E0-C-129	Elemtex Ltd., Cornwall	135	1218.5	731.5	29.4	-9.65	-4.42
E0-C-128	Elemtex Ltd., Cornwall	135.25	1219.5	730.5	29.4	-9.32	-4.7
E0-C-127	Elemtex Ltd., Cornwall	135.5	1220.4	729.6	29.5	-9.41	-4.82
E0-C-126	Elemtex Ltd., Cornwall	135.75	1221.1	728.9	29.9	-8.71	-5.5
E0-C-124	Elemtex Ltd., Cornwall	136.25	1223.1	726.9	30.4	-9.13	-5.43
E0-C-123	Elemtex Ltd., Cornwall	136.5	1223.9	726.1	30.6	-8.51	-5.07
E0-C-122	Elemtex Ltd., Cornwall	136.75	1225.1	724.9	30.8	-9.29	-4.83
E0-C-120	Elemtex Ltd., Cornwall	137.25	1226.8	723.2	31.4	-8.9	-4.76
E0-C-119	Elemtex Ltd., Cornwall	137.5	1227.6	722.4	31.4	-8.96	-4.98
E0-C-117	Elemtex Ltd., Cornwall	138	1229.4	720.6	32	-8.64	-5.2
E0-C-116	Elemtex Ltd., Cornwall	138.25	1230.3	719.7	32.4	-8.78	-5.18
E0-C-114	Elemtex Ltd., Cornwall	138.75	1232	718	32.6	-9.15	-4.15
E0-C-113	Elemtex Ltd., Cornwall	139	1233.1	716.9	32.8	-9.29	-4.71
E0-C-112	Elemtex Ltd., Cornwall	139.25	1234.1	715.9	33	-9.26	-4.67
E0-C-111	Elemtex Ltd., Cornwall	139.5	1235.3	714.7	33.5	-9.21	-4.5
E0-C-110	Elemtex Ltd., Cornwall	139.75	1236.2	713.8	34	-9	-4.29
E0-C-108	Earth Sciences, Heidelberg University	140.25	1238.3	711.7	34.3	-8.61	-4.71
E0-C-106	Earth Sciences, Heidelberg University	140.75	1239.9	710.1	35	-8.24	-4.81
E0-C-104	Earth Sciences, Heidelberg University	141.25	1242.3	707.7	35.2	-8.62	-5.17
E0-C-103	Elemtex Ltd., Cornwall	141.5	1243.1	706.9	35.5	-8.55	-5.04
E0-C-102	Earth Sciences, Heidelberg University	141.75	1244.1	705.9	35.4	-8.88	-5.14
E0-C-101	Elemtex Ltd., Cornwall	142	1245	705	35.4	-8.67	-4.39
E0-C-100	Earth Sciences, Heidelberg University	142.25	1246	704	35.2	-8.72	-5.07
E0-C-099	Elemtex Ltd., Cornwall	142.5	1246.8	703.2	35.5	-8.81	-5.89
E0-C-098	Earth Sciences, Heidelberg University	142.75	1247.8	702.2	35.2	-8.32	-4.96
E0-C-094	Earth Sciences, Heidelberg University	143.75	1251.5	698.5	35.3	-9	-4.29
E0-C-092	Earth Sciences, Heidelberg University	144.25	1253.6	696.4	35.4	-8.9	-4.63
E0-C-091	Elemtex Ltd., Cornwall	144.5	1254.5	695.5	35.5	-8.64	-5.51
E0-C-090	Earth Sciences, Heidelberg University	144.75	1255.6	694.4	35.7	-8.71	-4.62
E0-C-088	Earth Sciences, Heidelberg University	145.25	1257.6	692.4	35.6	-8.66	-5.75
E0-C-086	Earth Sciences, Heidelberg University	145.75	1259.6	690.4	35.4	-8.38	-6.06

Continued on next page

Table A8 – *Continuation of Stable Isotopes ($\delta^{13}C$, $\delta^{18}O$) for stalagmite E0-C*

Sample ID	**Analyzing laboratory**	**Distance [mm] (from top)**	**Age [a BP]**	**Age [a AD]**	**Age error [a]**	**$\delta^{13}C_{carb}$ [‰ VPDB]**	**$\delta^{18}O_{carb}$ [‰ VPDB]**
E0-C-085	Elemtex Ltd., Cornwall	146	1260.6	689.4	35.3	-8.54	-7.22
E0-C-084	Earth Sciences, Heidelberg University	146.25	1261.6	688.4	35.2	-8.81	-6.49
E0-C-083	Elemtex Ltd., Cornwall	146.5	1262.8	687.2	34.7	-8.29	-6.35
E0-C-082	Earth Sciences, Heidelberg University	146.75	1264	686	34.5	-8.09	-5.41
E0-C-081	Elemtex Ltd., Cornwall	147	1265.1	684.9	34.8	-8.59	-5.35
E0-C-080	Earth Sciences, Heidelberg University	147.25	1266.1	683.9	34.9	-8.33	-4.9
E0-C-079	Elemtex Ltd., Cornwall	147.5	1267.3	682.7	35	-8.48	-5.41
E0-C-078	Earth Sciences, Heidelberg University	147.75	1268.2	681.8	35.1	-8.7	-4.8
E0-C-076	Earth Sciences, Heidelberg University	148.25	1270.2	679.8	34	-8.59	-4.92
E0-C-075	Elemtex Ltd., Cornwall	148.5	1271.2	678.8	33.8	-8.88	-5.13
E0-C-074	Earth Sciences, Heidelberg University	148.75	1272.3	677.7	34.1	-8.53	-5
E0-C-073	Elemtex Ltd., Cornwall	149	1273.4	676.6	34	-9.07	-4.96
E0-C-072	Earth Sciences, Heidelberg University	149.25	1274.6	675.4	33.4	-8.81	-5.05
E0-C-070	Earth Sciences, Heidelberg University	149.75	1276.9	673.1	33.4	-8.73	-6.27
E0-C-069	Elemtex Ltd., Cornwall	150	1278.2	671.8	32.7	-8.54	-5.33
E0-C-068	Earth Sciences, Heidelberg University	150.25	1279.3	670.7	31.9	-7.99	-5.03
E0-C-067	Elemtex Ltd., Cornwall	150.5	1280.5	669.5	31.6	-7.64	-5.55
E0-C-066	Earth Sciences, Heidelberg University	150.75	1281.9	668.1	30.7	-7.98	-6.12
E0-C-064	Earth Sciences, Heidelberg University	151.25	1284.2	665.8	30.3	-7.62	-5.76
E0-C-063	Elemtex Ltd., Cornwall	151.5	1285.4	664.6	28.8	-7.76	-5.61
E0-C-062	Earth Sciences, Heidelberg University	151.75	1286.5	663.5	28.4	-7.9	-4.99
E0-C-060	Earth Sciences, Heidelberg University	152.25	1288.5	661.5	26.3	-7.75	-4.99
E0-C-058	Earth Sciences, Heidelberg University	152.75	1289.9	660.1	25.7	-7.96	-5.06
E0-C-057	Elemtex Ltd., Cornwall	153	1290.5	659.5	24.5	-7.87	-5.71
E0-C-056	Earth Sciences, Heidelberg University	153.25	1291.1	658.9	22.8	-7.59	-4.57
E0-C-055	Elemtex Ltd., Cornwall	153.5	1291.5	658.5	21.9	-7.71	-5.79
E0-C-054	Earth Sciences, Heidelberg University	153.75	1291.9	658.1	21.4	-7.89	-4.57
E0-C-053	Elemtex Ltd., Cornwall	154	1292.5	657.5	19.1	-7.96	-4.48
E0-C-052	Earth Sciences, Heidelberg University	154.25	1292.9	657.1	17.7	-7.9	-4.62
E0-C-051	Elemtex Ltd., Cornwall	154.5	1293.3	656.7	16.6	-8.06	-4.93
E0-C-050	Earth Sciences, Heidelberg University	154.75	1293.7	656.3	15.9	-7.9	-4.73
E0-C-049	Elemtex Ltd., Cornwall	155	1294.1	655.9	14.4	-7.8	-5.04
E0-C-048	Earth Sciences, Heidelberg University	155.25	1294.3	655.7	14	-7.53	-4.75
E0-C-046	Earth Sciences, Heidelberg University	155.75	1294.9	655.1	13.8	-7.74	-4.9
E0-C-044	Earth Sciences, Heidelberg University	156.25	1295.7	654.3	13	-7.77	-4.97
E0-C-042	Earth Sciences, Heidelberg University	156.75	1296.5	653.5	13.1	-7.48	-5.1
E0-C-041	Elemtex Ltd., Cornwall	157	1296.9	653.1	12.9	-7.89	-5.7
E0-C-040	Earth Sciences, Heidelberg University	157.25	1297.5	652.5	12.9	-7.53	-4.99
E0-C-038	Earth Sciences, Heidelberg University	157.75	1298.4	651.6	12.8	-7.87	-5.03
E0-C-036	Earth Sciences, Heidelberg University	158.25	1299.2	650.8	12.9	-7.57	-5.17
E0-C-035	Elemtex Ltd., Cornwall	158.5	1299.8	650.2	13.1	-7.77	-5
E0-C-034	Earth Sciences, Heidelberg University	158.75	1300.3	649.7	13.1	-7.48	-4.4
E0-C-032	Earth Sciences, Heidelberg University	159.25	1301.3	648.7	14.3	-7.32	-4.32
E0-C-030	Earth Sciences, Heidelberg University	159.75	1302.1	647.9	15.7	-7.52	-4.36
E0-C-029	Elemtex Ltd., Cornwall	160	1302.5	647.5	17.2	-6.82	-4.84
E0-C-028	Elemtex Ltd., Cornwall	160.25	1303.2	646.8	18	-7.36	-4.9
E0-C-026	Elemtex Ltd., Cornwall	160.75	1304.1	645.9	20.4	-7	-4.99
E0-C-025	Elemtex Ltd., Cornwall	161	1304.7	645.3	21.3	-7.57	-4.49
E0-C-024	Elemtex Ltd., Cornwall	161.25	1305.3	644.7	22.8	-7.13	-4.31
E0-C-023	Elemtex Ltd., Cornwall	161.5	1305.9	644.1	25.6	-7.28	-5.47
E0-C-022	Elemtex Ltd., Cornwall	161.75	1306.4	643.6	26	-7.48	-5.31
E0-C-021	Elemtex Ltd., Cornwall	162	1307.2	642.8	27.3	-7.25	-4.68

Continued on next page

Table A8 – *Continuation of Stable Isotopes ($\delta^{13}C$, $\delta^{18}O$) for stalagmite E0-C*

Sample ID	**Analyzing laboratory**	**Distance [mm] (from top)**	**Age [a BP]**	**Age [a AD]**	**Age error [a]**	**$\delta^{13}C_{carb}$ [‰ VPDB]**	**$\delta^{18}O_{carb}$ [‰ VPDB]**
E0-C-020	Elemtex Ltd., Cornwall	162.25	1307.8	642.2	28.2	-7.48	-5.23
E0-C-018	Elemtex Ltd., Cornwall	162.75	1309.4	640.6	29.2	-7.64	-5.07
E0-C-017	Elemtex Ltd., Cornwall	163	1310.5	639.5	29.3	-7.19	-5.3
E0-C-015	Elemtex Ltd., Cornwall	163.5	1312.9	637.1	30.1	-7.29	-6.88
E0-C-013	Elemtex Ltd., Cornwall	164	1315.8	634.2	33.3	-6.15	-5.06
E0-C-011	Elemtex Ltd., Cornwall	164.5	1320.1	629.9	34.8	-6.41	-4.96
E0-C-008	Elemtex Ltd., Cornwall	165.25	1324.7	625.3	37.2	-6.31	-6.07
E0-C-006	Elemtex Ltd., Cornwall	165.75	1327.4	622.6	37.4	-5.72	-5.35
E0-C-004	Elemtex Ltd., Cornwall	166.25	1329.7	620.3	37.5	-6.8	-6.34
E0-C-003	Elemtex Ltd., Cornwall	166.5	1330.6	619.4	37.9	-6.69	-5.38
E0-C-002	Elemtex Ltd., Cornwall	166.75	1331.7	618.3	37.8	-6.43	-4.62
E0-C-001	Elemtex Ltd., Cornwall	167	1332.7	617.3	38.1	-6.61	-3.99

Table A9. Stable Isotopes ($\delta^{13}C$, $\delta^{18}O$) for stalagmite E1. The age of each sample corresponds to the chronology discussed in Chapter III.2.

Sample ID	**Analyzing laboratory**	**Distance [mm] (from top)**	**Age [a BP]**	**Age [a AD]**	**Age error [a]**	**$\delta^{13}C_{carb}$ [‰ VPDB]**	**$\delta^{18}O_{carb}$ [‰ VPDB]**
E1-001	Earth Sciences, Heidelberg University	0.56	12.2	1937.8	21.6	-9.82	-4.78
E1-002	Earth Sciences, Heidelberg University	0.66	12.7	1937.3	21.5	-9.76	-4.77
E1-003	Earth Sciences, Heidelberg University	0.76	13.2	1936.8	21.4	-9.15	-4.52
E1-004	Earth Sciences, Heidelberg University	0.86	13.7	1936.3	21.3	-9.72	-4.82
E1-005	Earth Sciences, Heidelberg University	0.96	14.1	1935.9	21.2	-9.89	-4.71
E1-006	Earth Sciences, Heidelberg University	1.06	14.6	1935.4	21.1	-10.4	-4.87
E1-007	Earth Sciences, Heidelberg University	1.16	15.0	1935.0	21.1	-10.97	-5.05
E1-008	Earth Sciences, Heidelberg University	1.26	15.4	1934.6	21.0	-11.72	-5.18
E1-009	Earth Sciences, Heidelberg University	1.36	15.9	1934.1	21.0	-11.61	-5.07
E1-010	Earth Sciences, Heidelberg University	1.46	16.3	1933.7	20.9	-10.94	-5.13
E1-011	Earth Sciences, Heidelberg University	1.56	16.7	1933.3	20.8	-10.71	-5.2
E1-012	Earth Sciences, Heidelberg University	1.66	17.3	1932.7	20.7	-10.67	-5.15
E1-013	Earth Sciences, Heidelberg University	1.76	17.7	1932.3	20.7	-10.97	-5.21
E1-014	Earth Sciences, Heidelberg University	1.86	18.2	1931.8	20.6	-11.46	-5.28
E1-015	Earth Sciences, Heidelberg University	1.96	18.6	1931.4	20.6	-11.66	-5.56
E1-016	Earth Sciences, Heidelberg University	2.06	19.1	1930.9	20.5	-11.15	-5.53
E1-017	Earth Sciences, Heidelberg University	2.16	19.6	1930.4	20.4	-10.51	-5.54
E1-018	Earth Sciences, Heidelberg University	2.26	20.1	1929.9	20.3	-9.6	-5.07
E1-019	Earth Sciences, Heidelberg University	2.36	20.6	1929.4	20.3	-10.31	-5.71
E1-020	Earth Sciences, Heidelberg University	2.46	21.1	1928.9	20.2	-10.7	-5.39
E1-021	Earth Sciences, Heidelberg University	2.56	21.6	1928.4	20.1	-10.41	-5.45
E1-022	Earth Sciences, Heidelberg University	2.66	22.1	1927.9	20.1	-10.14	-5.47
E1-023	Earth Sciences, Heidelberg University	2.76	22.6	1927.4	20.0	-10.69	-5.09
E1-024	Earth Sciences, Heidelberg University	2.86	23.0	1927.0	19.9	-11.32	-5.02
E1-025	Earth Sciences, Heidelberg University	2.96	23.5	1926.5	19.8	-11.38	-4.84
E1-026	Earth Sciences, Heidelberg University	3.06	24.0	1926.0	19.7	-10.13	-4.36
E1-027	Earth Sciences, Heidelberg University	3.16	24.5	1925.5	19.7	-9.92	-4.2
E1-028	Earth Sciences, Heidelberg University	3.26	24.9	1925.1	19.6	-9.41	-3.87
E1-029	Earth Sciences, Heidelberg University	3.36	25.4	1924.6	19.5	-9.2	-3.89
E1-030	Earth Sciences, Heidelberg University	3.46	25.8	1924.2	19.5	-9.19	-4.06
E1-031	Earth Sciences, Heidelberg University	3.56	26.3	1923.7	19.4	-9.14	-4.07
E1-032	Earth Sciences, Heidelberg University	3.66	26.9	1923.1	19.3	-9.16	-3.98

Continued on next page

Table A9 – *Continuation of Stable Isotopes ($\delta^{13}C$, $\delta^{18}O$) for stalagmite E1*

Sample ID	**Analyzing laboratory**	**Distance [mm] (from top)**	**Age [a BP]**	**Age [a AD]**	**Age error [a]**	**$\delta^{13}C_{carb}$ [‰ VPDB]**	**$\delta^{18}O_{carb}$ [‰ VPDB]**
E1-033	Earth Sciences, Heidelberg University	3.76	27.3	1922.7	19.2	-9.24	-4.22
E1-034	Earth Sciences, Heidelberg University	3.86	27.7	1922.3	19.2	-9.65	-4.05
E1-035	Earth Sciences, Heidelberg University	3.96	28.2	1921.8	19.1	-10.42	-4.36
E1-036	Earth Sciences, Heidelberg University	4.06	28.7	1921.3	19.0	-10.3	-4.34
E1-037	Earth Sciences, Heidelberg University	4.16	29.2	1920.8	18.8	-10.57	-4.57
E1-038	Earth Sciences, Heidelberg University	4.26	29.6	1920.4	18.7	-10.28	-4.36
E1-039	Earth Sciences, Heidelberg University	4.36	30.1	1919.9	18.7	-11.11	-4.51
E1-040	Earth Sciences, Heidelberg University	4.46	30.5	1919.5	18.6	-11.2	-4.53
E1-041	Earth Sciences, Heidelberg University	4.56	31.0	1919.0	18.6	-11.22	-4.5
E1-042	Earth Sciences, Heidelberg University	4.66	31.5	1918.5	18.4	-10.79	-4.5
E1-043	Earth Sciences, Heidelberg University	4.76	31.9	1918.1	18.4	-10.62	-4.55
E1-044	Earth Sciences, Heidelberg University	4.86	32.4	1917.6	18.3	-10.93	-4.72
E1-045	Earth Sciences, Heidelberg University	4.96	32.9	1917.1	18.2	-11.14	-4.65
E1-046	Earth Sciences, Heidelberg University	5.06	33.4	1916.6	18.1	-11.78	-4.86
E1-047	Earth Sciences, Heidelberg University	5.16	33.9	1916.1	18.1	-11.39	-4.69
E1-048	Earth Sciences, Heidelberg University	5.26	34.4	1915.6	18.0	-10.15	-4.33
E1-049	Earth Sciences, Heidelberg University	5.36	34.9	1915.1	17.9	-10.29	-4.42
E1-050	Earth Sciences, Heidelberg University	5.46	35.3	1914.7	17.8	-10.1	-4.3
E1-051	Earth Sciences, Heidelberg University	5.56	35.8	1914.2	17.8	-10.66	-4.73
E1-052	Earth Sciences, Heidelberg University	5.66	36.2	1913.8	17.7	-11.41	-4.87
E1-053	Earth Sciences, Heidelberg University	5.76	36.7	1913.3	17.6	-11.13	-4.73
E1-054	Earth Sciences, Heidelberg University	5.86	37.2	1912.8	17.5	-10.58	-4.42
E1-055	Earth Sciences, Heidelberg University	5.96	37.6	1912.4	17.5	-11.31	-4.66
E1-056	Earth Sciences, Heidelberg University	6.06	38.1	1911.9	17.4	-11.74	-4.9
E1-057	Earth Sciences, Heidelberg University	6.16	38.5	1911.5	17.3	-11.67	-4.88
E1-058	Earth Sciences, Heidelberg University	6.26	39.1	1910.9	17.3	-11.61	-4.77
E1-059	Earth Sciences, Heidelberg University	6.36	39.6	1910.4	17.2	-11.72	-4.88
E1-060	Earth Sciences, Heidelberg University	6.46	40.1	1909.9	17.1	-11.65	-4.87
E1-061	Earth Sciences, Heidelberg University	6.56	40.6	1909.4	17.0	-11.77	-4.9
E1-062	Earth Sciences, Heidelberg University	6.66	41.1	1908.9	16.9	-11.94	-4.88
E1-063	Earth Sciences, Heidelberg University	6.76	41.6	1908.4	16.8	-11.9	-4.95
E1-064	Earth Sciences, Heidelberg University	6.86	42.0	1908.0	16.7	-12.04	-5.11
E1-065	Earth Sciences, Heidelberg University	6.96	42.6	1907.4	16.5	-11.91	-5.21
E1-066	Earth Sciences, Heidelberg University	7.06	43.0	1907.0	16.5	-11.63	-5.19
E1-067	Earth Sciences, Heidelberg University	7.16	43.5	1906.5	16.4	-11.22	-5.08
E1-068	Earth Sciences, Heidelberg University	7.26	44.1	1905.9	16.4	-11.6	-5.2
E1-069	Earth Sciences, Heidelberg University	7.36	44.6	1905.4	16.3	-11.37	-5.1
E1-070	Earth Sciences, Heidelberg University	7.46	45.1	1904.9	16.2	-11.41	-4.97
E1-071	Earth Sciences, Heidelberg University	7.71	46.4	1903.6	16.0	-11.04	-4.9
E1-072	Earth Sciences, Heidelberg University	7.96	47.6	1902.4	15.8	-9.98	-4.56
E1-073	Earth Sciences, Heidelberg University	8.21	48.9	1901.1	15.5	-10.88	-4.77
E1-074	Earth Sciences, Heidelberg University	8.46	50.2	1899.8	15.3	-11.5	-4.72
E1-075	Earth Sciences, Heidelberg University	8.71	51.5	1898.5	15.1	-11.54	-4.71
E1-076	Earth Sciences, Heidelberg University	8.96	52.8	1897.2	14.8	-11.73	-4.67
E1-078	Earth Sciences, Heidelberg University	9.46	55.5	1894.5	14.7	-11.26	-4.47
E1-079	Earth Sciences, Heidelberg University	9.71	57.0	1893.0	14.8	-11.32	-4.65
E1-080	Earth Sciences, Heidelberg University	9.96	58.6	1891.4	15.0	-11.44	-4.66
E1-081	Earth Sciences, Heidelberg University	10.21	60.1	1889.9	15.0	-11.09	-4.62
E1-082	Earth Sciences, Heidelberg University	10.46	61.6	1888.4	14.8	-11.28	-4.65
E1-083	Earth Sciences, Heidelberg University	10.71	63.2	1886.8	14.7	-11.22	-4.7
E1-084	Earth Sciences, Heidelberg University	10.96	64.8	1885.2	14.6	-11.07	-4.65
E1-085	Earth Sciences, Heidelberg University	11.21	66.5	1883.5	14.3	-10.95	-4.43

Continued on next page

Table A9 – *Continuation of Stable Isotopes ($\delta^{13}C$, $\delta^{18}O$) for stalagmite E1*

Sample ID	**Analyzing laboratory**	**Distance [mm] (from top)**	**Age [a BP]**	**Age [a AD]**	**Age error [a]**	**$\delta^{13}C_{carb}$ [‰ VPDB]**	**$\delta^{18}O_{carb}$ [‰ VPDB]**
E1-086	Earth Sciences, Heidelberg University	11.46	68.2	1881.8	14.1	-10.96	-4.5
E1-087	Earth Sciences, Heidelberg University	11.71	69.9	1880.1	13.8	-11.42	-4.58
E1-088	Earth Sciences, Heidelberg University	11.96	71.7	1878.3	13.6	-11.42	-4.53
E1-089	Earth Sciences, Heidelberg University	12.21	73.6	1876.4	13.4	-11.29	-4.75
E1-090	Earth Sciences, Heidelberg University	12.46	75.4	1874.6	13.1	-11.21	-4.63
E1-091	Earth Sciences, Heidelberg University	12.71	77.3	1872.7	13.0	-11.24	-4.62
E1-092	Earth Sciences, Heidelberg University	12.96	79.1	1870.9	12.9	-11.16	-4.5
E1-093	Earth Sciences, Heidelberg University	13.21	80.9	1869.1	12.8	-11.28	-4.51
E1-094	Earth Sciences, Heidelberg University	13.46	82.7	1867.3	12.8	-11.32	-4.54
E1-095	Earth Sciences, Heidelberg University	13.71	84.6	1865.4	12.8	-11.15	-4.41
E1-096	Earth Sciences, Heidelberg University	13.96	86.4	1863.6	12.8	-11.08	-4.65
E1-097	Earth Sciences, Heidelberg University	14.21	88.2	1861.8	12.7	-11.46	-4.47
E1-098	Earth Sciences, Heidelberg University	14.46	90.0	1860.0	12.6	-11.32	-4.31
E1-099	Earth Sciences, Heidelberg University	14.71	91.8	1858.2	12.6	-11.47	-4.41
E1-100	Earth Sciences, Heidelberg University	14.96	93.5	1856.5	12.5	-11.23	-5.28
E1-101	Earth Sciences, Heidelberg University	15.21	95.3	1854.7	12.4	-10.34	-4.45
E1-102	Earth Sciences, Heidelberg University	15.46	97.1	1852.9	12.4	-9.92	-4.31
E1-103	Earth Sciences, Heidelberg University	15.71	98.8	1851.2	12.3	-9.72	-4.32
E1-104	Earth Sciences, Heidelberg University	15.96	100.6	1849.4	12.3	-9.47	-4.66
E1-105	Earth Sciences, Heidelberg University	16.21	102.3	1847.7	12.2	-9.65	-4.87
E1-106	Earth Sciences, Heidelberg University	16.46	104.1	1845.9	12.1	-9.67	-4.94
E1-107	Earth Sciences, Heidelberg University	16.71	105.8	1844.2	12.0	-9.32	-4.8
E1-108	Earth Sciences, Heidelberg University	16.96	107.5	1842.5	11.9	-9.35	-4.71
E1-109	Earth Sciences, Heidelberg University	17.21	109.2	1840.8	11.9	-9.46	-4.89
E1-110	Earth Sciences, Heidelberg University	17.46	110.9	1839.1	11.8	-9.11	-4.88
E1-111	Earth Sciences, Heidelberg University	17.71	112.6	1837.4	11.8	-9.35	-5.08
E1-112	Earth Sciences, Heidelberg University	17.96	114.3	1835.7	11.7	-9.38	-4.99
E1-113	Earth Sciences, Heidelberg University	18.21	116.0	1834.0	11.7	-9.28	-4.65
E1-114	Earth Sciences, Heidelberg University	18.46	117.7	1832.3	11.6	-9.25	-4.81
E1-115	Earth Sciences, Heidelberg University	18.71	119.3	1830.7	11.6	-9.42	-4.8
E1-116	Earth Sciences, Heidelberg University	18.96	121.0	1829.0	11.6	-9.15	-5.11
E1-117	Earth Sciences, Heidelberg University	19.21	122.6	1827.4	11.5	-9.2	-4.54
E1-118	Earth Sciences, Heidelberg University	19.46	124.2	1825.8	11.5	-8.82	-4.22
E1-119	Earth Sciences, Heidelberg University	19.71	125.7	1824.3	11.5	-9.01	-4.38
E1-120	Earth Sciences, Heidelberg University	19.96	127.3	1822.7	11.4	-9.04	-4.31
E1-121	Earth Sciences, Heidelberg University	20.21	128.8	1821.2	11.4	-8.9	-4.39
E1-122	Earth Sciences, Heidelberg University	20.46	130.3	1819.7	11.4	-8.91	-4.36
E1-123	Earth Sciences, Heidelberg University	20.71	131.8	1818.2	11.3	-9.51	-4.64
E1-124	Earth Sciences, Heidelberg University	20.96	133.2	1816.8	11.3	-9.35	-4.89
E1-125	Earth Sciences, Heidelberg University	21.21	134.7	1815.3	11.2	-9.23	-4.52
E1-126	Earth Sciences, Heidelberg University	21.46	136.1	1813.9	11.1	-9.45	-4.53
E1-127	Earth Sciences, Heidelberg University	21.71	137.4	1812.6	11.0	-9.61	-4.57
E1-128	Earth Sciences, Heidelberg University	21.96	138.6	1811.4	11.0	-9.56	-4.77
E1-129	Earth Sciences, Heidelberg University	22.21	139.9	1810.1	10.7	-9.93	-4.91
E1-130	Earth Sciences, Heidelberg University	22.46	141.1	1808.9	10.5	-9.51	-4.77
E1-131	Earth Sciences, Heidelberg University	22.71	142.3	1807.7	10.3	-9.64	-4.83
E1-133	Earth Sciences, Heidelberg University	23.21	145.2	1804.8	9.5	-9.26	-4.68
E1-134	Earth Sciences, Heidelberg University	23.46	146.8	1803.2	8.9	-8.94	-4.75
E1-135	Earth Sciences, Heidelberg University	23.71	148.5	1801.5	8.2	-8.66	-4.38
E1-136	Earth Sciences, Heidelberg University	23.96	150.5	1799.5	6.9	-9.58	-4.48
E1-137	Earth Sciences, Heidelberg University	24.21	151.5	1798.5	6.5	-9.41	-4.29
E1-138	Earth Sciences, Heidelberg University	24.46	152.1	1797.9	6.5	-9.64	-4.24

Continued on next page

Table A9 – *Continuation of Stable Isotopes ($\delta^{13}C$, $\delta^{18}O$) for stalagmite E1*

Sample ID	**Analyzing laboratory**	**Distance [mm] (from top)**	**Age [a BP]**	**Age [a AD]**	**Age error [a]**	**$\delta^{13}C_{carb}$ [‰ VPDB]**	**$\delta^{18}O_{carb}$ [‰ VPDB]**
E1-139	Earth Sciences, Heidelberg University	24.71	152.3	1797.7	7.1	-9.72	-4.36
E1-140	Earth Sciences, Heidelberg University	24.96	152.5	1797.5	7.8	-10.18	-4.61
E1-141	Earth Sciences, Heidelberg University	25.21	153.0	1797.0	8.0	-10.01	-4.99
E1-142	Earth Sciences, Heidelberg University	25.46	153.4	1796.6	8.5	-10.14	-4.99
E1-143	Earth Sciences, Heidelberg University	25.71	154.1	1795.9	8.7	-10.3	-4.9
E1-144	Earth Sciences, Heidelberg University	25.96	154.8	1795.2	8.8	-10.07	-4.88
E1-145	Earth Sciences, Heidelberg University	26.21	155.5	1794.5	8.9	-10.33	-5.03
E1-146	Earth Sciences, Heidelberg University	26.46	156.3	1793.7	9.0	-10.07	-5.02
E1-147	Earth Sciences, Heidelberg University	26.71	157.3	1792.7	9.0	-10.46	-5.38
E1-148	Earth Sciences, Heidelberg University	26.96	158.3	1791.7	9.0	-10.29	-5.64
E1-149	Earth Sciences, Heidelberg University	27.21	159.4	1790.6	9.0	-10.06	-5.63
E1-150	Earth Sciences, Heidelberg University	27.46	160.6	1789.4	8.9	-10.25	-5.42
E1-151	Earth Sciences, Heidelberg University	27.71	161.8	1788.2	8.8	-10.13	-5.33
E1-152	Earth Sciences, Heidelberg University	27.96	163.1	1786.9	8.7	-9.9	-5.15
E1-154	Earth Sciences, Heidelberg University	28.46	165.5	1784.5	8.7	-9.91	-5.23
E1-155	Earth Sciences, Heidelberg University	28.71	166.7	1783.3	8.7	-9.99	-5.27
E1-156	Earth Sciences, Heidelberg University	28.96	168.0	1782.0	8.7	-9.77	-5.25
E1-158	Earth Sciences, Heidelberg University	29.46	170.6	1779.4	8.6	-9.65	-5.16
E1-159	Earth Sciences, Heidelberg University	29.71	171.8	1778.2	8.6	-9.15	-4.5
E1-160	Earth Sciences, Heidelberg University	29.96	173.0	1777.0	8.6	-9.63	-4.66
E1-161	Earth Sciences, Heidelberg University	30.21	174.1	1775.9	8.7	-8.96	-4.35
E1-162	Earth Sciences, Heidelberg University	30.46	175.3	1774.7	8.8	-9.75	-4.78
E1-163	Earth Sciences, Heidelberg University	30.71	176.3	1773.7	8.8	-10.13	-4.81
E1-165	Earth Sciences, Heidelberg University	31.21	178.5	1771.5	8.7	-10.15	-4.5
E1-166	Earth Sciences, Heidelberg University	31.46	179.6	1770.4	8.5	-10.22	-4.37
E1-167	Earth Sciences, Heidelberg University	31.71	180.7	1769.3	8.3	-10.55	-4.44
E1-168	Earth Sciences, Heidelberg University	31.96	181.9	1768.1	8.1	-10.9	-4.96
E1-169	Earth Sciences, Heidelberg University	32.21	183.0	1767.0	7.9	-10.96	-5.08
E1-170	Earth Sciences, Heidelberg University	32.46	184.2	1765.8	7.7	-10.74	-5.28
E1-171	Earth Sciences, Heidelberg University	32.71	185.5	1764.5	7.3	-10.05	-5.42
E1-172	Earth Sciences, Heidelberg University	32.96	186.6	1763.4	7.2	-9.77	-4.99
E1-175	Earth Sciences, Heidelberg University	33.71	190.0	1760.0	6.7	-10.1	-4.26
E1-176	Earth Sciences, Heidelberg University	33.96	191.0	1759.0	6.6	-9.91	-4.04
E1-180	Earth Sciences, Heidelberg University	34.96	194.6	1755.4	6.6	-10.72	-4.42
E1-181	Earth Sciences, Heidelberg University	35.21	195.4	1754.6	6.5	-10.77	-4.47
E1-182	Earth Sciences, Heidelberg University	35.46	196.1	1753.9	6.4	-11.07	-4.72
E1-183	Earth Sciences, Heidelberg University	35.71	196.8	1753.2	6.1	-11.19	-4.85
E1-184	Earth Sciences, Heidelberg University	35.96	197.6	1752.4	5.9	-11	-5.4
E1-185	Earth Sciences, Heidelberg University	36.21	198.2	1751.8	5.7	-10.96	-5.94
E1-186	Earth Sciences, Heidelberg University	36.46	198.9	1751.1	5.6	-11	-6.15
E1-187	Earth Sciences, Heidelberg University	36.71	199.6	1750.4	5.4	-10.58	-6.07
E1-188	Earth Sciences, Heidelberg University	36.96	200.3	1749.7	5.3	-10.49	-6.24
E1-189	Earth Sciences, Heidelberg University	37.21	201.1	1748.9	5.4	-10.13	-5.98
E1-190	Earth Sciences, Heidelberg University	37.46	201.9	1748.1	5.7	-9.88	-5.73
E1-191	Earth Sciences, Heidelberg University	37.71	202.6	1747.4	5.8	-9.96	-5.96
E1-192	Earth Sciences, Heidelberg University	37.96	203.4	1746.6	5.9	-10.03	-5.98
E1-193	Earth Sciences, Heidelberg University	38.21	204.3	1745.7	6.2	-9.71	-5.94
E1-194	Earth Sciences, Heidelberg University	38.46	205.0	1745.0	6.3	-10.09	-5.74
E1-195	Earth Sciences, Heidelberg University	38.71	205.8	1744.2	6.4	-10.46	-5.33
E1-196	Earth Sciences, Heidelberg University	38.96	206.7	1743.3	6.6	-10.3	-5.1
E1-197	Earth Sciences, Heidelberg University	39.21	207.7	1742.3	6.7	-9.73	-4.89
E1-199	Earth Sciences, Heidelberg University	39.71	209.7	1740.3	6.7	-9.94	-4.32

Continued on next page

Table A9 – *Continuation of Stable Isotopes ($\delta^{13}C$, $\delta^{18}O$) for stalagmite E1*

Sample ID	**Analyzing laboratory**	**Distance [mm] (from top)**	**Age [a BP]**	**Age [a AD]**	**Age error [a]**	**$\delta^{13}C_{carb}$ [‰ VPDB]**	**$\delta^{18}O_{carb}$ [‰ VPDB]**
E1-200	Earth Sciences, Heidelberg University	39.96	210.7	1739.3	6.8	-10.84	-4.55
E1-201	Earth Sciences, Heidelberg University	40.21	211.7	1738.3	6.8	-10.79	-5.41
E1-202	Earth Sciences, Heidelberg University	40.46	212.8	1737.2	6.8	-10.4	-5.36
E1-203	Earth Sciences, Heidelberg University	40.71	213.9	1736.1	6.8	-10.36	-5.17
E1-204	Earth Sciences, Heidelberg University	40.96	214.9	1735.1	6.8	-10.19	-4.94
E1-205	Earth Sciences, Heidelberg University	41.21	216.0	1734.0	6.8	-10.12	-4.41
E1-206	Earth Sciences, Heidelberg University	41.46	217.1	1732.9	6.9	-10.19	-4.41
E1-207	Earth Sciences, Heidelberg University	41.71	218.3	1731.7	6.9	-10.3	-4.2
E1-208	Earth Sciences, Heidelberg University	41.96	219.4	1730.6	7.0	-10.22	-4.18
E1-209	Earth Sciences, Heidelberg University	42.21	220.5	1729.5	7.1	-10.27	-4.27
E1-210	Earth Sciences, Heidelberg University	42.46	221.7	1728.3	7.2	-10.37	-4.33
E1-211	Earth Sciences, Heidelberg University	42.71	222.8	1727.2	7.3	-10.55	-4.3
E1-212	Earth Sciences, Heidelberg University	42.96	224.0	1726.0	7.5	-10.89	-4.46
E1-213	Earth Sciences, Heidelberg University	43.21	225.1	1724.9	7.6	-10.99	-4.6
E1-215	Earth Sciences, Heidelberg University	43.71	227.5	1722.5	8.0	-10.92	-4.8
E1-216	Earth Sciences, Heidelberg University	43.96	228.6	1721.4	8.2	-11.01	-5
E1-217	Earth Sciences, Heidelberg University	44.21	229.8	1720.2	8.4	-10.82	-4.97
E1-219	Earth Sciences, Heidelberg University	44.71	232.3	1717.7	8.8	-10.74	-5.12
E1-220	Earth Sciences, Heidelberg University	44.96	233.5	1716.5	9.0	-10.98	-5.19
E1-221	Earth Sciences, Heidelberg University	45.21	234.6	1715.4	9.2	-10.8	-5.16
E1-222	Earth Sciences, Heidelberg University	45.46	235.8	1714.2	9.5	-10.3	-4.87
E1-223	Earth Sciences, Heidelberg University	45.71	237.0	1713.0	9.6	-10.29	-4.65
E1-224	Earth Sciences, Heidelberg University	45.96	238.2	1711.8	9.8	-10.39	-4.76
E1-225	Earth Sciences, Heidelberg University	46.21	239.3	1710.7	10.0	-10.3	-4.87
E1-226	Earth Sciences, Heidelberg University	46.46	240.6	1709.4	10.2	-10.35	-4.88
E1-227	Earth Sciences, Heidelberg University	46.71	241.7	1708.3	10.4	-10.64	-5.16
E1-228	Earth Sciences, Heidelberg University	46.96	242.9	1707.1	10.6	-10.36	-5.09
E1-229	Earth Sciences, Heidelberg University	47.21	244.1	1705.9	10.8	-10.55	-5.18
E1-230	Earth Sciences, Heidelberg University	47.46	245.3	1704.7	11.0	-10.4	-5.32
E1-231	Earth Sciences, Heidelberg University	47.71	246.4	1703.6	11.2	-10.58	-5.1
E1-232	Earth Sciences, Heidelberg University	47.96	247.6	1702.4	11.3	-10.77	-5.55
E1-233	Earth Sciences, Heidelberg University	48.21	248.7	1701.3	11.4	-10.78	-5.48
E1-234	Earth Sciences, Heidelberg University	48.46	249.7	1700.3	11.5	-11.04	-5.54
E1-235	Earth Sciences, Heidelberg University	48.71	250.7	1699.3	11.4	-10.61	-5.41
E1-236	Earth Sciences, Heidelberg University	48.96	251.6	1698.4	11.4	-11.23	-5.79
E1-240	Earth Sciences, Heidelberg University	49.96	254.2	1695.8	9.4	-10.47	-5.03
E1-243	Earth Sciences, Heidelberg University	50.71	254.6	1695.4	6.7	-10.44	-5.58
E1-244	Earth Sciences, Heidelberg University	50.96	255.0	1695.0	6.4	-10.57	-5.57
E1-245	Earth Sciences, Heidelberg University	51.21	255.4	1694.6	6.5	-10.52	-5.46
E1-246	Earth Sciences, Heidelberg University	51.46	256.0	1694.0	6.6	-10.92	-5.66
E1-247	Earth Sciences, Heidelberg University	51.71	256.6	1693.4	7.1	-10.5	-5.58
E1-248	Earth Sciences, Heidelberg University	51.96	257.8	1692.2	8.3	-10.67	-5.39
E1-249	Earth Sciences, Heidelberg University	52.21	259.2	1690.8	9.7	-10.65	-5.27
E1-250	Earth Sciences, Heidelberg University	52.46	261.4	1688.6	11.9	-10.77	-5.43
E1-251	Earth Sciences, Heidelberg University	52.71	263.1	1686.9	13.1	-10.8	-5.51
E1-252	Earth Sciences, Heidelberg University	52.96	264.9	1685.1	14.2	-10.62	-5.41
E1-253	Earth Sciences, Heidelberg University	53.21	266.4	1683.6	15.1	-10.75	-5.21
E1-254	Earth Sciences, Heidelberg University	53.46	267.7	1682.3	15.7	-10.56	-4.94
E1-255	Earth Sciences, Heidelberg University	53.71	268.9	1681.1	16.1	-10.69	-4.43
E1-256	Earth Sciences, Heidelberg University	53.96	270.4	1679.6	16.7	-11.18	-5.24
E1-257	Earth Sciences, Heidelberg University	54.21	271.8	1678.2	16.9	-11.3	-5.24
E1-258	Earth Sciences, Heidelberg University	54.46	273.3	1676.7	17.0	-10.81	-5.11

Continued on next page

Table A9 – *Continuation of Stable Isotopes ($\delta^{13}C$, $\delta^{18}O$) for stalagmite E1*

Sample ID	**Analyzing laboratory**	**Distance [mm] (from top)**	**Age [a BP]**	**Age [a AD]**	**Age error [a]**	**$\delta^{13}C_{carb}$ [‰ VPDB]**	**$\delta^{18}O_{carb}$ [‰ VPDB]**
E1-259	Earth Sciences, Heidelberg University	54.71	275.0	1675.0	17.1	-11.14	-5.02
E1-260	Earth Sciences, Heidelberg University	54.96	276.6	1673.4	17.1	-11.3	-5.1
E1-261	Earth Sciences, Heidelberg University	55.21	278.3	1671.7	17.2	-11.02	-4.97
E1-262	Earth Sciences, Heidelberg University	55.46	280.3	1669.7	17.4	-11.08	-5.11
E1-263	Earth Sciences, Heidelberg University	55.71	282.0	1668.0	17.7	-10.88	-5.15
E1-264	Earth Sciences, Heidelberg University	55.96	283.8	1666.2	17.8	-11.14	-5.18
E1-266	Earth Sciences, Heidelberg University	56.46	287.6	1662.4	18.1	-10.94	-5.27
E1-267	Earth Sciences, Heidelberg University	56.71	289.6	1660.4	18.2	-11.14	-5.17
E1-268	Earth Sciences, Heidelberg University	56.96	291.6	1658.4	18.6	-10.75	-5.28
E1-269	Earth Sciences, Heidelberg University	57.21	293.7	1656.3	19.0	-10.85	-5.09
E1-270	Earth Sciences, Heidelberg University	57.46	295.6	1654.4	19.4	-11.02	-5.01
E1-271	Earth Sciences, Heidelberg University	57.71	297.4	1652.6	19.8	-11.29	-4.88
E1-272	Earth Sciences, Heidelberg University	57.96	299.2	1650.8	20.5	-11.38	-5
E1-273	Earth Sciences, Heidelberg University	58.21	301.0	1649.0	20.9	-11.38	-4.97
E1-274	Earth Sciences, Heidelberg University	58.46	302.7	1647.3	21.3	-12.41	-7.14
E1-275	Earth Sciences, Heidelberg University	58.71	304.2	1645.8	21.7	-11.64	-4.78
E1-277	Earth Sciences, Heidelberg University	59.21	307.2	1642.8	22.7	-11.92	-4.87
E1-279	Earth Sciences, Heidelberg University	59.71	309.7	1640.3	23.4	-11.79	-4.83
E1-283	Earth Sciences, Heidelberg University	61.7	375.1	1574.9	40.6	-11.82	-4.82
E1-284	Earth Sciences, Heidelberg University	61.95	376.0	1574.0	40.3	-11.5	-4.55
E1-285	Earth Sciences, Heidelberg University	62.2	376.9	1573.1	39.8	-11.5	-4.93
E1-286	Earth Sciences, Heidelberg University	62.45	377.9	1572.1	39.2	-10.63	-4.98
E1-287	Earth Sciences, Heidelberg University	62.7	378.8	1571.2	38.8	-10.67	-4.99
E1-288	Earth Sciences, Heidelberg University	62.95	379.7	1570.3	38.5	-11.15	-5.31
E1-289	Earth Sciences, Heidelberg University	63.2	380.7	1569.3	38.2	-11.22	-5.48
E1-290	Earth Sciences, Heidelberg University	63.45	381.6	1568.4	37.8	-11.63	-5.65
E1-291	Earth Sciences, Heidelberg University	63.7	382.5	1567.5	37.3	-11.77	-5.62
E1-292	Earth Sciences, Heidelberg University	63.95	383.3	1566.7	37.0	-11.76	-5.88
E1-293	Earth Sciences, Heidelberg University	64.2	384.2	1565.8	36.6	-11.44	-5.69
E1-294	Earth Sciences, Heidelberg University	64.45	385.1	1564.9	36.2	-11.44	-5.48
E1-295	Earth Sciences, Heidelberg University	64.7	386.2	1563.8	35.5	-11.14	-5.57
E1-296	Earth Sciences, Heidelberg University	64.95	387.2	1562.8	35.1	-10.96	-5.63
E1-297	Earth Sciences, Heidelberg University	65.2	388.0	1562.0	34.7	-10.89	-5.64
E1-298	Earth Sciences, Heidelberg University	65.45	388.9	1561.1	34.3	-10.71	-5.07
E1-299	Earth Sciences, Heidelberg University	65.7	389.7	1560.3	34.0	-10.87	-5.1
E1-300	Earth Sciences, Heidelberg University	65.95	390.6	1559.4	33.8	-10.63	-5.13
E1-301	Earth Sciences, Heidelberg University	66.2	391.4	1558.6	33.5	-10.78	-5.45
E1-302	Earth Sciences, Heidelberg University	66.45	392.2	1557.8	33.1	-10.97	-5.55
E1-303	Earth Sciences, Heidelberg University	66.7	393.0	1557.0	32.8	-10.7	-5.55
E1-305	Earth Sciences, Heidelberg University	67.2	394.8	1555.2	32.0	-9.85	-5.68
E1-306	Earth Sciences, Heidelberg University	67.45	395.7	1554.3	31.5	-10.35	-5.81
E1-307	Earth Sciences, Heidelberg University	67.7	396.6	1553.4	31.2	-10.08	-5.69
E1-308	Earth Sciences, Heidelberg University	67.95	397.6	1552.4	30.7	-10.2	-5.7
E1-309	Earth Sciences, Heidelberg University	68.2	398.5	1551.5	30.3	-10.23	-5.42
E1-310	Earth Sciences, Heidelberg University	68.45	399.3	1550.7	29.9	-10.33	-5.5
E1-311	Earth Sciences, Heidelberg University	68.7	400.2	1549.8	29.5	-10.24	-5.24
E1-312	Earth Sciences, Heidelberg University	68.95	401.1	1548.9	29.0	-10.41	-5.61
E1-313	Earth Sciences, Heidelberg University	69.2	401.9	1548.1	28.6	-10.19	-5.69
E1-314	Earth Sciences, Heidelberg University	69.45	402.9	1547.1	28.1	-10.13	-5.89
E1-315	Earth Sciences, Heidelberg University	69.7	403.8	1546.2	27.7	-10.02	-5.95
E1-316	Earth Sciences, Heidelberg University	69.95	404.6	1545.4	27.2	-10.09	-5.82
E1-317	Earth Sciences, Heidelberg University	70.2	405.5	1544.5	26.7	-10.23	-5.62

Continued on next page

Table A9 – *Continuation of Stable Isotopes ($\delta^{13}C$, $\delta^{18}O$) for stalagmite E1*

Sample ID	**Analyzing laboratory**	**Distance [mm] (from top)**	**Age [a BP]**	**Age [a AD]**	**Age error [a]**	**$\delta^{13}C_{carb}$ [‰ VPDB]**	**$\delta^{18}O_{carb}$ [‰ VPDB]**
E1-318	Earth Sciences, Heidelberg University	70.45	406.2	1543.8	26.4	-10.2	-5.48
E1-319	Earth Sciences, Heidelberg University	70.7	407.1	1542.9	25.6	-10.27	-5.38
E1-320	Earth Sciences, Heidelberg University	70.95	408.1	1541.9	25.0	-9.97	-5.13
E1-321	Earth Sciences, Heidelberg University	71.2	408.9	1541.1	24.4	-10.02	-5.1
E1-322	Earth Sciences, Heidelberg University	71.45	409.8	1540.2	24.0	-9.96	-5.19
E1-323	Earth Sciences, Heidelberg University	71.7	410.7	1539.3	23.3	-9.89	-5.2
E1-324	Earth Sciences, Heidelberg University	71.95	411.6	1538.4	22.5	-9.85	-5.14
E1-325	Earth Sciences, Heidelberg University	72.2	412.2	1537.8	22.2	-9.91	-5.29
E1-326	Earth Sciences, Heidelberg University	72.45	413.1	1536.9	21.7	-9.83	-5.35
E1-327	Earth Sciences, Heidelberg University	72.7	413.9	1536.1	20.9	-10	-5.47
E1-328	Earth Sciences, Heidelberg University	72.95	414.9	1535.1	20.0	-9.83	-5.3
E1-329	Earth Sciences, Heidelberg University	73.2	415.7	1534.3	19.6	-10.19	-5.65
E1-330	Earth Sciences, Heidelberg University	73.45	416.6	1533.4	18.7	-9.88	-5.49
E1-331	Earth Sciences, Heidelberg University	73.7	417.4	1532.6	18.1	-9.99	-5.41
E1-333	Earth Sciences, Heidelberg University	74.2	419.3	1530.7	16.3	-10.01	-5.52
E1-334	Earth Sciences, Heidelberg University	74.45	420.3	1529.7	15.5	-10.03	-5.52
E1-335	Earth Sciences, Heidelberg University	74.7	421.4	1528.6	14.4	-10.12	-5.52
E1-336	Earth Sciences, Heidelberg University	74.95	422.2	1527.8	13.7	-10.17	-5.34
E1-337	Earth Sciences, Heidelberg University	75.2	423.0	1527.0	13.6	-9.47	-4.78
E1-338	Earth Sciences, Heidelberg University	75.45	423.8	1526.2	13.7	-9.43	-4.71
E1-339	Earth Sciences, Heidelberg University	75.7	424.6	1525.4	13.7	-9.46	-4.62
E1-340	Earth Sciences, Heidelberg University	75.95	425.3	1524.7	13.6	-9.04	-4.47
E1-341	Earth Sciences, Heidelberg University	76.2	426.1	1523.9	13.4	-8.9	-4.34
E1-342	Earth Sciences, Heidelberg University	76.45	427.0	1523.0	13.3	-9.21	-4.41
E1-343	Earth Sciences, Heidelberg University	76.7	427.7	1522.3	13.2	-9.27	-4.38
E1-344	Earth Sciences, Heidelberg University	76.95	428.4	1521.6	13.1	-9.78	-4.92
E1-345	Earth Sciences, Heidelberg University	77.2	429.2	1520.8	13.0	-9.39	-4.83
E1-346	Earth Sciences, Heidelberg University	77.45	429.9	1520.1	13.1	-8.97	-5.18
E1-347	Earth Sciences, Heidelberg University	77.7	430.7	1519.3	13.1	-9.38	-5.07
E1-348	Earth Sciences, Heidelberg University	77.95	431.7	1518.3	13.0	-9.62	-5.22
E1-349	Earth Sciences, Heidelberg University	78.2	432.5	1517.5	13.0	-9.71	-5.29
E1-350	Earth Sciences, Heidelberg University	78.45	433.3	1516.7	13.0	-9.86	-5.23
E1-351	Earth Sciences, Heidelberg University	78.7	434.0	1516.0	13.0	-10.14	-5.63
E1-352	Earth Sciences, Heidelberg University	78.95	434.8	1515.2	13.1	-9.96	-5.56
E1-353	Earth Sciences, Heidelberg University	79.2	435.7	1514.3	13.1	-10	-5.89
E1-354	Earth Sciences, Heidelberg University	79.45	436.4	1513.6	13.1	-9.95	-5.88
E1-355	Earth Sciences, Heidelberg University	79.7	437.2	1512.8	13.1	-9.99	-5.87
E1-356	Earth Sciences, Heidelberg University	79.95	438.1	1511.9	13.1	-10.4	-6.2
E1-357	Earth Sciences, Heidelberg University	80.2	438.9	1511.1	13.2	-9.61	-5.81
E1-358	Earth Sciences, Heidelberg University	80.45	439.7	1510.3	13.1	-10.17	-5.97
E1-359	Earth Sciences, Heidelberg University	80.7	440.5	1509.5	13.1	-9.77	-5.82
E1-360	Earth Sciences, Heidelberg University	80.95	441.2	1508.8	13.3	-9.81	-5.92
E1-361	Earth Sciences, Heidelberg University	81.2	442.1	1507.9	13.3	-10.36	-6.37
E1-362	Earth Sciences, Heidelberg University	81.45	442.9	1507.1	13.5	-9.86	-6.13
E1-363	Earth Sciences, Heidelberg University	81.7	443.7	1506.3	13.4	-9.74	-6.19
E1-364	Earth Sciences, Heidelberg University	81.95	444.5	1505.5	13.7	-10.33	-6.25
E1-365	Earth Sciences, Heidelberg University	82.2	445.2	1504.8	13.8	-10.35	-7.09
E1-366	Earth Sciences, Heidelberg University	82.45	446.0	1504.0	13.7	-10.05	-6.23
E1-367	Earth Sciences, Heidelberg University	82.7	446.8	1503.2	13.7	-10.24	-6.54
E1-368	Earth Sciences, Heidelberg University	82.95	447.5	1502.5	13.9	-10.5	-6.1
E1-369	Earth Sciences, Heidelberg University	83.2	448.4	1501.6	13.9	-10.12	-6.17
E1-370	Earth Sciences, Heidelberg University	83.45	449.2	1500.8	13.9	-10.58	-6.08

Continued on next page

Table A9 – *Continuation of Stable Isotopes ($\delta^{13}C$, $\delta^{18}O$) for stalagmite E1*

Sample ID	**Analyzing laboratory**	**Distance [mm] (from top)**	**Age [a BP]**	**Age [a AD]**	**Age error [a]**	**$\delta^{13}C_{carb}$ [‰ VPDB]**	**$\delta^{18}O_{carb}$ [‰ VPDB]**
E1-371	Earth Sciences, Heidelberg University	83.7	450.1	1499.9	13.8	-10.19	-5.82
E1-372	Earth Sciences, Heidelberg University	83.95	450.8	1499.2	13.8	-9.96	-5.59
E1-374	Earth Sciences, Heidelberg University	84.45	452.4	1497.6	13.6	-10.41	-4.89
E1-375	Earth Sciences, Heidelberg University	84.7	453.1	1496.9	13.4	-9.99	-5.05
E1-376	Earth Sciences, Heidelberg University	84.95	453.9	1496.1	13.2	-10.06	-4.75
E1-377	Earth Sciences, Heidelberg University	85.2	454.6	1495.4	12.9	-10.22	-4.48
E1-378	Earth Sciences, Heidelberg University	85.45	455.4	1494.6	13.0	-9.36	-4.35
E1-379	Earth Sciences, Heidelberg University	85.7	456.2	1493.8	12.9	-10.28	-4.6
E1-380	Earth Sciences, Heidelberg University	85.95	457.0	1493.0	12.8	-10.66	-4.58
E1-381	Earth Sciences, Heidelberg University	86.2	457.8	1492.2	12.7	-11.16	-4.71
E1-382	Earth Sciences, Heidelberg University	86.45	458.5	1491.5	12.7	-11.04	-4.45
E1-384	Earth Sciences, Heidelberg University	86.95	460.2	1489.8	13.0	-11.59	-5.11
E1-385	Earth Sciences, Heidelberg University	87.2	461.1	1488.9	13.3	-11.6	-5.27
E1-387	Earth Sciences, Heidelberg University	87.7	463.0	1487.0	14.3	-11.6	-5.38
E1-388	Earth Sciences, Heidelberg University	87.95	463.8	1486.2	14.7	-11.5	-5.35
E1-389	Earth Sciences, Heidelberg University	88.2	464.7	1485.3	15.2	-11.03	-5.43
E1-390	Earth Sciences, Heidelberg University	88.45	465.7	1484.3	15.7	-11.37	-5.49
E1-391	Earth Sciences, Heidelberg University	88.7	466.6	1483.4	16.2	-11.36	-5.64
E1-392	Earth Sciences, Heidelberg University	88.95	467.6	1482.4	16.5	-11.13	-5.54
E1-393	Earth Sciences, Heidelberg University	89.2	468.6	1481.4	16.8	-11.17	-5.5
E1-394	Earth Sciences, Heidelberg University	89.45	469.7	1480.3	17.4	-11.04	-5.78
E1-395	Earth Sciences, Heidelberg University	89.7	470.7	1479.3	18.0	-10.92	-5.58
E1-396	Earth Sciences, Heidelberg University	89.95	471.9	1478.1	18.5	-11.29	-5.51
E1-397	Earth Sciences, Heidelberg University	90.2	473.2	1476.8	19.0	-11.24	-5.48
E1-398	Earth Sciences, Heidelberg University	90.45	474.6	1475.4	19.9	-11.11	-5.26
E1-399	Earth Sciences, Heidelberg University	90.7	476.5	1473.5	20.4	-11.06	-5.28
E1-400	Earth Sciences, Heidelberg University	90.95	478.9	1471.1	20.4	-11.32	-5.39
E1-401	Earth Sciences, Heidelberg University	91.2	481.7	1468.3	20.2	-11.48	-5.65
E1-402	Earth Sciences, Heidelberg University	91.45	484.9	1465.1	20.3	-11.27	-5.7
E1-403	Earth Sciences, Heidelberg University	91.7	488.1	1461.9	21.0	-11.15	-5.61
E1-404	Earth Sciences, Heidelberg University	91.95	490.7	1459.3	21.8	-11.12	-5.42
E1-405	Earth Sciences, Heidelberg University	92.2	492.7	1457.3	22.8	-11.15	-5.54
E1-406	Earth Sciences, Heidelberg University	92.45	494.1	1455.9	23.8	-11.4	-5.56
E1-408	Earth Sciences, Heidelberg University	92.95	496.4	1453.6	25.8	-11.6	-6.08
E1-409	Earth Sciences, Heidelberg University	93.2	497.5	1452.5	27.0	-11.51	-5.99
E1-410	Earth Sciences, Heidelberg University	93.45	498.5	1451.5	28.1	-11.68	-6.25
E1-411	Earth Sciences, Heidelberg University	93.7	499.4	1450.6	29.1	-11.57	-6.17
E1-412	Earth Sciences, Heidelberg University	93.95	500.2	1449.8	29.9	-11.44	-6.34
E1-413	Earth Sciences, Heidelberg University	94.2	500.9	1449.1	30.8	-11.56	-6.27
E1-414	Earth Sciences, Heidelberg University	94.45	501.7	1448.3	31.7	-11.32	-6.32
E1-415	Earth Sciences, Heidelberg University	94.7	502.6	1447.4	32.6	-11.26	-5.98
E1-416	Earth Sciences, Heidelberg University	94.95	503.4	1446.6	33.4	-11.36	-5.48
E1-417	Earth Sciences, Heidelberg University	95.2	504.3	1445.7	34.3	-11.71	-5.79
E1-418	Earth Sciences, Heidelberg University	95.45	505.3	1444.7	35.2	-10.96	-5.52
E1-419	Earth Sciences, Heidelberg University	95.7	506.2	1443.8	36.1	-10.08	-4.91

Section between 30 and 26 mm dft was reanalyzed at a higher resolution!

Sample ID	**Analyzing laboratory**	**Distance [mm] (from top)**	**Age [a BP]**	**Age [a AD]**	**Age error [a]**	**$\delta^{13}C_{carb}$ [‰ VPDB]**	**$\delta^{18}O_{carb}$ [‰ VPDB]**
E1-460	Earth Sciences, Heidelberg University	26				-9.74	-4.82
E1-458	Earth Sciences, Heidelberg University	26.2				-10.23	-5.13
E1-457	Earth Sciences, Heidelberg University	26.3				-10.08	-5.2
E1-455	Earth Sciences, Heidelberg University	26.5				-10.69	-5.52

Continued on next page

Table A9 – *Continuation of Stable Isotopes ($\delta^{13}C$, $\delta^{18}O$) for stalagmite E1*

Sample ID	**Analyzing laboratory**	**Distance [mm] (from top)**	**Age [a BP]**	**Age [a AD]**	**Age error [a]**	**$\delta^{13}C_{carb}$ [‰ VPDB]**	**$\delta^{18}O_{carb}$ [‰ VPDB]**
E1-454	Earth Sciences, Heidelberg University	26.6				-10.1	-5.42
E1-453	Earth Sciences, Heidelberg University	26.7				-10.42	-5.49
E1-451	Earth Sciences, Heidelberg University	26.9				-10.13	-5.65
E1-449	Earth Sciences, Heidelberg University	27.1				-10.22	-5.35
E1-448	Earth Sciences, Heidelberg University	27.2				-10.19	-5.45
E1-447	Earth Sciences, Heidelberg University	27.3				-10.04	-5.2
E1-446	Earth Sciences, Heidelberg University	27.4				-9.82	-5.19
E1-445	Earth Sciences, Heidelberg University	27.5				-9.51	-4.53
E1-444	Earth Sciences, Heidelberg University	27.6				-9.62	-4.98
E1-443	Earth Sciences, Heidelberg University	27.7				-9.81	-5.13
E1-442	Earth Sciences, Heidelberg University	27.8				-9.85	-5.2
E1-441	Earth Sciences, Heidelberg University	27.9				-9.59	-5.09
E1-440	Earth Sciences, Heidelberg University	28				-9.89	-5.24
E1-439	Earth Sciences, Heidelberg University	28.1				-9.91	-5.15
E1-438	Earth Sciences, Heidelberg University	28.2				-9.51	-5.23
E1-437	Earth Sciences, Heidelberg University	28.3				-9.64	-4.99
E1-436	Earth Sciences, Heidelberg University	28.4				-10.29	-5.38
E1-435	Earth Sciences, Heidelberg University	28.5				-9.86	-5.34
E1-434	Earth Sciences, Heidelberg University	28.6				-9.39	-5.13
E1-433	Earth Sciences, Heidelberg University	28.7				-9.41	-5.01
E1-432	Earth Sciences, Heidelberg University	28.8				-9.91	-5.14
E1-431	Earth Sciences, Heidelberg University	28.9				-10.03	-5.13
E1-430	Earth Sciences, Heidelberg University	29				-9.34	-4.84
E1-428	Earth Sciences, Heidelberg University	29.2				-9.69	-4.95
E1-427	Earth Sciences, Heidelberg University	29.3				-9.22	-4.73
E1-426	Earth Sciences, Heidelberg University	29.4				-8.97	-4.56
E1-425	Earth Sciences, Heidelberg University	29.5				-9.69	-4.64
E1-424	Earth Sciences, Heidelberg University	29.6				-10.21	-4.91
E1-423	Earth Sciences, Heidelberg University	29.7				-9.45	-4.53
E1-422	Earth Sciences, Heidelberg University	29.8				-9.01	-4.47
E1-420	Earth Sciences, Heidelberg University	30				-9.7	-4.62

Table A10. Stable Isotopes (δ^{13}C, δ^{18}O) for stalagmite E8. The age of each sample corresponds to the chronology discussed in Chapter III.2.

Sample ID	**Analyzing laboratory**	**Distance [mm] (from top)**	**Age [a BP]**	**Age [a AD]**	**Age error [a]**	**$\delta^{13}C_{carb}$ [‰ VPDB]**	**$\delta^{18}O_{carb}$ [‰ VPDB]**
E8-001	Earth Sciences, Heidelberg University	0.1				-10.40	-4.99
E8-002	Earth Sciences, Heidelberg University	0.2				-9.99	-4.57
E8-003	Earth Sciences, Heidelberg University	0.3				-9.69	-4.73
E8-004	Earth Sciences, Heidelberg University	0.4				-8.93	-4.33
E8-005	Earth Sciences, Heidelberg University	0.5				-9.45	-4.95
E8-006	Earth Sciences, Heidelberg University	0.6				-9.09	-4.70
E8-007	Earth Sciences, Heidelberg University	0.7				-8.92	-4.40
E8-008	Earth Sciences, Heidelberg University	0.8				-9.40	-4.60
E8-009	Earth Sciences, Heidelberg University	0.9	217.4	1732.6	32.7	-9.63	-5.08
E8-010	Earth Sciences, Heidelberg University	1	217.9	1732.1	32.6	-9.29	-5.01
E8-011	Earth Sciences, Heidelberg University	1.1	218.3	1731.7	32.6	-9.13	-4.67
E8-012	Earth Sciences, Heidelberg University	1.2	218.8	1731.2	32.5	-9.24	-4.51
E8-013	Earth Sciences, Heidelberg University	1.3	219.3	1730.7	32.4	-9.53	-4.74

Continued on next page

Table A10 – *Continuation of Stable Isotopes ($\delta^{13}C$, $\delta^{18}O$) for stalagmite E8*

Sample ID	**Analyzing laboratory**	**Distance [mm] (from top)**	**Age [a BP]**	**Age [a AD]**	**Age error [a]**	**$\delta^{13}C_{carb}$ [‰ VPDB]**	**$\delta^{18}O_{carb}$ [‰ VPDB]**
E8-014	Earth Sciences, Heidelberg University	1.4	219.8	1730.2	32.3	-9.65	-4.59
E8-015	Earth Sciences, Heidelberg University	1.5	220.3	1729.7	32.2	-9.46	-4.74
E8-016	Earth Sciences, Heidelberg University	1.6	220.7	1729.3	32.1	-9.12	-4.55
E8-017	Earth Sciences, Heidelberg University	1.7	221.2	1728.8	32.0	-9.22	-4.65
E8-018	Earth Sciences, Heidelberg University	1.8	221.7	1728.3	31.8	-8.75	-4.52
E8-019	Earth Sciences, Heidelberg University	1.9	222.1	1727.9	31.8	-8.56	-4.33
E8-020	Earth Sciences, Heidelberg University	2	222.6	1727.4	31.8	-8.40	-4.25
E8-021	Earth Sciences, Heidelberg University	2.25	223.7	1726.3	31.4	-8.32	-4.08
E8-023	Earth Sciences, Heidelberg University	2.75	225.8	1724.2	30.6	-8.95	-4.10
E8-024	Earth Sciences, Heidelberg University	3	226.8	1723.2	30.3	-10.75	-4.71
E8-025	Earth Sciences, Heidelberg University	3.25	228.0	1722.0	30.0	-10.72	-4.68
E8-026	Earth Sciences, Heidelberg University	3.5	229.1	1720.9	29.7	-10.73	-4.86
E8-027	Earth Sciences, Heidelberg University	3.75	230.2	1719.8	29.4	-10.56	-4.72
E8-028	Earth Sciences, Heidelberg University	4	231.3	1718.7	29.0	-10.38	-4.27
E8-029	Earth Sciences, Heidelberg University	4.25	232.4	1717.6	28.6	-10.26	-4.60
E8-030	Earth Sciences, Heidelberg University	4.5	233.5	1716.5	28.1	-10.68	-4.80
E8-031	Earth Sciences, Heidelberg University	4.75	234.6	1715.4	27.7	-10.65	-4.95
E8-032	Earth Sciences, Heidelberg University	5	235.8	1714.2	27.0	-9.70	-4.76
E8-033	Earth Sciences, Heidelberg University	5.25	236.9	1713.1	26.7	-10.62	-5.15
E8-034	Earth Sciences, Heidelberg University	5.5	237.9	1712.1	26.1	-10.22	-5.05
E8-035	Earth Sciences, Heidelberg University	5.75	239.1	1710.9	25.6	-9.74	-4.95
E8-036	Earth Sciences, Heidelberg University	6	240.3	1709.7	25.1	-10.12	-5.06
E8-037	Earth Sciences, Heidelberg University	6.25	241.4	1708.6	24.6	-9.72	-5.02
E8-038	Earth Sciences, Heidelberg University	6.5	242.5	1707.5	24.2	-10.24	-5.05
E8-039	Earth Sciences, Heidelberg University	6.75	243.7	1706.3	23.6	-10.37	-5.12
E8-040	Earth Sciences, Heidelberg University	7	244.8	1705.2	23.1	-9.50	-5.03
E8-041	Earth Sciences, Heidelberg University	7.25	245.9	1704.1	22.4	-10.46	-4.98
E8-042	Earth Sciences, Heidelberg University	7.5	247.0	1703.0	21.9	-9.34	-4.75
E8-043	Earth Sciences, Heidelberg University	7.75	248.2	1701.8	21.2	-9.73	-4.91
E8-044	Earth Sciences, Heidelberg University	8	249.3	1700.7	20.5	-9.08	-4.82
E8-045	Earth Sciences, Heidelberg University	8.25	250.5	1699.5	19.6	-9.16	-4.58
E8-046	Earth Sciences, Heidelberg University	8.5	251.9	1698.1	18.2	-9.72	-4.79
E8-047	Earth Sciences, Heidelberg University	8.75	253.0	1697.0	17.4	-9.76	-4.85
E8-048	Earth Sciences, Heidelberg University	9	254.1	1695.9	17.0	-9.85	-4.95
E8-049	Earth Sciences, Heidelberg University	9.25	255.2	1694.8	16.3	-10.06	-4.93
E8-050	Earth Sciences, Heidelberg University	9.5	256.6	1693.4	15.4	-10.32	-4.94
E8-051	Earth Sciences, Heidelberg University	9.75	257.7	1692.3	14.8	-10.56	-4.93
E8-052	Earth Sciences, Heidelberg University	10	259.0	1691.0	14.4	-10.83	-5.15
E8-053	Earth Sciences, Heidelberg University	10.25	260.3	1689.7	13.7	-9.95	-4.58
E8-054	Earth Sciences, Heidelberg University	10.5	261.5	1688.5	13.3	-10.61	-5.03
E8-055	Earth Sciences, Heidelberg University	10.75	262.9	1687.1	13.0	-10.58	-4.99
E8-056	Earth Sciences, Heidelberg University	11	264.2	1685.8	12.7	-10.42	-4.85
E8-057	Earth Sciences, Heidelberg University	11.25	265.5	1684.5	12.4	-10.66	-4.96
E8-058	Earth Sciences, Heidelberg University	11.5	266.8	1683.2	12.4	-10.52	-5.07
E8-059	Earth Sciences, Heidelberg University	11.75	268.2	1681.8	12.4	-10.28	-4.97
E8-060	Earth Sciences, Heidelberg University	12	269.3	1680.7	12.6	-9.49	-4.65
E8-061	Earth Sciences, Heidelberg University	12.25	270.6	1679.4	12.8	-9.86	-4.48
E8-062	Earth Sciences, Heidelberg University	12.5	271.8	1678.2	12.9	-9.99	-4.51
E8-063	Earth Sciences, Heidelberg University	12.75	273.0	1677.0	12.9	-10.34	-4.66
E8-064	Earth Sciences, Heidelberg University	13	274.2	1675.8	13.0	-10.46	-4.60
E8-065	Earth Sciences, Heidelberg University	13.25	275.4	1674.6	13.1	-10.81	-4.77
E8-066	Earth Sciences, Heidelberg University	13.5	276.6	1673.4	13.1	-10.60	-4.68

Continued on next page

Table A10 – *Continuation of Stable Isotopes ($\delta^{13}C$, $\delta^{18}O$) for stalagmite E8*

Sample ID	**Analyzing laboratory**	**Distance [mm] (from top)**	**Age [a BP]**	**Age [a AD]**	**Age error [a]**	**$\delta^{13}C_{carb}$ [‰ VPDB]**	**$\delta^{18}O_{carb}$ [‰ VPDB]**
E8-067	Earth Sciences, Heidelberg University	13.75	277.8	1672.2	13.0	-10.40	-4.81
E8-068	Earth Sciences, Heidelberg University	14	278.9	1671.1	13.1	-11.48	-4.99
E8-069	Earth Sciences, Heidelberg University	14.25	280.0	1670.0	13.0	-11.91	-5.25
E8-070	Earth Sciences, Heidelberg University	14.5	281.1	1668.9	12.9	-11.99	-5.27
E8-071	Earth Sciences, Heidelberg University	14.75	282.1	1667.9	12.8	-11.65	-5.56
E8-072	Earth Sciences, Heidelberg University	15	283.0	1667.0	12.4	-11.81	-5.55
E8-073	Earth Sciences, Heidelberg University	15.25	284.1	1665.9	12.1	-11.70	-5.41
E8-074	Earth Sciences, Heidelberg University	15.5	285.1	1664.9	11.9	-11.56	-5.42
E8-075	Earth Sciences, Heidelberg University	15.75	286.1	1663.9	11.7	-11.42	-5.54
E8-076	Earth Sciences, Heidelberg University	16	287.0	1663.0	11.4	-11.37	-5.11
E8-077	Earth Sciences, Heidelberg University	16.25	288.0	1662.0	11.3	-11.27	-5.31
E8-078	Earth Sciences, Heidelberg University	16.5	289.0	1661.0	11.0	-11.40	-5.36
E8-079	Earth Sciences, Heidelberg University	16.75	289.9	1660.1	10.9	-11.74	-5.43
E8-080	Earth Sciences, Heidelberg University	17	290.9	1659.1	10.7	-11.75	-5.32
E8-081	Earth Sciences, Heidelberg University	17.25	291.9	1658.1	10.6	-11.22	-5.67
E8-082	Earth Sciences, Heidelberg University	17.5	292.9	1657.1	10.5	-10.40	-5.08
E8-083	Earth Sciences, Heidelberg University	17.75	293.9	1656.1	10.6	-10.78	-5.22
E8-084	Earth Sciences, Heidelberg University	18	295.0	1655.0	10.5	-9.77	-4.90
E8-085	Earth Sciences, Heidelberg University	18.25	296.1	1653.9	10.5	-10.76	-4.92
E8-086	Earth Sciences, Heidelberg University	18.5	297.2	1652.8	10.7	-9.74	-4.73
E8-087	Earth Sciences, Heidelberg University	18.75	298.2	1651.8	10.9	-10.92	-4.47
E8-088	Earth Sciences, Heidelberg University	19	299.2	1650.8	11.1	-11.98	-4.75
E8-089	Earth Sciences, Heidelberg University	19.25	300.3	1649.7	11.4	-11.11	-4.61
E8-090	Earth Sciences, Heidelberg University	19.5	301.4	1648.6	11.7	-10.93	-4.46
E8-091	Earth Sciences, Heidelberg University	19.75	302.4	1647.6	12.2	-11.56	-4.77
E8-092	Earth Sciences, Heidelberg University	20	303.4	1646.6	12.5	-11.65	-4.76
E8-093	Earth Sciences, Heidelberg University	20.25	304.5	1645.5	12.7	-11.43	-4.87
E8-094	Earth Sciences, Heidelberg University	20.5	305.6	1644.4	13.0	-11.49	-4.95
E8-095	Earth Sciences, Heidelberg University	20.75	306.5	1643.5	13.1	-11.36	-4.98
E8-096	Earth Sciences, Heidelberg University	21	307.6	1642.4	13.3	-11.19	-4.96
E8-097	Earth Sciences, Heidelberg University	21.25	308.7	1641.3	13.4	-11.20	-5.00
E8-098	Earth Sciences, Heidelberg University	21.5	310.0	1640.0	13.4	-11.04	-5.08
E8-099	Earth Sciences, Heidelberg University	21.75	311.3	1638.7	13.4	-11.31	-5.12
E8-100	Earth Sciences, Heidelberg University	22	312.6	1637.4	13.3	-11.28	-5.17
E8-101	Earth Sciences, Heidelberg University	22.25	313.9	1636.1	13.3	-11.07	-4.85
E8-102	Earth Sciences, Heidelberg University	22.5	315.3	1634.7	13.5	-11.08	-5.01
E8-103	Earth Sciences, Heidelberg University	22.75	316.8	1633.2	13.6	-11.16	-4.96
E8-104	Earth Sciences, Heidelberg University	23	318.3	1631.7	13.7	-11.29	-4.98
E8-105	Earth Sciences, Heidelberg University	23.25	319.8	1630.2	13.7	-11.48	-5.05
E8-106	Earth Sciences, Heidelberg University	23.5	321.4	1628.6	13.7	-11.41	-5.00
E8-107	Earth Sciences, Heidelberg University	23.75	322.8	1627.2	13.9	-11.50	-4.84
E8-108	Earth Sciences, Heidelberg University	24	324.4	1625.6	13.9	-11.78	-4.93
E8-109	Earth Sciences, Heidelberg University	24.25	326.0	1624.0	14.1	-11.90	-5.11
E8-110	Earth Sciences, Heidelberg University	24.5	327.6	1622.4	14.5	-12.06	-5.21
E8-111	Earth Sciences, Heidelberg University	24.75	329.2	1620.8	14.9	-11.92	-5.32
E8-112	Earth Sciences, Heidelberg University	25	330.8	1619.2	15.8	-11.93	-5.33
E8-113	Earth Sciences, Heidelberg University	25.25	332.4	1617.6	16.8	-11.87	-5.36
E8-114	Earth Sciences, Heidelberg University	25.5	333.9	1616.1	17.6	-11.80	-5.18
E8-115	Earth Sciences, Heidelberg University	25.75	335.3	1614.7	18.5	-11.53	-4.69
E8-116	Earth Sciences, Heidelberg University	26	336.4	1613.6	18.9	-11.79	-4.79
E8-117	Earth Sciences, Heidelberg University	26.25	337.5	1612.5	19.2	-11.32	-4.91
E8-118	Earth Sciences, Heidelberg University	26.5	338.7	1611.3	19.7	-11.13	-5.22

Continued on next page

Table A10 – *Continuation of Stable Isotopes ($\delta^{13}C$, $\delta^{18}O$) for stalagmite E8*

Sample ID	**Analyzing laboratory**	**Distance [mm] (from top)**	**Age [a BP]**	**Age [a AD]**	**Age error [a]**	**$\delta^{13}C_{carb}$ [‰ VPDB]**	**$\delta^{18}O_{carb}$ [‰ VPDB]**
E8-119	Earth Sciences, Heidelberg University	26.75	339.8	1610.2	20.4	-10.83	-5.14
E8-120	Earth Sciences, Heidelberg University	27	341.2	1608.8	21.4	-11.09	-5.30
E8-121	Earth Sciences, Heidelberg University	27.25	342.3	1607.7	22.1	-10.93	-5.36
E8-122	Earth Sciences, Heidelberg University	27.5	343.6	1606.4	23.0	-11.27	-5.95
E8-123	Earth Sciences, Heidelberg University	27.75	344.7	1605.3	23.6	-11.39	-5.88
E8-124	Earth Sciences, Heidelberg University	28				-11.46	-5.90
E8-125	Earth Sciences, Heidelberg University	28.25				-11.02	-5.84
E8-126	Earth Sciences, Heidelberg University	28.5				-10.77	-5.56
E8-127	Earth Sciences, Heidelberg University	28.75				-10.90	-5.48
E8-128	Earth Sciences, Heidelberg University	29				-10.87	-5.79
E8-129	Earth Sciences, Heidelberg University	29.25				-10.78	-5.98
E8-130	Earth Sciences, Heidelberg University	29.5				-10.69	-6.17
E8-131	Earth Sciences, Heidelberg University	29.75				-10.68	-6.05
E8-132	Earth Sciences, Heidelberg University	30				-10.23	-5.63
E8-133	Earth Sciences, Heidelberg University	30.25				-10.27	-5.25
E8-134	Earth Sciences, Heidelberg University	30.5				-10.19	-4.92
E8-135	Earth Sciences, Heidelberg University	30.75				-9.69	-5.00
E8-136	Earth Sciences, Heidelberg University	31				-9.39	-5.43
E8-137	Earth Sciences, Heidelberg University	31.25				-9.59	-5.57
E8-138	Earth Sciences, Heidelberg University	31.5				-10.07	-5.64
E8-139	Earth Sciences, Heidelberg University	31.75				-10.22	-5.67
E8-140	Earth Sciences, Heidelberg University	32				-10.70	-5.91
E8-141	Earth Sciences, Heidelberg University	32.25				-9.60	-5.28
E8-142	Earth Sciences, Heidelberg University	32.5				-9.78	-5.32
E8-143	Earth Sciences, Heidelberg University	32.75				-10.07	-5.27
E8-144	Earth Sciences, Heidelberg University	33				-10.20	-5.31
E8-145	Earth Sciences, Heidelberg University	33.25				-9.94	-5.46
E8-146	Earth Sciences, Heidelberg University	33.5				-10.35	-5.43
E8-147	Earth Sciences, Heidelberg University	33.75				-10.16	-5.27
E8-148	Earth Sciences, Heidelberg University	34				-10.49	-5.34
E8-149	Earth Sciences, Heidelberg University	34.25				-10.85	-5.42
E8-150	Earth Sciences, Heidelberg University	34.5				-10.26	-5.18
E8-151	Earth Sciences, Heidelberg University	34.75				-9.88	-4.94
E8-152	Earth Sciences, Heidelberg University	35				-10.26	-5.09
E8-153	Earth Sciences, Heidelberg University	35.25				-9.90	-4.85
E8-154	Earth Sciences, Heidelberg University	35.5				-9.87	-5.20
E8-155	Earth Sciences, Heidelberg University	35.75				-10.08	-5.33
E8-156	Earth Sciences, Heidelberg University	36				-9.60	-4.09
E8-157	Earth Sciences, Heidelberg University	36.25				-9.57	-4.73
E8-158	Earth Sciences, Heidelberg University	36.5				-10.10	-4.89
E8-159	Earth Sciences, Heidelberg University	36.75				-10.89	-5.08
E8-160	Earth Sciences, Heidelberg University	37				-9.87	-4.44
E8-161	Earth Sciences, Heidelberg University	37.25				-10.07	-4.52
E8-162	Earth Sciences, Heidelberg University	37.5				-10.03	-4.31
E8-163	Earth Sciences, Heidelberg University	37.75				-9.77	-4.11
E8-164	Earth Sciences, Heidelberg University	38				-9.74	-4.16
E8-165-A	Earth Sciences, Heidelberg University	38.25				-10.06	-4.15
E8-167	Earth Sciences, Heidelberg University	38.75				-9.94	-4.43
E8-168	Earth Sciences, Heidelberg University	39				-9.83	-4.41
E8-169	Earth Sciences, Heidelberg University	39.25				-9.76	-4.46
E8-170	Earth Sciences, Heidelberg University	39.5				-10.21	-4.55
E8-171	Earth Sciences, Heidelberg University	39.75				-10.26	-4.34

Continued on next page

Table A10 – *Continuation of Stable Isotopes ($\delta^{13}C$, $\delta^{18}O$) for stalagmite E8*

Sample ID	**Analyzing laboratory**	**Distance [mm] (from top)**	**Age [a BP]**	**Age [a AD]**	**Age error [a]**	**$\delta^{13}C_{carb}$ [‰ VPDB]**	**$\delta^{18}O_{carb}$ [‰ VPDB]**
E8-172	Earth Sciences, Heidelberg University	40				-9.66	-4.24
E8-173	Earth Sciences, Heidelberg University	40.25				-9.72	-4.41
E8-174	Earth Sciences, Heidelberg University	40.5				-9.97	-5.03
E8-175	Earth Sciences, Heidelberg University	40.75				-9.31	-4.87
E8-176	Earth Sciences, Heidelberg University	41				-10.09	-5.25
E8-177	Earth Sciences, Heidelberg University	41.25				-9.79	-5.38
E8-178	Earth Sciences, Heidelberg University	41.5				-9.24	-5.19
E8-179	Earth Sciences, Heidelberg University	41.75				-9.78	-5.39
E8-180	Earth Sciences, Heidelberg University	42				-10.64	-5.62
E8-181	Earth Sciences, Heidelberg University	42.25				-9.22	-5.23
E8-184	Earth Sciences, Heidelberg University	43				-10.18	-5.48
E8-185	Earth Sciences, Heidelberg University	43.25				-10.54	-5.60
E8-186	Earth Sciences, Heidelberg University	43.5				-10.80	-5.81
E8-187	Earth Sciences, Heidelberg University	43.75				-10.65	-5.74
E8-188	Earth Sciences, Heidelberg University	44				-10.39	-5.59
E8-189	Earth Sciences, Heidelberg University	44.25				-9.52	-5.33
E8-190	Earth Sciences, Heidelberg University	44.5				-9.37	-5.34
E8-191	Earth Sciences, Heidelberg University	44.75				-9.46	-5.32
E8-192	Earth Sciences, Heidelberg University	45				-9.46	-5.58
E8-193	Earth Sciences, Heidelberg University	45.25				-9.49	-5.26
E8-194	Earth Sciences, Heidelberg University	45.5				-9.32	-5.17
E8-195	Earth Sciences, Heidelberg University	45.75				-8.56	-5.09
E8-196	Earth Sciences, Heidelberg University	46				-9.71	-5.30
E8-197	Earth Sciences, Heidelberg University	46.25				-9.73	-5.16
E8-198	Earth Sciences, Heidelberg University	46.5				-9.68	-4.91
E8-199	Earth Sciences, Heidelberg University	46.75				-9.35	-5.16
E8-200	Earth Sciences, Heidelberg University	47				-9.53	-5.24
E8-201	Earth Sciences, Heidelberg University	47.25				-9.56	-5.45
E8-202	Earth Sciences, Heidelberg University	47.5				-10.23	-5.66
E8-203	Earth Sciences, Heidelberg University	47.75				-9.24	-5.59
E8-204	Earth Sciences, Heidelberg University	48				-8.95	-5.43
E8-205	Earth Sciences, Heidelberg University	48.25				-9.02	-5.17
E8-206	Earth Sciences, Heidelberg University	48.5				-8.92	-4.67
E8-207	Earth Sciences, Heidelberg University	48.75				-8.86	-4.41
E8-208	Earth Sciences, Heidelberg University	49				-9.44	-4.71
E8-209	Earth Sciences, Heidelberg University	49.25				-9.42	-4.79
E8-210	Earth Sciences, Heidelberg University	49.5				-8.22	-4.28
E8-211	Earth Sciences, Heidelberg University	49.75				-8.31	-4.26
E8-212	Earth Sciences, Heidelberg University	50				-8.74	-4.48

Table A11. Stable Isotopes ($\delta^{13}C$, $\delta^{18}O$) for stalagmite E23-3. The age of each sample corresponds to the chronology discussed in Chapter III.2.

Sample ID	**Analyzing laboratory**	**Distance [mm] (from top)**	**Age [a BP]**	**Age [a AD]**	**Age error [a]**	**$\delta^{13}C_{carb}$ [‰ VPDB]**	**$\delta^{18}O_{carb}$ [‰ VPDB]**
E23-3-001	Earth Sciences, Heidelberg University	0.15	-70.8	2020.8		-11.92	-5.04
E23-3-002	Earth Sciences, Heidelberg University	0.4	-68.9	2018.9		-12.31	-5.02
E23-3-003	Earth Sciences, Heidelberg University	0.65	-67.3	2017.3		-12.07	-4.95
E23-3-004	Earth Sciences, Heidelberg University	0.9	-65.6	2015.6		-12.28	-5.08
E23-3-005	Earth Sciences, Heidelberg University	1.15	-64.1	2014.1		-12.26	-5.28

Continued on next page

Table A11 – *Continuation of Stable Isotopes ($\delta^{13}C$, $\delta^{18}O$) for stalagmite E23-3*

Sample ID	**Analyzing laboratory**	**Distance [mm] (from top)**	**Age [a BP]**	**Age [a AD]**	**Age error [a]**	**$\delta^{13}C_{carb}$ [‰ VPDB]**	**$\delta^{18}O_{carb}$ [‰ VPDB]**
E23-3-006	Earth Sciences, Heidelberg University	1.4	-62.6	2012.6		-11.73	-5.18
E23-3-007	Earth Sciences, Heidelberg University	1.65	-61.2	2011.2		-11.76	-5.24
E23-3-008	Earth Sciences, Heidelberg University	1.9	-59.3	2009.3		-11.93	-4.73
E23-3-009	Earth Sciences, Heidelberg University	2.15	-57.6	2007.6		-11.5	-4.3
E23-3-010	Earth Sciences, Heidelberg University	2.4	-56.6	2006.6		-11.15	-4.19
E23-3-011	Earth Sciences, Heidelberg University	2.65	-55.8	2005.8		-11.08	-4.2
E23-3-012	Earth Sciences, Heidelberg University	2.9	-54.7	2004.7		-11.03	-4.22
E23-3-013	Earth Sciences, Heidelberg University	3.15	-53.9	2003.9		-10.88	-4.21
E23-3-014	Earth Sciences, Heidelberg University	3.4	-52.3	2002.3		-11.13	-4.21
E23-3-015	Earth Sciences, Heidelberg University	3.65	-50.8	2000.8		-11.02	-4.19
E23-3-016	Earth Sciences, Heidelberg University	3.9	-50.0	2000.0		-10.73	-4.22
E23-3-017	Earth Sciences, Heidelberg University	4.15	-49.4	1999.4		-10.56	-4.22
E23-3-018	Earth Sciences, Heidelberg University	4.4	-48.1	1998.1		-10	-4.03
E23-3-019	Earth Sciences, Heidelberg University	4.65	-47.1	1997.1		-10.36	-4.17
E23-3-020	Earth Sciences, Heidelberg University	4.9	-46.4	1996.4		-10.79	-4.26
E23-3-021	Earth Sciences, Heidelberg University	5.15	-45.3	1995.3		-11.31	-4.51
E23-3-022	Earth Sciences, Heidelberg University	5.4	-44.1	1994.1		-11	-4.37
E23-3-023	Earth Sciences, Heidelberg University	5.65	-43.0	1993.0		-10.89	-4.47
E23-3-024	Earth Sciences, Heidelberg University	5.9	-40.8	1990.8		-10.2	-4.1
E23-3-025	Earth Sciences, Heidelberg University	6.15	-40.3	1990.3		-9.68	-3.99
E23-3-026	Earth Sciences, Heidelberg University	6.4	-38.7	1988.7		-10.48	-4.26
E23-3-027	Earth Sciences, Heidelberg University	6.65	-37.9	1987.9		-10.06	-4.2
E23-3-028	Earth Sciences, Heidelberg University	6.9	-36.8	1986.8		-11.07	-4.48
E23-3-029	Earth Sciences, Heidelberg University	7.15	-35.7	1985.7		-11.02	-4.82
E23-3-030	Earth Sciences, Heidelberg University	7.4	-35.1	1985.1		-11.38	-5.01
E23-3-031	Earth Sciences, Heidelberg University	7.65	-34.1	1984.1		-11.16	-5.03
E23-3-032	Earth Sciences, Heidelberg University	7.9	-33.1	1983.1		-10.6	-4.59
E23-3-033	Earth Sciences, Heidelberg University	8.15	-32.5	1982.5		-10.74	-4.33
E23-3-034	Earth Sciences, Heidelberg University	8.4	-31.8	1981.8		-10.17	-4.04
E23-3-035	Earth Sciences, Heidelberg University	8.65	-31.1	1981.1		-11.24	-4.19
E23-3-036	Earth Sciences, Heidelberg University	8.9	-30.4	1980.4		-10.91	-3.93
E23-3-037	Earth Sciences, Heidelberg University	9.15	-29.3	1979.3		-11.06	-4.21
E23-3-038	Earth Sciences, Heidelberg University	9.4	-28.5	1978.5		-11.13	-4.28
E23-3-039	Earth Sciences, Heidelberg University	9.65	-27.8	1977.8		-10.92	-4.21
E23-3-040	Earth Sciences, Heidelberg University	9.9	-26.9	1976.9		-11.13	-4.33
E23-3-041	Earth Sciences, Heidelberg University	10.15	-26.1	1976.1		-10.91	-4.34
E23-3-042	Earth Sciences, Heidelberg University	10.4	-25.0	1975.0		-10.6	-4.34
E23-3-043	Earth Sciences, Heidelberg University	10.65	-23.7	1973.7		-10.89	-4.53
E23-3-044	Earth Sciences, Heidelberg University	10.9	-22.0	1972.0		-11.15	-4.6
E23-3-045	Earth Sciences, Heidelberg University	11.15	-20.6	1970.6		-11.33	-4.81
E23-3-046	Earth Sciences, Heidelberg University	11.4	-19.5	1969.5		-10.81	-4.56
E23-3-047	Earth Sciences, Heidelberg University	11.65	-18.2	1968.2		-10.43	-4.36
E23-3-048	Earth Sciences, Heidelberg University	11.9	-17.4	1967.4		-10.39	-4.04
E23-3-049	Earth Sciences, Heidelberg University	12.15	-16.8	1966.8		-10.51	-4.01
E23-3-050	Earth Sciences, Heidelberg University	12.4	-15.6	1965.6		-10.74	-4.16
E23-3-051	Earth Sciences, Heidelberg University	12.65	-13.8	1963.8		-11.25	-4.3
E23-3-052	Earth Sciences, Heidelberg University	12.9	-12.9	1962.9		-10.77	-4.35
E23-3-053	Earth Sciences, Heidelberg University	13.15	-11.5	1961.5		-10.82	-4.34
E23-3-054	Earth Sciences, Heidelberg University	13.4	-10.8	1960.8			
E23-3-055	Earth Sciences, Heidelberg University	13.65	-10.2	1960.2		-11.02	-4.5
E23-3-056	Earth Sciences, Heidelberg University	13.9	-9.5	1959.5		-11.21	-4.66
E23-3-057	Earth Sciences, Heidelberg University	14.15	-8.6	1958.6		-10.88	-4.47

Continued on next page

Table A11 – *Continuation of Stable Isotopes ($\delta^{13}C$, $\delta^{18}O$) for stalagmite E23-3*

Sample ID	**Analyzing laboratory**	**Distance [mm] (from top)**	**Age [a BP]**	**Age [a AD]**	**Age error [a]**	**$\delta^{13}C_{carb}$ [‰ VPDB]**	**$\delta^{18}O_{carb}$ [‰ VPDB]**
E23-3-058	Earth Sciences, Heidelberg University	14.4	-7.6	1957.6		-11.33	-4.73
E23-3-059	Earth Sciences, Heidelberg University	14.65	-6.7	1956.7		-11.35	-4.91
E23-3-060	Earth Sciences, Heidelberg University	14.9	-5.6	1955.6		-10.61	-4.93
E23-3-061	Earth Sciences, Heidelberg University	15.15	-4.7	1954.7		-9.91	-5.06
E23-3-062	Earth Sciences, Heidelberg University	15.4	-4.2	1954.2		-11.05	-5.37
E23-3-063	Earth Sciences, Heidelberg University	15.65	-3.5	1953.5		-10.43	-5.34
E23-3-064	Earth Sciences, Heidelberg University	15.9	-2.9	1952.9		-10.26	-5.27
E23-3-065	Earth Sciences, Heidelberg University	16.15	-2.3	1952.3		-10.81	-5.44
E23-3-066	Earth Sciences, Heidelberg University	16.4	-1.7	1951.7		-10.07	-5.22
E23-3-067	Earth Sciences, Heidelberg University	16.65	-1.0	1951.0		-10.45	-4.79
E23-3-068	Earth Sciences, Heidelberg University	16.9	-0.4	1950.4		-10.81	-4.6
E23-3-069	Earth Sciences, Heidelberg University	17.15	0.3	1949.7		-10.27	-4.23
E23-3-070	Earth Sciences, Heidelberg University	17.4	0.9	1949.1		-11.51	-4.65
E23-3-071	Earth Sciences, Heidelberg University	17.65	1.4	1948.6		-9.73	-4.08
E23-3-072	Earth Sciences, Heidelberg University	17.9	1.9	1948.1		-10.9	-4.17
E23-3-073	Earth Sciences, Heidelberg University	18.15	2.3	1947.7		-9.9	-4.15
E23-3-074	Earth Sciences, Heidelberg University	18.4	2.7	1947.3		-9.84	-4.3
E23-3-075	Earth Sciences, Heidelberg University	18.65	3.2	1946.8		-10.69	-4.4
E23-3-076	Earth Sciences, Heidelberg University	18.9	3.8	1946.2		-11.53	-4.6
E23-3-077	Earth Sciences, Heidelberg University	19.15	4.4	1945.6		-10.6	-4.32
E23-3-078	Earth Sciences, Heidelberg University	19.4	5.1	1944.9		-10.98	-4.33
E23-3-079	Earth Sciences, Heidelberg University	19.65	6.0	1944.0		-11.36	-4.58
E23-3-080	Earth Sciences, Heidelberg University	19.9	6.6	1943.4		-10.26	-4.24
E23-3-081	Earth Sciences, Heidelberg University	20.15	7.1	1942.9		-10.23	-4.35
E23-3-082	Earth Sciences, Heidelberg University	20.4	7.6	1942.4		-9.43	-4.12
E23-3-083	Earth Sciences, Heidelberg University	20.65	8.1	1941.9		-10.98	-4.43
E23-3-084	Earth Sciences, Heidelberg University	20.9	8.7	1941.3		-11.42	-4.65
E23-3-085	Earth Sciences, Heidelberg University	21.15	9.4	1940.6		-11.43	-4.79
E23-3-086	Earth Sciences, Heidelberg University	21.4	10.3	1939.7		-11.71	-4.97
E23-3-087	Earth Sciences, Heidelberg University	21.65	11.3	1938.7		-11.29	-4.97
E23-3-088	Earth Sciences, Heidelberg University	21.9	12.1	1937.9		-11.28	-5.14
E23-3-089	Earth Sciences, Heidelberg University	22.15	12.5	1937.5		-10.04	-4.78
E23-3-090	Earth Sciences, Heidelberg University	22.4	13.0	1937.0		-11.03	-5.22
E23-3-091	Earth Sciences, Heidelberg University	22.65	13.5	1936.5		-10.02	-5.13
E23-3-092	Earth Sciences, Heidelberg University	22.9	14.0	1936.0		-10.41	-5.2
E23-3-093	Earth Sciences, Heidelberg University	23.15	15.1	1934.9		-9.89	-5.14
E23-3-094	Earth Sciences, Heidelberg University	23.4	15.7	1934.3		-10.93	-5.12
E23-3-095	Earth Sciences, Heidelberg University	23.65	16.4	1933.6		-12.33	-5.44
E23-3-096	Earth Sciences, Heidelberg University	23.9	17.1	1932.9		-11.5	-4.97
E23-3-097	Earth Sciences, Heidelberg University	24.15	17.6	1932.4		-11.81	-5.09
E23-3-098	Earth Sciences, Heidelberg University	24.4	18.2	1931.8		-10.89	-4.64
E23-3-099	Earth Sciences, Heidelberg University	24.65	18.7	1931.3		-11.79	-4.88
E23-3-100	Earth Sciences, Heidelberg University	24.9	19.2	1930.8		-10.74	-4.68
E23-3-101	Earth Sciences, Heidelberg University	25.15	19.5	1930.5		-10.76	-4.46
E23-3-102	Earth Sciences, Heidelberg University	25.4	19.7	1930.3		-11.75	-4.79
E23-3-103	Earth Sciences, Heidelberg University	25.65	20.0	1930.0		-11.26	-4.67
E23-3-104	Earth Sciences, Heidelberg University	25.9	20.4	1929.6		-12.28	-4.85
E23-3-105	Earth Sciences, Heidelberg University	26.15	20.9	1929.1		-12.09	-4.88
E23-3-106	Earth Sciences, Heidelberg University	26.4	21.6	1928.4		-11.49	-4.87
E23-3-107	Earth Sciences, Heidelberg University	26.65	22.6	1927.4			
E23-3-108	Earth Sciences, Heidelberg University	26.9	23.7	1926.3		-11.93	-5.08
E23-3-109	Earth Sciences, Heidelberg University	27.15	25.9	1924.1		-11.89	-4.86

Continued on next page

Table A11 – *Continuation of Stable Isotopes ($\delta^{13}C$, $\delta^{18}O$) for stalagmite E23-3*

Sample ID	**Analyzing laboratory**	**Distance [mm] (from top)**	**Age [a BP]**	**Age [a AD]**	**Age error [a]**	**$\delta^{13}C_{carb}$ [‰ VPDB]**	**$\delta^{18}O_{carb}$ [‰ VPDB]**
E23-3-110	Earth Sciences, Heidelberg University	27.4	27.6	1922.4		-11.97	-4.9
E23-3-111	Earth Sciences, Heidelberg University	27.65	31.9	1918.1		-11.98	-4.75
E23-3-112	Earth Sciences, Heidelberg University	27.9	33.4	1916.6		-11.87	-4.7
E23-3-113	Earth Sciences, Heidelberg University	28.15	35.5	1914.5		-12.26	-5.28
E23-3-114	Earth Sciences, Heidelberg University	28.4	36.5	1913.5		-11.9	-5.71
E23-3-115	Earth Sciences, Heidelberg University	28.65	37.8	1912.2		-11	-5.4
E23-3-116	Earth Sciences, Heidelberg University	28.9	39.2	1910.8		-10.92	-5.17
E23-3-117	Earth Sciences, Heidelberg University	29.15	40.9	1909.1		-11.57	-5.23
E23-3-118	Earth Sciences, Heidelberg University	29.4	41.9	1908.1		-11.96	-4.92
E23-3-119	Earth Sciences, Heidelberg University	29.65	44.8	1905.2		-11.91	-4.72
E23-3-120	Earth Sciences, Heidelberg University	29.9	49.3	1900.7		-10.15	0.89
E23-3-121	Earth Sciences, Heidelberg University	30.4	52.0	1898.0		-12.17	-4.72
E23-3-122	Earth Sciences, Heidelberg University	30.9	54.4	1895.6		-11.96	-4.87
E23-3-123	Earth Sciences, Heidelberg University	31.4	56.1	1893.9		-11.45	-4.95
E23-3-124	Earth Sciences, Heidelberg University	31.9	57.6	1892.4		-11.74	-5.36
E23-3-125	Earth Sciences, Heidelberg University	32.4	59.1	1890.9		-11.39	-5.28
E23-3-126	Earth Sciences, Heidelberg University	32.9	61.9	1888.1		-11.02	-4.97
E23-3-127	Earth Sciences, Heidelberg University	33.4	64.5	1885.5		-11.07	-4.63
E23-3-128	Earth Sciences, Heidelberg University	33.9	67.5	1882.5		-12.04	-4.83
E23-3-129	Earth Sciences, Heidelberg University	34.4	69.9	1880.1		-11.65	-4.77
E23-3-130	Earth Sciences, Heidelberg University	34.9	71.9	1878.1		-11.55	-4.85
E23-3-131	Earth Sciences, Heidelberg University	35.4	74.4	1875.6		-11.73	-4.98
E23-3-132	Earth Sciences, Heidelberg University	35.9	77.9	1872.1		-11.18	-4.44
E23-3-133	Earth Sciences, Heidelberg University	36.4	80.2	1869.8		-11.54	-4.38
E23-3-134	Earth Sciences, Heidelberg University	36.9	81.8	1868.2		-11.67	-4.7
E23-3-135	Earth Sciences, Heidelberg University	37.4	83.5	1866.5		-11.51	-4.77
E23-3-136	Earth Sciences, Heidelberg University	37.9	85.3	1864.7		-11.17	-4.35
E23-3-137	Earth Sciences, Heidelberg University	38.4	87.0	1863.0		-11.05	-4.42
E23-3-138	Earth Sciences, Heidelberg University	38.9	89.8	1860.2		-11.1	-4.48
E23-3-139	Earth Sciences, Heidelberg University	39.4	92.1	1857.9		-10.55	-4.37
E23-3-140	Earth Sciences, Heidelberg University	39.9	94.1	1855.9		-10.74	-4.41
E23-3-141	Earth Sciences, Heidelberg University	40.4	95.8	1854.2		-10.51	-4.36
E23-3-142	Earth Sciences, Heidelberg University	40.9	97.2	1852.8		-10.57	-4.49
E23-3-143	Earth Sciences, Heidelberg University	41.4	98.4	1851.6		-10.06	-4.64
E23-3-144	Earth Sciences, Heidelberg University	41.9	100.5	1849.5		-8.48	-0.85
E23-3-145	Earth Sciences, Heidelberg University	42.4	102.3	1847.7		-9.47	-4.72
E23-3-146	Earth Sciences, Heidelberg University	42.9	105.5	1844.5		-9.72	-4.89
E23-3-147	Earth Sciences, Heidelberg University	43.4	108.7	1841.3			
E23-3-148	Earth Sciences, Heidelberg University	43.9	112.1	1837.9		-10.34	-5.41
E23-3-149	Earth Sciences, Heidelberg University	44.4	114.9	1835.1		-10.06	-4.81
E23-3-150	Earth Sciences, Heidelberg University	44.9	117.7	1832.3		-10.49	-4.71
E23-3-151	Earth Sciences, Heidelberg University	45.4	119.9	1830.1		-10.21	-5.09
E23-3-152	Earth Sciences, Heidelberg University	45.9	122.4	1827.6		-10.4	-5.18
E23-3-153	Earth Sciences, Heidelberg University	46.4	124.4	1825.6		-10.12	-5.11
E23-3-154	Earth Sciences, Heidelberg University	46.9	126.6	1823.4		-9.99	-4.99
E23-3-155	Earth Sciences, Heidelberg University	47.4	129.4	1820.6		-9.92	-5.08
E23-3-156	Earth Sciences, Heidelberg University	47.9	131.5	1818.5		-10.08	-5.11
E23-3-157	Earth Sciences, Heidelberg University	48.4	133.3	1816.7		-10.2	-5.38
E23-3-158	Earth Sciences, Heidelberg University	48.9	135.1	1814.9		-9.82	-4.96
E23-3-159	Earth Sciences, Heidelberg University	49.4	136.7	1813.3		-9.91	-4.35
E23-3-160	Earth Sciences, Heidelberg University	49.9	139.0	1811.0		-9.85	-4.2
E23-3-161	Earth Sciences, Heidelberg University	50.4	140.4	1809.6		-9.72	-4.07

Continued on next page

Table A11 – *Continuation of Stable Isotopes ($\delta^{13}C$, $\delta^{18}O$) for stalagmite E23-3*

Sample ID	**Analyzing laboratory**	**Distance [mm] (from top)**	**Age [a BP]**	**Age [a AD]**	**Age error [a]**	**$\delta^{13}C_{carb}$ [‰ VPDB]**	**$\delta^{18}O_{carb}$ [‰ VPDB]**
E23-3-162	Earth Sciences, Heidelberg University	50.9	141.7	1808.3		-9.45	-3.97
E23-3-163	Earth Sciences, Heidelberg University	51.4	142.8	1807.2		-9.08	-3.79
E23-3-164	Earth Sciences, Heidelberg University	51.9	144.2	1805.8		-9.3	-3.96
E23-3-165	Earth Sciences, Heidelberg University	52.4	145.6	1804.4		-9.33	-3.98
E23-3-166	Earth Sciences, Heidelberg University	52.9	147.1	1802.9		-9.83	-4.31
E23-3-167	Earth Sciences, Heidelberg University	53.4	149.0	1801.0		-10.19	-4.47
E23-3-168	Earth Sciences, Heidelberg University	53.9	151.0	1799.0		-10.14	-4.5
E23-3-169	Earth Sciences, Heidelberg University	54.4	153.4	1796.6		-10.19	-4.57
E23-3-170	Earth Sciences, Heidelberg University	54.9	155.1	1794.9		-9.88	-4.61
E23-3-171	Earth Sciences, Heidelberg University	55.4	156.9	1793.1		-9.87	-4.61
E23-3-172	Earth Sciences, Heidelberg University	55.9	159.4	1790.6		-9.77	-4.54
E23-3-173	Earth Sciences, Heidelberg University	56.4	161.1	1788.9		-10.37	-4.54
E23-3-174	Earth Sciences, Heidelberg University	56.9	162.7	1787.3		-11.43	-4.68
E23-3-175	Earth Sciences, Heidelberg University	57.4	164.6	1785.4		-10.9	-5.17
E23-3-176	Earth Sciences, Heidelberg University	57.9	167.0	1783.0		-11.06	-5.17
E23-3-177	Earth Sciences, Heidelberg University	58.4	168.5	1781.5		-10.63	-4.94
E23-3-178	Earth Sciences, Heidelberg University	58.9	169.9	1780.1		-10.9	-5.57
E23-3-179	Earth Sciences, Heidelberg University	59.4	171.3	1778.7		-11.02	-5.68
E23-3-180	Earth Sciences, Heidelberg University	59.9	172.4	1777.6		-10.92	-5.39
E23-3-181	Earth Sciences, Heidelberg University	60.4	173.2	1776.8		-10.13	-5.1
E23-3-182	Earth Sciences, Heidelberg University	60.9	174.5	1775.5		-10.38	-5.29
E23-3-183	Earth Sciences, Heidelberg University	61.4	176.0	1774.0		-10.58	-5.4
E23-3-184	Earth Sciences, Heidelberg University	61.9	177.4	1772.6		-10.14	-5.47
E23-3-185	Earth Sciences, Heidelberg University	62.4	178.8	1771.2		-10.1	-5.46
E23-3-186	Earth Sciences, Heidelberg University	62.9	179.6	1770.4		-9.85	-5.49
E23-3-187	Earth Sciences, Heidelberg University	63.4	180.6	1769.4		-10.05	-5.28
E23-3-188	Earth Sciences, Heidelberg University	63.9	182.1	1767.9		-10.22	-5.12
E23-3-189	Earth Sciences, Heidelberg University	64.4	184.8	1765.2		-9.82	-4.6
E23-3-190	Earth Sciences, Heidelberg University	64.9	187.2	1762.8		-10.65	-4.71
E23-3-191	Earth Sciences, Heidelberg University	65.4	188.5	1761.5		-11.58	-5.2
E23-3-192	Earth Sciences, Heidelberg University	65.9	190.0	1760.0		-9.77	-5.2
E23-3-193	Earth Sciences, Heidelberg University	66.4	191.5	1758.5		-9.93	-5.23
E23-3-194	Earth Sciences, Heidelberg University	66.9	194.0	1756.0		-9.69	-4.89
E23-3-195	Earth Sciences, Heidelberg University	67.4	195.7	1754.3		-9.63	-4.72
E23-3-196	Earth Sciences, Heidelberg University	67.9	199.0	1751.0		-9.6	-4.57
E23-3-197	Earth Sciences, Heidelberg University	68.4	202.1	1747.9		-10.17	-4.71
E23-3-198	Earth Sciences, Heidelberg University	68.9	204.4	1745.6		-11.72	-6.17
E23-3-199	Earth Sciences, Heidelberg University	69.4	207.8	1742.2		-11.33	-6.07
E23-3-200	Earth Sciences, Heidelberg University	69.9	210.6	1739.4		-10.79	-5.52
E23-3-201	Earth Sciences, Heidelberg University	70.4	213.0	1737.0		-11.35	-5.01
E23-3-202	Earth Sciences, Heidelberg University	70.9	214.5	1735.5		-11.45	-5.36
E23-3-203	Earth Sciences, Heidelberg University	71.4	215.6	1734.4		-11.21	-5.57
E23-3-204	Earth Sciences, Heidelberg University	71.9	216.5	1733.5		-10.47	-5.29
E23-3-205	Earth Sciences, Heidelberg University	72.4	218.0	1732.0		-9.88	-4.53
E23-3-206	Earth Sciences, Heidelberg University	72.9	219.9	1730.1		-9.74	-4.24
E23-3-207	Earth Sciences, Heidelberg University	73.4	221.8	1728.2		-10.02	-4.07
E23-3-208	Earth Sciences, Heidelberg University	73.9	224.8	1725.2		-9.86	-4.14
E23-3-209	Earth Sciences, Heidelberg University	74.4	226.4	1723.6			
E23-3-210	Earth Sciences, Heidelberg University	74.9	227.9	1722.1		-11.05	-4.82
E23-3-211	Earth Sciences, Heidelberg University	75.4	230.5	1719.5		-10.55	-4.84
E23-3-212	Earth Sciences, Heidelberg University	75.9	232.7	1717.3		-10.23	-4.76
E23-3-213	Earth Sciences, Heidelberg University	76.4	234.6	1715.4		-10.2	-4.62

Continued on next page

Table A11 – *Continuation of Stable Isotopes ($\delta^{13}C$, $\delta^{18}O$) for stalagmite E23-3*

Sample ID	**Analyzing laboratory**	**Distance [mm] (from top)**	**Age [a BP]**	**Age [a AD]**	**Age error [a]**	**$\delta^{13}C_{carb}$ [‰ VPDB]**	**$\delta^{18}O_{carb}$ [‰ VPDB]**
E23-3-214	Earth Sciences, Heidelberg University	76.9	236.4	1713.6		-10.12	-4.67
E23-3-215	Earth Sciences, Heidelberg University	77.4	238.3	1711.7		-10.12	-4.69
E23-3-216	Earth Sciences, Heidelberg University	77.9	240.6	1709.4		-10.34	-4.74
E23-3-217	Earth Sciences, Heidelberg University	78.4	242.4	1707.6		-10.5	-4.98
E23-3-218	Earth Sciences, Heidelberg University	78.9	243.5	1706.5		-10.04	-4.98
E23-3-219	Earth Sciences, Heidelberg University	79.4	244.3	1705.7		-9.89	-4.97
E23-3-220	Earth Sciences, Heidelberg University	79.9	245.1	1704.9		-10.26	-5.04
E23-3-221	Earth Sciences, Heidelberg University	80.4	246.2	1703.8		-10.67	-5.1
E23-3-222	Earth Sciences, Heidelberg University	80.9	249.1	1700.9		-10.17	-5.01
E23-3-223	Earth Sciences, Heidelberg University	81.4	251.1	1698.9		-10.78	-5.39
E23-3-224	Earth Sciences, Heidelberg University	81.9	252.9	1697.1		-10.4	-5.44
E23-3-225	Earth Sciences, Heidelberg University	82.4	254.8	1695.2		-10.75	-5.48
E23-3-226	Earth Sciences, Heidelberg University	82.9				-7.92	-4.73
E23-3-227	Earth Sciences, Heidelberg University	83.4				-8.62	-5
E23-3-228	Earth Sciences, Heidelberg University	83.9				-8.66	-4.89

Danksagung

An dieser Stelle möchte ich die Gelegenheit nutzen, um allen herzlich zu danken, die mich während meiner Promotion in den letzten Jahren auf verschiedenste Weise unterstützt und begleitet haben.

Zuallererst geht ein herzliches Dankeschön an meine beiden Betreuer dieser Arbeit, Prof. Dr. Wolfgang Stinnesbeck und Prof. Dr. Norbert Frank, die in mir das Interesse an der Speläothem- und Klimaforschung geweckt und mir ermöglicht haben, über dieses spannende Projekt promovieren zu dürfen. Vielen Dank für die zahlreichen anregenden Diskussionen, eure kontinuierliche Unterstützung und eure stets motivierende Art.
Ebenso gebührt Dr. Sophie Warken mein besonderer Dank, die mich mit ihrer Expertise in der Speläothemforschung und mit mindestens genauso viel Enthusiasmus all die Jahre begleitet hat – sei es bei Geländearbeiten in Mexiko oder auf Konferenzen. Vielen Dank für all deine Zeit, deine wertvollen Ratschläge und deine kontinuierliche Unterstützung in allen Angelegenheiten, die im Laufe dieser Arbeit aufkamen und durch die meine Arbeit bis zur letzten Minute deutlich profitiert hat. Prof. Dr. Oliver Friedrich und Prof. Dr. Mario Trieloff danke ich sehr dafür, dass sie sich bereit erklärt haben, Teil meines Prüfungskomitees zu sein.

Mein Bezug zu Mexiko und die Begeisterung für dieses Land begannen schon vor meiner Promotion im Jahr 2017, als ich im Rahmen einer Masterexkursion unter der Leitung von Wolfgang Stinnesbeck das erste Mal die faszinierende Kultur und Landschaft Mexikos kennenlernen durfte. Vielen Dank an dieser Stelle auch an Dr. Christina Ifrim, die ich zweimal begleiten durfte, um im Norden Mexikos nach dem größten Ammoniten der Welt zu suchen. Es hat mir sehr viel Spaß bereitet, und ich habe viele schöne Eindrücke und bleibende Erinnerungen mitgenommen.

Ein Großteil der Stalagmiten, die ich in meiner Arbeit untersucht habe, entstammt der Geländekampagne im Jahr 2018, bei der ich selbst jedoch nicht mit dabei war, da ich zu dieser Zeit mit meiner Masterarbeit beschäftigt war. Bei der Exkursion 2018 und der Bergung der Stalagmiten war ebenfalls Julia Becker vom Naturkundemuseum in Karlsruhe mit dabei. Ihr gilt mein besonderer Dank für ihren großen Einsatz und die umfangreiche Arbeit, die sie in die Entstehung dieses Projekts und die Bergung der Stalagmiten investiert hat. Besonders das detaillierte Protokollieren der Geländekampagne hat mir viele nützliche Hinweise geliefert. Ebenfalls beteiligt waren unsere mexikanischen Kollegen der „Grupo Espeleológico AJAU“ (Fátima Tec Pool, Carlos Evia und María José Gómez), die seit Jahren neben der Kartierung der Höhle vor allem die archäologischen Funde dokumentieren und untersuchen. Ein besonderer Dank geht an Jeronimo Avilés Olguín, der uns bei allen Exkursionen in den letzten Jahren, insbesondere bei den Höhlenbesuchen und der Navigation durch diese, begleitet hat. Es hat mir jedes Mal sehr viel Spaß gemacht. Für all deine Mühen und deinen endlosen Einsatz bin ich dir sehr dankbar! Ich freue mich auf ein hoffentlich baldiges Widersehen. Bedanken möchte ich mich außerdem bei Fernanda Lases-Hernandez, nicht nur für den wissenschaftlichen Austausch, sondern auch für den Besuch der wunderschönen Río Secreto Höhle.

Im Folgenden gilt mein Dank allen, die mit ihren Messungen und Analysen zur Datengrundlage meiner Dissertation beigetragen haben.
René Eichstädter möchte ich für die unzähligen U/Th-Datierungen danken, die er in den letzten Jahren für mich und dieses Projekt durchgeführt hat. Vielen Dank für deine bedingungslose Unterstützung – sowohl in wissenschaftlichen Belangen als auch bei privaten Belangen außerhalb des Uni-Alltags. Auch an die Hiwis aus dem Labor im 1. OG möchte ich hier ein großes Dankschön aussprechen.
Martina Schmidt und Michael Sabasch danke ich für die stabilen Isotopenmessungen an den Tropfwasserproben. Bei Stefan Rheinberger, Silvia Rheinberger und Christian Scholz möchte ich mich vielmals für die ICP-OES-Messungen bedanken sowie für das engagierte Mithelfen und Organisieren, wenn es darum ging, die Außenflächen rund ums Institut von Müll und Unrat zu befreien.
Stefan Rheinberger, Bernd Knape, Markus Greule, Alexa Fischer und Frank Keppler danke ich für die unzähligen stabilen Isotopenanalysen, die einen Großteil meiner Arbeit ausmachen. Ein großer Dank geht an dieser Stelle auch an die Hiwi's, die einen Teil der Proben gemillt und eingewogen haben: Danke an Antonia Wantzen, Alexander Karol Slavik und vor allem Johannes Thommes für das Einspringen beim Einwiegen der letzten Proben in der Endphase meiner Promotion.
Dominik Hennhöfer (Khalifa University, Abu Dhabi, inzwischen Hessisches Landesmuseum in Darmstadt) möchte ich ebenfalls für zahlreiche Isotopenmessungen danken sowie für das Auswerten der Daten im Nachgang. Vielen Dank für deine Bemühungen und deine Unterstützung.

Bedanken möchte ich mich auch bei Ilse Glass für die XRD-Analysen sowie bei Oliver Wienand und Ilona Fin für das Anfertigen der Dünnschliffe und das Polieren der Stalagmiten. Gregor Austermann, Anne Hildenbrandt sowie der Klaus Tschira Stiftung danke ich für die Nutzung ihres Mikroskops.
Mein Dank geht ebenfalls an Ronny Friedrich (CEZ Mannheim) und Marcus Christl (ETH Zürich) für die Radiokarbonanalysen. Ich danke auch Steffen, Elvira, Celine und den Hiwis aus dem C14-Labor für die Probenaufbereitung, Organisation und Datenauswertung. Ein besonderes Dankeschön geht noch einmal an Celine für die vielen Gespräche und Diskussionen rund um C14 und DCF, die mir besonders in der Endphase der Promotion eine große Hilfe waren.

Günther Balschbach (IUP) und Francisco Cueto (Geow), die die IT-Infrastruktur am Laufen halten und mich bei sämtlichen IT-Angelegenheiten unterstützen, möchte ich ebenfalls danken.
Ein herzliches Dankeschön geht an das gesamte Verwaltungsteam, das mich über die letzten Jahre bei allen möglichen administrativen Angelegenheiten unterstützt hat. Besonders danken möchte ich Torsten Hoffmann und Ayten Eicher vom Institut für Geowissenschaften sowie Karoline Thomas, Rebecca Benetatos, Angelika Gassama und Reinhold Beyer vom Institut für Umweltphysik.

Danke an die gesamte PUA-Gruppe für die schöne Zeit in den letzten Jahren und die Unterstützung bei allen möglichen Anliegen. Besonderer Dank gilt den Promovierenden und PostDocs der Gruppe (sowohl aktiven als auch inzwischen ehemaligen): Andrea, Sophie, Thomas, Steffen, Evan, Jasmin, Marleen, Inga, Eva, Elvira, Yao, Sahra und Aaron. Danke für eure Unterstützung bei diversen Angelegenheiten sowie die schöne Zeit, sei es beim Mittagessen, Grillen oder der einen oder anderen Runde Darts nach Feierabend.

Abschließend möchte ich mich bei meiner Familie bedanken, die mir dieses Studium erst ermöglicht hat und mich in all den Jahren immer unterstützt und in dem, was ich tue, bestärkt hat. Vielen Dank dafür! Ein ganz besonderer Dank geht an Sahra, die mich immer und überall unterstützt und an mich glaubt. Besonders in den letzten Wochen hast du es immer wieder geschafft, mich positiv zu stimmen und zu motivieren. Danke, dass du stets für mich da bist! Ich bin sehr froh, dich in meinem Leben zu haben und werde dich beim Erreichen deiner Ziele ebenfalls mit all meiner Kraft unterstützen.